THE UNIVERSITY *of* EDINBURGH

THE UNIVERSITY OF EDINBURGH
Division of Neuroimaging Sciences
Centre for Clinical Brain Sciences

P H D T H E S I S

to obtain the title of

PhD of Science

of the University of Edinburgh
Specialty : Neuroimaging & Computer Sciences

Defended by

Islem Rekik

Novel Mathematical Modeling Approaches to Assess Ischemic Stroke Lesion Evolution on Medical Imaging

Thesis Supervisors :

Prof. Joanna Wardlaw - BRIC, The University of Edinburgh, UK
Dr. Trevor Carpenter - BRIC, The University of Edinburgh, UK
Dr. Stephanie Allassonniere - CMAP, Ecole Polytechnique, France

Examiners :

Prof. Malcolm Macleod - CCBS, The University of Edinburgh, UK
Prof. John Ashburner - Wellcome Trust CIN, University College London, UK

submitted on December 4, 2013
defended on March 31, 2014

Novel Mathematical Modeling Approaches to Assess Ischemic Stroke Lesion Evolution on Medical Imaging

Declaration:

I declare that the research described within this thesis is my own work and that this thesis was composed by myself unless otherwise stated.

Neither this thesis nor any part thereof has been submitted for any other degree or professional qualification.

Name: Islem Rekik

Signature:

Date: 04/12/2013

Novel Mathematical Modeling Approaches to Assess Ischemic Stroke Lesion Evolution on Medical Imaging

Abstract:

Stroke is a major cause of disability and death worldwide. Although different clinical studies and trials used Magnetic Resonance Imaging (MRI) to examine patterns of change in different imaging modalities (eg: perfusion and diffusion), we still lack a clear and definite answer to the question: "How does an acute ischemic stroke lesion grow?" The inability to distinguish viable and dead tissue in abnormal MR regions in stroke patients weakens the evidence accumulated to answer this question, and relying on static snapshots of patient scans to fill in the spatiotemporal gaps by "thinking/guessing" make it even harder to tackle. Different opposing observations undermine our understanding of ischemic stroke evolution, especially at the acute stage: viable tissue transiting into dead tissue may be clear and intuitive, however, "visibly" dead tissue restoring to full recovery is still unclear.

In this thesis, we search for potential answers to these raised questions from a novel dynamic modeling perspective that would fill in some of the missing gaps in the mechanisms of stroke evolution. We divided our thesis into five parts. In the first part, we give a clinical and imaging background on stroke and state the objectives of this thesis. In the second part, we summarize and review the literature in stroke and medical imaging. We specifically spot gaps in the literature mainly related to medical image analysis methods applied to acute-subacute ischemic stroke. We emphasize studies that progressed the field and point out what major problems remain. Noticeably, we have discovered that macroscopic (imaging-based) dynamic models that simulate how stroke lesion evolves in space and time were completely overlooked: an untapped potential that may alter and hone our understanding of stroke evolution. Progress in the dynamic simulation of stroke was absent –if not inexistent.

In the third part, we answer this new call and apply a novel current-based dynamic model âpreviously applied to compare the evolution of facial characteristics between Chimpanzees and Bonobos [Durrleman 2010] – to ischemic stroke. This sets a robust numerical framework and provides us with mathematical tools to fill in the missing gaps between MR acquisition time points and estimate a four-dimensional evolution scenario of perfusion and diffusion lesion surfaces. We then detect two characteristics of patterns of abnormal tissue boundary change: spatial, describing the direction of change –outward as tissue boundary expands or inward as it contracts–; and kinetic, describing the intensity (norm) of the speed of contracting and expanding ischemic regions. Then, we compare intra- and inter-patients estimated patterns of change in diffusion and perfusion data. Nevertheless, topology change limits this approach: it cannot handle shapes with different parts that vary in number over time (eg: fragmented stroke lesions, especially in diffusion scans, which are common).

In the fourth part, we suggest a new mathematical dynamic model to increase rigor in the imaging-based dynamic modeling field as a whole by overcoming the topology-change hurdle. Metamorphosis. It morphs one source image into a target one [Trouvé 2005]. In this manuscript, we extend it into dealing with more than two time-indexed images. We propose a novel extension of image-to-image metamorphosis into longitudinal metamorphosis for estimating an evolution scenario of both scattered and

solitary ischemic lesions visible on serial MR. It is worth noting that the spatiotemporal metamorphosis we developed is a generic model that can be used to examine intensity and shape changes in time-series imaging and study different brain diseases or disorders.

In the fifth part, we discuss our main findings and investigate future directions to explore to sharpen our understanding of ischemia evolution patterns.

Keywords: Stroke evolution modeling, perfusion imaging, diffusion imaging, spatiotemporal modelling, longitudinal metamorphosis

"Even if the end of time is upon you and you have a seedling in your hand, plant it!"

by Muhammed PBUH.

Acknowledgments

After an amazingly enriching and delightful research journey that I passionately enjoyed under the invaluable guidance of my supervisors Prof. Joanna Wardlaw, Dr. Trevor Carpenter and Dr. Stéphanie Allassonnière, I would like to start by warmly and wholeheartedly thank them: thank you for your invaluable tips and tricks, constructive feedback suggestions, and uplifting and motivating encouragement, which were always timely. I have learned a lot from your deep scientific knowledge and skills and outstanding visions and guidance. Thank you for building on my strengths and showing me the way towards excellence and uniqueness. I also thank them for pouring their time and cutting-edge expertise into this project to bring it into life and helping me to publish it in scientific journals. I am also very thankful to them for the financial support that enabled me to present my work at international research conferences and set up new promising collaborations. I will always cherish in my heart our thought-provoking and constructive discussions from which I learned multidimensional thinking. Thank you for teaching me how to walk the scientific path and enjoy the talk and contribute to the progress of science while keeping the margins of a critical mind intact. I am extremely grateful.

I am very grateful to the reviewers, Prof. Malcolm Macleod, Prof. John Ashburner for having spent their precious time to read and correct this long manuscript, and for being part of my jury. It has been such a delight and a great honor to present and explain my work to you. I warmly thank them for their constructive comments on my work. Thank you.

I am also extremely grateful to the sources which funded my PhD work: the Scottish Funding Council through the Scottish Imaging Network, A Platform for Scientific Excellence (SINAPSE) Collaboration (http://www.sinapse.ac.uk/), the Centre for Clinical Brain Sciences (CCBS), the Tony Watson Bequest and a Scottish Overseas Research Award from the University of Edinburgh (to myself), the

Scottish Funding Council SINAPSE Collaboration (to Prof. Joanna Wardlaw), the Cohen Charitable Trust (to Dr. Trevor Carpenter), the Chief Scientist Office of the Scottish Government.

I am hugely indebted to all the Brain Imaging Research Center (BRIC), CCBS and SINAPSE members for their warm welcome and support and the great opportunities they offered us to come together for scientific and social purposes. I am also extremely grateful to Moira Henderson for her kind help and patience sorting all of my conference receipts out and to Kristen Shuler and Dominic Job for helping me along the way with different tasks.

I sincerely thank the brilliant and cheerful minds I shared good times with in the PhD Annexe: Xin Wang, Anna Jones, Natalie Royle, Andreas Glatz, Anna Heye, Stewart Wiseman, David Dickie, Jehill Parikh and Simon Cox. I also warmly thank Sam Preston for providing me with the AtlasWerks library and for Dr. Stanley Durrleman for sharing with us his current-based surface matching source code.

I owe a great amount of gratitude to all the people who believed in me and made me into who I am today with their boundless love: pointing out my own faults and showing me their unswerving support and encouragements in times of difficulties and ease alike. To my wonderful parents Hayet and Abdelmajid, my soul-sister Arwa who never gave up on me and whose beautiful words are engraved in my heart '*"You've got the heart and soul to do it and bring out the best in your field and in whatever you set your mind to"*, to my brother Muhammed Ali and all my family members, I pay tribute and give my most heartfelt thanks. To all my friends for their beautiful prayers, enlightening wisdom and never-ending support and patience, in particular my beloved sisters Refka Ben Romdhane, Sana Abidi, Fadoua Guezzi Messaoud, Najet Neji, Sameh Ben Fredj, Dorra Wechtati, Yosra Mani, Sirine Kharroubi, Carmen Elez, Gosia Dobosz, my friend Pawel Stankiewicz and the beautiful and warm hearts I met in Majlis Naseeha Baltimore Maysa Elsheikh, Arooj Aslam, Sarah H.

Abdelbarr, Petrina Boucher, Aamir Ali, Rafee Al-Mansur and Sharif Braxton, I extend my most sincere and cosmic thanks and prayers. I would like to extend my most sincere love, prayers, respect and gratitude to both my teachers Sh. Amer Jamil and Sh. Ruzwan Muhammad and all the beautiful souls I met in Edinburgh and the UK and in iSyllabus. The love I received and the things I learnt are priceless. And first and foremost, all my gratitude goes to the One and Only who revealed to Muhammed peace and blessings be upon him the very first word that changed my life forever: *"Read"*.

Ever-grateful!

Contents

Part I - Stroke and Medical Imaging

"Ideas don't just arise of their own accord: there has to be an entry route, a natural line of thought that leads in the right direction, a bridge across the unknown. [...] Nobody knows where all this will end, but it sure is exciting."

Ian Stewart; From here to infinity 1

Stroke Evolution

"Anyone who has carried out scientific research knows that data are uncertain, that much depends on the way they are interpreted, and that all methods have their limitations."

Rupert Sheldrake; Science Delusion **105**

Part IV - From Image-to-image to Longitudinal Metamorphosis

"Mathematics is much like the Mississippi. Its delta is research mathematics: it is growing, it is going somewhere (but it may not always be apparent where), and what today looks like a major channel may tomorrow clog up with silt and be abandoned. Meanwhile a minor trickle may suddenly open out into a roaring torrent. The best mathematics always enriches the mainstream, sometimes by diverting it in an entirely new direction."

Ian Stewart; From here to infinity

Part I
Stroke and Medical Imaging

"*Ideas don't just arise of their own accord: there has to be an entry route, a natural line of thought that leads in the right direction, a bridge across the unknown. [...] Nobody knows where all this will end, but it sure is exciting.*"
Ian Stewart; From here to infinity

Chapter 1

Introduction

Contents

1.1 Context of the thesis

Stroke is a common cause of death and the commonest cause of serious dependence and long-term disability in adults [Bonita 1992, Sudlow 1997]. Ischemic stroke is the commonest type (80%) and presents suddenly following the occlusion of a brain artery. Brain imaging is important to diagnose ischemia and may identify patients most suited to acute treatment or not. There is a lack of evidence to why some patients recover or not. Imaging can help tackle this problem. This introduction will set the scene for key aspects of stroke as a disease and key aspects of what imaging can tell us about stroke-specific, tissue-specific and patient-specific features of ischemia. It will also give an overview of how this thesis is going to investigate these multiple aspects.

The early diagnosis of the stroke lesion is preferably limited to a 4.5h therapeutic time window for the use of 'clot-busting' (thrombolytic) drugs to recanalize the occluded artery. In a context where "time is brain" [Saver 2006], multi-modality brain imaging is available and, in some places, is widely used in acute stroke management for diagnosis, prognosis and treatment planning. Diffusion-weighted (DWI) and perfusion-weighted (PWI) imaging is commonly used to detect early ischemic changes and attempts to distinguish between permanently damaged and salvageable tissues. Although medical imaging has improved our understanding of stroke for the last decades, there is still no best treatment for stroke. As Dame Nancy Rothwell pointed out: "The hundreds of (clinical) trials in stroke have failed for all sorts of reasons, sometimes for unknown reasons. Even though that is a disease that affects millions of people, there are virtually no big companies left in the stroke research now. So many failures, often called 'the graveyard' ". There are many reasons for the failure of many drugs, developed from mechanistic understanding of stroke, to realize their promise seen in early experimental models, but it is not the role of this thesis to examine these multiple reasons for these failures in detail.

Images of the stroke lesion obtained over time, produced using serial imaging, provides consecutive stroke lesion 'snapshots' that show the dynamic aspect of stroke evolution and the wide variability in

lesion features (location, volume, shape, gray-scale intensity) – underlining its complexity. "Dynamic" and "complex": both of these aspects of stroke lesion evolution challenge the medical imaging research field to address two main questions:

1) how does a stroke lesion grow? and

2) can sophisticated mathematical models advance our understanding of its dynamics and assist clinicians in its management?

Understanding the dynamics of ischemic lesion evolution may help discriminate accurately between tissue that is still viable at the time of assessment and could be salvaged with thrombolytic treatment, and dead tissues. Imaging could help to characterize the stages of ischemic tissue damage and determine more efficient treatment methods to terminate its progression and –if possible– reverse the observed damage. However, in the stroke research literature, there is an absence of dynamic models of the continuous evolution of ischemic stroke from MR images. Previous studies used basic thresholding of images or volumetric subtraction of one image from another and standard statistical methods to explore stroke evolution pattern(s). However, only rather small steps were made in the last decade on the big questions: What factors drive stroke lesion evolution? Is there a potential "blueprint" of the dynamics of lesion evolution in stroke patients? What can perfusion and diffusion time-series imaging tell us about its dynamics? Can a unique perfusion threshold fit into a population of stroke

patients and distinguish between dead and at-risk tissues or is one threshold too simplistic? Does lesion morphology matter – e.g. do scattered stroke lesions evolve differently from solitary lesions?

To date, no clear-cut answers are available and stroke is still a highly challenging research field. On the one hand, medical image analysis methods and computational models for studying other brain diseases such as tumors, multiple sclerosis, Alzheimers disease, or bipolar disorders have made major progress [Commowick 2008, Meier 2003, Bosc 2003, Yotter 2010, Chen 2010, Lorenzi 2010, Lorenzi 2012a, Lorenzi 2012b]. On the other hand, we notice a poor interweaving between different research streams in stroke and sophisticated medical image analysis and modeling methods, meaning that image analysis in stroke can be said to lag somewhat behind other neurological areas. Furthermore, the rather limited stroke-to-medical image analysis interface has developed with some questionable assumptions about how stroke lesions evolve, what they look like on imaging, how patient-related factors might constrain certain types of imaging, etc. The subject will be reviewed in detail in the following chapter, but it is fair to say that interrogation of information in brain images of patients with stroke have generally not been investigated sufficiently using well-designed mathematical models for stroke that integrate the biological phenomena which are thought to be responsible for driving stroke evolution, or to explore others that

might affect tissue outcome.

It was all the aforementioned questions, plus an apparent lack of progress amongst stroke researchers to adopt some truly modern medical image analysis techniques, that motivated the development of this thesis and in particular stimulated our interest in the dynamic modeling of stroke lesion evolution. We are still far away from having a patient-specific model that accurately predicts the evolution of dead and salvageable ischemic tissues. However, we believe that dynamic modeling when applied to stroke lesions could strongly contribute to reshaping the way we approach stroke and understand its progression and factors that influence its development.

Stroke research suffers from two main barriers: one 'barrier' is the thrombus in the brain artery that causes the disease; the other is in the understanding of the stroke lesion dynamics. Both barriers need to be overcome. This thesis is an attempt to examine stroke lesions on imaging in a new way that might broaden how researchers think about stroke and remove barriers to understanding of stroke lesion evolution.

1.2 Problems investigated

The general context and previous gaps suggest that stroke research is at a crossroads where there are unprecedented opportunities to combine brain imaging methods with very sophisticated medical image

analysis methods to advance understanding of stroke pathophysiology. We begin this thesis by examining some new research directions to model ischemic stroke in the light of an exhaustive literature search and different 'interpretations' derived from examining stroke brain scans. We then attempt to provide some clarity about the dynamics of stroke lesions using both diffusion and perfusion MR longitudinal data. To follow our interest in modeling the dynamic evolution of acute ischemia, two main questions stimulate our thinking: are there any ready-made models in the literature that may accurately explain the clinical observations or should we develop a novel mathematical model of stroke lesion evolution?

This thesis investigates both of these modeling alternatives. However, it does not aim to provide solutions to all the aforementioned problems in stroke, but rather to explore new directions that challenge some weaknesses in previous image analysis methods applied to stroke and overcome their major limitations. In this respect we focus on two main problems:

1. *Reviewing stroke literature from a medical image analysis perspective:* Brain imaging and image processing have advanced and there is a scope for using these tools much more innovatively to understand processes occurring in the ischemic tissue. There are many limitations if we only examine 2D/3D cross-sectional images and snapshots as opposed to 3D plus time (ie. 4D or spatiotemporal) obser-

vations. Examining stroke and medical image analysis literature will enable us to shed light on two questions:

- What are the major barriers to advancing progress in stroke diagnosis and assessment?
- Are there any untapped modeling potentials in stroke for us to explore from a medical image modeling perspective?

2. *Modeling the spatiotemporal evolution of stroke lesions:* Dynamic modeling is a novel concept to evaluating stroke lesion evolution. We desire to model stroke lesion evolution using time-series MR images in a framework that encapsulates the variation in lesion boundary, shape and intensity and thus to identify what patient-specific, stroke-specific or tissue-specific factors influence these changes. This raises two main questions:

- Can we find or develop a mathematical patient-specific model that simulates the evolution of a wide spectrum of stroke lesions that reflect the variability of stroke lesions (solitary vs. scattered) in clinical patients?
- Can we relate the dynamic features estimated by the defined model to tissue-specific, stroke-specific and patient-specific features to quantify factors that influence pathological patterns?

1.3 Organization of the thesis and main contributions

The thesis is organized in three parts representing the three main contributions:

1. Reviewing the literature, identifying medical image analysis and computational models applied to human and animal stroke using both MR and CT data.

2. Modeling the spatiotemporal evolution of solitary stroke lesions as seen on diffusion and perfusion imaging using the current-based diffeomorphic regression model and evaluation using clinical data.

3. Development of longitudinal metamorphosis to simulate the evolution of solitary and scattered stroke lesions in both shape and intensity and evaluation using tissue-specific, stroke-specific and patient-specific data.

The definition of patient-specific used in this thesis implies that any features/measurements estimated from the model are specific to that patient's clinical data (age, gender, vascular risk factors, prior history, for example). Stroke-specific refers to features about the stroke (time from onset, neurological severity and features, etc). Tissue-specific refers to individual changes in the tissue (eg diffusion or perfusion values, background brain changes such as leukoaraiosis which might

affect the ability of the brain to withstand ischemia).

The thesis is divided into five main parts and parts are further divided into different chapters. The material covered in each chapter is as follows.

Part I: Stroke and Medical Imaging

Part I has two further chapters:

Chapter 2 provides a general background on stroke and more specifically ischemic stroke. It also introduces current acute intervention and disease management strategies.

Chapter 3 provides an overview of the use of medical imaging in acute stroke particularly the use and limitations of MR imaging methods. It also presents some imaging-dependent and biology-dependent issues, frequently encountered in ischemic stroke and suggests new ways of handling them.

Part II: Survey of Medical Image Analysis Methods in MR/CT-imaged Ischemic Stroke

Chapter 4 examines different semi-automatic or fully automatic 2D/3D medical image analysis methods and mathematical models that have already been applied to human, animal and/or simulated ischemic stroke to tackle one of the following three problems: (1) segmentation of infarcted and/or salvageable (also called penumbral) tissue, (2) prediction of final ischemic tissue fate (death or recovery) and (3) dynamic simulation of the evolution of the lesion core and/or

penumbra. To highlight the key features in the reviewed segmentation and prediction methods, we propose a common categorization pattern. We also emphasize some key aspects of the methods such as the imaging modalities required to build and test the approach presented, the number of patients/animals or synthetic samples, the external user interaction and the methods of assessment (clinical or imaging-based). Furthermore, we investigate how any key difficulties, posed by the evolution of stroke such as swelling or reperfusion, were detected (or not) by each method. By depicting the major pitfalls and the advanced aspects of the various methods reviewed, we present an overall critique of their performances and concluded our discussion by suggesting some recommendations for future research work focusing on one or more of the three problems that are addressed.

This critical appraisal identified new unexplored directions to focus on: stroke dynamic modeling.

Part III: Current-based Dynamic Modeling of Stroke Evolution

Chapter 5 investigates whether the current-based diffeomorphic model, developed in the field of statistical modeling for measuring the variability of anatomical surfaces, could estimate the patient-specific spatiotemporal continuous evolution for MR PWI and DWI lesions. We simulate the 4D evolution of DWI and PWI stroke lesions. We introduce the tools to compare the dynamic behavior of DWI and

PWI lesions by extracting kinetic features such as speed of lesion surface deformation and the location and the magnitude of the highly contracting and expanding areas. This provides us with interesting dynamic insights into stroke lesion behavior and an opportunity to search for common patterns of evolution. The current-based diffeomorphic model proved to be a mathematically robust representation of the lesion surface but was only able to model solitary lesions, i.e it could not model ischemic lesions consisting of several scattered components. More importantly, this model cannot incorporate intensity measures (eg perfusion-diffusion values) in its abstract mathematical framework, but only the geometry of the lesion surface. To overcome both of these limitations, we used a more versatile model: the metamorphosis model.

Part IV: From Image-to-image to Longitudinal Metamorphosis

Chapter 6 introduces the metamorphosis theory from which is derived the image-to-image metamorphosis model. The metamorphosis model is able to handle multi-component and solitary lesions and incorporates serial image intensities in the 3D image evolution. It deforms one source image into another in continuous time and space intervals. It is unique in its mathematical formulation, as it allows us to track both the change in grey-scale intensity and in velocity of lesion deformation between timepoints. In this chapter, we propose a novel

extension of image-to-image metamorphosis into longitudinal metamorphosis for estimating an evolution scenario, in patients with acute ischemic stroke, of both scattered and solitary ischemic lesions visible on MR perfusion and diffusion imaging (Chapters 7 and 8). This approach is generic as it could be applied to any medical data, can estimate and analyze the variability in images (gray-scale or binary), and extract scalar (intensity change) and kinetic (velocity change) characteristics from longitudinal metamorphosis. Therefore, it can be applied to characterize the evolution of different pathologies, brain disorders and lesions. This could be a new branch of computational patho-anatomy that may contribute to progress in the field.

Chapter 7 presents the first application of the longitudinal metamorphosis model using perfusion time-series images.

Chapter 8 presents a second application of the longitudinal metamorphosis model using diffusion and T2-w images.

Part V: Conclusions and perspectives

In this final chapter (Chapter 9), we discuss the implications for future research and clinical practice in stroke. We also expand on the potential application of our metamorphosis modeling approach to other brain diseases and we conclude this thesis with the list of contributions.

Chapter 2

Stroke

Contents

2.1 Epidemiology, subtypes and pathophysiology

Stroke was one of the first brain diseases to be identified in medical history. Its description dates back to the 2^{nd} millennium where Hippocrates was the first to name it in his pioneering writings on a strange phenomenon that caused sudden paralysis when it strikes patients: apoplexy –ie meaning in Greek "struck down with violence". However, it was in 1658 that the understanding of stroke began to deepen with the publication of "Apoplexia" by Johann Jacob Wepfer [Thompson 1996]. His discovery of the main brain arteries and the causes of ischemic stroke opened up new search lines for a better understanding of what happens in the brain when a stroke occurs. This discovery marked the beginning of research in the etiology of

stroke. Eventually in the 1970s, stroke was properly identified as a cerebrovascular disease by the World Health Organization and defined as a "neurological deficit of cerebrovascular cause that persists beyond 24 hours or is interrupted by death within 24 hours". Interestingly, this definition is more and more seriously debated nowadays since the advent of CT and MR imaging have demonstrated presence or absence of tissue damage which may be reversible, and has led to the introduction of the concept of 'tissue' rather than 'time' based definitions of stroke [Sacco 2013].

Prior to the stroke episode disturbing the cerebral blood flow, we generally see a well functioning brain: neurons getting their oxygen and nutrients from the blood across the thin walls of the cerebral capillaries and they are well protected by glia cells and the blood-brain barrier (controlling which 'blood elements' can pass through to neurons). Two types of stroke can dramatically disrupt this normality:

- **Hemorrhagic stroke:** A brain hemorrhage occurs when a cerebral blood vessel bursts and blood leaks into or around brain tissue and causes failure of neuronal function. About 15-20% of strokes are hemorrhagic. High blood pressure stretches a cerebral artery wall and causes it to bleed. This results in blood leaking into the brain tissue (ie. intracerebral hemorrhage) or into the spaces surrounding the brain –eg meninges or cerebrospinal fluid around the brain (ie. subarachnoid hemorrhage)

(Figure 2.1). Hemorrhagic strokes account for approximately 20% of all strokes.

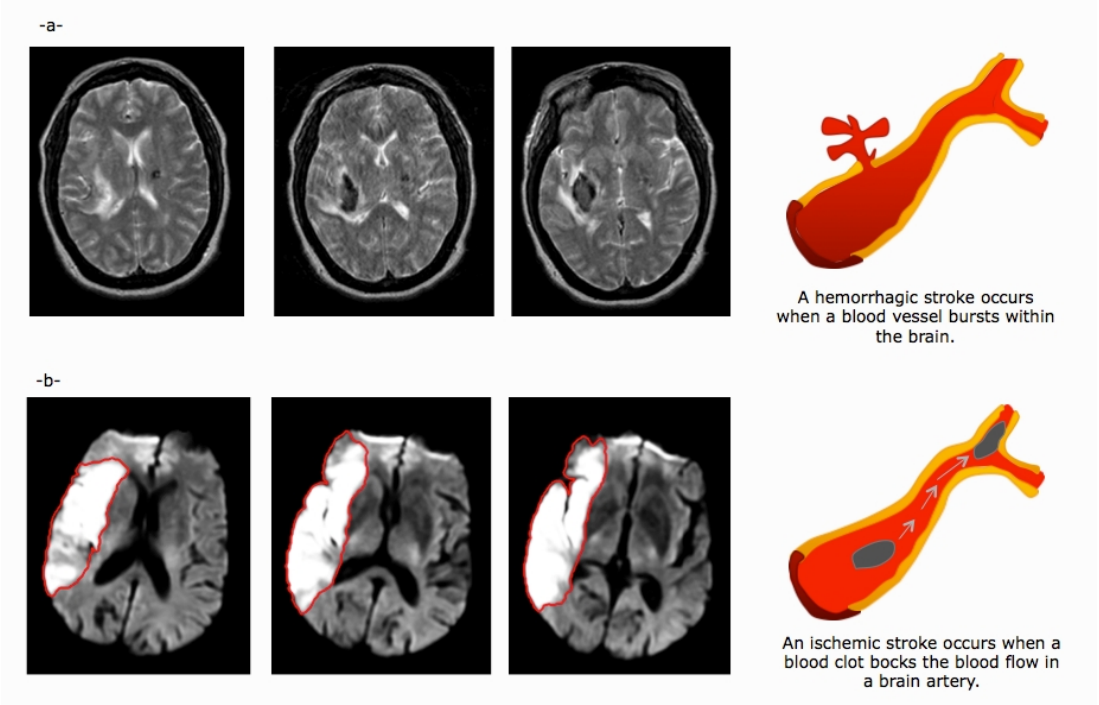

Figure 2.1: *Subtypes of stroke.* (a) Three axial slices from a T2-weighted MR brain scan showing a decrease in signal indicating a recent hemorrhagic stroke in the posterior aspect of the right lentiform nucleus. (b) Axial slices showing an ischemic stroke lesion on MR diffusion weighted imaging.

- **Ischemic stroke (brain ischemia)** The commonest type of stroke (80%) is an ischemic stroke, resulting from disruption of blood flow within the brain caused by occlusion of an artery usually by an embolus from the heart or from atheroma in the neck, or from acute thrombotic occlusion of an artery inside the head. This deprives the brain in the affected arterial territory of oxygen and nutrients and initiates a dynamic sequence of patho-

physiological events. The spatial progression of ischemic stroke is generally confined to one or more vascular territories as affected by the artery occlusion. The evolution of the tissue injury can take many weeks to evolve to a final 'scar' after stroke onset. The commonest injured cerebral territory is that of the middle cerebral artery (MCA) territory.

Where the blood flow interruption is too severe or for too long, cell death by necrosis or apoptosis occurs and an irreversibly injured infarct core is formed. If the blood supply is less badly disrupted, or the disruption only lasts for a short period of time, then the brain tissue may recover completely, or may survive for a variable period of time in a 'shut down' but viable state that can recover if blood flow is restored quickly enough.

Blood clots dissolve naturally, but often not quickly enough to prevent permanent tissue damage. This potentially reversibly damaged brain tissue is thought to surround the ischemic lesion core and is referred to as the "ischemic penumbra". The concept was first introduced by Symon and colleagues [Symon 1980] (Figure 2.2). The neurons in the penumbral tissue are functionally shut down, resulting in loss of neuronal function in all the tissue where blood flow has fallen below the critical blood flow level required to sustain neuronal function (hypoperfusion). Indeed, the reversibility of ischemic abnor-

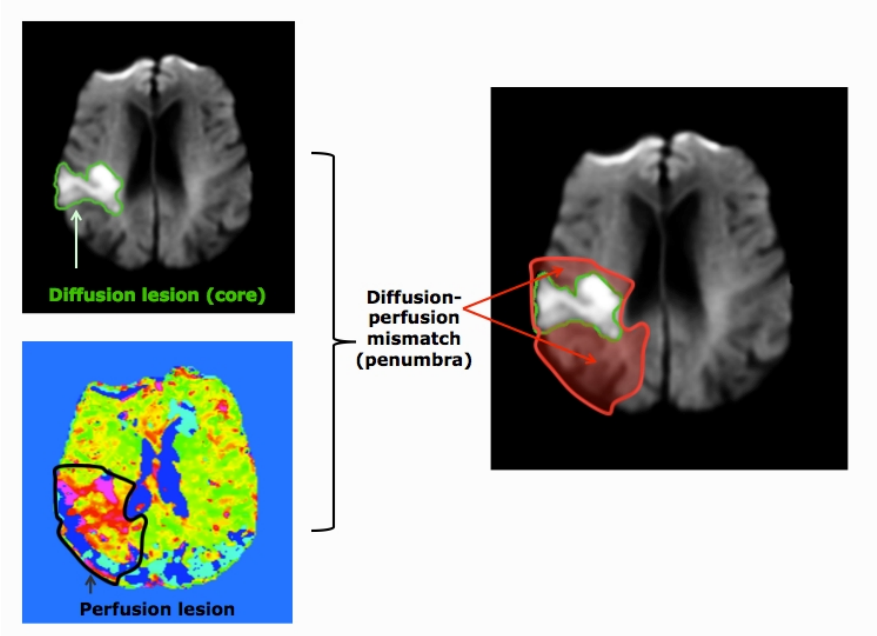

Figure 2.2: *MR Perfusion-diffusion 'mismatch'.* The 'mismatch' area corresponds to the red-shadowed area that represents the spatial difference between the diffusion lesion (top left image outlined in green) and the perfusion lesion (lower left image outlined in black). It is commonly thought that the perfusion lesion surrounds and includes the diffusion lesion as in the right hand image. Therefore, the 'mismatch' area is part of the hypoperfused ischemic area.

mality and the cascade of pathophysiological tissue changes depend on critical levels of blood flow as shown in figure 2.3. In complete absence of blood flow, neuronal viability can only be maintained for 2-3 minutes. Data from stroke studies [Astrup 1981, Bandera 2006] suggested that if the blood flow is moderately reduced (<35ml/100g/min) the electrical activity of neurons seems to shut down without affecting the tissue viability (benign oligaemia). At lower blood flow levels, eg ranging between 20 and 25 ml/100g/min, brain tissue shows the first 'penumbral' signs of early cell membrane failure as the cell membrane pumps start to fail and brain cells swell up (ie. intracellular edema). If the blood flow is not restored and continues to drop to less than 12ml/100g/min, then the penumbral tissue will proceed to infarction and the original core lesion will grow to occupy a larger part of the brain with much greater functional disability than if less tissue had been permanently damaged. Although previous observations showed that below certain blood flow levels neurons will start to die, there is little evidence from humans of how long the tissue can survive at particular flow levels.

From stroke onset, if the blood flow is not restored, a cascade of critical events starts as the functioning of sodium-potassium cell membrane pumps, and calcium pumps in the affected neuronal cells is interrupted during the acute stage (3 - 24 hours) and the blood brain barrier (BBB) breaks down during the subacute stage (2 days

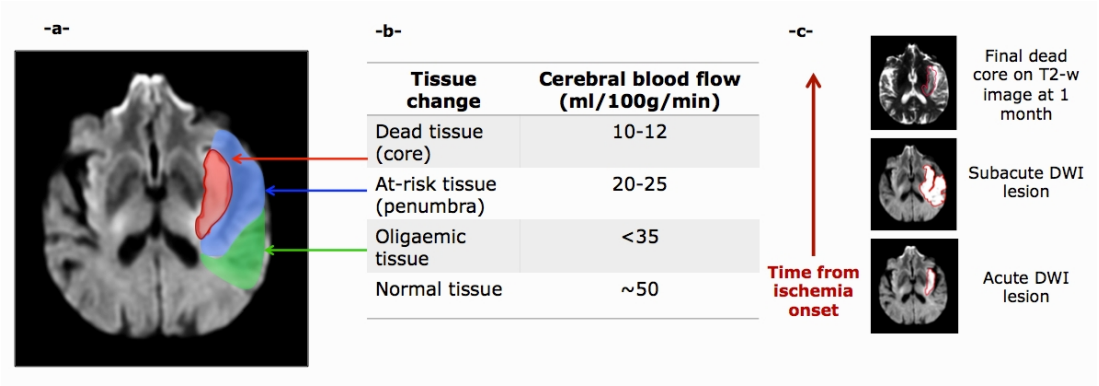

Figure 2.3: *Cerebral blood flow thresholds for electrical shutdown and then neuronal cell death.* (a) Axial diffusion-weighted imaging showing different areas thought to be associated with a specific ranges of cerebral blood flow values: (1) the oligaemic tissue with a slightly decreased blood flow that does not affect the viability of brain cells (green), (2) the at-risk of infarction or 'penumbral' tissue where neurons ceased to function (electrical shutdown) but are structurally still intact (blue) and (3) the dead infarcted core where severely hypoperfused brain cells have died (red). (c) Three axial slices illustrating the lesion changes from acute to final stages (bottom to top). We can clearly see the diffusion lesion core progression from acute to subacute timepoints, then a part of the subacute ischemic diffusion tissue reversing back to normal ('healing') as shown in the final T2-w image.

- 2 weeks):

- *Sodium-Potassium (Na^+-K^+) pump interruption*: In a normally functional brain cell, 3 Na^+ ions are pumped out of the brain cell and 2 K^+ ions are pumped in to maintain the cell's electrical potential. Ischemic stroke causes passive diffusion of Na^+ ions (Sodium influx) into the cells which leads to a rapid accumulation of Sodium in the intracellular space, therefore disrupting the equilibrium between fluid concentrations inside and outside the cells (the osmotic equilibrium). Furthermore, the extracellular space starts to suffer from a relative decrease in Na^+ ions and increase in K^+ ions. To maintain the osmotic equilibrium of the injured cells, water molecules shift from the extracellular into cells –causing swelling of these cells and eventually leading to cytotoxic edema without causing a net increase in brain volume or brain fluid (Figure 2.4- 2.5). Later brain tissue swells up and volume increases.

- *Calcium (Ca^{2+}) pump interruption*: In the normal brain tissue, when neurons are not firing they are polarized (inside negatively charged and outside positively charged). When enough positive Ca^{2+} ions cross the cell membrane, a change in the negative/positive membrane charge takes place (called depolarization). In the ischemic tissue, calcium channels can stay open for

a long time which increases Ca^{2+} ions influx into cells, slowing the damaging of the intracellular walls and ultimately causing cell necrosis and apoptosis.

- *Blood brain barrier (BBB) breakdown*: Ischemic damage of the capillary endothelial cells that form the BBB allows water to come out of the blood vessels and accumulate in the extracellular space. This also contributes to the appearance of the vasogenic edema which causes an absolute increase in the net volume of water in the ischemic tissue (Figure 2.4).

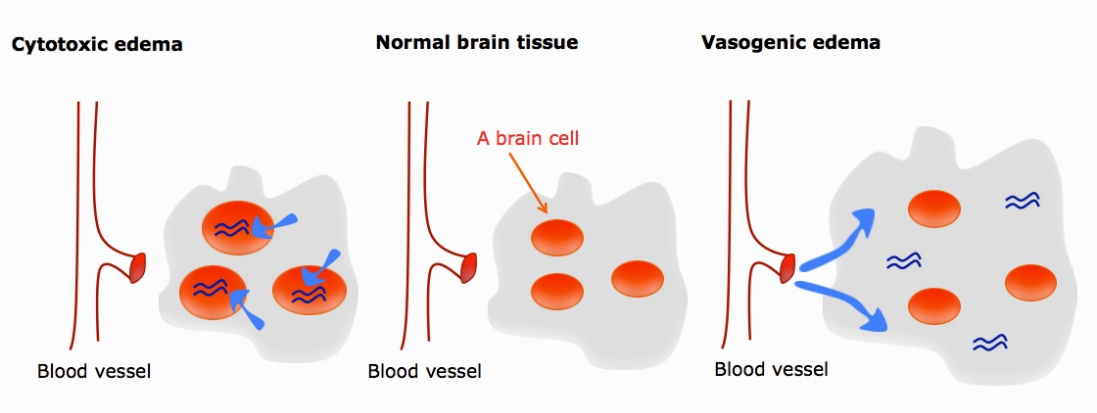

Figure 2.4: *Cytotoxic and vasogenic edema following an ischemic stroke.* Left: The cytotoxic edema happens when water shifts from the extracellular space into cells without causing a net increase in brain fluid. Right: The vasogenic edema happens when water comes out of blood vessels and accumulates in the extracellular space which increases brain fluid/volume.

If blood flow is restored quickly (within a few minutes to hours at most) and cells survive, then the edema can recover and there is little BBB breakdown and so little vasogenic edema and the tissue

may eventually recover leaving no scarring. If on the other hand the tissue has died, then during later stages (eg 2 weeks - 3 months), inflammatory cells invade the damaged tissue and 'mop up' dead cells to leave a scar where the normal brain was originally (Figure 2.5). We will explain in more detail in Sections 3. 3.2 and 3. 3.3 how this shows on MR brain imaging of ischemic stroke.

Since the 1970s, salvage of this penumbral tissue has been the main target of stroke therapy [Astrup 1977, Astrup 1981, Ginsberg 1997, Wardlaw 2010, Wardlaw 2012]. In this thesis, we only focus on studying the evolution of ischemic stroke as seen on imaging.

2.2 Acute intervention for ischemic stroke

Identifying effective stroke treatments remains a difficult challenge since it is assumed that the penumbral tissue is only salvageable within the first few hours after onset of ischemia [Wardlaw 2010]. Therefore, the main therapeutic decisions are to quickly recanalize the main blocked artery to prevent the infarct expansion. This can be done by thrombolytic drugs that dissolve clots or mechanical extractions [Wardlaw 2012]. We will discuss this later (see below).

Imaging methods could play a key role in defining the extent of tissue at risk of infarction if it were possible to define perfusion levels or changes in tissue imaging signatures that indicated viable or non-viable tissue reliably [Dani 2012]. Indeed, imaging using positron

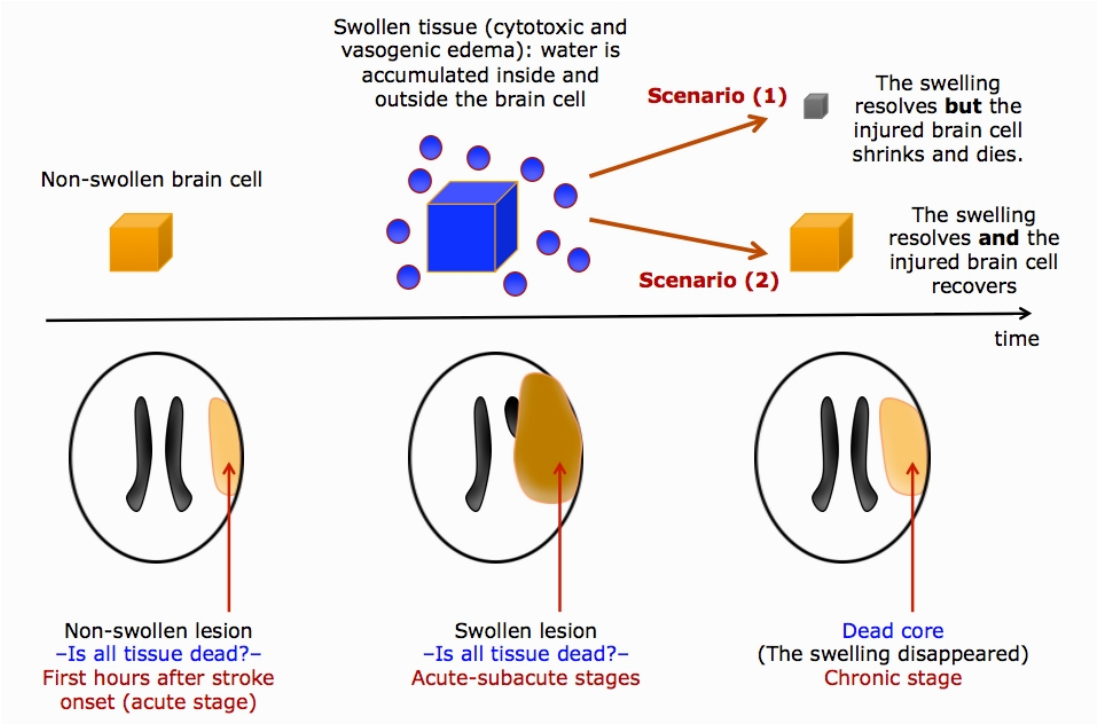

Figure 2.5: *The impact of swelling on ischemic stroke lesion development.* As the ischemic brain tissue swells up, two different scenarios can be envisioned: (1) the cerebral blood flow will be restored (spontaneously or with thrombolytic treatment), the swelling would resolve with time but the injured tissue will shrink to a scar as it was already dead, or (2) the cerebral blood flow will be restored quickly, the cells would recover, the swelling would resolve and the injured tissue will recover.

emission tomography (PET) [Marchal 1993, Baron 1999, Heiss 2000] was the first method in humans to demonstrate the existence of penumbral tissue by identifying areas where there was low blood flow but persisting increased oxygen extraction from the blood and ongoing glucose metabolism. In contrast, areas that had progressed beyond the point of no viability showed low flow and no glucose metabolism or oxygen extraction from the blood.

PET is not widely available and is not a practical technique for use in acute stroke diagnosis. More practical and available methods include CT or MR with perfusion imaging. MR offers considerable opportunities through image processing and analysis methods to quantify the tissue diffusion and perfusion changes precisely and particularly define viable and non-viable tissues. CT can show perfusion changes. Although CT scanners are more accessible than MR scanners, MR imaging (sensitivity = 83%, specificity = 98%) detects more subtle changes in brain tissue content than CT imaging without contrast enhancements (sensitivity = 16%, specificity = 96%) [Chalela 2007].

Following the acute imaging of stroke, basic visual assessment techniques and manual volumetric measurements (eg: subtracting the core volume from the penumbral volume) have been used to predict the eventual outcome in stroke and determine the best therapeutic intervention [Baird 1997, Barber 1998, Mukherjee 2000, Sorensen 1999].

Different stroke assessment approaches were based on calculating the numeric volume of the diffusion lesion to predict final tissue fate [Hand 2002, Wardlaw 2002]. Other studies investigated the accuracy and specificity of different perfusion maps in determining stroke outcome [Kane 2007a, Dani 2012]. Examining stroke using both diffusion and perfusion data was the main focus of many previous studies [Barber 1998, Tong 1998, Keir 2000, Oppenheim 2001, Arenillas 2002, Coutts 2003, Rivers 2007, Kane 2009] –some of which investigated whether the perfusion-diffusion mismatch could identify the salvageable tissue (penumbra). We will give more details about this concept in Section 3.6. However, there is a major limitation to using numeric volumes of diffusion, perfusion and perfusion-diffusion lesion overlap as this does not consider geometric lesion overlap or the lesion shape and anatomical boundaries. This will be discussed in more details in Parts III and IV.

2.3 Treatment investigation and clinical trials

Stroke treatment is still one of the most challenging clinical decision-making processes since it needs to be determined within the first few hours after stroke onset. The ultimate goal of any stroke treatment is to rapidly restore the cerebral blood flow in the affected brain tissue, before brain cells die by removing of the arterial occlusion. Although thrombus is dissolved by the body's natural fibrinolysis systems, this

rarely occurs fast enough to prevent tissue damage. This therapeutic clot removal can be achieved mechanically (thrombectomy) or by dissolving the thrombus using clot-busting drugs (thrombolysis).

- **Thrombectomy** is the removal by interventional neuroradiological methods of blood clots in the cerebral arteries. There are several methods for doing this but none have yet proved to be more effective than intravenous thrombolysis in randomized trials [Broderick 2013, Ciccone 2013]. Further trials are ongoing.

- **Thrombolysis** rapidly recanalizes the occluded artery and improves the chances for a good neurological outcome in acute ischemic stroke using recombinant tissue plasminogen activator (rtPA) [Wardlaw 2012]. When rtPA is given within the first 4.5, possibly up to six hours after stroke, this improves functional outcome [Wardlaw 2009, Wardlaw 2012]. However, thrombolysis suffers from the hazard of increasing serious brain hemorrhage in about 6.4% of patients [Wardlaw 2012]. Reasons for severe hemorrhage are not completely understood but relate to large lesions, low blood flow and other factors. The benefit of rt-PA declines rapidly with time: those treated between three and six hours benefit less from rt-PA than those who were treated within three hours [Wardlaw 2012].

Clot-busting drugs are frequently used in clinical trials for patients who are selected based on specific inclusion criteria. For instance, the concept that the mismatch between perfusion and diffusion would identify patients with salvageable penumbra who would benefit most from thrombolysis was investigated in several randomized clinical trials of thrombolysis conducted in multiple stroke research centers. These clinical trials include DIAS [Hacke 2005] (104 patients), DEDAS [Furlan 2006] (37 patients) and EPITHET [Davis 2008] (100 patients). However, so far, these trials and other observational studies eg DEFUSE [Albers 2006] (74 patients) did not lead to reliable conclusions –ie. did not definitely identify patients who benefitted more from thrombolysis [Wardlaw 2012]. Thrombolysis decisions based on volumetric assessment of stroke lesions visible on PWI and DWI images (EPITHET trial [Davis 2008]) did not provide a clear evidence of better recovery from stroke. Numerous further analyses of the EPITHET data have led to suggestions that some perfusion thresholds may identify core and penumbra, but these still need to be tested in independent trials. Randomized clinical trials have generally relied on visual or computerized diffusion and perfusion lesion volume assessment using a visual scoring system like ASPECTS (Alberta Stroke Program Early CT Score: 10 point topographic scoring system where normal middle cerebral artery (MCA) territory is assigned 10 points and one point gets deducted for each affected area visible on CT/MR

scans) or other scoring systems and volume measurement tools. However, these techniques have variable accuracy as it is quite difficult to judge with the naked eye if the perfusion lesion volume is 20% or more larger than the diffusion lesion volume (the criterion used in some trials for treatment) [Wardlaw 2012]. They are not sufficient to give us a more nuanced understanding of how hypoperfused tissue shifts from ischemic to dead and vice versa. This suggests that perhaps one needs better methods to study lesion dynamics. Several studies showed the potential for MR DWI and PWI images to define stroke outcome by correlating them to the final imaged outcome or the neurological status [Wardlaw 2010].

Chapter 3

Imaging ischemic stroke with Magnetic Resonance

Contents

3.1 Introduction

Ischemia causes changes in water content in the injured tissue. This temporal water change from acute to late stages of ischemic stroke

can be detected as a change in tissue signal using MR and in tissue attenuation using CT imaging. Ischemia evolution patterns are also related to multiple features that are related to space (eg: occlusion site, attacked vascular territory, white and gray matter) and time (eg: continuous decrease of blood flow in the absence of reperfusion or increase when the blocked artery opens) (Figure 3.1). For instance, as the water moves from extracellular to intracellular space (cytotoxic edema), water diffusion is restricted –this becomes visible on diffusion weighted imaging, as it will be explained in the next section. Cells inflating with water because of cytotoxic edema results in T2-weighted hyperintensity on MRI and a reduced attenuation in CT images [Moseley 1990]. Changes in blood flow can be detected as changes in signal or attenuation as a bolus of intravenously injected contrast agent passes through the brain, the basis of perfusion imaging (PWI) [Østergaard 1996b, Østergaard 1996a, Østergaard 1998b, Østergaard 1998a, Wardlaw 2010]. Indeed, the change of water is related to the critical blood flow levels that the tissue undergoes (explained in Figure 2.3) and becomes more 'visible' as we trace the temporal change of ischemic tissue using series of multimodal images (Figure 3.1).

To determine the final infarct extent, many studies use conventional T1-weighted or T2-weighted MR images at 1 or 3 months post-stroke as a reference standard for the final infarcted tissue. While

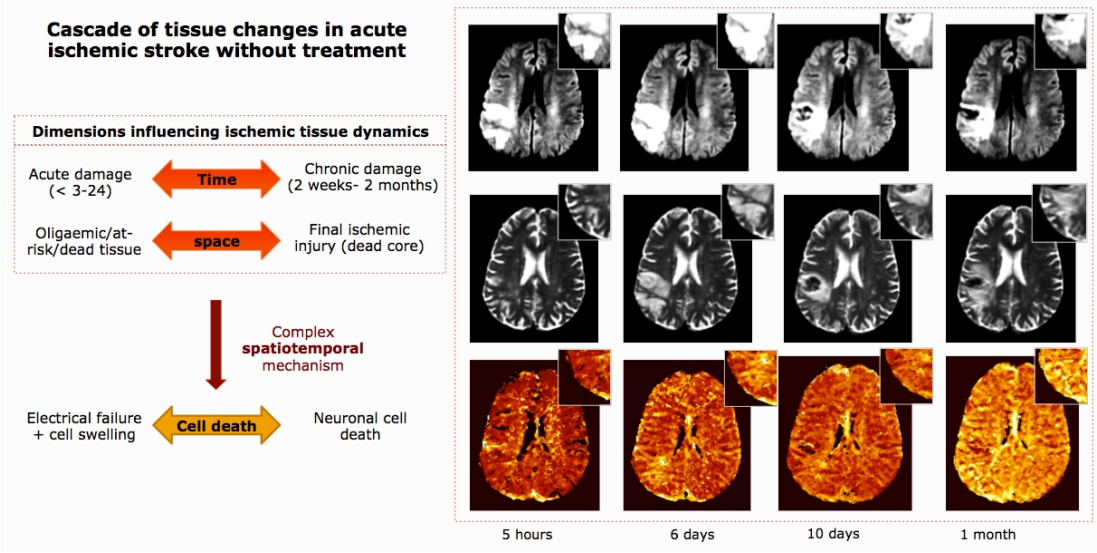

Figure 3.1: *Tissue changes in acute ischemic stroke (without treatment).* Time and space are key elements that influence stroke dynamics and its spatiotemporal pattern of evolution. On the right, we display the axial slices of ischemic stroke temporal changes for one representative patient (top row: diffusion-weighted images, middle row: T2-w images, bottom row: perfusion-weighted images (mean transit time map). At the first acquisition timepoint, the acute infarct is clearly visible (white area) on DWI image whereas T2-w image barely shows any intensity changes. However at later timepoint (6 days, 10 days, $\geq$ 1 month), T2-w shows the evolving lesion and the final lesion outcome than DWI. The black area (part of the acute DWI lesion) that appeared at 10 days reflects tissue secondary hemorrhage. The displayed sequence of perfusion imaging shows the changes in mean transit time values.

exploring this variety of MR based diffusion, perfusion and structural imaging tools, it is worth noting that assessing the dynamic visible ischemic tissue changes during the acute/subacute stages requires at least two parameters, with contrast based upon either the diffusion or perfusion physiological phenomenon [Jacobs 2001a, Soltanian-Zadeh 2003, Yuh 1991].

In the following subsections of this chapter, we will present the traditional view of the ischemic lesion visible on diffusion, perfusion and T2-w at $\geq$ 1 month from stroke onset images and present our definitions for at-risk and dead tissues.

3.2 Diffusion weighted imaging

3.2.1 Diffusion principles and sensitivity of MRI to diffusion

DWI MR sequences are highly sensitive in detecting early cerebral ischemic changes in acute stroke. They are fast to acquire and do not necessitate injection of a contrast agent. The investigation of diffusion weighted imaging in neurological disorders was introduced in 1986 [Le Bihan 1986]. It was also reported in [Moseley 1990] that DWI imaging shows alterations in water diffusion within a few minutes from stroke onset. The MR acquisition of the diffusion signal is quite similar to the acquisition of conventional T1-w and T2-w MR images where protons in water tissue will be excited using a large magnet

and aligned with the direction of the applied magnetic field. Their relaxation times T1 and T2 during which they come back to a state of equilibrium encode the MR intensity signal of every voxel within the magnetized/scanned brain tissue). However it is made sensitive to water motion in scanned tissue by applying a non-homogeneous magnetic field: two gradient pulses with same magnitude but opposite directions –one to dephase the proton spins and the second to rephrase them. If water molecules are in some areas where they are freer to move (ie. excited protons in these water molecules have also moved) between the two pulses then 'rephasing process' will not bring them back to the exact initial state, therefore, resulting in a decrease of the acquired DWI signal as the relaxation takes longer (Figure 3.2). This idea of double-gradient proton excitation process was introduced by Stejskal and Tanner in [Stejskal 1965] where they derived the DWI signal attenuation formula 3.1 determined by a diffusion coefficient and the strength and the duration of the applied gradients:

$$S_{DWI} = \underbrace{\underbrace{\underbrace{\rho}_{proton\ density} \underbrace{e^{-TE/T_2}}_{T_2-weighting}}_{T2-weighted\ image\ (S_0)} \underbrace{e^{-bD}}_{diffusion\ weighting}}_{diffusion\ weighted\ image} . \quad (3.1)$$

Where D represents the diffusion coefficient and b value depends on the gradient strength (ie. the higher the b value, the stronger the

DWI signal) with:

$b = \gamma^2 G^2 \delta^2 (\Delta - \delta/3)$.

Increasing the b-value increases the contrast between slow and fast diffusing water molecules.

γ denotes the gyromagnetic ratio, G the strength of the gradient pulse, δ the duration of the pulse and Δ the time separating the two pulses (Figure 3.2)

S_0 denotes the signal intensity in the T2-weighted image ($b = 0s/mm^2$) and TE is the echo time. The signal intensity SDWI, associated with every voxel, is related to the b-value and the diffusion coefficient, D, through the Steyskal Tanner Equation 3.1. This equation has two unknowns: the signal intensity for $b = 0(S_0)$ and diffusion coefficient D. Therefore to calculate D, one needs to make at least two different measurements (ie. gradients) at a different b-value.

In free medium, water molecules move freely. However, in brain tissue, the path of the water molecule is restricted by the fine structure of white and gray matter, thus reducing its diffusion coefficient. Moreover, if the tissue structures are oriented (eg: white matter fiber tracts), water diffusion coefficient will reflect this 'directionality' when it is measured in specific direction (Figure 3.3). Hence, DWI 'senses' the different structures of the tissue where water molecules diffuse based on their directionality. For instance, in white matter, water molecules diffuse along fiber bundles, the basis of tractography.

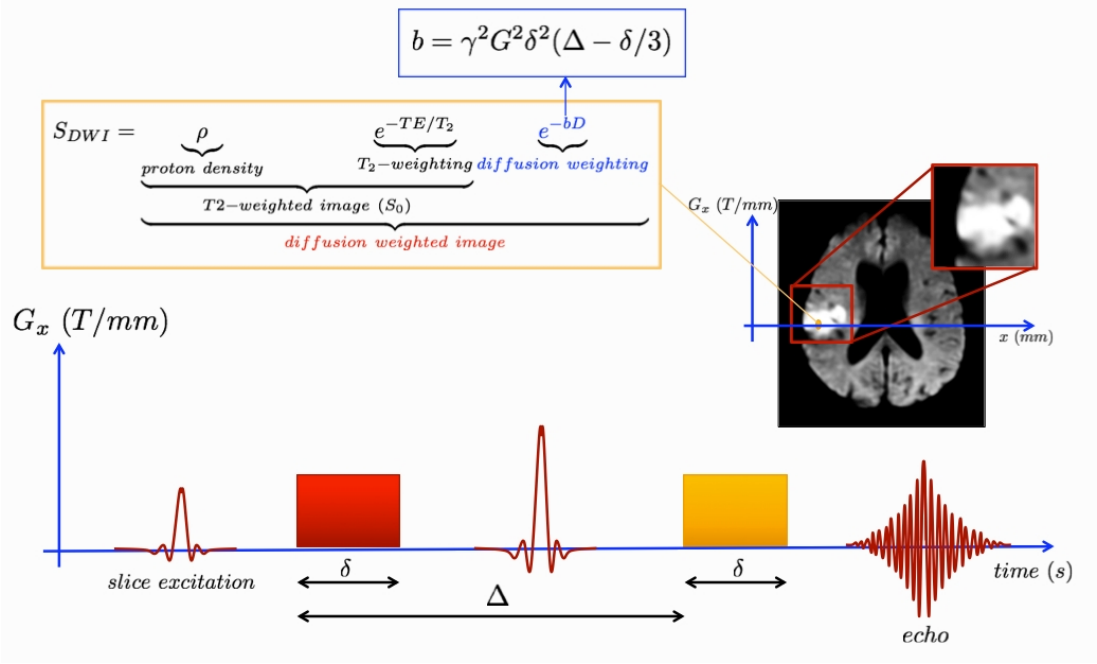

Figure 3.2: *Reconstruction of the diffusion weighted image (DWI).* As a specific voxel in the brain tissue is excited using two consecutive strong gradient pulses G_x (red and yellow rectangles) separated by a Δ time interval, the echo of its response encodes the DWI MR signal S_{DWI}. Tissue with slow diffusion is increased in signal (eg: the ischemic hypoperfused tissue visualized as a bright white area on DWI) whereas brain tissue with high diffusion such as free water (eg: the cerebral spinal fluid in the ventricles) appears low signal or black.

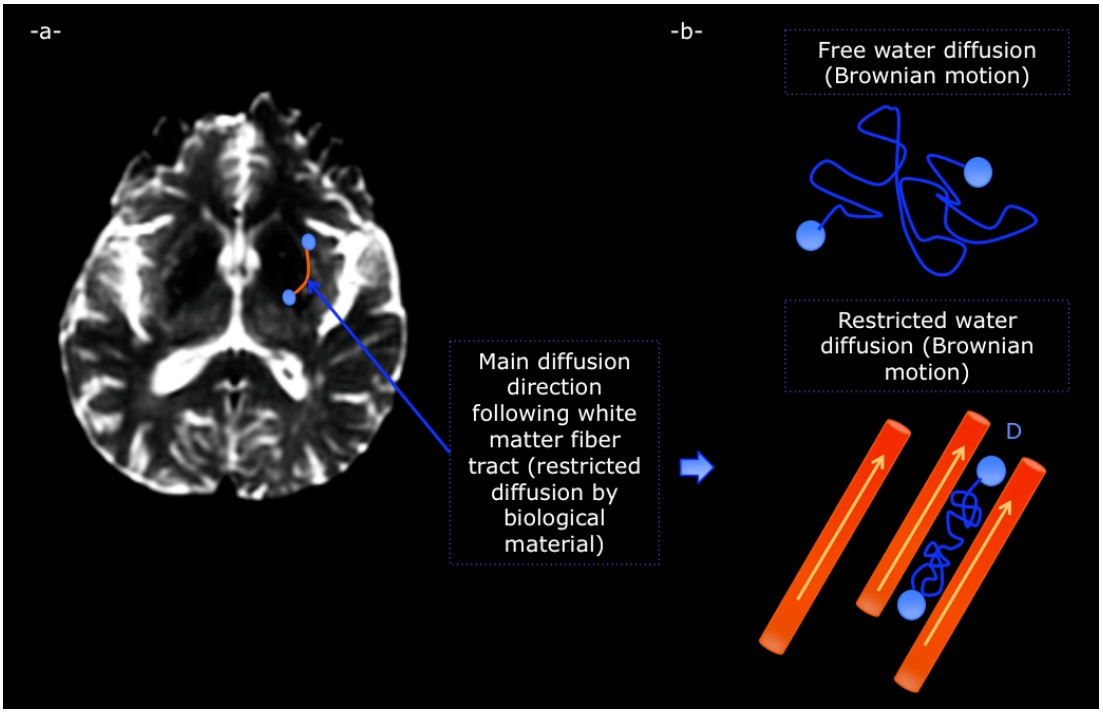

Figure 3.3: *Water diffusion and directionality.* (a) Water diffusion in brain tissue is constrained by the structure of gray and white matter. (b) Diffusion along fiber bundle (represented by the orange tubes) is the main diffusion direction for water molecules in brain tissue and the diffusion coefficient (D) reflects the rate of water diffusion in one specific direction.

DWI imaging has a major limitation: it does not 'measure' tissue anisotropy (ie diffusion rate depends on the direction) since the diffusion coefficient is measured along one gradient axis (with opposed directions). Therefore, different maps (Figure 3.3) that indicate water diffusion directionality were derived from the acquisition of multiple diffusion images using six gradient directions for diffusion tensor reconstruction. The eigenvectors of the diffusion tensor represent the main direction of water diffusion and its eigenvalues give the diffusion magnitude in that direction. Following these acquisitions, one could generate the mean diffusivity (MD) map and the fractional anisotropy (FA) map which quantifies the degree of tissue anisotropy (areas with high anisotropy appear hyperintense) [Nomura 1994, Wimberger 1995]. Both MD and FA maps are calculated from the eigenvalues of the diffusion tensor. Moreover, an apparent diffusion coefficient (ADC) map –entangling diffusion and relaxation effects on image contrast– can be generated by varying b-values. In Figure 3.4, we show axial slices for a patient with acute ischemic stroke and we can clearly notice that DWI is the best modality to visualize the spatial boundaries of a 'white' and 'bright' lesion (Figure 3.4). This brief overview of MR DWI allows us to get a better understanding of how ischemia appears as a hyperintense area on diffusion brain scans.

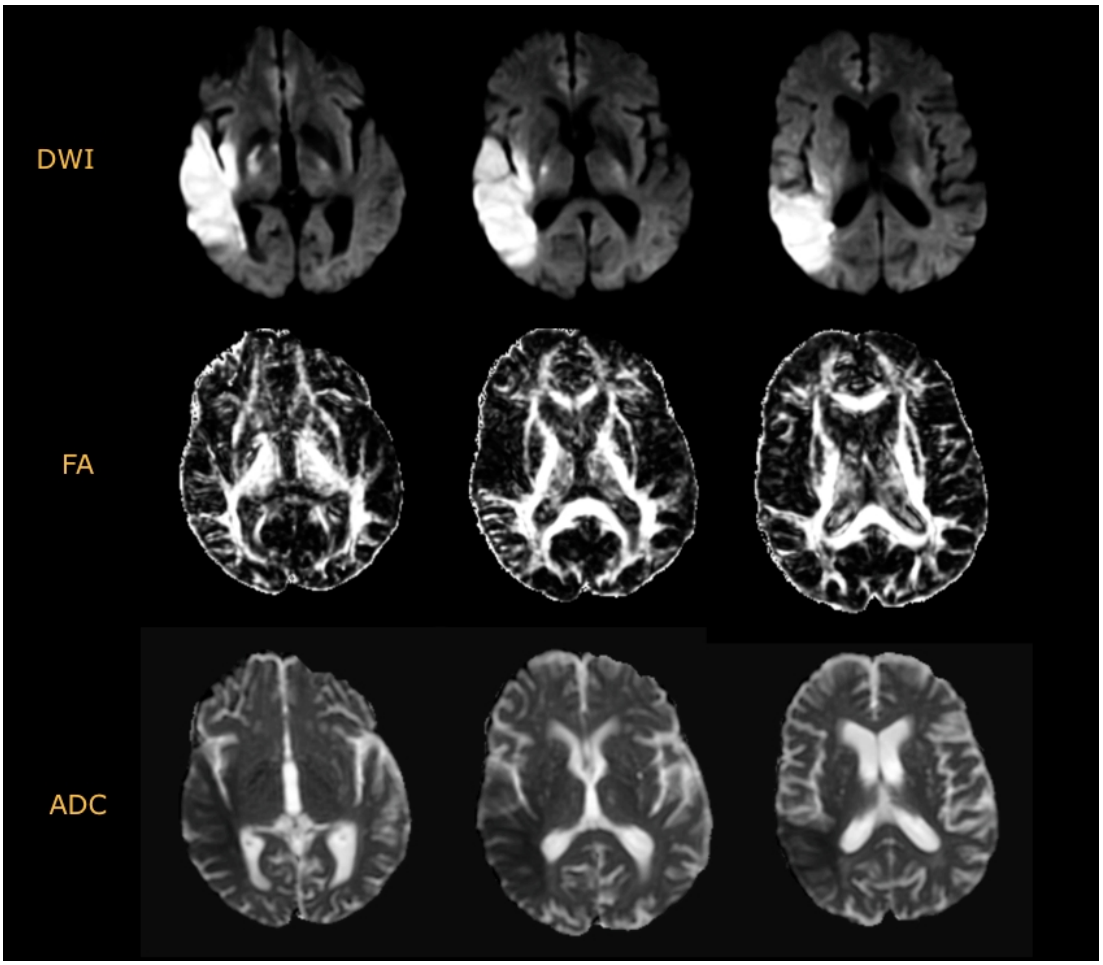

Figure 3.4: Axial slices for a patient with acute ischemic stroke using diffusion-weighted imaging (top row), fractional anisotropy map (middle row) and apparent diffusion coefficient map (bottom row). The lesion is more visible on DWI (bright area) and ADC images (dark area) than FA map.

3.2.2 Diffusion weighted imaging and ischemic stroke

The limited sensitivity of CT (38 to 48%) and conventional MRI (18 to 46%) for ischemia detection within 6 hours after stroke onset was reported in several studies [Mohr 1995, Mullins 2002]. In contrast, diffusion weighted imaging was demonstrated to rapidly and efficiently visualize the early ischemic changes within minutes after stroke onset [Wardlaw 2010, Keir 2000]. Early studies on diffusion imaging in stroke patients speculated that the hyperintense bright area on MR images was irreversibly damaged tissue and it was operationally referred to as the lesion core [Baird 1997, Warach 1992, Moseley 1990] although consideration of the perfusion levels at which tissue changes occur indicates that many DWI lesions must contain both penumbral and core tissue [Rivers 2005] . This implies that the acute diffusion lesion core can only increase in size and volume from the acute imaging acquisition timepoint to the next one (ie. its spatial extent always progresses and never regresses). Therefore, the identification of DWI infarct slices and the boundary and the volume of the supposedly 'dead tissue' was thought to be a surrogate marker for lesion outcome. This assumption was demonstrated to be incorrect as studies indicating the possibility that parts of the acute diffusion lesion will disappear and return to normal emerged (Figure 3.5) [Kranz 2009, Wardlaw 2010]. Figure 3.5 shows four different patterns of the diffusion abnormal-

ity evolution in different patients where the lesion enlarges and/or disappears.

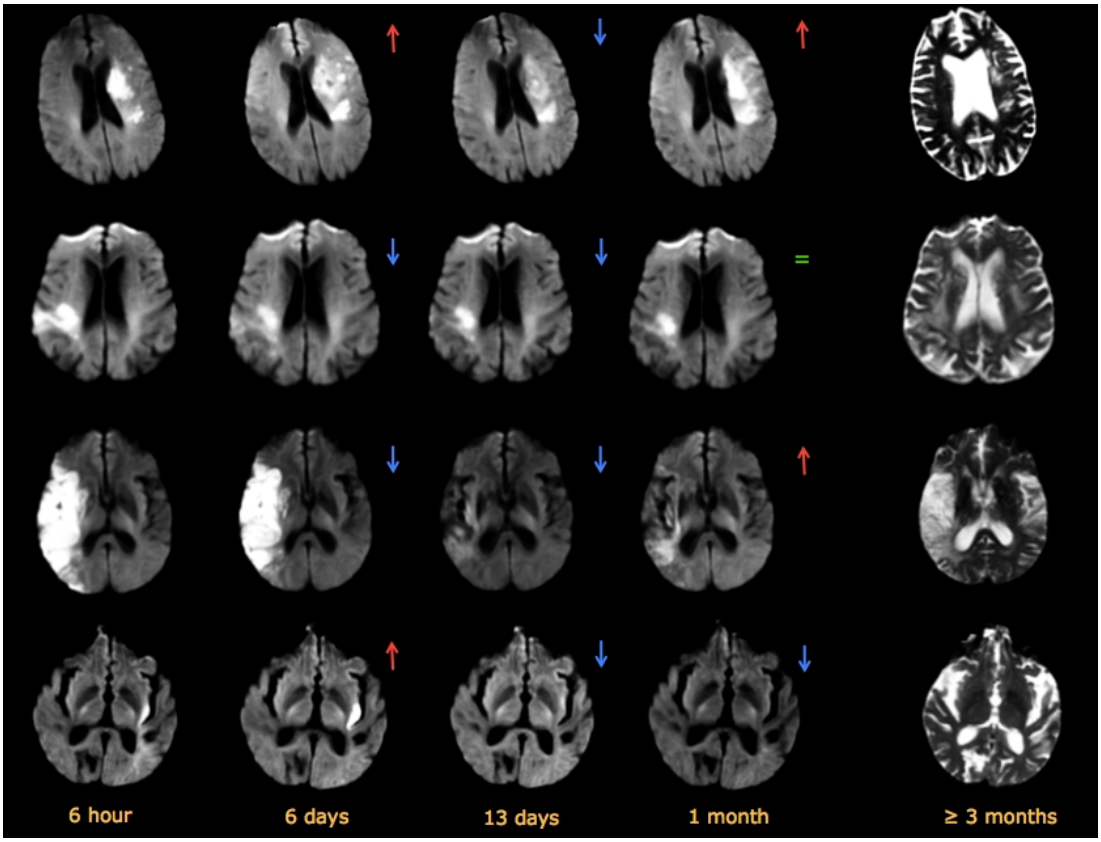

Figure 3.5: Lesion temporal change in 4 representative patients. The first four columns show the lesion changes on DWI images and the last one on T2-w final image. The red (vs. blue) arrow to the right of the MR axial slice indicates that the lesion has increased (vs. decreased or disappeared) when compared to the previous timepoint. The 'equal green symbol' indicates that the lesion did not change from the previous acquisition timepoint. The four displayed patterns of DWI lesion evolution are completely different.

Stroke diffusion lesions are endowed with a very complex geometry (different sizes, changing topology from one timepoint to another, irregular and widely variable shapes) and mixed levels of signal intensities inside the lesion (bright intensity inside the lesion that may slightly wane at the edges or in some parts of the lesion) (Figure 3.5).

The more cell death, the 'whiter' the lesion in DWI. Furthermore, swelling of the ischemic or infarcted tissue contributes to lesion size causing distortion and compression of surrounding brain tissue (Figure 2.5). Both swelling and tissue death (irreversible damaged lesion core) are depicted by DWI as hyperintense areas since they both depend on changes in water content. However, in the presence of a mass effect induced by large brain edema, a reliable identification of the true lesion growth spatial pattern becomes very difficult. In general, more swelling implies more dead tissue, but this is not an absolute [Rivers 2007]. Once the swelling disappears, we can more accurately measure the irreversible damage that has occurred in brain tissue and know what is what.

Another ambiguous observation of the DWI lesion in recent work showed that the bright lesion core on diffusion imaging overestimates (ie including normal or still viable parts of the ischemic brain tissue) or underestimates (ie. missing out some parts of the permanently dead tissue) the boundaries of dead tissue that cannot be saved when the blood flow is perfectly restored [Wardlaw 2010, Wardlaw 2012]. Others have shown that the DWI 'core' can recover at least in part if the abnormal brain tissue becomes normally perfused [Kidwell 2000, Fiehler 2004, Kranz 2009]. Furthermore, this interpretation of DWI abnormal tissue as 'dead' or not does not account for other subtleties – for example increasing whiteness of the diffusion lesion and increasing

likelihood that tissue therein is dead [Maniega 2004, Cvoro 2010].

Drawing valid conclusions on diffusion imaging specificity for differentiating core from at-risk tissue is still of considerable interest in stroke research. This thesis does not aim to solve this problem. However, we do investigate the relation between diffusion and perfusion abnormalities. As we use manual delineations of the white abnormal area on diffusion imaging, we assume that the outlined region contains mainly dead tissue as it may also contain parts of abnormal tissue that could resolve completely (See patient 4 (bottom row) in Figure 3.5) Our assumption is assessed in the discussion of our stroke evolution modeling results.

3.3 Perfusion weighted imaging

3.3.1 Perfusion principles and MR imaging

An MR sequence is applied during the injection of gadolinium (Gd) (a contrast material) at a flow rate of at least $2ml/s$ [Axel 1980, Reith 1997]. Then, the arrival of the bolus during the gadolinium's first circulation is calculated in each voxel of the scanned tissue using a voxel-specific curve fitting to an estimated gamma-variate function [Østergaard 1996b, Østergaard 1998b]. As shown in (Figure 3.6), several perfusion maps can be generated using this curve-fitting technique such as the cerebral blood flow (CBF) or the mean transit time

(MTT) or the cerebral blood volume (CBV = CBF × MTT).

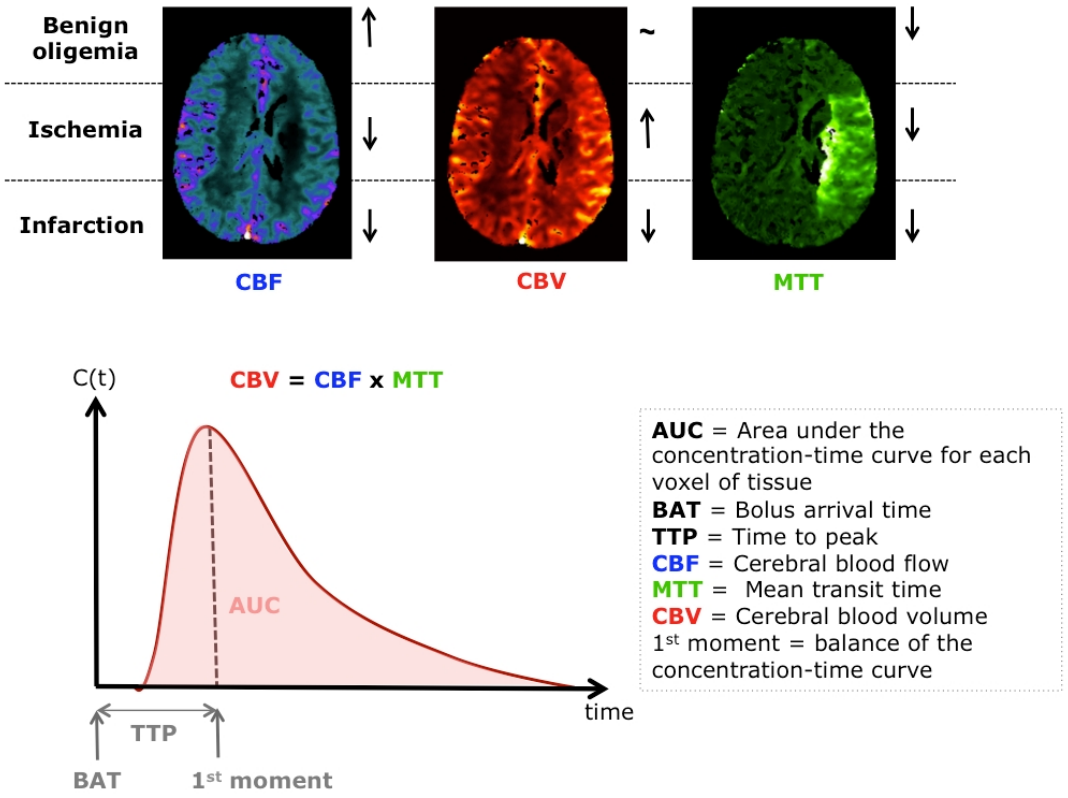

Figure 3.6: The different perfusion parameters derived from the concentration curve of the contrast as it passes through a brain voxel. The arrows next to the perfusion images indicate whether the perfusion value increases or decreases depending on the stroke stage the tissue is at (from oligaemia to ischemia then infarction).

3.3.2 Perfusion weighted imaging and ischemic stroke:

Perfusion imaging is an active area of investigation in ischemic stroke. In the area of a blocked artery, the contrast takes longer to get to ischemic tissue and there is also less total contrast that reaches badly injured brain tissue. Therefore, the hypoperfused brain area becomes visible on PWI maps (Figure 3.6). During the 1990s, the use of mag-

netic resonance imaging to assess perfusion in brain tissue defined a new era for stroke research where a different side of stroke abnormality was revealed [Rosen:1990]. Indeed, while the use of diffusion data focused on the identification of the irreversible dead tissue, perfusion data aimed to identify reversible ischemic penumbral tissue (Figure 2.3).

In Figure 3.7, we schematize the different changes in blood flow levels as the hypoperfused tissue proceeds to infarction. We can clearly see the heterogeneity and the anisotropy of the distribution of perfusion values in hypoperfused brain tissue. Imagine slowly depriving a brain voxel from blood, it will take with time one of the following tissue states: oligaemic, penumbral or dead. If CBF continues to decrease (ie no reperfusion), a very common evolution scenario is likely to happen in stroke –depending on the range of blood flow the tissue is in, the voxel in the affected tissue swells then shrinks and dies. The other possible scenario where tissue reperfuses is explained in Figure 2.5. The state of a tissue-voxel may affect the states of its neighbors according to specific as yet undiscovered rules (eg: anisotropy). Although each voxel is confined to CBF changes in the affected cerebrovascular territory, this does not necessarily negate the possibility of interactions between close (ie solitary diffusion lesion) or far (ie scattered diffusion lesion) neighboring voxels –within that territory.

What is not obvious from 'the tissue change scenario' (Figure 3.7) is

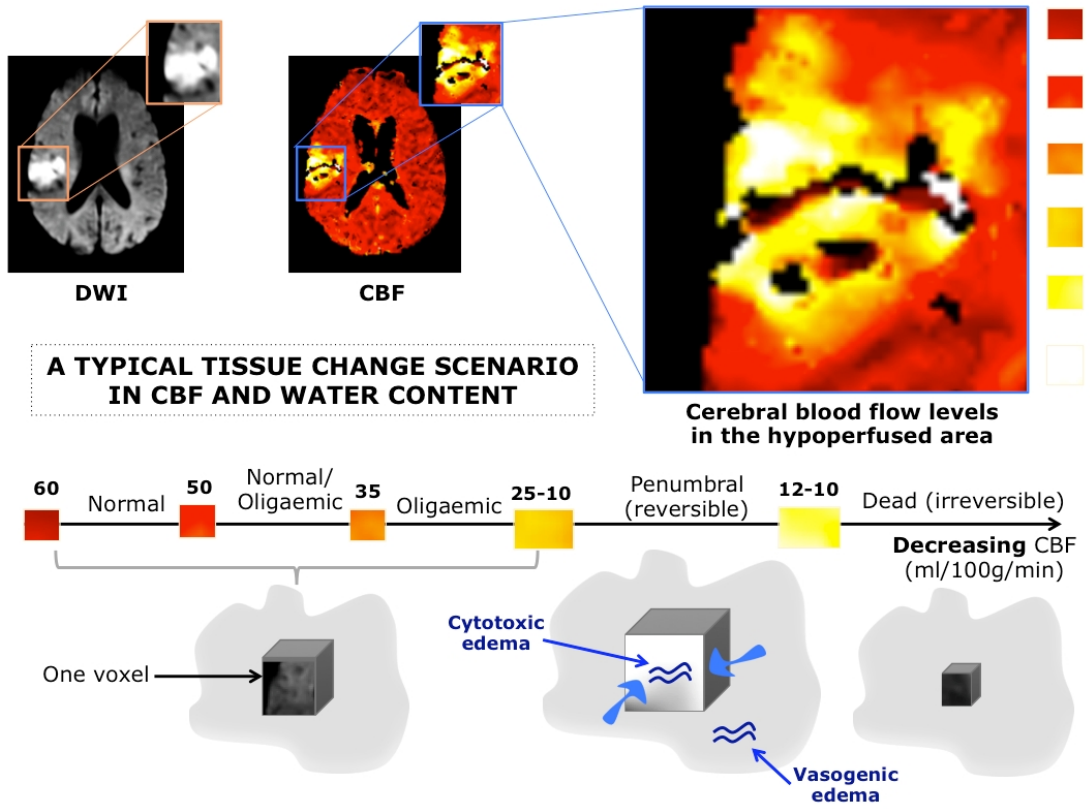

Figure 3.7: *Typical tissue change scenario in cerebral blood flow and water content in the absence of reperfusion.* (Top) We zoom in on the diffusion and perfusion lesions using an axial slice of diffusion-weighted image and cerebral blood flow perfusion (CBF) map. (Bottom) In this figure, a brain voxel represents a cube of brain tissue. We model its changes as the CBF continue to decrease: as it goes into a penumbral state, it gets inflated with water (cytotoxic edema) and surrounded by more water (vasogenic edema). Then, as the blood flow continues to decrease, it goes into an irreversible state of damage: it shrinks and dies.

the exact transition phase of a voxel from an oligaemic state to penumbral or penumbral to dead (or the reversal state in case of reperfusion). These tissue changes occur gradually at different blood flow levels; however, the quite variable blood flow in the brain [Dani 2011] lays down the challenge of accurately identifying these transition phases. However, there is still no evidence that this can be achieved using only blood flow levels. More information derived from diffusion maps may help differentiating the different states of abnormal brain tissue.

We would like to think that perfusion imaging would make our understanding of stroke evolution patterns a lot easier, but it turns out that this is far more complicated that it had been anticipated. Indeed, MR or CT perfusion imaging can be visualized and interpreted in different ways depending on how we 'read' the signal-time curve capturing the passage of the contrast bolus through cerebral blood vessels. The various perfusion measurements (eg: MTT, CBF, CBV) inform us about perfusion levels in the brain. However, they do not display the same boundaries for the hypoperfused brain tissue (Figure 3.6) [Calamante 2002, Kane 2007a].

This increases the complexity of the problem for differentiating dead from oligaemic and at-risk tissue as there is no agreement on which perfusion measurement to use in a standardized clinical setting [Hjort 2005, Bandera 2006, Provenzale 2008, Wardlaw 2010]. The recent pivotal review paper on perfusion thresholds identified the wide

variability of perfusion threshold values as 'identifiers' of tissue state and potential predictors of tissue fate [Dani 2012]. Moreover, it can be discomforting to make strong assumptions on what these curve-driven perfusion values accurately mean as we have become more aware of some issues that may influence the characteristics of this curve –such as how to determine its start and end points, pathophysiological factors delaying the arrival of the bolus to a specific voxel in the brain (eg: carotid stenosis), the rate of injection of the contrast agent, the strength of the cardiac output, etc [Carpenter 2003]. Although we still do not know what exactly we are setting out to measure using these perfusion maps, we can at least make the assumption that areas that do seem abnormal on PWI are hypoperfused. Noticing the wide variability of these measurements, the use of a particular perfusion map for volumetric assessment of the perfusion lesion size and as a criterion in some clinical trials to determine the eligibility of patients for treatment in clinical trials may add to variability [Wardlaw 2010]. Another factor that adds up to the complexity of the problem: the heterogeneity of perfusion values (ie. blood flow in grey matter is inherently higher than in white matter) [Maniega 2004].

Whichever perfusion measurement we use in our 4D modeling approaches, in this thesis we assumed that the manually delineated area by an expert contains the majority of brain tissue with a significant drop in blood flow. This does not negate the possibility that the man-

ually outlined perfusion lesion can leave out some hypoperfused areas or include some oligaemic not-at risk tissue due to the high fluctuations of perfusion values, but it provides a useful working definition using a perfusion parameter. We carefully keep this in mind in addition to the heterogeneity of perfusion values when discussing our results.

3.4 T2-weighted imaging at ≥ 1 month after stroke onset

After 6-12 hours from stroke onset, T2-w images were demonstrated to be able to show lesion areas due to the cytotoxic and later vasogenic edema [Grunwald 2002]. However, its use during the first time window spanning over the first few hours from stroke onset is not recommended for visual assessment. One of the keys to determining to what extent perfusion and diffusion lesions are surrogate markers for final tissue outcome lies in identifying the final spatial extents of dead tissue. Structural T2-weighted images at ≥ 1 month after stroke onset are commonly used to locate the boundaries of the irreversibly damaged tissue –ie chronic stroke lesion.

Many studies conducted on stroke used T2-w images as a 'ground truth' to visualize all parts of brain tissue that were permanently damaged [Grunwald 2002, Wardlaw 2010]. Nonetheless, we would like to highlight two factors not considered in this assumption: (i) there may be other damaged tissue round about the outside of the manu-

ally outlined visible T2-lesion and (ii) not all 'final infarct' on T2-w is necessarily all dead tissue. We also make the same working assumption in this thesis considering the tissue included in the final T2-w lesion as "so damaged" that at least it shows up on the scan.

3.5 Other imaging modalities

In a clinical setting, CT is still the number one imaging modality for stroke assessment: quick and easy to use [Kummer 1997]. Ischemic tissue is shown on CT scans as hypodense areas. As we have mentioned before, the early signs in the acute-subacute cascade of ischemia includes an increase in tissue water (or cell swelling), which in turn causes a decrease in tissue density (measured in "Hounsfield Unites") (Figure 3.8). Experimental studies suggest a 1% change in water content causes a CT signal attenuation of 2.6 Hounsfield units (HU). Early ischemic changes generally fall in a small density range of 5-10 HU (ie more than 3% increase in tissue water content) [Unger 1988]. The sensitivity of CT to early hemodynamic changes in ischemia is limited, but perfusion imaging may help to identify the penumbra as with MR perfusion imaging. This will be discussed in details in Section 3.6.

3.6 Imaging-dependent issues

Extracting relevant information from ischemic stroke images obtained over the acute/subacute time window, from a medical image analysis perspective, is challenging due primarily to the following imaging-dependent and biology-dependent factors that affect image processing of stroke lesions.

Frequency and detail of image acquisition. Stroke patients are often very unwell at first presentation. Speed is of the essence –'time is brain'– so acute treatments must be initiated as quickly as possible: the imaging must be rapid and not unduly affect patient care or delay treatment. It is not easy to obtain high quality volumetric MR imaging data from some stroke patients, as they are restless, and may not comply even with a 10 minute examination. Hence

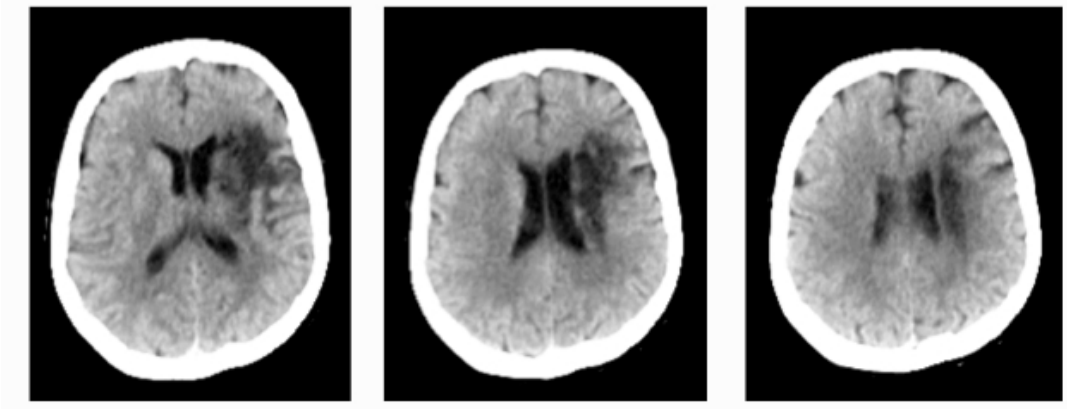

Figure 3.8: Computed tomography (CT) axial slices showing an established stroke lesion as a dark area of cerebromalacea and tissue shrinkage.

image acquisition parameters tend to emphasize speed, with as few sequences and slices as possible. This is difficult for image analysis which requires high quality/resolution of the acquired images to extract meaningful clinical features. Also, it is not possible to perform serial imaging at short time intervals (e.g. every few hours) as this would interfere so much with acute care and would be unethical. Even scanning on alternate days in the first week may be difficult. This few 'snapshots' of the early lesion may be obtained. The net effect is that stroke imaging tends to use sequences that are not optimal for complex image processing in either the spatial or the temporal domains. Although this is listed under imaging-dependent issues, it is actually a simple consequence of the stroke itself, the restraints imposed by treatment delivery, the fact that scanning itself may not be good for the patient, and the characteristics of the older population that stroke tends to affect.

Perfusion/diffusion mismatch and the definition of the core and penumbra. At acute/subacute stages, the ability of both DWI (diffusion weighted imaging) and PWI to detect early temporal dynamic tissue changes in either animal or human stroke [Moseley 1990, Le Bihan 1986, Sorensen 1996, Warach 1992] led to the concept of "perfusion-diffusion mismatch" –hypothetically- reflecting salvageable tissue. Several studies [Arenillas 2002, Barber 1998, Coutts 2003, Oppenheim 2001, Rivers 2007, Tong 1998] explored the

prognostic potential of the DWI-PWI mismatch, although questions surrounding its validation remained [Wardlaw 2010, Kane 2007b, Ma 2011]. The spatial boundaries of the mismatch and its measurement strictly depend on how the penumbra and the core are defined. However, the assumption that the diffusion lesion represents the core whereas abnormalities visible in certain perfusion weighted images include both the core and the penumbra is still applied in many studies [Ford 2012, James 2006, Petrella 2000]. Nevertheless, there is still an ambiguity surrounding the definition of the penumbra using thresholds [Ford 2012]. In Figures 2.2 and 3.8, we can clearly see how the choice of the perfusion parameters (e.g.: MTT or CBF) might alter considerably the spatial boundaries of the detected mismatch. It is also possible to have "reverse mismatch" [Coutts 2003] where the volume of the DW lesion exceeds that of the PWI lesion. This was explained by patients being scanned after spontaneous reperfusion [Coutts 2003, James 2006]. Similar variation is found on CT perfusion imaging. It is still unclear which PWI parameter best defines the true limit of salvageable tissue; and will need to be clarified before the mismatch concept can be used reliably.

Invisibility at acute stage. Acute ischemic change on CT is subtle and often does not show infarct until 12-24 h after stroke onset; nevertheless, it is commonly used for stroke assessment [Wardlaw 1998, Wardlaw 2003, Wardlaw 2005, Wardlaw 2007]. Inter-

pretation of acute stroke CT scan requires training, and the findings are often subtle, [Wardlaw 2005, Wardlaw 2009, Jóźwiak 2011]. The more severe the stroke the more likely the lesion is to be visible on CT, eg 80% of patients with severe stroke have a CT-visible acute lesion [Wardlaw 2005]. Even DWI may not show the acute lesion in all cases [Wardlaw 2007]. Expert interpretation is required to identify some acute lesions on CT, but may not be able to accurately define the lesion boundaries.

Slice thickness. Most PWI and DWI images use slice thickness of between 4 mm and 14 mm [Gupta 2008], and often with a gap between slices. Most modern plain CT is acquired as a thin section (1-2 mm) contiguous volume image, however the signal to noise ratio in such images is too low for diagnostic use in stroke with 3-6 mm reconstructions being more commonly used in stroke diagnosis. Many of the more sophisticated image processing algorithms require volumetric scans with thin contiguous slices otherwise low resolution can increase partial volume effects and be misleading when interpreting the image-processing-driven results especially in 3D and 4D models.

Choice of perfusion-diffusion parameters. To interpret perfusion data, different parameter maps are estimated. These include, imaged cerebral blood flow (CBF), mean transit time (MTT), time-to-peak (TTP) map and cerebral blood volume (CBV) map [Dani 2012, Carpenter 2003, Kane 2007b]. Each of these produces

a different-sized lesion from the same data, with the processing algorithm also influencing the lesion size, even when the same parameter is estimated. Identifying which perfusion parameter should be used remains a key question [Grandin 2002]. Similarly, raw diffusion weighted acquisitions can be post-processed in different ways to provide traditional diffusion weighted images, apparent diffusion coefficient maps [Na 2004, Moseley 1990], fractional anisotropy or the diffusion tensors [Agam 2007].

'Fogging' and 'T2-shine through'. The "fogging" effect refers to the tendency of tissue in the initially hyperintense DWI lesion (or hypodense CT lesion) to appear normal or disappear between 7 and 14 days after stroke, probably related to tissue reperfusion [Choi 2011, O'Brien 2004] or disappearance of the edema [Grunwald 2007]. This makes some lesions almost completely disappear between 7 and 21 days so that the assessment of the final infarct in this time window will underestimate final tissue damage. 'T2-shine through' may also distort lesion size at subacute stages [Burdette 1999]. 'T2-shine through' refers to the persistent increased DWI signal even after several weeks or months from stroke onset. However, T2-shine through areas were associated with persistent high blood flow [Rivers 2007]. There is still a lack of certainty about its main cause as being biology-derived or imaging-derived.

3.7 Biology-dependent issues

Lesion swelling and shrinking. Lesion swelling is commonly observed soon after ischemic stroke, starting within the first few hours and peaking at 3-5 days. Over time, the stroke lesion shrinks as the swelling reduces and tissue damaged by the injury is lost, replaced by cerebrospinal fluid (CSF) leaving an area of cerebromalacia with ex vacuo effect on adjacent structures [Wardlaw 1993]. From an imaging-based perspective, the swelling can be observed as a "mass effect" where the infarct distorts the adjacent tissues (brain anatomical deformation) e.g. by compressing the ventricles and other CSF spaces (sulcal effacement) or causing midline shift (Figure 3.9). Swelling increases the volume of the ischemic tissue even though the anatomical extent remains unchanged. The later ex vacuo effect can result in an underestimation of the actual extent of the final injury [Wardlaw 2010].

Spontaneous reperfusion. Spontaneous reperfusion occurs in about 20% of patients by 24 h and 80% by 5 days and alters tissue outcome [Bang 2008, Rha 2007, Zanette 1989]. This would alter the dynamic evolution pattern of the ischemic tissue core and the penumbra as shown in Figures 2.3 and 3.9. It also probably accounts for some rapid early recovery and may explain why some patients have no arterial occlusions on imaging soon after stroke even though they have

early extensive ischemic changes after stroke. However, it is unpredictable and occurs too early in most patients to provide much tissue salvage, hence the need for therapies to open the artery. The lesion fate is also influenced by collateral blood supply which varies considerably between individuals, making the prediction of stroke evolution and tissue fate more complex (Figure 3.9). In fact, if the collateral arteries are poor within a specific blood territory, a proximal occlusion of the artery supplying this territory will produce a larger ischemic core and penumbra than a similar occlusion in a patient with good collateral arteries.

No re-flow phenomenon. No re-flow phenomenon occurs when recanalization of the blocked artery fails to reperfuse the tissue capillaries and is likely to be associated with a worse tissue outcome than if blood flow was fully restored [Ames 1968, Majno 1967, Soares 2009, Wardlaw 2010]. This may occur in up to 50% of patients with large middle cerebral artery (MCA) infarcts [Rivers 2006]. It is thought to be one explanation for persistent tissue swelling and T2-shine through in subacute lesions. Its causes and risk factors remain "unknown" though a putative explanation would be the narrowing of the vessels by the swollen perivascular tissue including pericytes preventing ischemic tissue reperfusion even if the proximal artery reopens.

Scattered lesions. Stroke lesions are rarely seen as single large lesions on acute DWI or final T2-w images, but are more often mul-

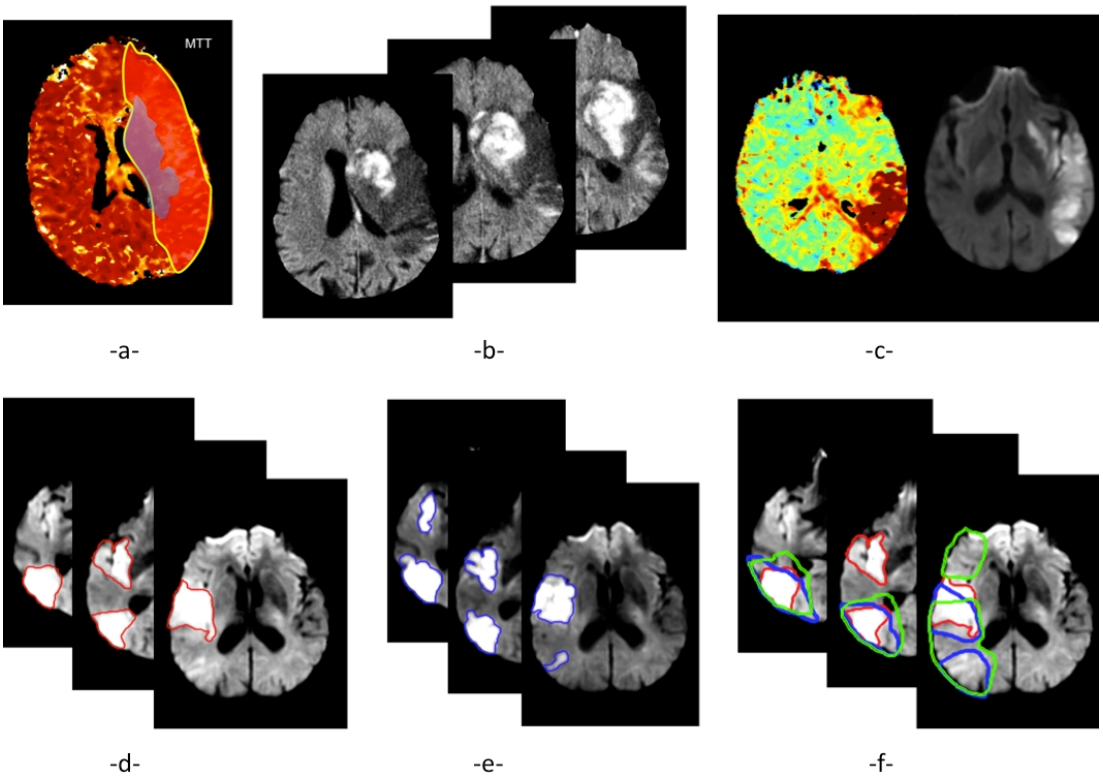

Figure 3.9: (a) Ischemic penumbra and infarct core at the acute time. Red shaded region represents the ischemic penumbra identified using an MTT perfusion map while the blue one rep- resents the infarct core manually delineated on the DWI image. A large area of perfusion/diffusion mismatch is clearly distinguishable. (b) Swelling at acute time of stroke onset observed in a DWI image. A massive swollen infarct occupies most of the MCA territory distorting the right ventricle. (c) An example of the influence of partial reperfusion in penumbra and core evolution patterns. The acute DWI (left) and the acute perfusion TTP map (right) demonstrates the "reverse" mismatch revealing a partial reperfusion where the TTP appears normal in the anterior portion of the MCA territory. (d) Scattered lesion at acute timepoint (3 h). The manually delineated lesion in 3 different axial slices in a DWI image is composed of two topologically separate components. (e) Scattered lesion at a subacute timepoint (6 days). For the same patient showed in (d), the evolution of the spatial boundaries of the manually delineated scattered lesion is shown at a subacute timepoint. (f) Perfusion/diffusion mismatch and the influence of perfusion parameters on the boundary of the visible mismatch. The red contour represents the DWI lesion depicted at an acute timepoint superimposed with both MTT (in blue) and CBF (in green) lesions manually delineated at an acute timepoint.

tifocal scattered lesions with more than one topologically connected component (Figure 3.9), even though these components may all lie in the same arterial territory. Different biological scenarios have been supposed to explain this phenomenon: one being that a clot has blocked a proximal artery but because there is good collateral supply from adjacent arterial territories, some of the blocked artery territory has not infarcted while some has; another is that a shower of emboli went into one artery and affected different smaller branches within the same territory. Other possibilities are that one single clot entered a proximal artery and stuck for a short time but then the clot broke up and fragments went into distal branches, or that this appearance is possibly due to imaging not showing the true extent of the tissue at any one acute/ sub-acute timepoint. It is likely that although similar in appearance on imaging, this phenomenon has different explanations in different patients. No previous studies of PWI/DWI mismatch, that we have found, have mentioned this before [Arenillas 2002, Barber 1998, Coutts 2003, Oppenheim 2001, Rivers 2007, Tong 1998, Petrella 2000], but the practical implication in image processing terms is that most algorithms were designed to cope with one lesion only, not with multiple fragments.

3.8 Conlusion

Considering all the biology and imaging-derived issues, studying and modeling the dynamics of acute stroke seems to be no easy task. Although this thesis does not aim to solve all these issues, it will investigate some of them such as the evolution of scattered and solitary stroke lesions and the perfusion/diffusion mismatch concept. We will also take elaborate precautions to exclude some of the clinical effects that may be misleading when interpreting our results such as swelling. The thesis is organized in three parts which closely follow our published and submitted studies

In the next chapter (Chapter 4), we propose some specific inclusion/exclusion criteria to search stroke literature for medical image analysis methods and mathematical modeling approaches that have advanced our understanding of stroke infarct and penumbra development. As stroke research field has many difficulties for the image analyst, like spontaneous reperfusion, the "no re-flow phenomenon" and early swelling, we will also examine whether and how these methods addressed stroke imaging-dependent and biology-dependent issues (Chapter 4).

Part II

Survey of Medical Image Analysis Methods in MR/CT-imaged Ischemic Stroke

"*One cannot recognize what is unsound in any of the sciences unless one has such a grasp of the furthest reaches of that science that you are the equal of those most learned in it. Then, and only then, will it be possible to see the errors it contains.*"

Abu Hamid Al Ghazali; –1058-1111 AD

Chapter 4

Reviewing stroke literature from a medical image analysis perspective

Contents

4.1 Introduction:

As we have briefly mentioned in the Introduction of this thesis (Chapters 1 and 3) that approaches to stroke-related questions have relied on

basic thresholding techniques and commonly used standard statistical correlation-based data analysis tools mostly applied to 2D images, such as in [Astrup 1981, Na 2004, Olivot 2009, Shih 2003]. These have been used to depict or predict stroke evolution but have resulted in the identification of multiple different thresholds with overlap in values from different studies for lesion core and penumbra [Dani 2012]. This was compounded by differences in definitions of non-viable and penumbral tissues (18 different definitions of penumbra and 11 of lesion core in studies using CT or MR perfusion imaging [Dani 2012]). Furthermore, it was only fairly recently that the importance of geographical co-location of perfusion and structural images in mapping the evolution of viable–non-viable tissue was more widely recognized [Nagakane 2011]. Prior to that, most analyses simply used numeric volume measures.

Medical image analysis has advanced substantially in recent years and we looked beyond the techniques used so far in stroke by identifying studies, such as dynamic evolution models that might be able to handle the more complex problems encountered in typical ischemic stroke image [Duncan 2000]. Coalescing spatial and temporal information into models characterizing changes in cancerous lesions suggested that these new approaches might help understand factors influencing spatiotemporal evolution of other brain diseases like strokes [Duncan 2000]. It was these developments that initiated our search for

studies exploring more sophisticated image analysis of acute/subacute ischemic stroke. Notably, in the past decade, clinicians primarily used 2D visual and manual assessment of MR/CT images to guide their decisions for patient treatment. However, much more powerful methods that made efficient use of medical image analysis methods and robust computational mathematical frameworks may be available. Failure to use these may delay advances in stroke research.

In this chapter, we survey the current literature to identify methods to overcome three key barriers to advancing our understanding of ischemic stroke lesion evolution and hence therapy planning at acute and subacute stages: (i) the differentiation of potentially salvageable and permanently damaged brain from normal tissue using automatic/semi-automatic segmentation algorithms. (ii) The prediction of the ischemic tissue fate (progression to infarction or salvage). (iii) Finally to simulate the dynamic evolution of the ischemic region. Hence, we looked for papers that developed new or adapted existing medical image analysis methods to quantify changes in the acute/subacute (3h to 6 days) ischemic stroke lesion using MR or CT clinical human/animal data and/or synthetic data.

We aim to:

(1) Document the state-of-the art of the medical image analysis approaches applied to acute/subacute ischemic stroke tackling segmentation, prediction, or dynamic evolution modeling;

(2) Evaluate the overall performance of any identified methods including a critique of potential limitations and how any key problematic issues have been addressed;

(3) Identify any promising method that has not yet been applied to differentiate tissue state or model lesion evolution in acute stroke.

4.2 Literature search and methods

4.2.1 Literature search

We searched the literature using Medline and GoogleScholar from 1^{st} January 1986 to the 1^{st} of June 2012 for publications using human, animal and synthetic stroke data in the following areas (Figure 4.1):

- Segmentation of acute/sub-acute ischemic penumbra and/or core;

- Prediction of ischemic tissue fate outcome;

- Dynamic acute ischemic lesion evolution modeling and simulation methods.

We used the following key headings, separately or in combination, to identify relevant papers in these three main research areas: "ischemic stroke", "middle cerebral artery", "prediction", "segmentation", "tissue identification", "lesion detection", "dynamic model", "dynamic evolution", "penumbra", "infarct", "Magnetic Resonance Imaging (*vs.* MRI)", "rats/rodents", "Computed tomography (*vs.* CT)", "perfusion" and "diffusion". To expand the search and check for all relevant pa-

pers, two additional research layers were performed through reviewing the sub-references of each initially identified paper and then also scanning the references of the sub-references.

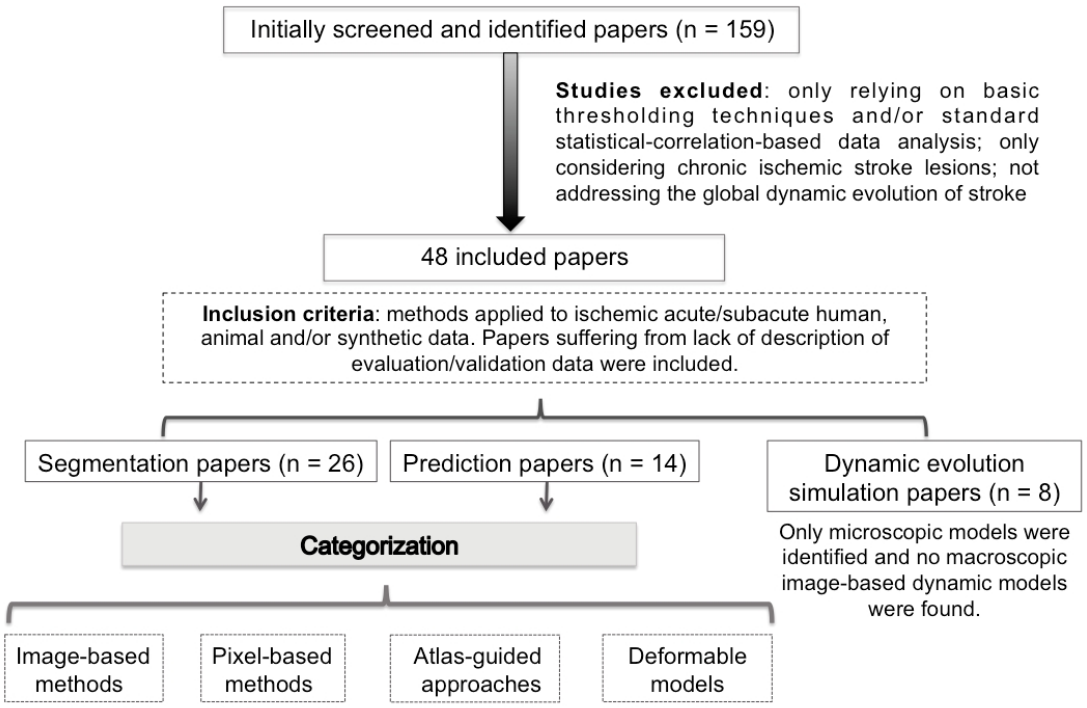

Figure 4.1: *Overall view of the search strategy and paper categorization method.*

4.2.2 Exclusion-inclusion criteria

We excluded studies that only used standard thresholding techniques and/or basic statistical-correlation tools in their analysis of acute/subacute ischemic stroke lesions. We also excluded any studies that definitely only considered chronic lesions. Identified studies that proposed dynamic models simulating the effect of collateral

phenomena contributing to stroke evolution process and not directly addressing the global dynamic evolution of ischemic stroke were also excluded (eg: studying the effect of inflammation in ischemic stroke [Lelekov-Boissard 2009]).

We included all research papers using or defining a new image analysis approach or dynamic evolution simulation models that were applied to ischemic acute/sub-acute stroke using human, animal, phantoms or simulated data. We used an inclusive approach so as not to overlook any promising new methods and therefore also included papers with little or no detailed information about the test data such as the acquisition stage (acute, sub-acute, chronic as long as it was not solely chronic) or the number of the recruited patients or simulated data.

4.2.3 Included studies categorization and key features

To help us assess the practicality and reliability of any identified promising methods, we highlighted whether the applied method:

i. required user interaction,

ii. required a training dataset (supervised approach),

iii. required single or multiple acquisition time points,

iv. addressed the problem of swelling,

v. addressed reperfusion phenomenon,

vi. (in segmentation) segmented the ischemic area with or without

a distinction between the penumbra and the core,

vii. (in prediction and dynamic simulation) was assessed using imaging-based outcome, clinical-based outcome or both.

Furthermore, both segmentation and prediction methods can be approached as a classification/clustering problem so we applied a common categorization pattern to the identified ischemic lesion penumbra/core segmentation and ischemic tissue final outcome prediction methods composed from the following categories as introduced in [Dawant 2000, Pham 2000] and shown in (Fig 4.1):

- image-based;

- pixel-based classification;

- atlas-guided-approaches;

- deformable models.

In every included paper, we determined whether the applied method used solely or in combination human, animal and/or synthetic data and the number of the recruited patients, animals or simulations. We also extracted the MR and CT imaging modalities used to build and evaluate the described model.

4.3 Results:

4.3.1 Paper identification

The initial search identified 159 papers, however, eventually only included 47 papers that met the inclusion criteria. These were published between 1998 and 2012. We categorized them into 3 main research fields: segmentation (n=25, Table 4.1), prediction (n=14, Table 4.2) and dynamic evolution modeling (n=8, Table 4.3). Tables 4.1, 4.2 and 4.3 summarize the data extracted from each paper. In both segmentation and prediction methods we found: image-based (n=9), pixel-based classification (n=14), atlas-guided approaches (n=1) and deformable models (n= 2).

The papers that evaluated the segmentation, prediction and dynamic simulation approaches at the acute/subacute stages of stroke used human (30 papers, 563 subjects) and/or animal (10 papers, 158 rats/rodents) data and/or synthetic data (11 papers, 11 simulations). Among the 11 identified papers using synthetic data, only two mentioned the number of performed simulations [Dastidar 2000, Martel 1999]. The number of patients ranged from 1 to 63 (median 15) for segmentation and 8 to 74 (median 19) for prediction. For evaluations using animal data the sample size ranged from 9 to 51 (median 20) for segmentation and 6 to 36 (median 7) for prediction.

We found 8 phenomenological (*ie.* inspired from biological

phenomena) microscopic dynamic models simulating a biology-based evolution of ischemic stroke [Chapuisat 2008, Chapuisat 2010, Dronne 2004, Dronne 2006, Dumont 2010, Duval 2002, Grenier 2010, Louvet 2011] (Table 4.3). We found no papers that addressed imaging-based macroscopic dynamic models simulating a 4D evolution of acute ischemic stroke using MR or CT data and/or synthetic images. However, we were very keen to include the identified microscopic approaches since they provide clues about what drives the evolution of stroke lesion that can potentially initiate medical image analysis in macroscopic acute ischemic stroke MR/CT imaging-based dynamic modeling. Furthermore, tapping into the potentials of *in silico* research in medicine relying on accurate and realistic mathematical and computational models would help overcome the need for expensive clinical trials.

4.3.2 Segmentation methods

We have identified 25 papers addressing the problem of acute/subacute ischemic stroke segmentation: 21 (84%) of these methods were evaluated using patient data and 5 (20%) used animal data (rats or rodents). Synthetic data were also used in 6 (24%) of the reviewed papers. Eighteen (72%) of the segmentation methods were applied to MR structural and/or perfusion/diffusion data and 7 (28%) used CT datasets. One paper [Weinman 2003] did not provide

Paper	Basic Method Principle	Data	Medical Modalities	C	U	TD	T	Sw	R	S
Braun *et al.*, 2002	- Automated, multidimensional 3D histogram-based classification method	C(5,h) S(-)	MR(T2, DWI, ADC)	I	N	N	S	N	N	I
Chawla *et al.*, 2009	- Automatic histogram and wavelet-based 2-level classification algorithm	C(15,h)	CT	P	N	N	S	N	N	I
Contin *et al.*, 2010	- Local statistics	C(1,h)	CT(CBF, CBV, MTT)	I	Y	N	S	N	N	P I
Dastidar *et al.*, 2000	- Semi-automatic thresholding-derived region growing, and decision trees based algorithm	C(40,h) S(5)	MR(T1, T2)	I	Y	N	S	N	N	I
Dwyer *et al.*, 2008	- Semi-automatic Hidden Markov Random Fields	C(3,h) S(-)	MR(T2, FLAIR, DWI, ADC, MTT)	P	Y	N	S	N	N	P
Gosh *et al.*, 2011	- Hierarchical recursive region splitting using rescaling, histogram and distribution measures	C(51,a)	MR(T2)	I	Y	N	S	N	N	I
Hevia-Montiel *et al.*, 2007	- Nonparametric density estimation approach using edge confidence map	C(15,h)	MR(T2, DWI, ADC)	P	N	N	S	N	N	I
Jacobs *et al.*, 2000	- Multiparameter unsupervised K-means-derived clustering approach	C(22,a)	MR(T1, T2, DWI, ADC)	P	N	N	M	N	N	P I
Jacobs *et al.*, 2001a	- An unsupervised vector tissue model with a K-means-derived clustering technique	C(20,a)	MR(T1, T2, DWI)	P	N	N	M	N	N	I
Jacobs *et al.*, 2001b	- An unsupervised vector tissue model with a K-means-derived clustering technique	C(10,h)	MR(T1, T2, DWI)	P	N	N	M	N	N	I
James *et al.*, 2006	- Thresholding-based approach	C(6,h) S(-)	MR(T2, DWI, CBF, CBV, MTT)	I	Y	N	S	N	N	P I
Kabir *et al.*, 2007	- Multimodal Markov Random Field (MRF)	C(56,h)	MR(T2, FLAIR, DWI)	P	N	N	S	N	N	I
Li *et al.*, 2004	- Unsupervided adaptive multiscale statistical Bayesian classification and partial volume voxel reclassification	C(20,h) S(-)	MR(DTI)	P	N	N	S	N	N	I
Li *et al.*, 2009	- Unsupervised Mean-shift algorithm	C(19,h)	MR(T2, DWI, ADC)	P	N	N	S	N	N	I
Maldjian *et al.*, 2001	- Anatomical-atlas based segmentation	C(35,h)	CT	A	N	N	S	N	N	I
Martel *et al.*, 1999	- Adaptive thresholding algorithm using Markov Random Fields and Iterative Conditional Modes (ICM)	C(63,h) S(6)	MR(DWI)	P	Y	Y	S	N	N	I
Matesin *et al.*, 2001	- Symmetry-detection and seeded region-growing algorithm	C(-,h)	CT	I	Y	N	S	N	N	I
MeiluÃ¸nas *et al.*, 2003	- Local means and standard deviations intensity-based segmentation	C(-,h)	CT	I	Y	N	S	N	N	I
Prakash *et al.*, 2006	- Probabilistic neural network for an adaptive (two-level) and Gaussian mixture model	C(13,h)	MR(DWI)	P	N	Y	S	N	N	I
Soltanian-Zadeh *et al.*, 2003	- Unsupervised clustering-based tissue scoring method	C(15,a)	MR(T1, T2, DWI, PDWI)	P	N	N	S	N	N	I
Soltanian-Zadeh *et al.*, 2007	- Improved unsupervised clustering-based tissue scoring method	C(9,a) C(15,h)	MR(T1, T2, DWI, PDWI)	P	N	N	S	N	Y	I
Stein *et al.*, 2010	- 3D statistical and deformable snake-based model	C(6,h)	MR(T2, FLAIR)	D	Y	N	S	N	N	I
Ušinskas *et al.*, 2002	- Mean and standard-deviation based segmentation	C(-,h)	CT	I	N	N	S	N	N	I
Ušinskas *et al.*, 2004	- Unsupervised thresholding-derived joint features extraction based segmentation	C(-,h)	CT	I	Y	N	S	N	N	I
Weinman *et al.*, 2003	- Nonlinear diffusion scale-space and geometric deformable model with fast marching level sets	C(5,h)	MR(-)	D	Y	N	S	N	N	I

Table 4.1: *Overview of segmentation methods presented in 25 papers.* In "data" column, two acronyms are used: C(n,h/a): Clinical data, n: number of patients, h: human data, a: animal data. S(n, h/a): Synthetic data, n: number of simulations –if known–, h: human data, a: animal data. The fifth column "C" denotes the category if the reviewed method: (I) Image-based, (P) pixel-classification based, (A) atlas-based, (D) deformable based segmentation category. The sixth column "U" pinpoints whether a user interaction is needed (Y) or (N) not. The next column "TD" highlights whether a training data is required (Y) or (N) not. T: (S) single acquisition time point is required or (M) multiple. Sw: (Y) swelling or (N) No Swelling accounted for in the identified method. R: reperfusion process is considered (Y) or (N) not. S: segmented area included ischemic lesion or infarct core (I) and the penumbra (P).

sufficient information about which MR images were used. Only three papers [James 2006, Contin 2010, Jacobs 2000] tackled the problem of segmentation of the penumbra and the infarct core in a distinct way, whereas the remaining papers aimed at segmenting the whole ischemic area or only the infarct core.

4.3.2.1 Image-based segmentation (36%)

Image-based techniques include thresholding-derived, region-based and edge-based methods [Pham 2000]. Two papers [Dastidar 2000, Matesin 2001] used a region-growing approach. Region growing techniques aim to extract a connected region based on intensity information and/or edges, requiring a user to manually select a seed point within the target region. In [Dastidar 2000], a previously developed segmentation approach relying on a region-growing technique in [Heinonen 1998] was used to evaluate volumetric measurement of brain infarctions in structural T1W and T2W MRI. For the segmentation of stroke lesions in CT scans, [Matesin 2001] proposed an automatic segmentation method also based on a seeded region-growing and using a rule-based expert system yielding a fast labeling of the background, skull, gray, white matter, cerebrospinal fluid, and stroke lesions. [Ušinskas 2002, Meiluonas 2003] presented unsupervised learning methods based on mean and standard deviation computations to segment ischemic stroke regions in CT images. This

approach was extended in [Ušinskas 2004] by adding more intensity-based analysis tools such as histograms and gray-level co-occurrence matrices.

All of the segmentation methods mentioned above focus on segmenting either the ischemic region or the infarct without highlighting the distinction between the penumbra and the core. This problem was raised in [Contin 2010] where a new semi-automatic method based on computation of regional mean and standard deviation and local statistics was developed to identify both the core and the penumbra on acute perfusion CT maps (CBF, CBV, MTT). The algorithm required user interaction to select a seed that was grown according to acceptance criteria. In [James 2006], a semi-automated histogram-based segmentation technique was developed to identify both the core and penumbra and compute the perfusion/diffusion mismatch volume using DWI and PWI maps (CBF, CBV, MTT). In a recent paper [Ghosh 2011], a hierarchical recursive region splitting (HRS) approach addressed ischemic lesion segmentation in animal data with mild, moderate and severe stroke using T2-w images. Using the MR-based signal spectrum, adaptive thresholds were automatically selected leading to promising results when compared with manual segmentations.

Most of the proceeding papers (Table 4.1) provided little information about the number of patients or stroke severity

[Matesin 2001, Meiluonas 2003, Ušinskas 2002, Ušinskas 2004], one paper [Contin 2010] used a single patient without reporting any clinical information. All methods used images acquired at one single time point and did not address the effect that swelling might have on lesion distortion or volume measurement.

4.3.2.2 Pixel and voxel-based classification (52%)

Segmentation problems can be addressed using conventional classification methods, by applying supervised approaches requiring machine learning or unsupervised clustering methods to partition the image into separate classes composed of pixels which have similar pre-defined feature values. The commonly used unsupervised techniques are K-means and iterative self-organizing data analysis technique (ISODATA), which is K-means derived with additional splitting and merging steps [Pham 2000]. In [Braun 2002], another feature-based method was implemented to generate 3D histograms from a representative T2W, DWI and ADC dataset leading to an automatic segmentation of cerebral ischemia. We identified three studies [Jacobs 2001b, Jacobs 2000, Jacobs 2001a] that applied the ISODATA technique. In [Jacobs 2000], multiparametric ISODATA was applied to MR data including T1W, T2W and DWI to discriminate between ischemia-altered and morphologically intact tissue in rats and correlated with histologically identified areas. An improved

version was proposed in [Jacobs 2001a] also applied to rats, then in [Jacobs 2001b] to MR patient data and was correlated with the 3-month final extent on imaging. The multiparametric ISODATA map showed a better localization of the infarcted areas than separately using DWI, ADC and T2 maps at different times after stroke. Based on a comparison between ISODATA-derived damaged tissue volume and DWI-defined (*vs.* T2WI-defined) volumes correlation with the patients' functional outcome after stroke, this method was shown to significantly outperform the basic thresholding techniques which are mostly applied to a single imaging parameter.

ISODATA was used to identify ischemic tissue in similar studies [Soltanian-Zadeh 2003, Soltanian-Zadeh 2007]: in [Soltanian-Zadeh 2003] the identification process was extended to using an abnormality scoring system between 0 and 1 in rats, and in [Soltanian-Zadeh 2007], an improved version was proposed, applied to rats and extended to human data including the role of reinforced reperfusion in the recovery process. In [Hevia-Montiel 2007] a non-parametric clustering strategy using mean-shift algorithm and edge confidence map was developed to identify the lesion core in DW images. A similar approach developed in [Li 2009] also a used mean-shift algorithm to identify acute ischemic tissue in ADC maps.

Included in pixel-based classification techniques, we identified three papers applying Markov Random Fields (MRF), a statistically-based

segmentation model which incorporates information about neighboring voxels [Martel 1999, Kabir 2007, Dwyer 2008]. Martel combined an adaptive thresholding algorithm with MRF to model relationships between adjacent pixels. They obtained a semi-automatic segmentation by maximizing the a posteriori (MAP) probability using the iterated conditional modes (ICM) and applied to DT-MRI to measure the infarct volume.

In [Kabir 2007] a multimodal MRF model including T2, FLAIR and DWI modalities was used to automatically segment the infarct. The method developed in [Dwyer 2008] is among the few existing methods which aim to quantify the perfusion/diffusion mismatch. Perfusion (MTT), diffusion (DWI, ADC) and (T2, FLAIR) data were used in the hidden MRF model combined with an automated contralateral identification to discriminate normal tissue from penumbral non-infarcted tissue leading to a quantification of the salvageability of the hypoperfused tissue. It was also pointed out that the use of hidden MRF showed considerable improvement over basic thresholding techniques. Both the infarct core and contralateral mirror tissue were used as seed regions to initialize the segmentation. A new unsupervised approach, which accounted for the partial volume effect based on adaptive multiscale statistical Bayesian classification and applied to DT-MRI data was proposed in [Li 2004]. A different approach presented in [Prakash 2006], based on a probabilistic neural

network and an adaptive Gaussian mixture model, segmented infarct in DW images. All the previous methods were applied to MR images. For CT data, we only found one paper [Chawla 2009]: Chawla proposed an automatic histogram and wavelet-based two-level classification scheme to depict acute and chronic ischemic lesions separately.

Within this category, only one paper [Soltanian-Zadeh 2007] addressed the phenomenon of reperfusion, only one paper [Martel 1999] required a training dataset and three papers [Jacobs 2001b, Jacobs 2000, Jacobs 2001a] required more than one acquisition timepoint. Although these methods applied more sophisticated techniques, the phenomenon of swelling in acute/subacute ischemic stroke was not addressed.

4.3.2.3 Atlas-based segmentation (4%)

We identified one paper [Maldjian 2001] that used an atlas as anatomical reference to specifically register the target vascular territory during the segmentation process. This automatic method used CT scans of 20 normal subjects and 15 patients to identify potential areas of acute middle cerebral artery infarct. Although the quality of registration to the anatomical atlas was evaluated as excellent, the spatial identification of some infarcts' boundaries did not fit the ground truth observations. The integration of an anatomical atlas in the algorithm may be helpful in determining the anatomical extent of the swollen

ischemic area, however the swelling phenomenon was not addressed.

4.3.2.4 Deformable model-based segmentation (8%)

Deformable models are formulated as an energy-minimization problem using closed parametric curves or surfaces whose spatial deformation is guided by internal and external forces [Pham 2000]. We found two publications that applied deformable models to segmentation of stroke data. The first explored the intensity variations commonly observed within stroke lesions to define a new confidence-based model targeting a robust segmentation of ischemic lesions in MR images and an accurate estimation of the lesion volume [Weinman 2003]. This model combined nonlinear diffusion scale-space with a snake-based deformable model. Although the method led to overall satisfactory results, it cannot be applied to cases with scattered lesions (Fig 3.9) since the segmented lesions are meant to slowly blend together at a certain scale. In the cases where the technique failed to identify the ischemic lesion, user interaction was required to adjust the confidence level. In a second paper, [Stein 2001] introduced a 3D hybrid statistical snake-based deformable model to segment stroke lesions and estimate their volumes. Similarly to the previous paper, the results were promising especially when some of the limitations of the snakes were addressed by integrating additional statistical information. However the model assumed that the lesion was a smooth one-connected

spatial component, which would not apply to many acute ischemic lesions which are disconnected. The algorithm also required user interaction to initialise the snakes. The major limitations of these methods derive from the small sample of patients used for evaluation (5 in [Weinman 2003] and 6 in [Stein 2001]), the lack of information about the severity and the variability of stroke in terms of its location, topological connectivity and swelling.

4.3.3 Prediction methods

We found 14 papers (Table 4.2) describing methods to predict the ultimate tissue fate at acute and/or subacute stages of ischemic stroke: 8/14 (57%) of the identified papers used human ischemic stroke data and 6/14 (43%) used animal data, and MR data were used. In 12 papers (86%) a learning phase, using a training dataset was required, and the techniques described in 5 (36%) papers were based on the acquisition of observations at more than one timepoint. Although the learning phase might impede the development of a fully automatic approach, the reduction in the use of external interaction was only achieved in two papers [Montiel 2008, Rosso 2009]. Unlike the segmentation methods described in Section 4.2, the phenomenon of reperfusion was addressed in 7 (50%) of the prediction-based papers. Nonetheless, the effect of lesion swelling was constantly overlooked and only final infarct images were used to evaluate the different pre-

dictive models (Table 4.2). For a more consistent analysis of the prediction papers, we adopted the same categorization previously used to classify the segmentation methods.

4.3.3.1 Image-based segmentation (21%)

In this category, we identified only two papers [Montiel 2008, Rosso 2009] relying on region-growing approaches. In [Montiel 2008], a 3D nonparametric region-growing technique was applied to ADC maps to extract brain areas more likely to infarct in human acute stroke. The algorithm output was assessed using DW imaging-based final observed outcome and gave promising results. Making the assumption that DW images represent the infarct core and that ADC lesion represents the salvageable penumbra in [Rosso 2009], a thresholding-driven region-growing algorithm was initialized using DW acute lesion boundary and "grown" into the ADC lesion, yielding the final infarct volume. The growth of the initially smoothed 3D boundary was controlled by an energy-index minimization terminated when reaching a pre-set cut-off ADC value. Both of these papers used ADC and DW images, however, the effect of recanalisation on the prediction process was only investigated in [Rosso 2009]. A different non-linear learning approach was recently presented in [Scalzo 2012], where the hypothesis that locally extracted cuboids (voxel in a cube, surrounded by the regional distribution of image intensities) reveal

Paper	Basic Method Principle	Data	Medical Modalities	C	U	TD	T	Sw	R	E
Bagher-Ebadian *et al.*, 2009	- Probabilistic neural network for and an adaptive (two-level) Gaussian mixture model	C(13,h)	MR(DWI)	P	N	Y	S	N	N	I
Carano *et al.*, 1998	- Multispectral analysis using 2 unsupervised (K-mean, Fuzzy C-mean) and supervised (multivariate Gaussian, k-nearest neighbor) clustering techniques.	C(15,a)	MR(T2, ADC, CBF)	P	N	Y	M	N	Y	I
Hevia-Montiel *et al.*, 2008	- 3D region-growing technique	C(40,h)	MR(ADC, DWI)	I	Y	Y	S	N	N	I
Huang *et al.*, 2010	- Artificial neural network	C(36,a)	MR(T2, ADC, CBF)	P	N	Y	S	N	Y	I
Nguyen *et al.*, 2008	- A generalized linear model (GLM)	C(74,h)	MR(T2, DWI, ADC, CBF, CBV, MTT)	P	N	Y	S	N	N	I
Rose *et al.*, 2001	- Parametric normal classifier algorithm	C(29,h)	MR(T2, DTI, ADC, CBF, CBV, MTT)	P	N	Y	S	N	Y	I
Rose *et al.*, 2004	- Expectation maximization and k-means clustering algorithm	C(14,h)	MR(T2, DWI, ADC, CBF, MTT)	P	N	Y	S	N	N	I
Rosso *et al.*, 2009	- Region-growing based model	C(8,h)	MR(DWI, ADC)	I	Y	N	S	N	Y	I
Scalzo *et al.*, 2012	- Kernel spectral regression model trained on a set of locally extracted and normalized cuboids in MR images with known outcome	C(25,h)	MR(Tmax, ADC, FLAIR)	I	N	Y	M	N	N	I
Shen *et al.*, 2004	- Clustering technique related to k-means	C(6,a)	MR(T2, ADC, CBF)	P	N	N	M	N	N	I
Shen *et al.*, 2005	- Clustering technique related to k-means and generation of probability risk maps	C(6,a)	MR(T2, ADC, CBF)	P	N	Y	M	N	N	I
Shen *et al.*, 2008	- Clustering technique related to k-means, generation of probability risk maps and considering spatial susceptibility of infarction	C(6,a)	MR(T2, ADC, CBF)	P	N	Y	S	N	Y	I
Wu *et al.*, 2001	- Thresholding and generalized linear model (GLM) algorithms and generating maps of risk of future infarction	C(14,h)	MR(T2, DWI, ADC, CBF, CBV, MTT)	P	N	Y	M	N	Y	I
Wu *et al.*, 2007	- Voxel-based generalized linear model (GLM)	C(8,a)	MR(ADC, CBF, CBV, MTT)	P	N	Y	S	N	Y	I

Table 4.2: *Overview of ischemic tissue state prediction methods presented in 14 papers.* In "data" column, two acronyms are used: C(n,h/a): Clinical data, n: number of patients, h: human data, a: animal data. S(n, h/a): Synthetic data, n: number of simulations –if known–, h: human data, a: animal data. The fifth column "C" denotes the category if the reviewed method: (I) Image-based, (P) pixel-classification based. The sixth column "U" pinpoints whether a user interaction is needed (Y) or (N) not. The next column "TD" highlights whether a training data is required (Y) or (N) not. T: (S) single acquisition time point is required or (M) multiple. Sw: (Y) swelling or (N) No Swelling accounted for in the identified method. R: reperfusion process is considered (Y) or (N) not. E: (evaluation tools used in the method) (C) clinical-based outcome assessment, (I) Image-based outcome assessment; (B) Both Clinical-based and Image-based outcome assessment; (N) None.

the dynamic evolution of ischemic tissue and its ultimate fate. In a framework where kernel spectral regression is as well-performing as Support Vector Machines (SVM), Adaptive Boosting (AdaBoost) and decision trees, the authors chose it to predict ischemic voxel fate using time-to-maximum (Tmax) or ADC images as input and compared to final FLAIR intensity outcome. Using a leave-one-out crossvalidation as evaluation tool, the outcome was better predicted using Tmax images.

4.3.3.2 Pixel and voxel-based classification (79%)

Within this category, generalized linear models (GLM) were used in three papers [Nguyen 2008, Wu 2001, Wu 2007]. In [Wu 2001], a supervised learning model combining both diffusion and perfusion data was developed to predict tissue outcome in human ischemic stroke determined by a pixel-by-pixel risk of infarction map where both low risk and high risk of infarction areas were depicted and compared according to pre-selected multimodal predictive parameters. The evaluation of this perfusion-diffusion based predictive model using the two-month follow-up T2 image demonstrated vastly better performance when compared to standard thresholding techniques. In a subsequent paper [Wu 2007], a GLM-predicted infarction risk map using four MR modalities (ADC, CBF, CBV, MTT) in rat reperfused/nonreperfused stroke was generated. A recent extension of the GLM integrated ad-

ditional spatial correlation information in [Nguyen 2008], was applied to human structural, perfusion and diffusion data and compared to a spatial autoregression model (SAR) which individually outperformed GLM in the majority of cases.

For clustering K-means derived methods, we identified five papers [Carano 1998, Rose 2001, Rose 2004, Shen 2004, Shen 2005, Shen 2008]. In [Carano 1998], a multiparametric analysis using two unsupervised (K-means, fuzzy C-means) and two supervised (multivariate Gaussian, k-nearest neighbour) clustering techniques were used to classify ischemic tissue fate based on ADC maps, CBF maps and T2 in a rat stroke model. An additional evaluation of the outperformance of K-means, using correlation coefficient to postmortem infarct size, was highlighted when compared to both multivariate Gaussian and k-nearest neighbour supervised methods. In [Rose 2001], a parametric normal classifier algorithm used quantitative and relatives perfusion measures (CBF and CBV) and diffusion data (DWI) to predict the spatial location and size of infarcted MTT tissue. Expectation maximization and K-means clustering algorithm to predict tissue outcome were used in [Rose 2004], and investigated whether bolus-delay-corrected dynamic susceptibility perfusion MRI measures lead to a better estimation of the infarct volume in human ischemic stroke. Both diffusion and perfusion maps were used to implement the predictive model and the 30-day T2W final lesion was used to validate

its accuracy. In [Shen 2004] a K-means driven improved ISODATA cluster analysis was used to track the dynamic change of ischemic tissue within the core and the penumbra and predict its ultimate outcome in rats. The ADC map when combined with CBF map was used to determine the "mismatch fate" with the T2W lesion as the final infarcted region. This approach was improved in [Shen 2005] by generating probability maps of risk of future infarction using different combinations of input data (only ADC, only CBF or both ADC and CBF). An alternative improvement of this model taking into account vascular regional susceptibility to infarction was proposed in [Shen 2008] where an additional training-based supervised learning stage was used in the model to draw probability-of-infarction profiles based on ADC and CBF maps. Furthermore, both scenarios of spontaneous reperfusion and non-reperfusion were considered to build a more robust and reliable predictive model.

We found two recent studies [Bagher-Ebadian 2011, Huang 2010] based on artificial neural networks (ANN). In [Bagher-Ebadian 2011], the final extent of the 3-month T2-lesion was predicted using T1W, T2W, DW and PW training images at the acute timepoint. In [Huang 2010], Huang *et al.* defined six different conditions to predict the final tissue outcome by training an ANN and testing it using the leave-one-out approach. Spatial infarction incidence map and nearest-neighborhood information were fed into the model to guide

the training process. The model prediction performance was also compared with the previous animal models of [Shen 2005, Shen 2008] and gave a similar performance.

Almost half of the methods were evaluated using animal stroke data and using the same data as that in which the algorithm had been developed or trained. As shown in Table 4.2, the technique described in [Shen 2004] (and its subsequent developments in [Shen 2005, Shen 2008]) all used data obtained from 6 rats not clarifying if the same or different rats were used. Although the results were promising, achieving a similar level of accuracy and precision in human stroke is unlikely because of its increased complexity compared to animal models. As in segmentation methods, the induced swelling was not considered in any of the identified predictive approaches.

4.3.4 Stroke dynamic evolution modeling

We found eight papers (Table 4.3) that provided more insights into the dynamic progression of the infarct core and the spatio-temporal evolution of the penumbral region in acute/subacute ischemic stroke [Chapuisat 2008, Chapuisat 2010, Dronne 2004, Dronne 2006, Duval 2002, Grenier 2010] and that addressed different key phenomenon influencing the patterns of dynamic evolution of both animal and human ischemic strokes.

A simplified mathematical dynamic model depending on a set of

key parameters involved in the hyperacute phase of ischemic stroke was described in [Duval 2002]. The key factors involved in initiating the cascade of ischemic events were identified using MRI and PET quantitative data and translated into equations simulating a voxel-per-voxel early ischemic stroke episode and investigating the influence of the oedema on the penumbra evolution. Subsequently, through depicting the relevant components in the process of stroke evolution observed in human and animal strokes, a formal 2D microscopic dynamic model was presented [Dronne 2004]. The global model was built by combing two or more of ten sub-models, each denoting a key factor in evolving stroke (tissue reactions, ionic movements, oedema development, gluatamate excititixicity, spreading depression, NO synthesis, inflammation, necrosis, apoptosis, and reperfusion). A dynamic model describing the spatio-temporal evolution of the penumbra after a permanent occlusion or reperfusion was simulated by merging three dynamic sub-models. Another microscopic dynamic model was developed in [Dronne 2006] that focused on ion movement in gray matter that were considered to trigger cell swelling and shrinking. They ran different simulations for severe and moderate ischemic strokes, analyzing the effect of some ion channel blockers on the development of cytotoxic oedema.

A dynamic phenomenological model, that simulated the propagation of spreading depression (SD) in a 2D brain following energy re-

duction caused by local ischemia and taking into account the recovery mechanism through reperfusion, was presented in [Chapuisat 2008]. A set of mathematical multiparametric equations was defined considering cell death by apoptosis or necrosis. Through solving these equations, the model attempted to simulate the pattern of local ischemia using empirically set parameters.

The role of the duration and the intensity of CBF reduction on the final size of the ischemic core and on cell death by necrosis or apoptosis was investigated in [Chapuisat 2010]. Various ischemic conditions were identified and translated into ordinary and partial differential equations. The evaluation of the suggested mathematical model was evaluated using *in silico* experiments. In [Grenier 2010], the dynamic growth of the ischemic lesion core was modeled using a set of ordinary differential equations and used to explore the influence of the mode of cell death (by necrosis or apoptosis) on the final infarct size. Unlike previous dynamic models, for the first time, the mathematical reaction-diffusion equation extensively used to model biological phenomena and brain diseases [Murray 2002] was newly adapted to simulate ischemic stroke evolution in realistic 3D geometry of the human brain and differentiate ischemic evolution in white and gray matters [Dumont 2010], based on the model of [Dronne 2006]. The "realistic" tag associated to the approach stems from differentiating the dynamic evolution of ischemic in gray and white matter as the authors

used 10 reaction-diffusion equations in gray matter and 5 in white matter to simulate the propagation of tissue-damaging waves. This new simulative model was built upon an efficient numerical scheme to solve the partial differential equations (PDE) using multithreaded reaction solver. Later on, going back to hypothesizing a simple homogenous geometry of the brain (made only of gray matter), the first hour of 2D/3D human ischemic stroke evolution was simulated using a new numerical scheme to solve multi-scale reaction-diffusion equations [Louvet 2011], where the reaction term was also inspired from [Dronne 2006]. The multi-scale reaction diffusive waves were formulated based on main ionic mechanisms controlling cell death in stroke with 19 unknowns to estimate and solved on simplified brain geometry due to the limitations of the used adaptive mesh refinement techniques.

All of these dynamic models were evaluated through launching a set of simulations using different physiological values depicted from the literature (Table 4.3). None of the models were validated using imaging-based or clinical-based assessment or simulated the evolution of synthetic or real stroke lesions on MR or CT images. None of these papers also included an MR or CT image of an ischemic stroke. In addition, these models used simplified assumptions, such as hypothesizing a 1D or 2D homogeneous brain [Chapuisat 2008, Dronne 2004] and not considering the diffusion of the ionic species [Dronne 2006].

Paper	Basic Method Principle	Sw	R
Chapuisat *et al.*, 2008	- Global phenomenological microscopic dynamic model simulating ischemic stroke evolution.	N	Y
Chapuisat *et al.*, 2010	- Mathematical model simulating the influence of blood flow reduction in final infarct size.	N	N
Dronne *et al.*, 2004	- Mathematical dynamic microscopic model simulating the penumbra evolution.	N	Y
Dronne *et al.*, 2006	- Mathematical dynamic microscopic model simulating the main mechanisms involved in the penumbra development.	Y	N
Dumont *et al.*, 2010	- Reaction-diffusion based model simulating the heterogeneous 3D evolution is ischemia.	Y	N
Duval *et al.*, 2002	- Physiological based model of ischemic stroke.	Y	N
Grenier *et al.*, 2010	- Phenomenological dynamic microscopic model simulating the growth of the dead zone in ischemic stroke.	N	N
Louvet *et al.*, 2011	- Multi-scale reaction-diffusion based numerical model simulating a 2D/3D human ischemic stroke evolution during the first hour.	N	N

Table 4.3: *Overview of dynamic evolution models presented in 8 papers.* The acronym Sw denoted swelling, combined with the acronyms: (Y) swelling or (N) No Swelling accounted for in the identified method. R: reperfusion process is considered (Y) or (N) not. None of these studies used medical data or have been assessed using imaging or clinical outcome.

Moreover, all of the reviewed dynamic models are based on hypotheses drawn from different publications without considering the significant information that could be extracted from MR/CT images such as anatomical boundaries and lesion topological and shape properties. Unlike all the previously reviewed prediction and segmentation methods, the phenomenon of swelling was addressed in three papers [Dronne 2006, Dumont 2010, Duval 2002] and two papers [Chapuisat 2008, Dronne 2004] addressed possible effects of reperfusion.

4.4 Discussion

In this chapter, we have performed an extensive search to identify image analysis methods and mathematical models applied to acute/subacute ischemic lesions in human, animal and/or synthetic data. We identified 47 papers within 3 different objectives: segmentation of dead and/or salvageable tissue, prediction of final ischemic tissue outcome and dynamic modeling with simulation of ischemia evolution. Most of the medical image analysis and computational models in acute/subacute ischemic stroke firstly considered the penumbra and core tissue segmentation problem and secondly the prediction of the final irreversible damage. Through identifying studies that tackled both of these problems, we presented a common categorization to provide an overview of the approaches that have been proposed and their major drawbacks. Taking into account the limitations of the thresholding approaches [Pham 2000] as being blind to spatial characteristics of an image, very sensitive to image artifacts and that they cannot be easily applied to multi-channel images, we excluded all studies that only relied on basic thresholding techniques and/or standard statistical-correlation-based data analysis. Tools aimed at clinical practice such as the RAPID software [Straka 2010], which attempt to automatically segment both acute core and penumbra to estimate their volumetric mismatch, were also excluded because of

the use of absolute or relative thresholds. Relying on PWI/DWI threshold values has been demonstrated to be a misleading factor in measuring both perfusion and diffusion abnormalities [Dani 2012]. Segmentation and prediction methods that do not incorporate a non-rigid or deformable registration to account for the induced by acute swelling, may be expected to yield somewhat erratic results, due to the variation in the mass effect between patients.

Reviewing the 47 included papers, we noticed that these did not, in general, consider the underlying biology and imaging-dependent issues related to ischemic stroke evolution and the tissue fate. Indeed, swelling and all other aspects of lesion and peri-lesion tissue distortion were completely overlooked in all the prediction and segmentation methods, although it was integrated in the mathematical equations in one dynamic model with simplistic assumptions [Dronne 2006] (Table 4.3). Another key phenomenon that can alter the dynamic evolution process of acute ischemia is spontaneous or therapeutic reperfusion. Since segmentation methods are used to determine spatial boundaries of the core and/or penumbral regions at a specific fixed timepoint, the reperfusion is not to be included as a varying parameter in the method. The reperfusion problem was only highlighted in 7 prediction methods (50%) and in one dynamic model [Dronne 2004]).

Additionally none of the described segmentation, prediction and dynamic evolution methods accounted for the number of connected

components comprising the overall lesion. In fact, one might need to use different mathematical-driven approaches when tackling the problem of segmenting or predicting outcome in lesions made up of one-connected-component versus multiple connected-components. In the majority of the prediction methods described, the visible lesion on the T2W image at 3-months after stroke was considered as the ground truth for determining outcome. The problems of T2-shine through and fogging were not mentioned in any of the papers that used DW weighted imaging. All of these are common MR/CT imaging features of stroke and will distort the interpretation of lesion progression in the subacute phase using image analysis methods unless considered in the design of the method.

Looking at the performance of the included papers, most of the approaches described seemed to perform better than basic thresholding techniques, paving the way for more promising segmentation and prediction methods. Most studies in segmentation and prediction used the same models: K-means derived approaches such as ISODATA 8 (32%), region growing based approaches 4 (16%) and GLM 3 (12%). Many groups presented results in later papers that built upon models described in earlier papers but with improvements to overcome their main limitations and that seemed in some cases to be more promising (eg: [Shen 2008, Huang 2010] in prediction). However, it is difficult to assess the performance of these approaches, or the superiority of one

over another, due to repeated use of the same dataset, the wide variety of evaluation methods applied in animal, human and synthetic data, the wide range of combinations of perfusion and diffusion measures and the variation in the point at which the modeling builds up the ischemic pattern and the assumptions on which the model depends.

Regarding the need for external user interaction, 11 (44%) of the segmentation and 2 (14%) prediction methods required user interaction promoting for fully automatic approaches. From a data-driven perspective, 11 (79%) of the prediction approaches and 2 (8%) of the segmentation methods required training data. These supervised approaches can present a stumbling block to the wider clinical adoption of such techniques.

Ideally, predicting and modeling the dynamic evolution of acute stroke would be achieved relying on one single MR/CT image acquisition at the acute timepoint. Five (36%) of the predictive approaches needed time series (longitudinal) data rather defeating the purpose of trying to predict lesion change. Most segmentation and prediction methods lacked validation datasets and some only used synthetic data for validation. Another issue is the paucity of data available for development and testing with 8 (32%) of the segmentation (*vs.* 4 (29%) of the prediction) methods used less than 15 patients or only synthetic data. Five papers did not provide any information about the number of patients. None of the dynamic models were assessed using animal

or human data. Only image-based outcome assessments were used so it is unclear how these relate to the more clinically-relevant functional outcomes. A better assessment would combine both the image-based and clinical-based outcomes. Some papers provided no validation of their method [Kabir 2007]. Interestingly, in the prediction imaging-based category, the kernel spectral regression technique presented in [Scalzo 2012] was demonstrated to be more efficient when compared to basic linear regression model since with its *nonlinearity* it captures more the complexity of intensity-based spatial evolution of stroke.

From a medical image analysis perspective, only three papers [Weinman 2003, Maldjian 2001, Stein 2001] out of 25 dealing with segmentation did not rely on image-driven or pixel classification based approaches. For prediction, all of the included studies belong to one of these approaches. These image-driven and pixel classification-based approaches offer a limited framework for incorporating strong prior information to improve segmentation. Furthermore, a major weakness of these classifiers is the partial volume effects and intensity inhomogeneities in the images [Pham 2000]. Out of all of the identified prediction and segmentation methods, only one [Li 2004] dealt with the partial volume effects. Also the performance of parametric classifiers is dictated by the underlying statistical characteristics of the training data which increase the probability of obtaining biased results especially when using the same datasets in successive publications with

incremental improvements. Again this may reflect the small number of datasets available to researchers because of the difficulty of collecting such data, meaning that separate cases cannot be used for development or training and validation.

Additional problems arising from ISODATA technique [Soltanian-Zadeh 2003, Jacobs 2000, Soltanian-Zadeh 2007, Shen 2004], include its instability when applied to noisy images, artefacts and dependence on the assumption of normality for the distribution of clustered data [Bagher-Ebadian 2011]. Perfusion data, for example, are not normally distributed indicating a fundamental flaw in this assumption. All these factors can be misleading during the pixel-by-pixel based classification (*vs.* prediction). Interestingly, Contin *et al.* pointed out the scarce literature regarding the segmentation of ischemia in perfusion CT images, reflecting that this imaging facility is left out of consideration of medical image analysists.

Some of the included studies involved an empirical estimation of various parameters such as the use of 19 ordinary differential equations with 30 parameters to estimate in [Dronne 2006] and 17 in [Chapuisat 2010]. This is prohibitively time consuming and increases the computational load. The problem of how to estimate automatically any initial or fixed parameter values is still unsolved in many of the approaches. For example, when using artificial neural networks

[Huang 2010] the optimal number of hidden nodes and training epochs is not straightforward to determine.

Most of the dynamic models hypothesized a simple geometry of the brain: 1D or a square brain [Chapuisat 2008], 2D matrix [Chapuisat 2010] and that brain tissue was homogenous (eg: only gray matter [Dronne 2006, Louvet 2011]). In some prediction papers, spherical lesion simulations were used to validate the developed method [Shen 2008]. All these assumptions stray widely from the true characteristics of the brain, the ischemic stroke lesion and its evolution process. Finally, it is worthnoting that all the issues highlighted for prediction algorithms also apply to imaging-based or microscopic-based dynamic models.

The latter discussion reveals that ischemic stroke lesions are complex, with wide variation in, and relative unpredictability of their spatiotemporal evolution. Many promising new drugs emerging from preclinical testing have failed in clinical trials [Duval 2002]. There are many reasons for this, but one factor may be some misconceptions or perhaps oversimplification of our understanding of the acute ischemic stroke lesion evolution process. It is important that neuroimaging modalities and subsequent analysis techniques, like MRI and CT, properly address the key imaging-derived or biology-derived problems, that are inherent to ischemic stroke, though few if any do. It may be that the image analysis community has deliberately avoided acute is-

chemic stroke, recognizing the difficulty of dealing with thick section, non-contiguous image slices in a disease that causes marked tissue distortion, appears and disappears over time, most often consists of disconnected parts rather than a single lesion. In this light, more integrated approaches that unite the image processing and clinical communities are needed if any of these potentially promising methods are to realize their potential. To our knowledge, a book chapter, by Gosh *et al.* [Ghosh 2012], was the first to touch on previous computational noninvasive stroke analysis methods used to segment penumbral and infarcted tissue and to address tissue fate prediction. Others are starting to realize the importance of adopting alternative approaches to the traditional volume measurement or threshold delineated lesions studied so far. However, the majority of the biology-dependent and imaging-dependent issues weren't addressed in [Ghosh 2012].

In addition to including key biological phenomena like swelling, collateral flow and reperfusion and addressing the previously described imaging-derived problems, further difficulties lying ahead include, for example, the ongoing debate concerning the use of perfusion/diffusion mismatch [Rivers 2006, Chemmanam 2010]. Although this problem might seem on the periphery of the main focus of this chapter, it cannot be ignored when tackling prediction or dynamic simulation of image-based ischemic lesion evolution. Unlike other brain diseases which might succinctly rely on one unique modality to extract

the required information on evolution, ischemic stroke lesions cannot be properly understood without a "good combination" of both structural images and perfusion maps. The absence of any prediction model using CT data (Table 4.2) indicates unresolved issues for the future, like the subtle tissue attenuation changes during the hyperacute stage [Brott 1989, Kalafut 2000, Muir 2007, Wardlaw 1998]. Lesion enhancement methods might help overcome this major challenge [Takahashi 2005, Tsai 2005]. Nevertheless, a potential combination of both CT and CT-Perfusion (CTP) –as more acutely accessible data– might tweak the results of the prediction methods. Finally, valid lesion evolution or outcome prediction models would have to take account of differences in biological properties of gray and white matter, overlooked by all methods so far. Even in segmentation methods, Shen *et al.* pointed out that segmentation of ischemia and its progression quantification requires segmentation of white and gray matters [Shen 2008].

We also found a key untapped potential in that there was no image-based macroscopic dynamic model simulating the evolution of acute/subacute stroke. We tried to locate microscopic mathematical-driven dynamic models based on a set of partial and ordinary differential equations focusing on the stroke evolution process. These microscopic dynamic models can inform the development of macroscopic imaging-based dynamic models in acute ischemic stroke as has

occurred previously in other brain diseases [Duncan 2000]. Setting the bridge between microscopic and macroscopic ischemic progress simulation would need a translation of the *phenomenological equations* into imaging-derived equations where the variables can be measured using perfusion, diffusion or structural images. The great strides made in the microscopic simulation field of ischemia spatio-temporal progress, where more realistic models were developed reproducing the dynamics observed on MRI images in stroke patients [Dumont 2010], led to more promising results. However, the variables/parameters of the developed equations are not directly related to visually-measurable (or imaging-derived) quantities on medical images (eg: lesion boundary, shape, intensity etc), as it uses the decrease of the ionic currents through the ionic pumps. Although it was also mentioned that the experimental results were consistent with observations on MRI images, no patient data evaluating this *consistency* proved it right. Including the diffusion term into the phenomenological models in [Dumont 2010, Louvet 2011] showed interesting results. Nevertheless, the precision of the predictive power of the simulations was doomed by the expensive integration numerical scheme of the diffusion term as the spatial discretization increased.

The era of stratified medicine and stroke treatment targeted to the individual is emerging. An ultimate goal of our review is to create new *patient-specific* mathematical and medical image analysis meth-

ods that account for the considerable individual variability between stroke patients. We believe that spatio-temporal MR/CT imaging-based dynamic models, that our literature search shows do not currently exist for ischemic stroke, will further a more complete understanding of how the DWI core and the penumbra continuously and dynamically evolve. In the long term, novel patient-specific dynamic models that predict the evolution of the core and the penumbra from a single timepoint are possible. Going back to the "ambiguity" that may be surrounding the definition of the ischemic lesion core using DWI or other measures, this may be resolved once a 4D dynamic model adequate to capture the ischemic lesion optimally has been developed. Such a 4D approach will theoretically overcome the major limitations of current 2D or 3D approaches, if the lessons learned in the fields of tumour modeling can be applied to stroke. Spatio-temporal imaging-based dynamic modeling when applied to large representative populations of stroke, will also help identify common patterns of lesion evolution which may in turn help to refine our understanding and definitions of core and penumbra.

Such lines of research should be drawn to allow development, initial independent validation and then further wider evaluation in clinically relevant populations of any new methods. This requires access to large datasets and both clinical-based and imaging-based outcome validation criteria. With this in mind and in a context where "time is brain",

the computational time of any new method is also a critical challenge requiring a more robust and efficient computational framework. A brief summary of these key recommendations for any future research work aimed at tackling any one of these three medical image-analysis problems in ischemic stroke, and considering the key problematic issues cited above, is highlighted in Table 4.4. The recommendations link both of the fields of image processing and MR-CT analysis in the hope of honing new innovative models that can tackle the major challenges in acute/subacute ischemia and further a growing interest in a variety of possibilities, at present untapped because of the complexity of ischemic stroke.

4.5 Conclusion

In this chapter, we presented an overview of medical image analysis and mathematical models tackling problems of segmentation, prediction and dynamic evolution simulation in acute ischemic stroke using animal, human and/ or synthetic data published to 2012. As further improvements, including anatomical spatial information, tissue heterogeneity (e.g.: gray and white matter) and accounting for partial volume effects induced by thick image slices, may be considered. Taking into account the site of the arterial occlusion using MR angiograms (MRA) will be important in determining the biology-dependent factors influencing the evolution of both infarct and penumbra and po-

<table>
<tr><th>Category</th><th>Segmentation</th><th>Prediction</th><th>Dynamic Evolution Simulation</th></tr>
<tr><td>Setting clear targets</td><td>- Segmentation of the ischemic acute/subacute lesion core (supposedly dead) and/or the penumbra (supposedly salvageable), both presumably predefined in an adequate way.</td><td>- Prediction of the final outcome of the ischemic acute/subacute salvageable tissue (penumbra).</td><td>- Simulation of an imaging-based dynamic evolution of acute/subacute ischemic stroke (with or without distinction between spatio-temporal behavior of dead and salvageable tissue boundaries).</td></tr>
<tr><td rowspan="2">Datasets and imaging modalities</td><td>- Variability of the ischemic lesions to segment whether when choosing perfusion or diffusion data.
- The segmentation algorithm can use perfusion and/or diffusion data.</td><td colspan="2">- The combination of both perfusion and diffusion data is needed to develop realistic predictive and dynamic models.
- Ideally, the developed approach would rely on one unique acquisition time point at acute stage instead of using time series (longitudinal) data.
- Structural T1, T2 and FLAIR are commonly used to reveal the final imaging-based tissue outcome.
- The use of MR angiography (MRA) as efficient tool to include the location of the occlusion in the predictive/simulating model.</td></tr>
<tr><td colspan="3">- Provide information about the recruited patients (number, age, stroke severity, “abnormal” blood territory, etc) and about the how synthetic data was simulated.
- Better use both of the clinical and the simulated data.</td></tr>
<tr><td rowspan="2">Problematic issues and key challenges to consider</td><td>- Considering reperfusion phenomenon might not be considered since segmentation methods are used to determine spatial boundaries of the core and/or penumbral regions at a specific fixed timepoint.</td><td colspan="2">- Distinguish between the evolution of ischemic stroke in both white and gray matter as they have different hemodynamic behaviors.
- Account for reperfusion in its four possible states: (1) natural spontaneous reperfusion without using collateral arteries, (2) spontaneous reperfusion using collateral arteries, (3) no reflow phenomenon, (4) reinforced reperfusion through thrombolysis.
- Explore more the “predictive” power of the perfusion/diffusion mismatch and its influence on the dynamic behavior of ischemic strokes.
- Find a good combination of diffusion and perfusion maps to use in the predictive/dynamic model.
- Avoid oversimplified hypotheses about brain geometry (1D, 2D) and heterogeneity (eg: considering the brain as homogenous tissue).</td></tr>
<tr><td colspan="3">- Take into account swelling and shrinking processes to avoid drawing “unrealistic” conclusions about lesion spatial, temporal and volumetric evolution patterns.
- Consider the case of scattered ischemic lesions when developing segmentation algorithms and when estimating or predicting an evolution scenario.
- Use medical-image pre-processing tools to “remove” partial volume effect due to slice thickness in stroke data.
- Improve the computational speed of the developed approach.
- Avoid user interaction and aim for a fully automatic approaches.</td></tr>
<tr><td>Evaluation criteria</td><td>- Use various evaluation tools (eg: Dice formula) to assess the accuracy and the precision of segmentation method.</td><td colspan="2">- Use both clinical-based and image-outcome based evaluation tools to assess the outcome of both dynamic and prediction models.</td></tr>
</table>

Table 4.4: Recommendations for future research work addressing the segmentation of the dead and/or salvageable acute/subacute ischemic tissue, prediction of its final outcome and the simulation of an image-based dynamic evolution of ischemic stroke lesions.

tentially more accurately predicting their final outcome [Phan 2009].

An automatic segmentation method that would also predict ischemic tissue fate, and simulate the probable further evolution of the infarct core and the surrounding penumbra is a major goal that could be used to support stroke treatment. New levels of sophistication and several alternative approaches are required in medical image analysis to handle the complexity and the biological variability of acute ischemic stroke. Most of these issues have not even been considered or resolved. This lack of attention to acute ischemic stroke from an image-processing and computational perspective is underlined by the limited number of the studies on segmentation, prediction and dynamic simulation. Alternatively, it may indicate awareness of the technical difficulties posed by the pathophysiology of stroke. Some medical image analysis methods developed to detect tissue abnormality in other diseases appear promising for applying to acute ischemic stroke [Erus 2010, Seo 2009, Studholme 2006]. This would promote better understanding of different patterns of lesion evolution and provide insights into new treatment possibilities. Failure to recognize and address the difficulties is likely to delay progress in the field. Ultimately, image analysis applied to stroke may enable the selection of patients who will more likely benefit from thrombolytic threatment at a reduced risk of hemorrhage; thereby improving the efficacy and safety of this treatment.

More importantly, the results of this chapter drew our attention to a key untapped potential in stroke research: medical-imaging-based dynamic modeling of stroke lesion evolution. We propose in the next chapter a novel modeling approach that has not been tested on stroke. We explore the dynamics of perfusion and diffusion stroke lesions and their spatiotemporal interactions. This first attempt to model stroke lesion development will enable us to define novel metrics and tools to examine stroke behavior as it appears on MR medical images.

Part III

Current-based Dynamic Modeling of Stroke Evolution

"*Anyone who has carried out scientific research knows that data are uncertain, that much depends on the way they are interpreted, and that all methods have their limitations.*"

Rupert Sheldrake; Science Delusion

Chapter 5

Current-based dynamic modeling of perfusion and diffusion stroke lesion evolution

Contents

5.1 Context

In Chapter 4, we showed that numerous medical image analysis approaches have been applied to DWI and/or PWI data using 2D or 3D approaches to determine how the ischemic stroke lesions evolve and what factors influence this. Most of these studies evaluated MR (or CT) images of ischemic stroke as static 'snapshots' to predict tissue prognosis and its association with clinical outcome [Wardlaw 2010, Keir 2000]. These studies suggest considerable potential to identify the change in DWI hyperintense and PWI hypoperfused tissues using pixel-by-pixel algorithms or volumetric region of interest analyses [Oppenheim 2001, Wu 2001, Arenillas 2002, Grandin 2002, Schaefer 2002, Shen 2005]. Although many studies to date suggest that some patients conform to the expected growth of the DWI into the PWI lesion [Symon 1980, Baird 1997, Sobesky 2005], others did not. This might be due to insensitivity of visually assessed 2D lesions [Campbell 2010] and voxel-based analyses may be more sensitive [Kidwell 2003, Arenillas 2002, Barber 1998].

Many studies have tested different DWI or PWI thresholds to define their respective lesions, but there is still considerable variation in final tissue outcome that is not completely explained by the DWI/PWI mismatch hypothesis [Dani 2011, Dani 2012, Baron 2002, Barber 2004]. Furthermore, most of the standard approaches used in stroke did not come to fill in all gaping holes in the literature regarding the dynamics of dead/penumbral tissue boundary progression or regression visible on MR perfusion and diffusion images. Indeed, no patient-specific dynamic models have been developed to identify the kinetics of stroke evolution and to estimate the spatiotemporal deformation that abnormal tissue undergoes (Chapter 4).

In this chapter, we present the proof-of-concept application of a novel spatiotemporal model to DWI/PWI lesions that has not previously been applied in stroke. To capture the individual differences and enable a model that is as patient-specific as possible, we choose a 4D spatiotemporal approach that identifies individual differences independent of clinical factors such as stroke severity, the affected vascular territory or the location of the occluded artery and that did not require any information except the DWI and PWI lesion outlines. In this chapter, we define the perfusion-diffusion mismatch as a 3D spatial discrepancy (or a volumetric difference) between the PWI brain volume and DWI lesion volume or some portion there in [Kidwell 2003, Barber 2004] (Figure 5.1). Although patients with

MR mismatch are thought to be more likely to respond to treatment, other evidence indicates that even if re-perfusion occurs quickly the outcome may not conform to the expected evolution pattern [Zhao 2011, Kane 2007b]. This model will help us examine more accurately the spatiotemporal interactions between DWI and PWI lesion surfaces as they locally contract and expand with time.

By applying the 4D model to longitudinal PWI/DWI stroke data, we aim to:

1) Model individual DWI and PWI lesion dynamic changes separately to identify sub-regional differences in expansion and contraction of the respective DWI and PWI lesions and determined how well the model fitted the true lesion evolution as represented by the original image data.

2) Explore the pattern of change in the DWI and PWI lesions in relation to each other in individual patients, imputed to 3 hourly time intervals, from the three acquired imaging snapshots spaced many days apart.

3) Investigate the model's prognostic potential by identifying the timepoint at which the PWI/DWI lesions best matched the final observed T2-w lesion as an indicative estimate of the 'final' lesion damage.

In the next section, we will introduce a key concept on which the 4D model was built: the theory of currents.

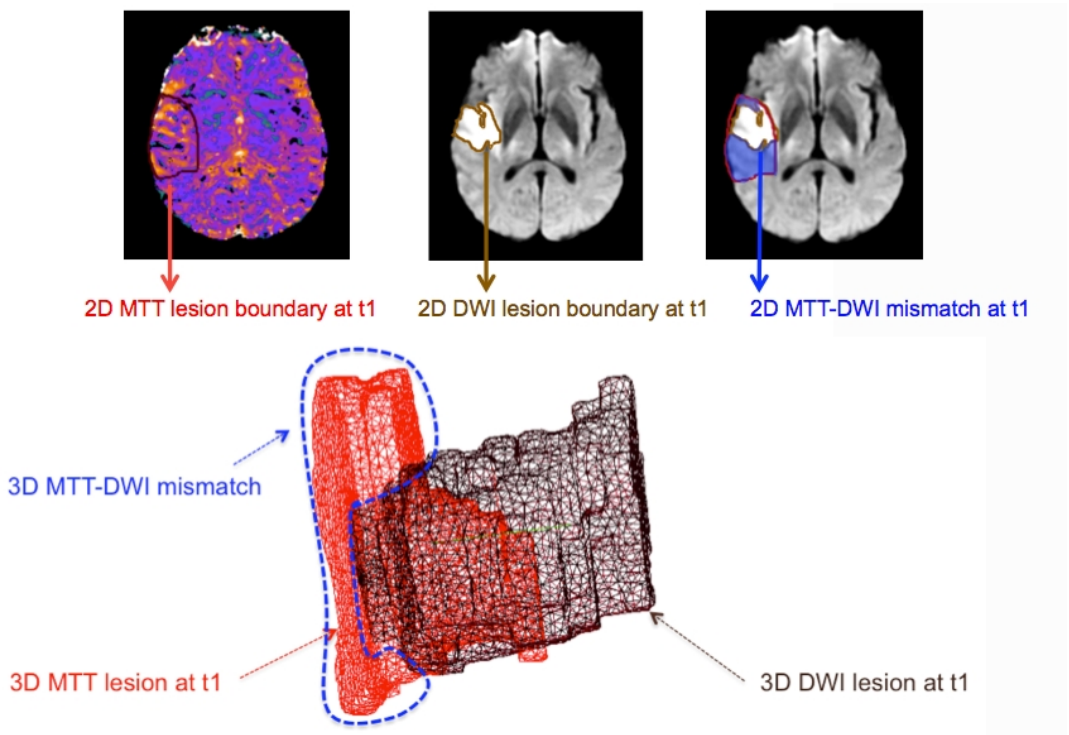

Figure 5.1: *MTT-DWI mismatch at first acquisition acute timepoint* t_1. Top row: MTT-DWI mismatch area in blue visualised on 2D MR axial slices. Bottom row: the 3D reconstruction of MTT and DWI surfaces and their corresponding mismatch spatially defined as the 'output space' produced when taking the diffusion volume out of the perfusion one, outlined in blue.

5.2 Surfaces represented by currents

5.2.1 Background

Stroke lesions can be viewed as an abnormal area visible on 2D MR image when compared to the contralateral region. However, this approach provides no information about the geometry of the lesion and the local deformation that cause its boundary to expand or contract. For instance, viewing the lesion as a 3D surface presents an interesting representation of stroke abnormality using time-series imaging (Figure 5.2). To extract relevant information from a set of lesion surfaces, one needs to set out a solid mathematical framework for lesion shape representation, matching and comparison. Semi-automated surface matching approaches [Bookstein 1997, Davatzikos 1997, Joshi 2000, Cam 2001, Glaunès 2004] were developed to compare changes in surface evolution. However these methods required marking by hand some points on the surfaces (landmarks) to match. Furthermore, even when these approaches have become automated [Chui 2003, Wang 2003], there is a fundamental limitation: every marked point on the baseline surface should have a homologous point on the other. In practice making this task even harder and more time-consuming, since the landmarks cannot be arbitrary and must be chosen after viewing all the images. Chui et al in [Chui 2003] suggested a solution to this problem by discarding points with no

corresponding pair. Looking at the lesion as a surface seems to be promising, however, as long as a surface is reduced to a set of points –ie overlooking all geometric information about the surface curvature and its normal vectors– it is really no more advantageous than looking at voxels on a 2D image (Figure 5.3). One also needs to properly define a norm to measure 'how close' is the baseline surface to the other surface. A well-grounded way to do this is to embed the multiple lesion surfaces in a common space and to endow this space with a computable norm that will allow us to measure this 'closeness' between pair-wise surfaces.

The work of [Vaillant 2005] addressed these issues as they suggested an elegant mathematical representation of a surface using currents –generalized distributions from geometric measure theory that also arise in electromagnetism to define the strength of an electromagnetic field. We will give more details about the abstract and mathematical definitions of current in the next subsection.

Recently, Durrleman et al. [Durrleman 2009, Durrleman 2010, Durrleman 2011] introduced a more generic approach to investigating geometric variability of anatomical structures. Durrleman's approach has the key features of two previous mathematical approaches: Kendall's approach [Kendall 1989] which focused on only capturing geometrical variations and used a metric defined in the space of shapes and measuring shape change; and Grenander's approach

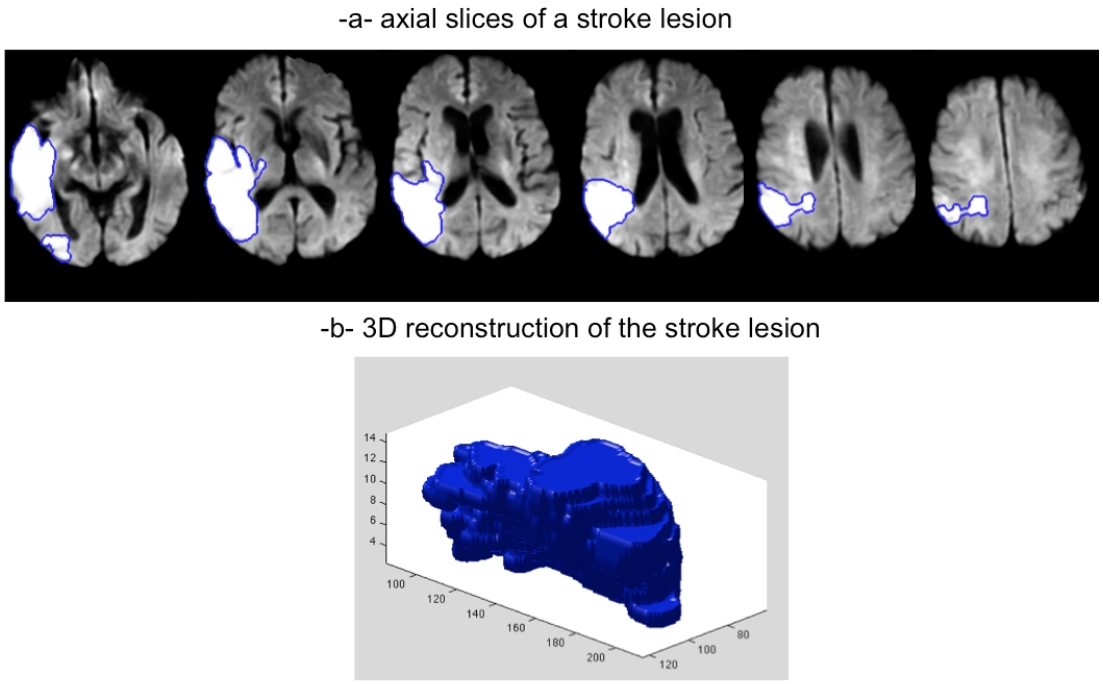

Figure 5.2: *Visualizing a stroke lesion as a 3D surface.* (a) Multiple DWI axial slices showing the bright stroke lesion manually outlined in blue. (b) A 3D reconstruction of the stroke lesion. More geometric information can be retrieved from representing the stroke lesion as a 3D surface construction such as curvature and normal/tangent vectors.

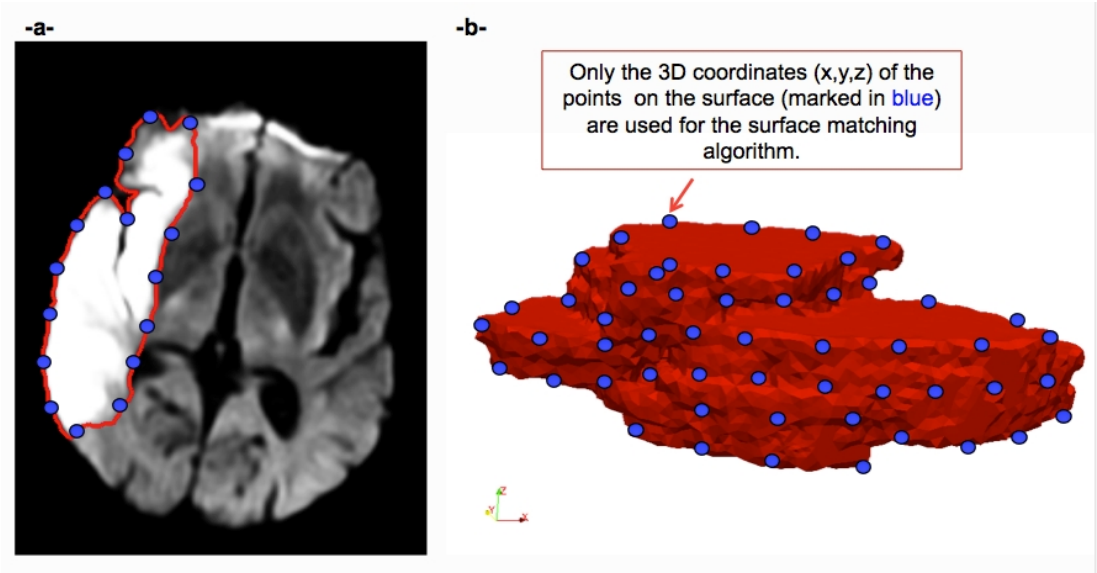

Figure 5.3: *Limitations of the landmark-based surface matching methods.* (a) An external user manually placed some landmarks (blue dots) on stroke lesion boundary (in red). (b) The marked landmarks are visualized on the 3D lesion surface. There is no difference between looking at the lesion using (a) or (b) –since both use 3D coordinates of the marked points. Without incorporating more interesting geometric features of the surface such as curvature and normal, the red surface is not represented as a 'real' surface as it is reduced to a set of blue 3D points (a one-dimensional list of 3D points).

[Grenander 1993] which added the 'texture part', also known as the 'deformation residual', and used a metric defined in the space of deformation. In merging both approaches, the distance between different shapes becomes a measure quantifying the 'optimal' deformation for morphing one shape onto another. A further step was to use the framework of currents, introduced by Vaillant in [Vaillant 2005], to define the deformation metric and the derived distance between shapes, as this was important for dealing with arbitrary non-uniform anatomical shapes.

This key step improved the generic ability of the new model [Durrleman 2010] to deal with any kind of data: eg. surface shapes –such as the skulls of bonobos and chimpanzees [Durrleman 2011]; curves –such as white matter bundles [Durrleman 2009, Durrleman 2010]. The major achievement of this approach is that it is subject-specific and that:

(i) this mathematical representation of surfaces does not require all objects to have the same number of landmarks (normals) to compute the distance between surfaces;

(ii) the metric of currents densely conserves all the geometric properties of the data (here the normal to the surface) up to a given scale. Furthermore, Durrleman's approach allows vector features (momentum and velocities of deformation) to be extracted and compared between surfaces. Unlike approaches based on extracting scalar features

such as rate of growth, these vector quantities allow more informative mathematical features –such as local curvature and orientation of the shape surface– to be used.

(iii) it is weakly sensitive to the sampling of surfaces.

(iv) it extends the pairwise surface registration model into a spatiotemporal regression model which estimates a mean evolution scenario tracking both morphological and kinetic (variation in speed) changes of the baseline surface from one timepoint to another.

Prior to introducing Durrleman's modeling approach for time-series surface matching, we present in the next section the key ingredient of this approach: *currents*.

5.2.2 Surfaces as currents

The name 'currents' comes from the introduction of a more mathematically precise 'way of perceiving a surface', inspired from Faraday's law of induction in physics, where the variation of a magnetic vector field B through a surface S induces a current within a wire loop delimiting S. The intensity of the current is proportional to the variation of the flux of this magnetic field $\Phi(B) = \int_S B^t n d\nu$, with $d\nu$ Lebesgue measure on the surface and n the normal vector to the surface. Therefore, as we measure the intensity of the current within the wire *via* the flux $\Phi(B)$ for every possible spatial variation of the magnetic field, the quantitative relationship allows us to retrieve the

geometry of the wire. Hence, as a current-object, a continuous surface S can be fully characterized by collective fluxes $S(\omega)$ associated with every possible vector field ω defined in a space W and encoded by the 3D surface unit normal vectors n:

$$S(\omega) = \int_S \omega(x)^t n(x) d\nu(x). \tag{5.1}$$

In our case, the space that contains 'the magnetic vector field' traversing the shape surface S is called a 'test space W' and defined as a 'reproducing kernel Hilbert space (RKHS)' with a regularity parameter λ_W tuning the regularity scale at which local curvature of the surface is captured or overlooked (eg: curvatures with radius $< \lambda_W$ are 'visually' unnoticed from the current-based shape modeling perspective). The vector space W can also be thought of as the space of all smooth magnetic vector fields that are acting on the surface and generating different currents.

In other terms, the parameter λ_W restricts the spatial variation of an element ω of the test space W. Defining the test space W as an RKHS endows it with an inner product and a reproducing property that will facilitate calculus and decrease the computational cost of the algorithm. As an RKHS, W is densely spanned by convolutions between any square integrable vector field ω and a smooth kernel $K^W(x,y) = exp(-\frac{||x-y||^2}{{\lambda_W}^2})$. Therefore, for any fixed point y

and vector β, an element $\omega \in W$ is defined as $\omega(x) = K^W(x, y).\beta = \sum_k K^W(x, y_k)\beta_k$.

Looking at the physical interpretation of the mathematical setting, the definition of a test space as an RKHS presents an elegant way to generate change in the magnetic flux ($B \sim S(\omega)$) passing through the loop delimiting the surface S which in turn generates an electric current in the loop. A current is then defined as a continuous linear mapping on the test space of square integrable vector fields W onto $\mathbb{R}$. The space of currents is the dual space of W, noted as W^*.

Since the lesion surface in this thesis work is 3D meshed, one needs to define a discrete approximation of the surface. After an extensive amount of theoretical work [Durrleman 2010], a fairly simple and intuitive definition for currents was presented through the introduction of infinitesimal Dirac delta current measured at the center of each surface facet k with n (the normal vector located at x_k) as follows:

$$\delta^n_{x_k}(\omega) = n^t \omega_{x_k}. \tag{5.2}$$

The Dirac current carries the normal and some parameterization of the area of the triangle that supports the normal n. This provides much more information than just the barycenter point of the triangle: a direction and a local shape. Subsequently, the surface S is approximated by the sum over its facets of these Dirac delta currents

(Figure 5.4):

$S \sim \sum_k \delta^n_{x_k}$.

This formula means that a surface can be viewed as a current that is a summation of all local Dirac delta currents measured at each facet of the surface. Thus, any surface S will be defined as an element of W^*, thus we are able now to compare surfaces via the dual space norm on W^*.

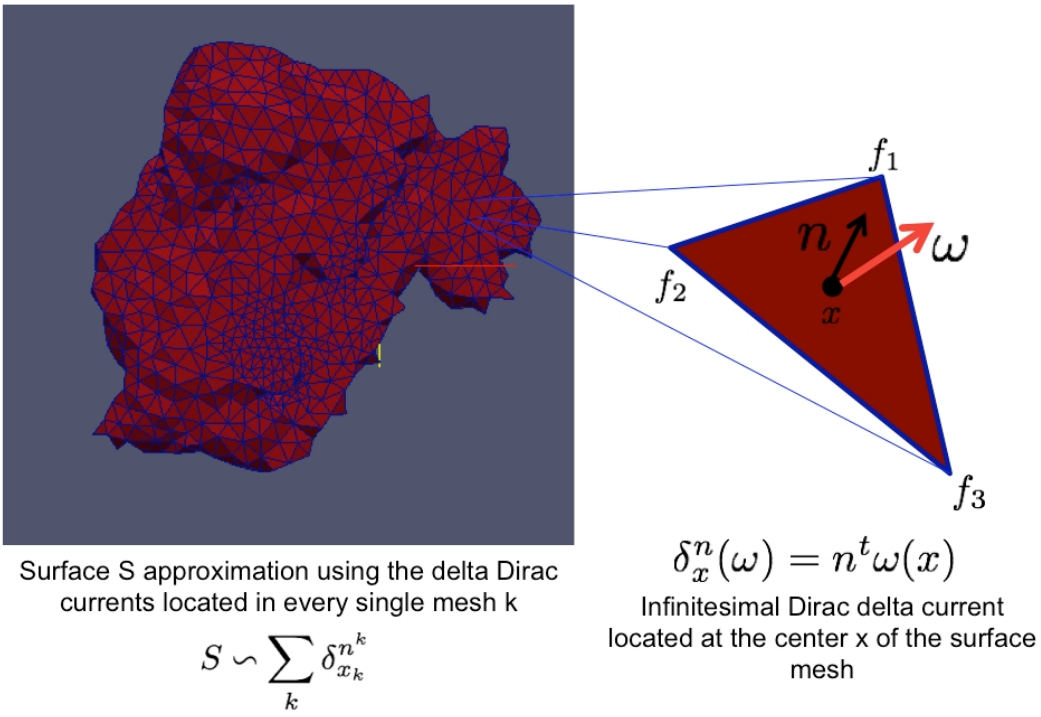

Figure 5.4: *Approximate of a 3D surface using infinitesimal Dirac delta currents.* A discrete 3D surface S (left) which belongs to the space of currents W^* is approximated by the sum over all its meshes k of the infinitesimal Dirac delta currents located at the center of each of its meshes (right). The vector n is the normal to the mesh measured at its center x and ω is a square integrable vector field traversing the mesh.

5.3 Current-based diffeomorphic regression model and stroke modeling

5.3.1 The diffeomorphic era and topology-preserving mappings

Serial medical imaging and increasingly acquired datasets to study changes in anatomy and brain diseases evolution have triggered the development of compelling mathematical frameworks based on deformations [Klein 2009]. A specific category of spatial deformations has spanned the attention of researchers in this field: diffeomorphisms (smooth deformation with a smooth inverse). Narrowing down the area of 'allowed' diffeomorphic transformations, a very specific class of diffeomorphisms was considered: those that can be expressed as flows of ordinary differential equations. These were largely used in different registration models [Klein 2009, Holland 2011] and became a part of the classical deformable template theory –especially after the establishment of LDDMM theory.

The LDDMM framework is based on the idea of a diffeomorphic metric. This metric is a distance on the object space –seen as a Riemannian manifold– which results from the transportation of a metric on the group of diffeomorphisms by a group action. This defines a distance between two objects through the geodesic diffeomorphic path which connects one to the other. On the following, we will only consider *objects* which are *images*. The estimated diffeomorphic

transformation g_1 connects a source image I_0 to a target image I_1 as follows: $I_0 \circ g_1^{-1} = I_1$. The central idea of LDDMM is that g_1 is the mapping at time 1 of a deformation path. What drives the evolution of this transformation from g_0 to g_1 is the flow equation:

$$\begin{cases} \frac{dg_t}{dt} = v_t(g_t). \\ g_0 = id. \end{cases} \tag{5.3}$$

Where id is the identity map.

Therefore, the diffeomorphism g_t can be computed by integrating the velocity path over the time interval $[0, 1]$ as follows ($g_1(x) = x + \int_0^1 v_t(g_t(x))\, dt$); thus, leading to divert our attention towards the estimation of the velocity field of deformation ($t \mapsto v_t$) which belongs to a vector space V that will be properly explained in the next section. The velocity field is a solution of the following exact matching problem:

$$\begin{cases} \min\limits_{v:\frac{dg_t}{dt}=v_t(g_t)} \int_0^1 ||v_t||_V^2 dt. \\ I_0 \circ g_1^{-1} = I_1. \end{cases} \tag{5.4}$$

This exact matching forces the deformation to exactly reach the target image which most of the time is not possible due to the smoothness constraint on the group of deformations which are considered. Therefore, this hard constraint has been lightened. Introducing the constraint into the energy with a Lagrangian multiplier $\frac{1}{\sigma^2}$ extends

out this exact matching into an inexact matching to allow the estimation of smooth deformation paths while reaching an image close to the target. The optimization can then be performed on the velocity field of deformation $(t \mapsto v_t)$ and the parameter σ is fixed by the user depending on his/her expected precision of the matching. Note that this constant can also be estimated in a population as presented in [Allassonnière 2007, Allassonnière 2010]. However, as first modelling, we choose to fix the parameter σ. Therefore, the inexact variational problem becomes:

$$\min_{v:\frac{dg_t}{dt}=v_t(g_t)} \left(\int_0^1 ||v_t||_V^2 dt + \frac{1}{\sigma^2} \, ||I_0 \circ g_t^{-1} - I_1||_{L^2}^2 \right). \tag{5.5}$$

Solving this problem has been addressed using different methods. For instance, [Beg 2005] presented a gradient descent algorithm using Euler-Lagrange equations for estimating the optimal smooth vector field (v_t) that generates the optimal diffeomorphic deformation $\hat{g}_t$ matching two images. Since it satisfies the flow equation, this vector field (v_t) can be thought of as representing the velocity of the moving flow g_t.

Most importantly, this approach generates a geodesic (curve achieving the shortest distance over all paths connecting two objects on the Riemannian manifold) transformation path. However, a major shortcoming of the *diffeormophic* metric underlining this large defor-

mation framework is that it does not allow variations in the topology of the deformed object. In the contrary, it preserves the topology of the object of study as it is based on diffeomorphisms. For this reason, it is commonly used to study changes in anatomical structures (as connected sets remain connected and disjoint sets remain disjoint) rather than brain lesions that may take dissimilar forms and undergo a topology change (such as the appearance of new disconnected sets of ischemic regions in stroke or the merging of different sets into a bigger one).

Remark: In what follows in this chapter, the diffeomorphic transformation g_t will be noted as χ_t so that it would be unified with the mathematical notations used in Durrleman's work since we will be referring readers interested in getting more details about the modeling approach to these references [Durrleman 2009, Durrleman 2010, Durrleman 2011].

5.3.2 A current-based longitudinal shape deformation model

This sets out a more realistic and efficient framework to represent stroke lesion surfaces as dynamic (rather than static) structures which contract, expand, swell, and shrink in different directions, with variation in the speed of these local changes. To estimate the pattern of change in ischemia, we used a sequence of time-indexed surfaces $\{S_0, S_1, ..., S_n\}$ from timepoints t_0 to t_n. Each S_i surface refers to the

time-indexed surface at the $i^{th}+1$ acquisition timepoint. For example, S_1 refers to the time-indexed surface at the second acquisition timepoint.

Considering a source baseline shape S_0 (in our case the 3D meshed lesion surface at the first acquisition timepoint) and $\{x_p\}_{\{1,..,N\}}$ set of points representing the centers of facets of S_0, the ultimate goal of the model is to estimate a continuous evolution deformation function $\chi(t)$ deforming the source shape S_0 successively onto the next shape until reaching the final shape S_n: $S(t) = \chi_t(S_0)$. A diffeomorphic flow equation ($\frac{d\chi_t(x)}{dt} = v_t(\chi_t(x)), \quad t \in [0,T], \ with \ \chi_0 = id$) guided the deformation function χ^v_{DWI} (resp. χ^v_{MTT}) of the DWI (resp. MTT) lesion shapes, using a dense and smooth kernel-induced vector field, without assuming any prior anatomical spatial constraints or any interdependencies of spatio-temporal MTT/DWI shapes. Note that the model does not allow lesion behavior such as folding, tearing or shearing.

To ensure that the solution at the final timestep ($t = 1$) of this flow equation is a piecewise geodesic diffeomorphism that best matches the set of our time-indexed currents (surfaces), the time-varying speed vector field $(v_t)_{t\in[0,1]}$ must belong to a space of smooth vector fields V [Trouvé 1998]. The smooth deformation vector space V belongs to a RKHS with a Gaussian kernel K^V and a standard deviation parameter λ_V determining the scale under which deformations are locally

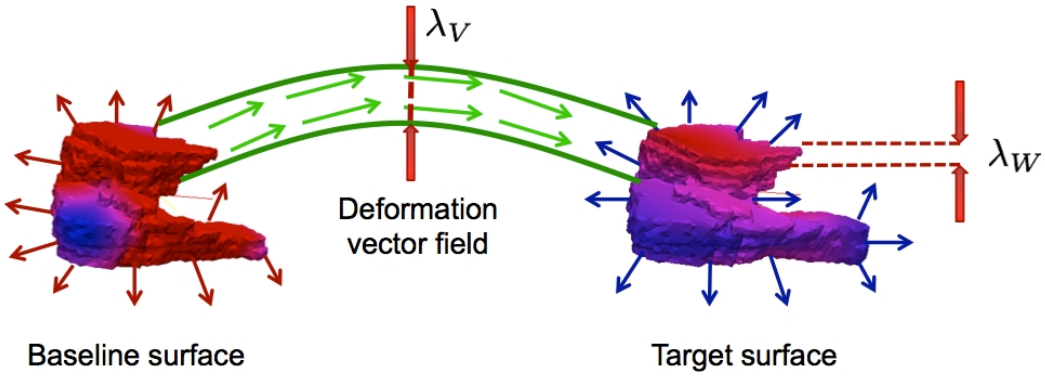

Figure 5.5: *Simplistic representation of the current-based surface deformation model.* We have manually drawn some representative normal vectors (in red for the baseline surface and in blue for the target surface). Each surface is defined as an element of the space of currents W^*, a dual space to W which is spanned by spatially varying square integrable vectors fields convoluted to Gaussian kernels. This convolution depends on a parameter λ_W which restricts the breadth of the variability of the vector field retrieving the geometry of the surface as it goes through it from different directions. Indeed, surface details of λ_W-width (eg: bumps) will not be 'viewed' by the vector field traversing the modeled surface. The same restriction applies to the deformation vector field V representing the driving force transforming the baseline surface into the target. Since it belongs to an RKHS, the standard deviation λ_V of the Gaussian Kernel densely spanning the smooth vector field V views integration over vector lines of V 'distant by less than λ_V' as identity maps (ie no deformation is allowed under that scale).

similar to the identity map (no deformation) (Figure 5.5). Thus, at a specific timepoint t, the velocity of the evolution of the surface mesh, with x as its center, is defined as a sum of convolutions between the Gaussian deformation kernels, respectively located at all centers x_p of the surface meshes, and their corresponding momenta $\alpha_p(t)$ guiding the deformation trajectory: $v_t(x) = \sum_{k=1}^{N} k_V(x_k(t), x)\alpha_k(t)$.

The integration of the estimated velocity field, ultimately, defines the deformation trajectories as geodesic paths between diffeomorphisms. To ascertain these smooth trajectories morphing one shape into another passing by the observed timepoints, we introduce a temporal regression functional $J(v)$ that we minimize through running a gradient descent algorithm as described in [Durrleman 2010].

The estimation of the final smooth deformation trajectories between lesion shapes is achieved by minimizing a temporal regression functional $J(v)$ as follows:

$$\begin{cases} J(v) = \sum_{t_i} A_i(x_1^v(t_i), ..., x_N^v(t_i)) + \gamma \int_0^T ||v_t||_V^2 dt \\ v_t(x) = \sum_{i=1}^{N} K^V(x, x_i(t))\alpha_i(t) \\ \chi_t^v(x_i) = x_i + \int_0^t v_s(x_i(s))ds \\ A_i = ||\chi_{t_i}^v(S_0) - S_i||_{W^*}^2. \end{cases} \tag{5.6}$$

Where $x_i(t)$ represents the 3D coordinates of the center of each facet x_i of the baseline surface S_0 changing with time t, the fidelity term A_i is a squared similarity measure in the space of currents W^*

between the original shape S_i associated to timepoint t_i (in our case the MR observation of the perfusion or diffusion ischemic lesion) and the measured one as a deformation of the baseline surface S_0 at time t_i of the estimated evolution scenario. The action term $\chi(S_0(x))$ denotes the morphological deformation of each point x of the surface S_0 as it moves to the new position $\chi(x)$. Since a surface is represented as a sum of Dirac delta currents, the deformation of an infinitesimal Dirac delta current directed by α and located at x is a Dirac delta current located at the transported location $\chi(x)$ by the deformation χ and directed by the transported vector $|d_x\chi|d_x\chi^{-1}\alpha$ ($d_x\chi$ is the Jacobian matrix of χ and $|d_x\chi|$ its determinant) as follows:

$\chi(\delta_x^\alpha) = \delta_{\chi(x)}^{|d_x\chi|d_x\chi^{-1}\alpha}$.

For more details on the vector transportation calculus, we refer the reader to Durrleman's thesis. The second energy term measures the regularity of the final deformation χ_T^v as a geodesic distance between id and χ_T^v measured by integrating the norm of the speed vector over time: $d_V^2(Id, \chi_T^v) = \int_0^1 ||v(t)^2||dt$. The parameter γ represents the trade-off between both fidelity-to-data and regularity terms. By minimizing the energy functional $J(v)$, we estimate the lesion surface evolution that best meets the time-indexed observed surfaces as every facet center x_i follows a smooth deformation trajectory. For more technical details, we refer the reader to Durrleman's Thesis [Durrleman 2010].

To optimize the initial momenta, we calculate the energy gradient with respect to the deformation momentum ∇J_α and minimize the functional J *via* a typical gradient descent scheme with adaptive time step [Durrleman 2010]. The minimum of the functional $J(v)$ achieves simultaneously: a) the minimum of the regularity of the deformation that represents physically the kinetic energy of the estimated deformation; and b) a second term that represents the fidelity of the estimated data to the observed data.

The estimation of the functional $J(v)$ depends on four main parameters, which are automatically fixed as follows: a scalar parameter γ representing a trade-off between the regularity and the fidelity to data terms set to 10^{-4}, a scalar parameter denoting the deformation scale λ_V above which points move in an uncorrelated way set to 30% of the bounding box enclosing the three observed lesions, a scalar parameter λ_W characterizing the regularity current-related scale under which the algorithm will be blind to shape regularities variations set to $5mm$ or $35mm$ depending on the observed shape regularity and a time discretization step δt set to 3 hours. To set the parameter λ_W, we visually quantify the surface regularity.

The ultimate estimation of the 'spatiotemporal' variability in DWI and MTT lesions will provide us with a clear representation of the similarities and differences between MTT and DWI kinetic patterns, and thereafter to evaluate some biological assumptions.

5.3.3 Methodological tools for comparing the estimated PWI and DWI lesion evolution

In order to assess the dynamic changes in PWI and DWI lesions across three successive timepoints from acute and subacute stages (from t_1 to t_3), we used the manually-delineated PWI and DWI lesions and reconstructed their surfaces as time-indexed sets of shapes embedded in a three-dimensional space (Figure 5.6). Observing DWI/MTT lesions in three dimensions provides us with more specific spatial information about their shapes, in terms of the geometric mathematical constructs of 'cavities','curvatures', 'compactness' and 'closeness'. The analysis of the baseline surface (S_0) deformation with time provides an estimate of the diffeomorphic dynamic patterns of change that we will refer to as the estimated evolution scenario, and that fully describes the kinetic change driving the contractions and expansions of different areas of the lesion surface from the initial timepoint. To show the differences and similarities in the dynamic behavior of the MTT and DWI lesions as they evolve over time, we needed to define appropriate mathematical tools that would adequately set a connection between the changes in the DWI lesion and the MTT lesion as they both evolved with time. This connection is defined as a geodesic diffeomorphism (smooth deformation with a smooth inverse) $\phi_t(x)$, that automatically identified corresponding areas in MTT and DWI baseline surfaces. We used the same framework of currents as above

to estimate this additional deformation function. Thus we estimated this additional spatial deformation $\phi_{t_1}(x)$ by mapping each DWI lesion surface mesh onto the MTT lesion surface mesh at t_1, thereby avoiding any inter and intra-observer variability that would inevitably result from any attempt to match these anatomical points manually. Spatially connecting the DWI and MTT lesions through identifying the correspondences between them was achieved through the same energy minimization scheme between the two baseline shapes $S_{DWI}(t_1)$ and $S_{MTT}(t_1)$, as introduced earlier in the previous section.

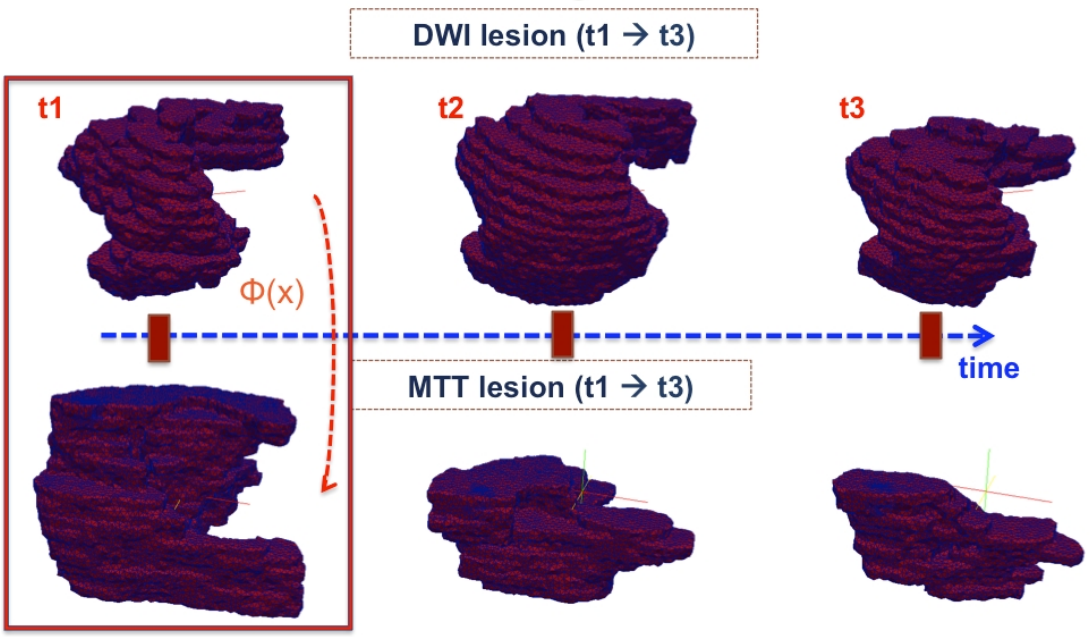

Figure 5.6: *3D meshed reconstruction of DWI and MTT lesions at three acquisition timepoints.* An additional spatial deformation ϕ mapping DWI into MTT at t_1 is estimated, also noted ϕ_{t_1}.

Note that the estimation of $\phi_{t_1}(x)$ is not constrained by any anatomical paths and does not require any initially selected anatom-

ical landmarks. We used the new estimated final shape $\tilde{S}_{MTT}(t_1) = \phi_{t_1}(S_{DWI}(t_1))$ as the baseline lesion shape for the MTT scenario at t_1 to estimate the perfusion lesion evolution function χ^v_{MTT}. Therefore, we can now spatially link both estimated MTT and DWI evolution scenarios, respectively noted as χ^v_{MTT} and χ^v_{DWI}, by using ϕ_{t_1} and its inverse $\phi^{-1}_{t_1}$ as a continuous junction to connect DWI and MTT lesions at the first timepoint (Figures 5.6 and 5.7). We can also follow back in time the spatio-temporal change respectively within each MTT and DWI lesion evolution pattern by using the inverses of the estimated evolution functions $\chi^{-1}_{MTT}(t)$ and $\chi^{-1}_{DWI}(t)$. Now that we can navigate throughout each DWI and MTT 4D evolution scenario separately, and between anatomically corresponding DWI and MTT co-ordinates at each individual timepoint, we can extract the kinetic similarities and differences in DWI versus MTT lesion evolution as follows:

a) We firstly compute the norm of the speed at each time step t_i at each point of the continuously evolving lesion 3D surface,

(b) We then extract contracting (corresponding to inward speed direction to the surface) and expanding (corresponding to outward speed direction to the surface) local areas at t_1 of the DWI-estimated evolution scenario $\chi^v_{DWI}(t)$. We compute the mean evolution speed of the initially depicted contraction (*vs.* expansion) areas at each time step of $\chi^v_{DWI}(t)$. Using the mean evolution speed minus (*vs.* plus)

its standard deviation as an automatic contraction (*vs.* expansion) threshold, we only mark areas with high contractions (*vs.* expansions) from the DWI lesion surface at t_1 then spatially map them into the MTT lesion at t_1, as deformed by ϕ_{t_1}.

(c) Finally we compute the mean speed for these contracting and expanding areas over their spatio-temporal evolution for the 8 representative patients, in both DWI and MTT abnormalities.

5.3.4 Identification of the time at which the final DWI/PWI lesions matched the final T2-w lesion

The ability to know precisely at which time the DWI and MTT lesions are most spatially coherent with the final T2-w lesion means that we can better evaluate the prognostic potentials of DWI and MTT modalities. To our knowledge, up to this date, detailed information on 4D stroke lesion shape change between two acquisition timepoints is limited (see Chapter 4). For instance, as shown in Figure 5.8, the details of the mechanism of the penumbra boundary at t_1 (in orange) extending into the yellow manual outline at t_2, and then shrinking back to the red boundary at t_3 while intercepting the green T2-w boundary remains unclear and quite difficult to accurately envision in space and time. We determined the exact timepoints $t_{DWI,T2}$ and $t_{MTT,T2}$ (in hrs from stroke) where the estimated DWI/MTT lesion boundaries were spatially closest to the final T2 lesion surface S_{T2} by

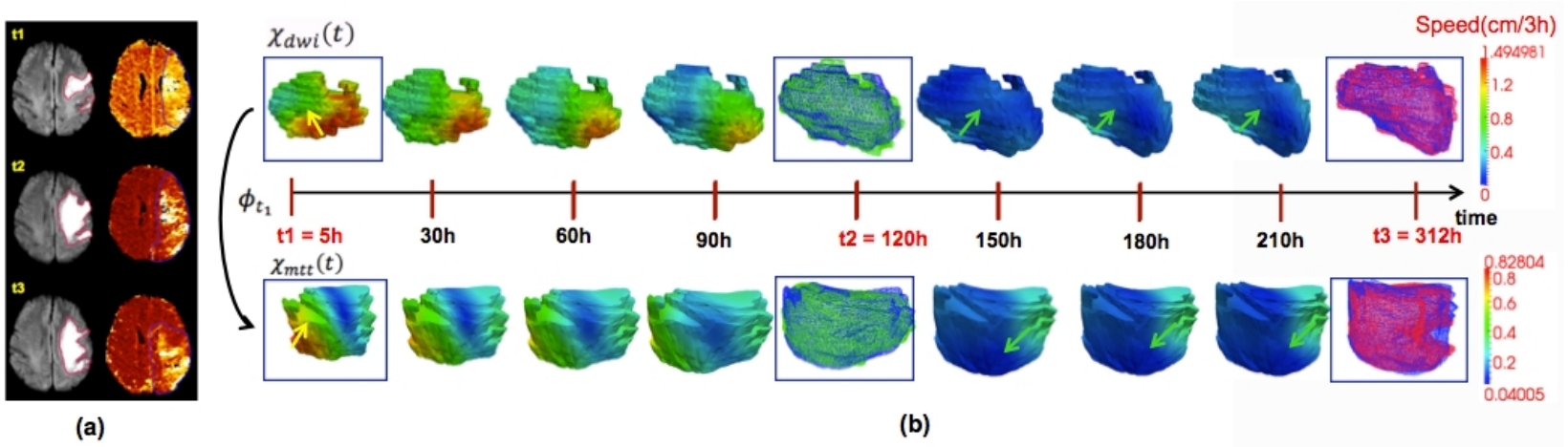

Figure 5.7: *Estimated DWI/MTT lesion evolution scenarios.*(a) DWI (vs. MTT) axial slice at 3 timepoints in the first (vs. second) column. (b) Estimated DWI/MTT evolution scenarios with estimated velocity norm (speed) in cm/3h. At t2 (vs. t3), the green (vs. red) surface represents the observed lesion and the blue one represents the estimated lesion. Green arrows represent contraction areas and yellow ones expansion areas.

computing the dice index – a measure that quantifies the volumetric overlap between the estimated lesion volume delimited by the dynamic surface and the final static T2-lesion volume and ranges from $0 to 1$– at each time step t_i as follows:

$$dice_{DWI}(t) = \frac{2\ V(\chi^v_{DWI}(S_{DWI,t1})) \cap V(S_{T2})}{V(\chi^v_{DWI}(S_{DWI,t1})) + V(S_{T2})}, \quad t \in [t1, t3]. \quad (5.7)$$

We also computed, at each time step t_i, the symmetric distance –averaging the symmetric closeness of both shapes in millimeters– to provide a quantitative spatial discrepancy measure between the time-varying DWI and MTT surfaces ($S_{DWI}(t)$ and $S_{MTT}(t)$) and the static final T2 lesion S_{T2} and establish a more intuitive understanding of how close the dynamic surfaces get to the static T2-w surface. Noting that, $\chi^v_{DWI}(S_{DWI,t1}) = S_{DWI}(t)$, we have:

$$d_{sym}(t) = \frac{1}{|S_{T2}| + |S_{DWI}(t)|} \left[\sum_{x \in S_{T2}} min\ d(x, S_{DWI}(t)) + \sum_{x \in S_{DWI}(t)} min\ d(x, S_{T2}) \right]. \quad (5.8)$$

where d denotes the closest Euclidean distance between a point and a surface.

The last step was to identify the timepoint $t^{dice}_{DWI,T2}$ ($resp\ t^{d_{sym}}_{DWI,T2}$) where S_{T2} is the closest to $S_{DWI}(t)$ by seeking the maximum over $t \in [t_1, t_3]$ of $dice_{DWI}(t)$ ($resp$ the minimum of $d_{sym}(t)$):

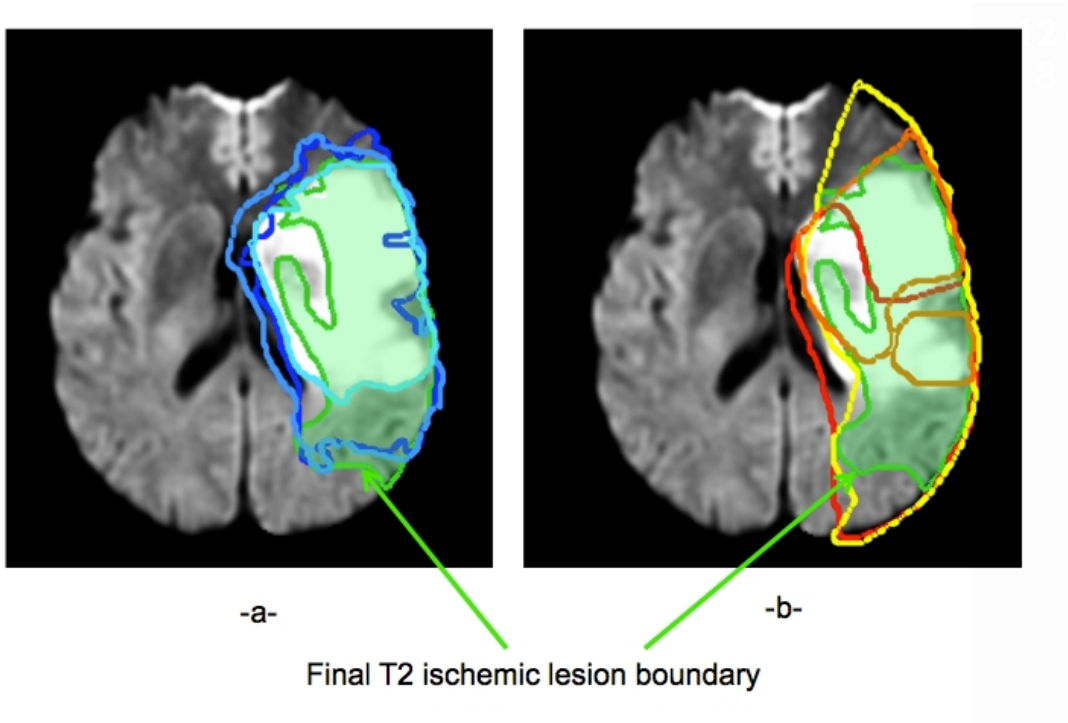

Figure 5.8: *Time-indexed penumbra and core lesion boundaries combined to final T2-w boundary imaged at* ≥ 1 *month.* On the right: MTT manually delineated penumbra boundaries consecutively at t_1 (in orange), t_2 (in yellow) and t_3 (in red). On the left: DWI lesion boundaries ranging from light to dark blue as time evolves from t_1, to t_2 then t_3. In both MR axial slices, the final T2-boundary is displayed in green shading.

$$t^{dice}_{DWI,T2} = \max_{t\in[t_1,t_3]} \quad dice_{DWI}(t). \tag{5.9}$$

In a similar way, we computed the same measures for the MTT estimated lesion evolution. These specific identified timepoints (t_{dice} and $t_{d_{sym}}$) would for example give us insights into the hypothesis that acute DWI abnormality is a surrogate marker for permanently dead tissue, as well as the hypothesis that acute MTT surface boundary is the maximum boundary of infarct progression.

5.4 Results

5.4.1 Data selection and MRI acquisition and preprocessing steps

Data selection:

In order to apply and test this model, we selected eight representative patients (5 males, 3 females) from a study of MR imaging in hyperacute stroke of original sample size 48. Primary study methods were previously described [Rivers 2006]. These 8 patients represented a range of stroke severity (NIHSS = 11.63+/−7.8), age (72+/−5.2 years) and all patients had solitary acute ischemic lesions on DWI and PWI with evidence of mismatch (ie. MTT > DWI) on MTT. Additionally, for the initial application of the model we required that: (i) the MTT and DWI lesions should both be visible at at least 3 timepoints, (ii) the MTT/DWI mismatch should be larger than $3cm^3$,

and (iii) the lesion consisted of one solitary lesion only and that this did not vary between timepoints (ie, we avoided lesions consisting of several separate acute lesions or where the number of lesions varied between timepoints). We chose this limit to minimize resolution artifact problems during this proof-of-concept phase of model application. To further simplify the model development, we excluded patients who received thrombolytic or other reperfusion therapies. All model development and analyses were performed blind to all clinical data. The first acquisition timepoint was at around 5 hours, the second at around 5 +/− 1 days and the third at 10.5 +/− 2.5 days after stroke [Rivers 2006]. The median DWI lesion volume was $43.42cm^3$ and MTT volume was 66 cm^3 when measured by manual outlining in the original study from which the acute data were taken.

MRI acquisition and pre-processing steps:

All MR images were acquired using a GE Signa LX 1.5-T MR scanner (General Electric, Milwaukee, Wisconsin) with a birdcage quadrature coil and a standardised protocol for acute stroke [Rivers 2006]. The spin-echo echoplanar imaging diffusion tensor axial sequences and dynamic susceptibility contrast echoplanar imaging PWI had 15 axial slices each of 6mm thickness with an interslice gap of 0.97mm and an imaging matrix 128 × 128 encompassing a 240 × 240mm field of view. MTT perfusion maps were generated using PWI data, full details of the image acquisition and processing protocol have been de-

scribed previously [Rivers 2006]. The DWI, MTT and final follow-up T2-weighted images (at >= 1 month after stroke) were co-registered using rigid affine transformation and their corresponding lesions manually delineated on every slice on which they were visible by an expert. For the model we pre-processed the images to subsample slice thickness and reduced it to 1mm by splitting each 6-mm voxel into 6 sub-voxels along the z-axis. We used un-thresholded MTT at this stage in model application as it generally provides a single contiguous lesion.

5.4.2 Evaluation of the estimated MTT and DWI spatiotemporal lesion evolution

We evaluated the accuracy of our estimation of DWI and MTT lesion evolution by computing the mean and standard deviation (SD) values of the dice index between the estimated and the true lesion volumes at the second and third timepoints for the 8 patients. We found good agreement between the estimated lesion evolution scenarios for MTT and DWI lesions and the observed samples (mean dice $\pm SDvalues$: $MTT(t2$:0.76 $\pm$0.09; t3: 0.8 ± 0.08) and DWI (t2, t3: 0.9 ± 0.02)) (Table 5.1). An example is shown in Figure 5.7 of how the model visualizes the kinetic change in DWI and MTT lesion shapes. The color of the dynamic surface indicates the estimated speed at which the lesion surface is contracting or expanding: changes from blue to

	$DWI(t_1)$	$DWI(t_3)$	$DWI(t_1)$ to $MTT(t_1)$	$MTT(t_2)$	$MTT(t_3)$
Mean(dice)	0.90	0.90	0.86	0.76	0.80
SD(dice)	0.02	0.02	0.06	0.09	0.08

Table 5.1: *Evaluation of the estimated DWI/MTT lesion evolution scenarios.*The mean dice index value (a measure quantifying the volumetric overlap between two volumes and ranges from 0 to 1 for the best match) and its standard deviation are computed over the 8 patients between the estimated and the manually delineated DWI/MTT lesions at t_2 and t_3. They are also computed for the additional spatial deformation ϕ_{t_1} –mapping DWI lesion into MTT lesion at t_1– to show how good is the mapping of DWI lesion into MTT lesion at t_1.

green, and then to yellow into red indicate increasing speed of change. This figure shows representative snapshots at equal time intervals across the entire estimated lesion evolution scenario. Additionally, we can also see clearly the very good agreement between the model's estimated time-evolving blue lesion surface and the original lesions at t_2 (in green) and at t_3 (in red).

5.4.3 Comparison of the MTT and DWI Kinetic Patterns

We compared the deformation of corresponding DWI and MTT lesion regions to determine any correlations between their contractions and expansions. We first examined lesion behaviour in individual patients and then identified common patterns of lesion change across all eight representative patients.

Individual observations: Figure 5.9 shows in a single subject the spatial distribution of highly expanding areas on the DWI lesion surface and their corresponding areas on the MTT lesion surface us-

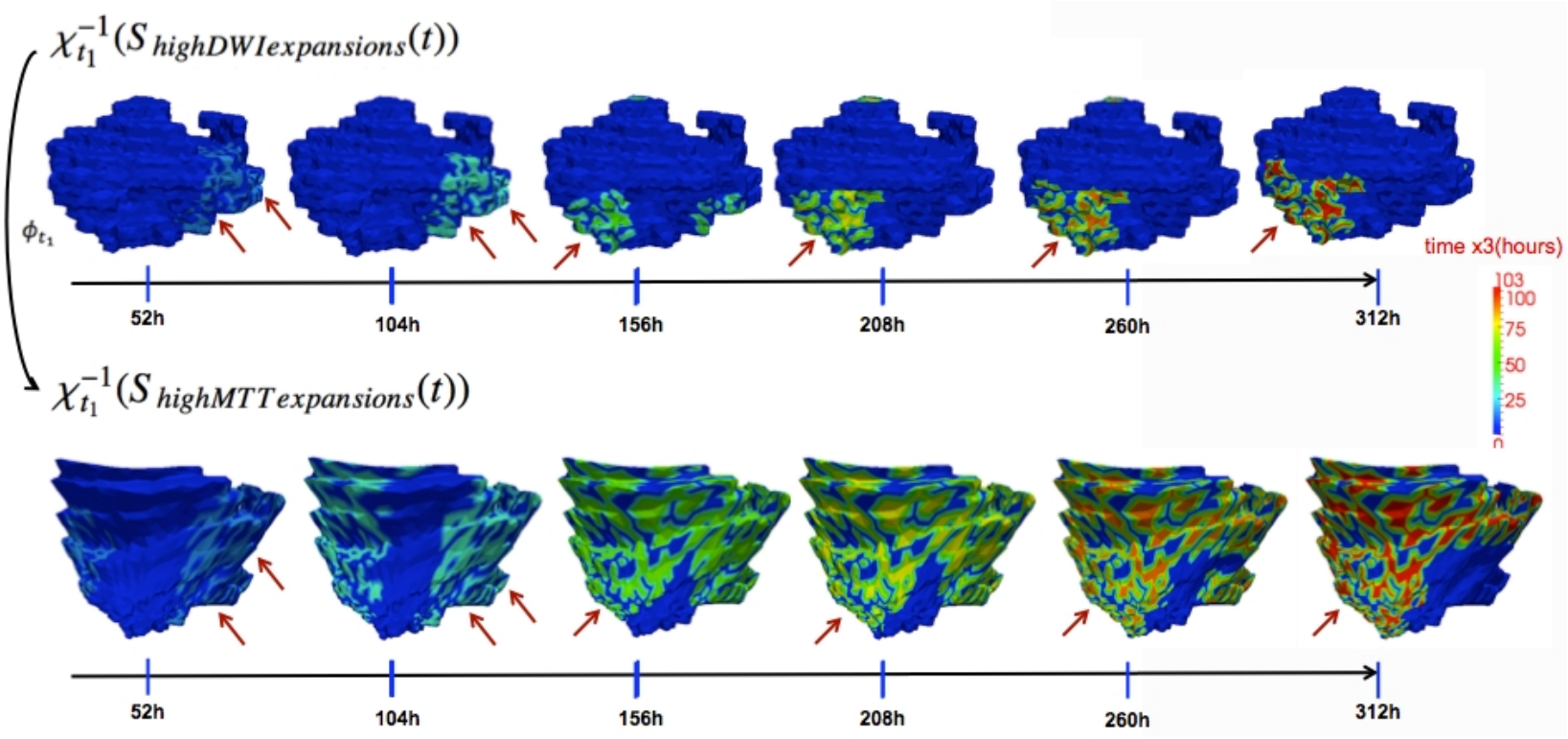

Figure 5.9: *Comparison between highly expanding DWI and MTT areas extracted across the spatiotemporal estimated scenarios.* As the color ranges from blue to green to red, the different successive areas with high expansion speed are 'lit up' at each time step, all mapped back at the baseline lesion shape acquired at t_1 using the inverse of the estimated evolution function $\chi_{t_1}^{-1}(S_{highDWIexpansions}(t))$ for DWI lesion and $\chi_{t_1}^{-1}(S_{highMTTexpansions}(t))$ for MTT lesion. The mapping-back enables us to foresee the upcoming dynamic changes –more precisely expansions– on the acute baseline lesion surface. The red arrows point to highly expanding areas in DWI lesion and their corresponding areas that also expanded in the MTT lesion. The dark blue areas –that didn't change color as time evolved– did not expand *ie* they contacted.

ing the additional deformation ϕ_{t_1}. The change of color from blue to green, and to red indicates the progress in time from t_1 to t_3. We also used the inverse of the estimated DWI evolution function $\chi_{t_1}^{-1}(S_{highDWIexpansions}(t))$ to map back all highly expanding DWI areas at later timepoints onto the static baseline acute DWI surface. The DWI areas that expanded quickly from the acute surface are shown successively highlighting the 'new' expansion areas at each subsequent timepoint. Similarly, we also highlighted consecutive areas of expansion on the baseline acute MTT lesion. This facilitates the comparison of areas of subsequent expansion on the static acute DWI and MTT lesions (Figure 5.9). In this one subject, there were areas where the DWI lesion expanded into the MTT lesion (red arrows point out to spatially corresponding local areas that simultaneously expanded), but there were also areas where the opposite occurred *ie* DWI shrank (dark blue contractions) where MTT expanded (areas not marked by red arrows) or DWI expanded into an area of MTT contraction. We found similarly varied patterns in other subjects, eg. Figure 5.10 shows limited correlation between high contracting (vs. expanding) areas of the DWI surface and their corresponding areas in MTT surface at the acute stage. It also shows how MTT lesion surface (in red, Figure 5.10-a) started by rapidly expanding (light blue curve in Figure 5.10-d) then went through an ultimate phase of shrinking in the space where the DWI lesion (in blue) expanded. In a different

patient, we observe a more rapid change in the DWI lesion than the MTT lesion that remains quasi static (Figure 5.11).

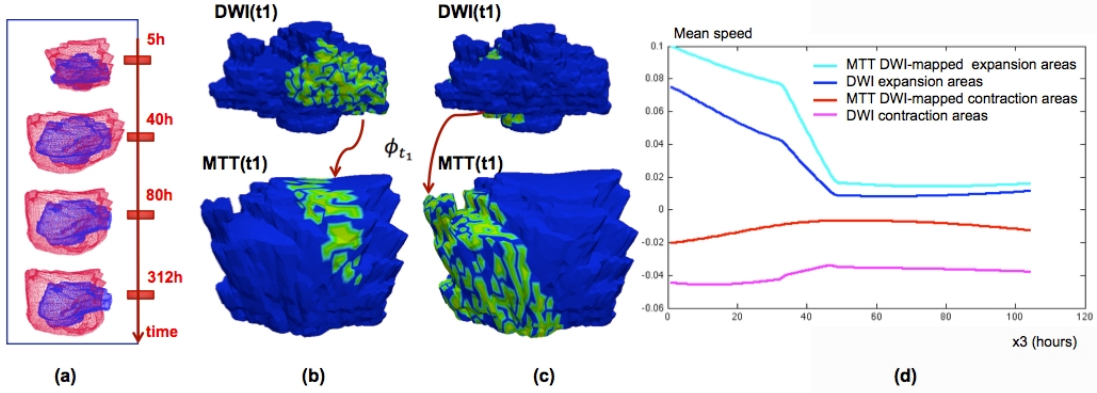

Figure 5.10: *Patient-specific estimated kinetic patterns of change in one patient.* (a) The estimated spatiotemporal evolution of DWI (in blue) and MTT (in red) lesions. (b) Detection of highly contracting (vs. expanding in (c)) areas in DWI lesion at t_1 and spatially mapping them into MTT lesion at t_1. (d) Spatiotemporal mean speed evolution of highly contracting and expanding DWI lesion areas for this patient and their corresponding areas in MTT lesion.

In two different patients, we observe two opposite perfusion-diffusion dynamic behaviors (Figure 5.12): in *patient A* the DWI lesion grows into the roughly unchanged MTT lesion than slightly contracts while in *patient B* the MTT lesion rapidly shrinks into the DWI lesion.

Population-based observations: We plotted the mean speed of highly contracting and expanding areas for the eight representative patients (Figure 5.13). This figure demonstrates that DWI areas with large contractions changed faster than their corresponding regions within the MTT lesion. In 6 patients, rapidly expanding DWI areas

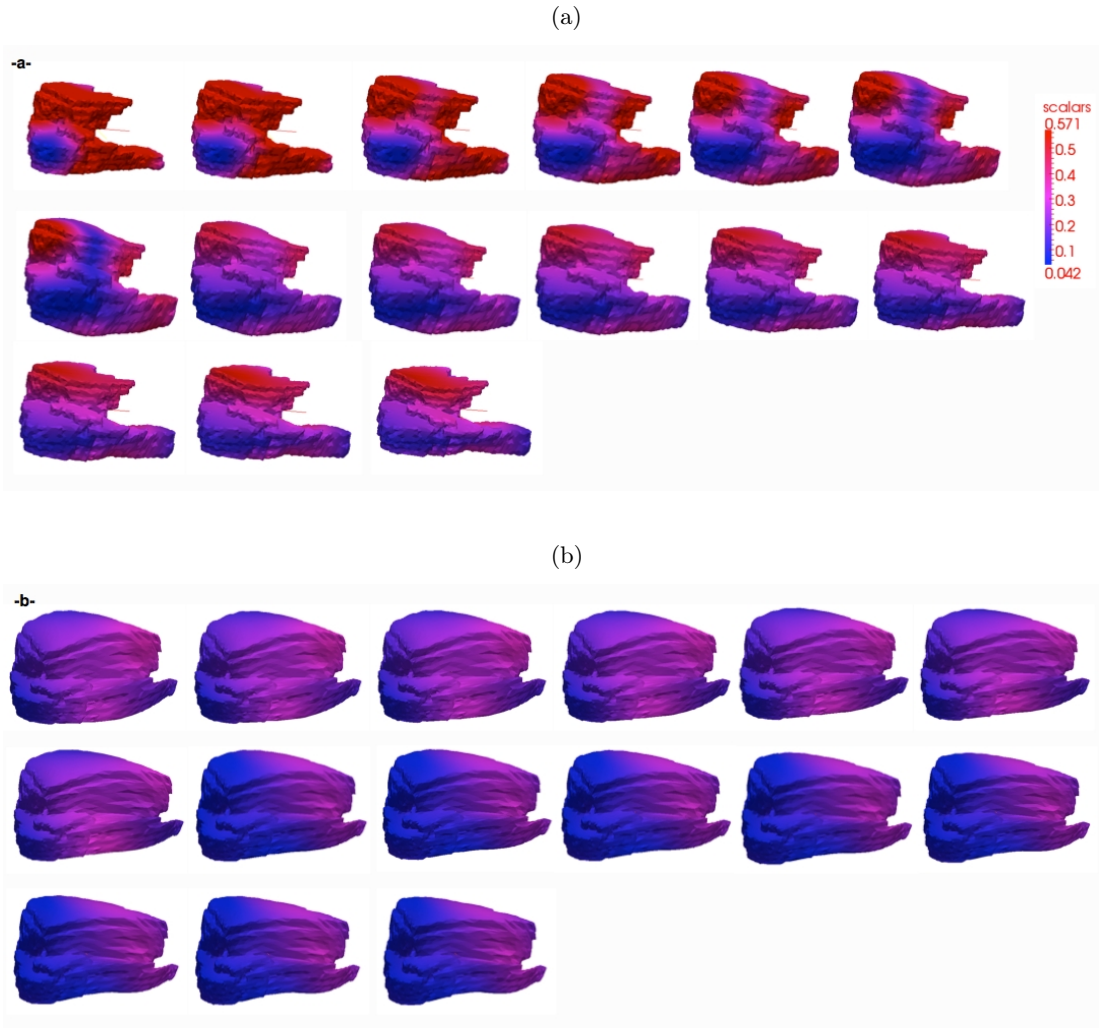

Figure 5.11: *Morphological and kinetic changes for stroke diffusion lesion (a) and perfusion lesion (b).* The color bar encodes the speed of deformation. We can clearly see that most visible parts of the diffusion abnormality (a) deform faster (red-pink color dominates the surface) than those in the perfusion abnormality (coded by blue-purple color). We can also notice that the perfusion surface remains roughly unchanged whereas the diffusion surface goes through a noticeable inflation then a shrinkage almost returning to the first baseline shape.

changed more slowly than their corresponding areas in the MTT lesion. In other words, expanding MTT areas and shrinking DWI areas displayed the speediest dynamic change. While some patients showed

a monotonic (*ie* entirely increasing or decreasing) mean speed evolution, others showed both MTT and DWI contracting and expanding areas. The large variation in the increasing/decreasing mean speeds with fluctuations made it difficult to see any common monotonic kinetic evolution pattern in both MTT and DWI lesions between patients.

5.4.4 Localization in space and time of final T2-w lesion in the DWI/PWI estimated evolution scenarios

We computed the two complementary measures (the dice index and the symmetric distance). We then extracted the corresponding timepoints (in hrs) where the maximum spatial concordance between the

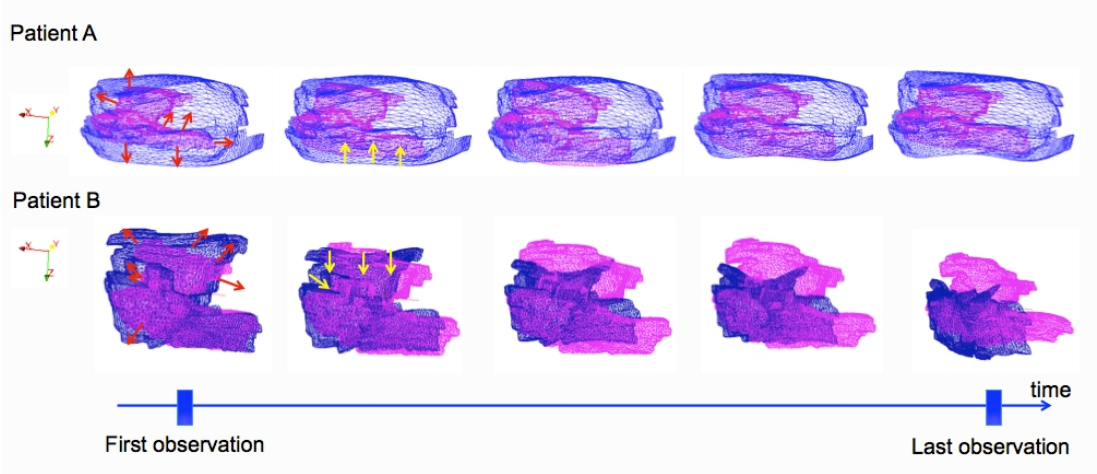

Figure 5.12: *Perfusion-diffusion abnormality dynamics.* Two different dynamic behaviors are observed for patient A and B. We remark that for patient A all parts of the diffusion lesion surface (in pink) expand into the perfusion lesion surface (in blue) without exceeding its boundary. A completely different dynamic behavior is observed in patient B: the perfusion lesion surface shrinks quickly (yellow arrows) in areas where the diffusion lesion surface expanded (red arrows).

two shapes occurred. Both measures produced quite similar results as follows (Table 5.2):

a) *Maximum special closeness between DWI/MTT surface and T2 surface*: the dice index averaged for the 8 patients for the spatiotemporal DWI and MTT lesion evolution vs final T2 lesion indicated wide inter-patient variation (DWI dice range 0.0008 to 0.77, median 0.58; MTT dice range 0.003 to 0.63, median 0.39) and similarly wide variation in the temporal symmetric distance for DWI 3.8 to 24.2, median 6.1 mm and MTT 6.1 to 33.2, median 9.8 mm *vs* final T2. In 5/8 patients, the mean DWI-T2 overlap volume over time exceeded 55% (corresponding to less than 6.2mm in symmetric distance). This

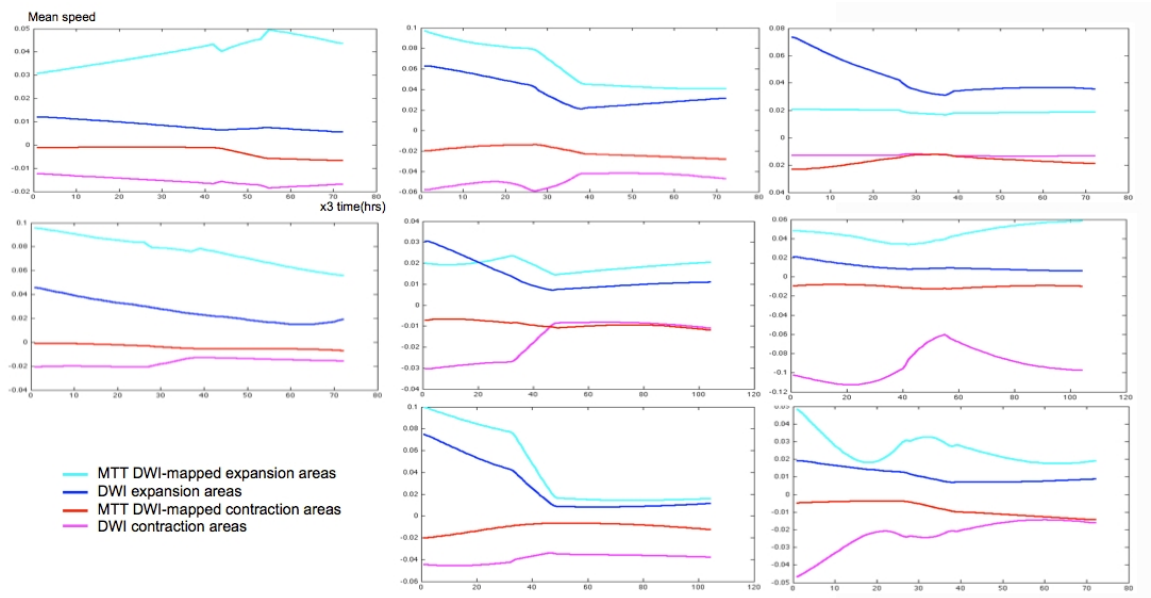

Figure 5.13: *Spatiotemporal mean speed evolution of DWI high contraction and expansion lesion areas for the 8 representative patients and their corresponding areas in the moving MTT lesion.* Each box represents a different patient.

indicates that in most cases there is a good geometric concordance between the T2 and DWI surfaces although this did not necessarily occur at the subacute stage (last acquired DWI image), *ie* in disagreement with the assumption that acute DWI will grow into the final T2 lesion. Three patients showed almost no MTT-DWI spatiotemporal lesion evolution overlap *vs* final T2 (mean dice index < 0.05). The fact that the dice index did not converge to 1 and the symmetric distance did not fall to 0 mm shows that the time-evolving DWI abnormality does not converge to the final T2-boundary but rather encounters it as it progresses or regresses with time.

b) *Time of maximum DWI/MTT surface overlap with the final T2 surface*: the time $t^{dice}_{DWI,T2}$ when DWI most closely matched final T2 lesion ranged from 6 to 237 hrs, median 138 hrs from stroke onset. For MTT the time of best match to final T2 $t^{dice}_{MTT,T2}$ ranged from 9 to 270 hrs, median 78 hrs. Five patients showed better, later in time geometric concordance of DWI than MTT with final T2 boundaries. Furthermore, 'the time of appearance' of the final T2 lesion according to the symmetric distance varied considerably between MTT and DWI lesion evolution scenarios in different patients. In four patients the estimated MTT 4D scenario met the final T2 lesion boundary earlier than did the DWI lesion ($t^{d_{sym}}_{MTT,T2} > t^{d_{sym}}_{DWI,T2}$), supporting the assumption that the MTT lesion extent in the acute phase may indicate the final irreversibly damaged ischemic tissue better than the

$mean_t\ dice_{MTT}(t)$	$t^{dice}_{MTT,T2}$	$mean_t\ dice_{DWI}(t)$	$t^{dice}_{DWI,T2}$	$mean_t\ d_{sym\,MTT}(t)$	$t^{d_{sym}}_{MTT,T2}$	$mean_t\ d_{sym\,DWI}(t)$	$t^{d_{sym}}_{DWI,T2}$
0.574	**30**	0.682	**144**	6.109	**42**	4.719	**144**
0.598	**9**	0.817	**129**	7.086	**9**	3.828	**132**
0.052	**216**	0.029	**216**	33.23	**216**	24.285	**216**
0.003	**3**	0.227	**216**	28.593	**3**	16.681	**216**
0.007	**123**	0.0008	**123**	23.886	**123**	26.128	**120**
0.364	**273**	0.556	**273**	9.295	**270**	6.151	**99**
0.42	**54**	0.61	**6**	10.45	**87**	6.160	**6**
0.681	**75**	0.77	**198**	7.925	**69**	4.713	**237**

Table 5.2: *Insights into final T2 outcome* Columns 1 and 3 show the mean value of dice index over time for the 8 patients between the estimated evolving DWI/MTT lesion boundaries from acute to subacute stages and the final T2 lesion boundary. Columns 2 and 4 show the time corresponding to the maximum value that the dice index reached, where the final T2 lesion is spatially closest to the estimated DWI/MTT evolution. Columns 5 and 7 display the mean value of the symmetric distance over time computed in mm (the spatial discrepancy) between the evolving DWI/MTT boundaries and the final T2 boundary. Columns 6 and 8 depict the time of the 'appearance' (in hours) of the T2 within the DWI and MTT evolution scenarios corresponding to the minimum of the symmetric distance that varied with time –for each patient.

DWI lesion.

5.5 Discussion

We applied a 4D model to evaluate the change in acute stroke lesions from the first few hours to 1-3 months after stroke, to our knowledge, the first time a 4D model has been used to simulate the dynamic evolution of stroke lesions [Rekik 2012a] (see Chapter 4). The current-based longitudinal shape regression model –based on an energy minimization problem derived from a diffeomorphic flow equation– provided a simulation of lesion surface evolution that fitted well to the true data. It also demonstrated the potential to obtain more insights into the spatio-temporal behaviour of acute stroke lesions within an anatomically specific space. While some features fitted the expected

patterns of lesion growth into tissue at risk, other patterns did not. Although this study is too small to determine reliably any relationship between estimated contraction and expansion speeds and final outcome, it demonstrated the proof-of-principle that a 4D model can provide a solid basis for examining similarities and differences between DWI and MTT kinetic evolution patterns and thence the biological (eg. the effect of having an area of leukoaraiosis adjacent to one part of the stroke lesion, or of specific anatomical structures that might constrain lesion change, or of vascular occlusion location) or treatment factors (eg. use of hypothermia, or thrombolysis) that may affect these in a much wider range of patients.

This model has some innovative mathematical aspects that we took advantage of, such as: a) there is no need for a point-to-point landmark matching between consecutive surfaces since the metric of currents does not assume any *prior* landmark matching, (b) the metric of currents conserves all geometric properties of the surface such as curvature, and (c) embedding these 3D lesion shapes into an RKHS space, which is a dense span of vector fields and equipped with an inner product, provides a robust numerical framework to efficiently estimate morphological and kinetic changes in evolving shapes. Furthermore, the model allows an examination of the whole time course (from 3hrs to the latest imaging time) dynamically or to obtain 'snapshots' of directions and speeds of contraction and expansion at indi-

vidual timepoints.

The model also has some key limitations, particularly when applied to a disease such as stroke where lesions commonly are not solitary: it does not handle topological changes such as lesions with changing numbers of connected components and it does not incorporate any biological information –such as the homogeneity of brain tissue– in the flow equation.

Despite the small sample of only eight representative patients, we saw wide variance in the spatio-temporal interaction between PWI and DWI lesion surfaces in terms of correspondence between areas of high contraction and expansion (Figures 5.9 and 5.13). We also saw significant dynamic changes in MTT lesions, including expansion as well as contraction including in 6 of 8 patients the DWI lesion expanding more rapidly in areas of MTT expansion than in areas where MTT was static. Thus, as well as dynamic contraction and expansion patterns that were in line with that expected from mismatch theory (Figure 5.9), we saw the DWI lesion surface contracting faster than the corresponding MTT, and the hypoperfused MTT surface expanding faster than corresponding DWI. This means that this approach can be used to understand lesion evolution in much greater detail and in relation to anatomic, patient-specific, stroke-specific and treatment-specific factors than is possible through analysis of 2D or 3D image data. Through analysis of evolution of mean speed of lesion

change at different timepoints of DWI and MTT lesions (Figure 5.13), we identified an overall common pattern implying that diffusion lesions tend to change more slowly than MTT lesions (pink curves and red curves respectively). We also saw that DWI hyperintense tissue can contract (DWI reversal phenomenon), consistent with recent data [Kranz 2009]. There were variable rates of expansion and contraction of the DWI lesion (blue and pink curves respectively, Figure 5.13) demonstrating that the DWI lesion surface change is heterogeneous [Phan 2009].

The model also highlighted wide inter-patient variability in the time at which the estimated MTT and DWI evolution scenarios matched the final T2 lesion. In 5 patients, the geometric concordance between the moving acute lesion surface and the static final T2 reached its maximum later in DWI data than for MTT (Table 5.2). We also saw that the DWI lesion surface did not necessarily converge towards the final T2, although both overlapped partly at some point, again consistent with the theory that DWI abnormal tissue can survive. We also saw that the acute MTT lesion matched the T2 lesion at an earlier stage than for DWI consistent with the hypothesis that failure to re-perfuse the perfusion lesion will result in tissue death, at least in some areas. However we also saw in 3 cases that there was little overlap between the static final T2 and the dynamic DWI or MTT lesions (table A2). Larger studies using this approach and an

accurate analysis of the speed of DWI and PWI lesion evolution in a much more diverse range of patients are now justified to determine reasons for these variations in lesion behavior.

Our study has limitations. We were not able to differentiate dynamic lesion behavior in white and grey matter [Koga 2005], although the blood flow levels and ability to withstand ischemia differs between these tissues. Many of the original 48 patients were excluded at this proof-of-concept stage because their lesions consisted of a changing number of components or they did not have both PWI and DWI lesions visible at all 3 timepoints. However scattered multi-focal lesions are common in stroke and would need to be included in future developments [Ogata 2011]. We did not address patient-related factors which might influence lesion evolution such as age, leukoaraiosis, or stroke-specific factors such as timing of vessel re-canalisation, as these were beyond the scope of the present development stage. However these are the subject of future work.

Future technical developments should include the ability to model ischemic lesions variation in the number of components, to address anatomical deformation resulting from lesion swelling rather than true lesion expansion, and to use individual voxels throughout the lesion –eg. derived from DWI/PWI values– rather than just the surface/outline. Further testing of the model requires larger data sets including more patient-specific variables and stroke-specific variables

such as the site of vascular occlusion as well as acute treatment affects.

5.6 Conclusion

In this chapter, we estimated a continuous 4D PWI and DWI ischemic lesion evolution and evaluated individual patient differences in stroke lesion evolution. Our blinded and prior-free individualized analysis of 8 representative patients of the correspondence in dynamic evolution of DWI and MTT lesions in space and time showed some similarities but also differences in the way the ischemic lesion progressed or resolved. Some of the observations in this proof-of-concept model were partly in line with the mismatch concept, while others contradicted that acute diffusion abnormality is irreversible and cannot exceed the boundaries of acute perfusion abnormality. We were also able to detect subtle and rapid differences in lesion evolution between DWI and MTT lesions imputed to 3 hourly intervals. The applied current-based diffeomorphic model allows individual lesions and patients to be examined to provide greater insights in speed and time as to what drives stroke lesion evolution and thus other opportunities for developing further interventions. However it is limited in the type of lesion morphology that it can handle. In future studies this may in turn enhance understanding of stroke pathophysiology and allow greater patient-specific personalized treatment.

The current-based model proved to be a mathematically robust

representation of the lesion surface, but had two major limitations. It was only able to model solitary lesions, i.e it could not model the more commonly seen ischemic lesion morphologies, eg. consisting of several areas of abnormal tissue separated by normal tissue where the number of components varied with time. This limitation reduced the proportion of patients that the model could be applied to down to 16% in several recent study datasets. More importantly, this model cannot incorporate image intensity measures in its abstract mathematical framework (eg. perfusion-diffusion values), but only the geometry of the lesion surface. Indeed, the abstract setting current-based deformation model clearly restricts the measurements of changes in DWI and PWI abnormal tissues to a few kinetic local measures on the lesion surface (such as the localized speed of contraction and expansion). A lesion was simply considered as a geometric surface. Hence, there was no possibility of using this model to study the effects of DWI or PWI or other tissue parameter values on lesion dynamics.

To overcome both of these limitations, we use a different more versatile approach: the metamorphosis model that will be introduced in Chapter 6 and evaluated in Chapters 7 and 8.

Part IV

From Image-to-image to Longitudinal Metamorphosis

"Mathematics is much like the Mississippi. Its delta is research mathematics: it is growing, it is going somewhere (but it may not always be apparent where), and what today looks like a major channel may tomorrow clog up with silt and be abandoned. Meanwhile a minor trickle may suddenly open out into a roaring torrent. The best mathematics always enriches the mainstream, sometimes by diverting it in an entirely new direction."

Ian Stewart; From here to infinity

The same vision applies to stroke research.

Chapter 6

Building the longitudinal metamorphosis model

Contents

6.1 Context

To partly overcome the limitations of the current-based model described in the previous Chapter 5, we considered other models and identified that metamorphosis theory handles topology change and

tracks serial intensity variation, so can exhibit and indeed make use of actual perilesional diffusion or perfusion values. Therefore, we propose in this chapter the extension of an image-to-image metamorphosis model into a longitudinal metamorphosis that captures the continuous stroke lesion evolution from one timepoint to the next one using serial MR imaging. This may aid understanding of ischemic lesion progression. Image-to-image registration methods have been extensively investigated and improved over the last few decades. More recently, the development of regression models using longitudinal data grew from the widespread use of medical time-series imaging to track the spatiotemporal changes in brain structures or lesions. Finding image correspondences, defining a quantitative measure for local/global deformations characterizing the evolution of different objects (eg: anatomical structures, brain lesions, etc), is essential to advance our understanding of critical problems in neuroimaging, such as tracking the directional change of ischemic stroke lesion over time.

In this chapter, we present the theoretical background of the image-to-image metamorphosis theory and its extension into handling longitudinal data.

6.2 Image-to-image metamorphosis

Numerous image-to-image registration models could be categorized into two distinctive groups:

A. *Non-metamorphic image temporal registration/regression methods:*

The longitudinal scenarios estimated from a sequence of images given at different timepoints is based on registration methods –some pointed out in [Klein 2009]. We focus our study to one method in particular, the Large Deformation Diffeomorphic Metric Mapping (LDDMM) –pioneered by [Trouvé 1995, Trouvé 1998] and [Dupuis 1998] registration framework, that will be the basis of our generalization. Its extension to aligning longitudinal data has become a standard tool in recent regression methods such as the parallel transport of time-series point clouds method for tracking time-dependent shape changes presented in [Qiu 2009] or piecewise geodesic path as in [Durrleman 2013]. In [Craene 2012], a new multiple time point diffeomorphic temporal registration algorithm was presented; however, it does not deal with changes in lesion topology. A recent paper [Niethammer 2011] approximated a least-squares geodesic regression line for image time-series as a weighted average of pairwise individual regression lines. This concatenation process of these individual lines uses the initial momenta obtained by registering the baseline image with another image from a temporal image-sequence, thus estimating a smooth spatiotemporal trajectory of image evolution. A later paper [Hong 2012b] also used this method [Niethammer 2011] with a distance approximation for image-to- image registration as proposed

in [Yang 2011]. Although progress has been made in refining spatiotemporal regression models, the aforementioned methods present some limitations for stroke: topology change is not taken into account since they are all based on a diffeomorphic metric that preserves the initial topology of the evolving object.

B. *Metamorphic image temporal registration/regression methods:*

We identified one recent paper that addressed longitudinal image evolution using metamorphosis. Hong et al in [Hong 2012a] adapted the work of [Niethammer 2011] by proposing a metamorphic geodesic regression using appropriate averaging of the initial momenta of independent pairwise metamorphoses. These initial momenta – determined using an augmented Lagrangian shooting method– fully define the spatiotemporal deformation and intensity variation paths from time-series images. This allows capturing both spatial and morphological changes in the longitudinal data.

In this chapter, we present a different and more compact formulation for spatiotemporal metamorphosis using an ordered set $\Im = \{I_0, I_1, , I_{N-1}\}$ of N images. Unlike [Hong 2012a], our approach does not require a pairwise estimation of N metamorphoses to concatenate using geodesic regression. Hence, we do not need to fit all metamorphoses from the baseline image to all the measurement points individually. Instead, the method estimates a single metamorphosis that exactly meets all the intermediate images (observations) in

$\Im$, while enforcing regularity in time for the estimated velocity field (Figure 6.1). In our formulation of *longitudinal metamorphosis*, we expand the work presented in [Garcin 2005] from two-image based metamorphosis into time-series based spatiotemporal metamorphosis. However, we use the Cauchy-Navier differential operator as presented in [Beg 2005], instead of using wavelets as in [Garcin 2005], to estimate deformation vector field v_t. We chose this differential operator to provide greater smoothing of our data, justified in our study since we focus on obtaining a quantified estimate of the dynamics of ischemic lesion spatial margins.

Stroke perfusion images are dynamic and part of the acute-subacute perfusion value variability may be due to differences in the acute ischemic lesion or clinical characteristics (eg: site of arterial occlusion, the adequacy of the collateral flow, etc). In the present work, we modelled the continuous changes in perfusion from acute presentation, inside and outside the boundaries of the tissue that ultimately perished and appeared in the final T2-w image at $\geq$ 1 month after stroke.

Note that the extension to time series of observations can easily be described and numerically solved once the image-to-image metamorphosis is clearly exposed. Therefore, in the following subsections, we are going to explore the key construction steps of the Riemannian *metamorphic metric*, driving the metamorphosis theory and its

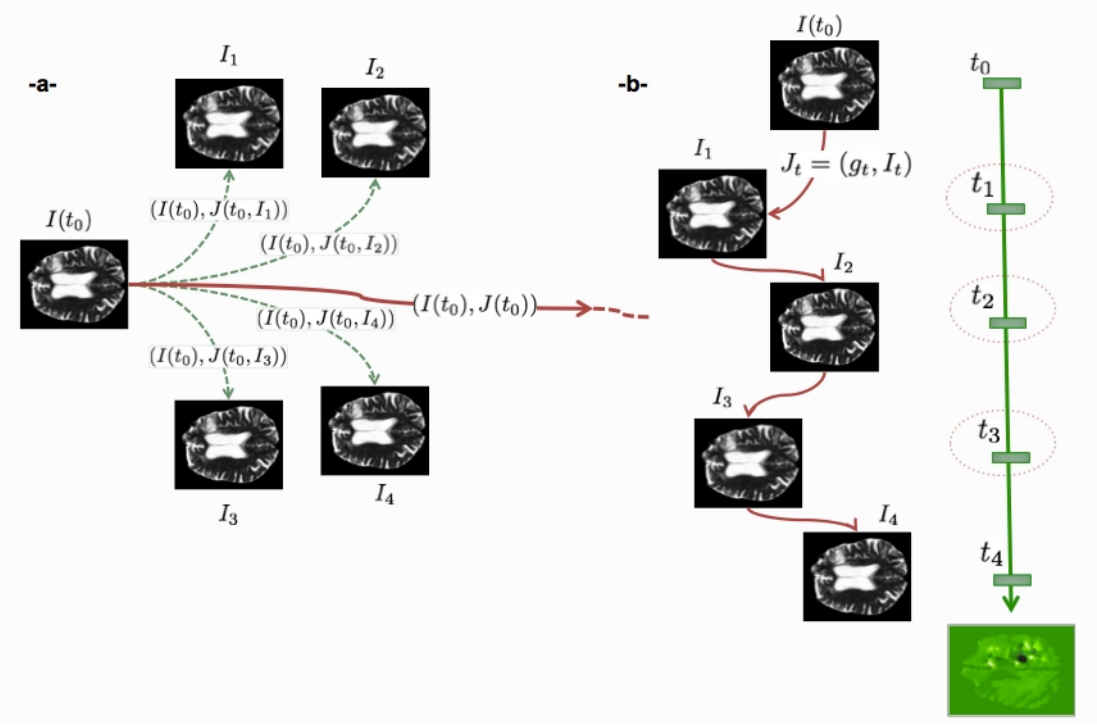

Figure 6.1: *Comparison between metamorphic regression scheme presented in [Hong 2012a] (a) and our longitudinal metamorphosis (b).* The red bold line in (a) represents the metamorphic regression line determined by pairwise metamorphoses between the baseline image $I(t_0)$ and the images I_i. Each individual metamorphosis is defined by the initial momentum of the geodesic shooting. In (b), the estimated longitudinal metamorphosis path J_t morphs the baseline image successively into I_1, I_2, I_3 till merging with the final image I_4. To avoid the velocity jumps we force the estimated velocity to be continuous in time at the observation timepoints (circled in red). Therefore, this will avoid to bias the metamorphic deformation map (in green, superimposed with the brain image), reconstructed while integrating the velocity path v_t over the evolution time interval $[t_0, t_4]$.

derived variational problem to facilitate the presentation of the time series extension.

6.2.1 Abstract setting for the metamorphosis construction

Finding an alternative self-consistent type of geometric metric in a Riemannian setting and defining the binding forces acting on the manifold resolved the longstanding problem of incorporating topology and intensity changes into the LDDMM framework. The definition of this metric requires the use of appropriate spaces to which the images, the force acting on the images, and the velocity driving the evolution of the baseline image towards the target image belong. The mathematical framework for metamorphosis is composed of the three main ingredients:

- **Image:** an image I is an element of the square integrable set of functions L^2 considered as a Riemannian manifold denoted M (the object space) to avoid further confusion with other square integrable vector spaces. A curve $(t \mapsto I_t,\ t \in [0,1])$ on M is the path of evolution of a base line image I_0. M is equipped with the usual metric on L^2. We denote by Ω the space where an image I is defined.

- **Action (force):** an action g is a diffeomorphic transformation (a mapping) that belongs to a Lie group G endowed with a Lie algebra $\mathcal{G}$. An element g of the action group acts upon the object

space M. In the realm of a classical diffeomorphic deformation theory, we associate to the action g a velocity v that satisfies the flow equation (Eq 5.3). A curve $(t \mapsto g_t,\ t \in [0,1])$ on G acting on an image $I \in M$ describes a path of deformation morphing I over the time interval $[0,1]$.

- **Velocity:** for all $t \in [0,1]$, the velocity field v_t belongs to the vector space V, which is the tangent space to the action group G. We adopt similar construction as in [Beg 2005] for the velocity vector space V on which smoothness constraints are placed to ensure the existence of optimal smooth solutions in the space of diffeomorphisms for the flow equation (Eq 5.3). We endowed the velocity vector space V with an inner product $< ., . >_V$ defined through a differential Cauchy-Navier type operator L (with adjoint $L^\dagger$) given by: $< f, g >_V = < Lf, Lg >_{L^2} = < L^\dagger L f, g >_{L^2}$) where $< ., . >_{L^2}$ is the standard L^2 inner-product for square integrable vector fields on M and $L = -\alpha\nabla^2 + \gamma id$. Thus, the required smoothness of the deformations is specified by the norm of the space V of smooth velocity vector fields through L.

Both action group and velocity space settings highlight that the LDDMM framework is the gist of the metamorphic framework. In what follows, we will recall in this setting (image, action, velocity) the necessary tools for defining the metamorphosis metric and therefore

distance between images.

As defined by [Trouvé 2005], a metamorphosis is a pair of curves $((g_t, I(t)),\ t \in [0,1])$ on the product space $\mathcal{J} = G \times M$, with $g(0) = id$. The effective metamorphosis path $J(t)$ on M is defined as a combination of the action deformation path g_t and the image path $I(t)$ which is the residual of the deformation on M: $J(t) = g(t).I(t)$. We identify the case of a pure diffeomorphic deformation when the image residual $I(t)$ does not vary. The construction of the metamorphosis metric is recalled in the following section, all details are available in [Trouvé 2005].

6.2.2 Construction of the metamorphosis Riemannian metric

We recall the properties of metamorphosis that are useful for a better understanding of our method.

The construction of the Riemannian metamorphic metric is based on the following three applications associated with the action group: For $g \in G$ and $I \in M$, we define:

- Two components A_g and R_I of the action g:

$$A_g : M \to M$$
$$I \mapsto g.I$$

and

$$R_I : G \to M$$
$$g \mapsto g.I$$

- The right translation on G:

$$R_{g_1} : G \to G$$
$$g_2 \mapsto g_2.g_1$$

The differentiability of any curve $(t \mapsto g_t,\ t \in [0,1])$ on G allows us to define both derivatives of the C^1 maps R_I and R_g at the identity element $e \in G$. The generated derivatives define the following infinitesimal actions:

$$d_e R_I : V \to T_I M$$
$$v \mapsto v.I$$

$$d_e R_g : V \to V$$
$$v \mapsto v.g$$

The infinitesimal C^1 action $d_e R_I$ of an element $v \in V$ on M defines a continuous vector field over M and the infinitesimal C^1 action $d_e R_g$

defines a vector field over G. The velocity path $(t \mapsto v_t,\ t \in [0,1])$ in V of the differentiable action path $(t \mapsto g_t,\ t \in [0,1])$ in G satisfies the flow equation rewritten as:

$$\begin{cases} \partial_t g = d_e R_g(v(t)) = v(g_t) \\ g(0) = e. \end{cases}$$

With e denoting the identity element of the group G.

The differentiation of the effective metamorphosis path $J(t)$ at a given point t defines an infinitesimal metamorphosis $\partial_t J$ on the tangent space $T_I M$ as follows:

$\partial_t J(t) = \frac{dJ(t)}{dt} = d_{I(t)} A_{g_t}.\partial_t I(t) + d_{g_t} R_{I(t)}.\partial_t g_t.$

Recalling that $J(t) = g(t).I(t)$ and that $R_J = R_{g.I}$, then using the composition property $R_I = R_{g.I} \circ R_{g^{-1}}$ that leads to $d_g R_I = d_e R_{g.I}\ d_g R_{g^{-1}}$ we get:

$= d_{I(t)} A_{g_t}.\partial_t I(t) + d_e R_{g_t I(t)}\ d_{gt} R_{g_t^{-1}} \partial_t g_t$

$= d_{I(t)} A_{g_t}.\partial_t I(t) + d_e R_{J(t)}$

$= d_{I(t)} A_{g_t}.\partial_t I(t) + v(t).J(t)$ (Using the definition of an infinitesimal action).

Let $J(t)$ be a metamorphosis curve on M defined using a pair of curves $((g_t, I(t)),\ t \in [0,1])$ on the product space $\mathcal{M} = G \times M$ such as: $J(t) = g(t).I(t)$. The *infinitesimal metamorphosis* is a tangent vector $\eta(t)$ at a given point t to the metamorphosis trajectory $J(t)$. This trajectory is composed of two elements one belonging to the velocity vector space V and the other to the tangent space $T_{J(t)} M$ to

M at $J(t)$ as follows:

$$\eta(t) = (v(t), d_{I(t)}A_{g_t}.\partial_t I(t)).$$

This decomposition of a generic element $\eta = (v, \delta)$ of the product space $VT_{J(t)}M$ into one element $v \in V$ and another element $\delta \in T_{J(t)}M$, introduces a new map on $VT_{J(t)}M$:

$$\Phi^I : V \times T_{J(t)}M \to T_{J(t)}M;\ (v, \delta) \mapsto \delta + v.J.$$

Now we can use the tangent space $T_{J(t)}M$ –engendered from infinitesimal metamorphoses– and the map Φ^I to define a new Riemannian metric that will produce the *metamorphic* structure of an image curve I_t on M (Figure 6.2).

The following proposition demonstrates that the whole metamorphosis framework is consistent.

***Proposition 1.*:** metamorphosis metric [Trouvé 2005]

The norm of a vector $j \in T_J M$ defines a new Riemannian metric on M assuming that the application $(v \mapsto v.J)$ is continuous on V as follows:

$$||j||^2_{\mathcal{J}} = \inf_{v\in V}\{|v|^2_V + \tfrac{1}{\sigma^2}|\delta|^2_M :\ j = \Phi^I(v, \delta)\}$$
$$= \inf_{v\in V}\{|v|^2_V + \tfrac{1}{\sigma^2}|\delta|^2_M :\ j = \delta + vJ)\}$$
$$= \inf_{v\in V}\{|v|^2_V + \tfrac{1}{\sigma^2}|j - vJ|^2_M\}.$$

Where the subscript $\mathcal{J}$ denotes the product space (also metamorphosis space) $\mathcal{J} = G \times M$.

Thus, a metamorphosis consists in looking at both the deformation magnitude $|v|^2_V$ induced by the group of deformations G and the

intensity variation (residual part) $|j - vJ|^2_{\mathcal{J}}$ through the lenses of a metric placed on the tangent space $T_J M$. It smoothly adjusts image intensities along optimal streamlines of $T_J M$. The design of the new Riemannian metamorphic metric will allow us to define the energy of a metamorphosis curve J_t and find minimizing geodesics between two images on M.

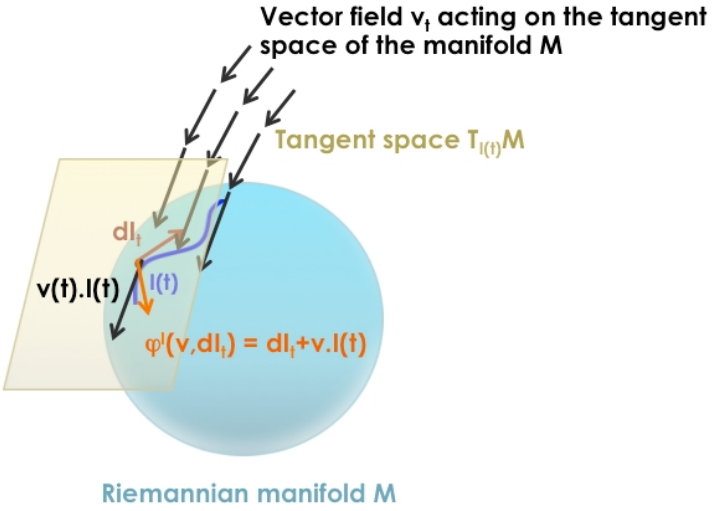

Figure 6.2: *Illustration of the map* Φ^I. Let $I(t)$ be a curve on M. All vectors dI_t in red, $v(t).I(t)$ in black and $\Phi^{I(t)}(v(t), dI_t)$ in orange belong to the tangent space $T_{I(t)}M$. A simple geometric construction also defines the residual of the deformation: $dI_t - v(t).I(t)$ on $T_{I(t)}M$.

6.2.3 Metamorphosis energy and geodesics

As shown in [Garcin 2005], for $(I(t),\ t \in [0,1])$ a curve on M, the energy of this curve using the metamorphic metric is:

$$E(I(t)) = \int_0^1 ||\tfrac{dI(t)}{dt}||^2_{\mathcal{J}} dt$$
$$= \int_0^1 \inf_{t \mapsto v(t) \in G} \{|v|^2_V + \tfrac{1}{\sigma^2} |\tfrac{dI(t)}{dt} - v(t)I(t)|^2_{I(t)}\} dt$$

$= \inf_{t \mapsto v(t) \in G} \{ \int_0^1 |v|_V^2 dt + \frac{1}{\sigma^2} \int_0^1 |\frac{dI(t)}{dt} - v(t)I(t)|_{I(t)}^2 dt \}$

Where the norm notation $||_{I(t)}$ is associated with the evolution curve $I(t)$ on the image manifold M. The energy $E(I(t))$ can be rewritten an infimum over velocity curves of an energy U as follows:

$$U(I, v) = \int_0^1 |v|_V^2 dt + \frac{1}{\sigma^2} \int_0^1 \left| \frac{dI(t)}{dt} - v(t).I(t) \right|_{I(t)}^2 dt. \qquad (6.1)$$

more This formulation unifies in a common mathematical framework intensity change and deformation.

In comparison to the diffeomorphic variational problem (Eq 5.5), we can clearly see now how the fidelity to data term is replaced by a residual of the deformation term $|\delta(t)|_{I(t)}^2 = |\frac{dI(t)}{dt} - v(t)I(t)|_{I(t)}^2$ that accounts for the variation in intensity of the estimated image path $I(t)$. Solving this variational problem comes down to finding optimal geodesics and simplifying the computation of the residual part.

6.2.4 Metamorphosis governed by the advection and flow equations

Since the group of deformations is a group of diffeomorphisms of M then the application R_I becomes:

$R_I : G \to M;\ g \mapsto g.I = I \circ g^{-1}$.

The computation of the *infinitesimal* action of g leads to the application:

$d_e R_I : V \to T_I M;\ v \mapsto v.I = - < \nabla I, v >$.

Therefore the magnitude of the deformation residual can be written as:

$|\delta(t)|^2_{I(t)} = |\frac{dI(t)}{dt} + < \nabla I, v >|^2_{I(t)}$.

Recalling that an advection equation is a partial differential equation that governs the motion of a conserved scalar field I_t as it is advected by a velocity vector field v_t, we interestingly identify at this stage an altered version of the advection equation ($\frac{dI(t)}{dt} + \nabla I_t.v_t = \delta(t)$). If the residual of the deformation is zero ($\delta(t) = 0$) then we find the original advection equation. This residual undertakes that the metamorphosis scheme includes the variations in the images induced by the deformation field v_t. It can be viewed as a condensed form that sums up both variations in intensity and shape.

6.2.5 Numerical scheme for energy discretization

As we need to minimize this energy for image matching, a discretization step in the time and space domains is required to simplify the non-linear advection equation and get stable numerical solutions. Therefore, we exhibit the energy gradient following the discretization step. We approximate the term $\nabla I_t.v_t$ by $(I(t+1, x+v(t,x)) - I(t,x))$ as we use the numerical scheme of its total derivative:

$\lim_{\varepsilon \to 0} \frac{I(t+\varepsilon, x+\varepsilon v(t,x)) - I(t,x)}{\varepsilon} = \frac{\partial I(t,x)}{dt} + \frac{\partial I(t,x)}{dx}.v(t,x)$.

As a next step, we first discretize the energy functional in the discrete time domain of evolution $[0, T]$ (with the size of a timestep

Δt being such that $T = N \times \Delta t$) using this approximation of the total intensity derivative as follows:

$\bar{U}(I, v) = \sum_{t=0}^{T-1} |v_t|_V^2 + \frac{1}{\sigma^2} \sum_{t=0}^{T-1} \int_0^1 |I_{t+1}(x + v_t(x)) + \nabla I_t . v_t|_{L^2}^2 dx.$

To discretize $U(I, v)$ in the image space domain (a grid), we use a trilinear interpolation as in [Garcin 2005] to define real values for $x + v_t(x)$. Therefore, by applying the trilinear operator Γ to $I_{t+1}(x + v_t(x))$, we get:

$$U(I, v) = \sum_{t=0}^{T-1} |v_t|_V^2 + \frac{1}{\sigma^2} \sum_{t=0}^{T-1} \sum_{x \in \Omega} |\Gamma(I_{t+1})(x + v_t(x)) + \nabla I_t . v_t|_{L^2}^2. \tag{6.2}$$

For further calculus, we introduce a simpler notation for the interpolation application:

$$\begin{aligned} \Gamma_{v_t} I_{t+1} : \Omega &\to \mathbb{R} \\ x &\mapsto \Gamma(I_{t+1})(x + v_t(x)) = I(t + 1, x + v(t, x)). \end{aligned}$$

As for the flow equation (Eq 5.3), we discretize it in time as $g_{t+1} = (id + v_t)(g_t)$. The search for a minimal metamorphosis path composed of both optimal image path ($t \mapsto I_t,\ t \in [0, 1]$) and the associated diffeomorphic path ($t \mapsto g_t,\ t \in [0, 1]$) is achieved through a discrete gradient descent minimization scheme. The details of the gradient calculations are given in the next Section.

The optimal velocity field and the intensity scalar field are calculated using the metamorphosis energy gradients (Eq 6.3-6.4) in a standard alternating steepest gradient descent algorithm, as we shall see now.

6.2.6 Metamorphosis energy variations *w.r.t* I_t and v_t for the minimization scheme

As the image manifold M, endowed with the inner product $< ., >_{L^2}$, is continuously differentiable, we can compute the variation of the metamorphosis energy functional $U(I, v)$ (Eq 6.2) with respect to a given point I_t on M. We therefore perturb I_t along an infinitesimal element $dI_t \in T_{I_t}M$.

- Metamorphosis energy perturbation along dI_t for $t \in [1, T-1]$:

  $< \nabla_{I_t} U(I, v), dI_t >_{L^2} = \frac{2}{\sigma^2}(< \Gamma_{v_t} I_{t+1} - I_t, -dI_t >_{L^2} +$

  $< \Gamma_{v_{t-1}} I_t - I_{t-1}, \Gamma_{v_{t-1}} dI_t >_{L^2})$

  $= \frac{2}{\sigma^2}(< I_t - \Gamma_{v_t} I_{t+1}, dI_t >_{L^2} +$

  $< \Gamma^T_{v_{t-1}}(\Gamma_{v_{t-1}} I_t - I_{t-1}), dI_t >_{L^2}).$

  Thus,

$$\nabla_{I_t} U(I, v) = \frac{2}{\sigma^2} I_t - \Gamma_{v_t} I_{t+1} + \Gamma^T_{v_{t-1}}(\Gamma_{v_{t-1}} I_t - I_{t-1}). \qquad (6.3)$$

- Metamorphosis energy perturbation along dv_t for $t \in [0, T-1]$:

  We also compute the variation of $U(I, v)$ under the perturbation of $v \in L^2([0,1], V)$ by $dv_t \in L^2([0,1], V)$.

  $< \nabla_{v_t} U(I,v), dv_t >_V = < 2v_t, dv_t >_V + \frac{2}{\sigma^2} < \Gamma_{v_t} I_{t+1} - I_t, \nabla v_t (\Gamma_{v_t} I_{t+1}) dv_t >_{L^2}$.

  The differentiation of the application $\Gamma_{v_t} I_{t+1}$ $w.r.t$ to v_t leads to:

  $d_{v_t}(\Gamma_{v_t} I_{t+1}) dv_t = < \nabla_x I_{t+1}(x + v_t(x)), dv_t >$, where ∇_x denotes the spatial gradient.

  Therefore, $\nabla v_t(\Gamma_{v_t}) I_{t+1}) = \nabla_x I_{t+1}(x + v_t(x)) = \Gamma_{v_t} \nabla_x I_{t+1}$.

  $< \nabla_{v_t} U(I,v), dv_t >_V = < 2v_t, dv_t >_V + \frac{2}{\sigma^2} < \Gamma_{v_t} I_{t+1} - I_t, \Gamma_{v_t} \nabla_x I_{t+1} dv_t >_{L^2}$

  $= 2 < Kv_t + \frac{1}{\sigma^2} (\Gamma_{v_t} \nabla_x I_{t+1})^T (\Gamma_{v_t} I_{t+1} - I_t), dv_t >_{L^2}$.

  Hence,

$$\nabla_{v_t} U(I,v) = 2Kv_t + \frac{2}{\sigma^2} [(\Gamma_{v_t} \nabla_x I_{t+1})^T (\Gamma_{v_t} I_{t+1} - I_t)]. \quad (6.4)$$

With K the self-adjoint compact operator as previsously introduced.

This operator is used in many formulas of LDDMM such as [Beg 2005]. A good review of $K, L^\dagger$ and L operators is presented in [Holden 2008]. To compute these operators, we adopted the discretized numerical scheme using the Fast Fourier Transform (FFT) and its inverse presented in Appendix 9 of Davis thesis [Davis 2007].

6.2.7 Finding the optimal metamorphosis: gradient descent scheme

The steps of the minimization algorithm for estimating the optimal metamorphosis path $(\hat{g}_t, \hat{I}_t)$ are below:

1. Initialize image evolution path from the source image I_0 to the target image I_1 through piece-wise trilinear interpolation (fixed boundary conditions for exact matching) as follows:

   $I(t) = (1-t)I_0 + tI_1;\ with\ t \in [0,T]$.

2. Compute U_{old} using the initial image evolution path:

   $U_{new} = \frac{1}{\sigma^2}\sum_{t=0}^{T-1}\sum_{x\in\Omega}|\Gamma(I_{t+1})(x+v_t(x)) - I_t(x)|^2_{L^2}$.

   $U_{old} = U_{new} + C$, with $C >> \varepsilon$.

3. while $|U_{new} - U_{old}| > \varepsilon$

   - Compute $\nabla_{v_t} U(I^{old}, v^{old})$.
   - Update at all timepoints: $v_t^{new} = v_t^{old} - \varepsilon_v \nabla_{v_t} U(I^{old}, v^{old})$, where ε_v is the gradient descent step associated with the velocity vector field.
   - Update diffeomorphic deformation trajectories g_t using Euler-centered integration scheme by solving the discrete version of the flow equation: $g_{t+1} = (Id + v_t)(g_t)$.
   - Compute $\nabla_{I_t} U(I^{old}, v^{new})$.

- Update at all timepoints except observations timepoints: $I_t^{new} = I_t^{old} - \varepsilon_I \nabla_{I_t} U(I^{old}, v^{new})$, where ε_I is the gradient descent step associated with the intensity scalar field.
- Compute $U_{new} = U(I^{new}, v^{new})$.
- If $U_{new} \geq U_{old}$ continue to decrease ε_v and ε_I until $U_{new} < U_{old}$. Then, reassign variables:
$$\begin{cases} I_t^{old} = I_t^{new}. \\ v_t^{old} = v_t^{new}. \\ U_{old} = U_{new}. \end{cases}$$
- Loop over step (3.) until convergence.

Note that for convergence purposes, the gradient step sizes may be adapted along the iterations.

Remark: To ensure an exact metamorphic matching, the gradient descent is performed in the in-between observations time interval while the observation timepoints (at t_0 and t_T) are remained unchanged. Therefore, the gradient $\nabla_{I_t} U$ at the observation timepoints is zero. This is perfectly in line with the mathematical formula of the energy gradient (Eq 6.3-6.4).

6.3 Piecewise geodesic longitudinal metamorphosis using N images

Now we will present the generalization to a set of time dependent observations. We aim at estimating a piecewise geodesic metamorphosis (w.r.t the metamorphosis metric) adding a continuity in time constraint on the velocity vector field $(v_t)_{t\in[0,1]}$ in particular at the observation timepoints. This is based on similar equations as before and the energy to minimize is:

$$U(I,v) = \sum_{t=0}^{T-1} |v_t|_V^2 + \frac{1}{\sigma^2} \sum_{t=0}^{T-1} \sum_{x\in\Omega} |\Gamma(I_{t+1})(x + v_t(x)) + \nabla I_t.v_t|_{L^2}^2. \tag{6.5}$$

where $(v_t)_{t\in[0,1]}$ is continuous in time.

In order to minimize this energy and get the longitudinal metamorphosis using N images $\Im = \{I_0, I_1, , I_{N-1}\}$, we exactly follow the steps of the gradient descent pipeline presented in the previous section, except that we modify two steps of the previous algorithm.

The first step encoding the initialization of the image path $I(t)$ becomes as follows:

1. Initialize image evolution path from the source image I_0 to the target image I_N trough piece-wise trilinear interpolation (fixed boundary conditions for exact matching) as follows:

$$\begin{cases} \text{For } t \in [t_i, t_{i+1}[\text{ with } i \in [0, T-1],\ I(t) = (1-t)I_{t_i} + tI_{t_{i+1}}. \\ t_{i+1} - t_i = \text{time interval seperating two images.} \end{cases}$$

Indeed, we have previously seen that step (1) in the image-to-image metamorphosis algorithm is where we initialize the intensity path as an interpolation between the source and the target images while keeping the ground truth observations unchanged. This initialization step (1) is what drives the metamorphosis optimization process between observation timepoints. Inserting additional 'observation points' between the source and the target image works as if we have 'slightly' changed the in-between observations interpolation path. In our extension of the image-to-image metamorphosis to longitudinal one, we force the algorithm to exactly go through all observations (time-series images) by keeping the observations unaltered and only updating the intensity path connecting them.

The second change is to enforce the continuity of the velocity vector field so that the whole path is continuous in time and piece-wise geodesic. This is done as follows: for any observation timepoint $t = t_{obs}$:

$$v_{t_{obs}} = v^{+}_{t_{obs}} = v^{-}_{t_{obs}}. \tag{6.6}$$

We choose a small time discretization step between the observations for this definition of regularity in time to be valid. This constraint forces the estimated metamorphosis to follow a relevant path (w.r.t. our application) and makes it differ from concatenated paths

as illustrated in Figure 6.3.

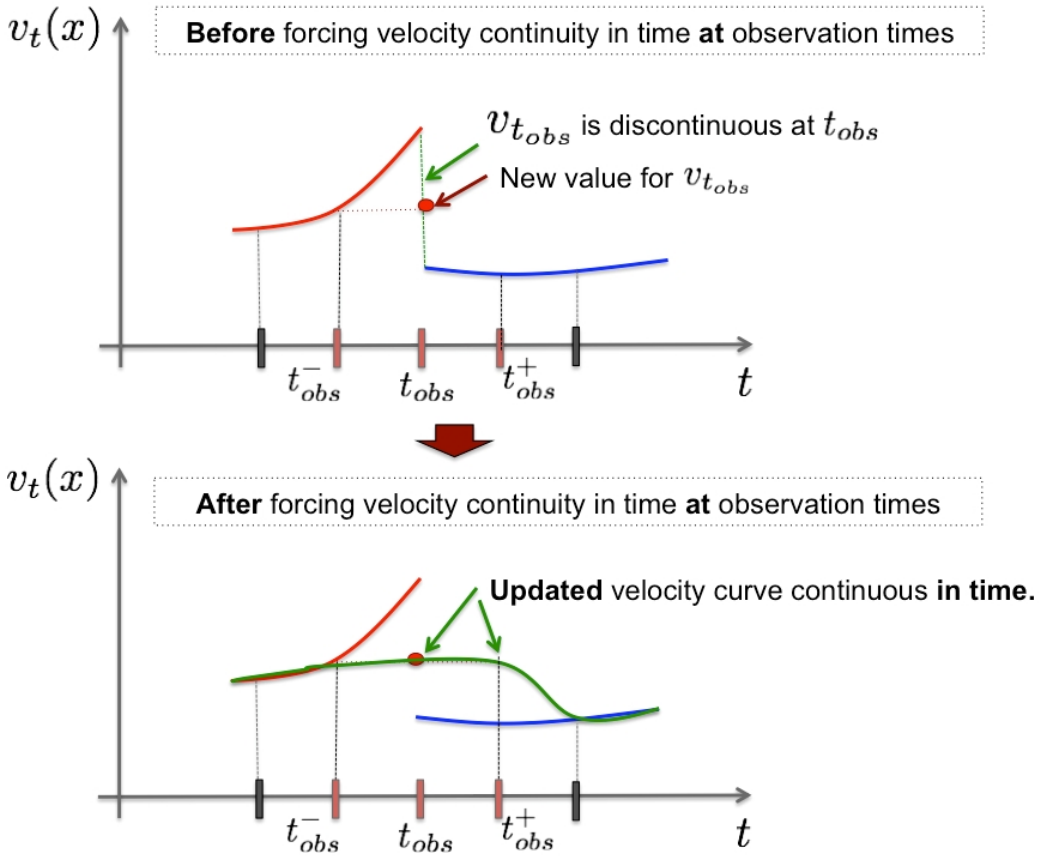

Figure 6.3: *Enforcing the continuity in time of the estimated velocity field* (v_t) *at observation timepoints.* (Top) For a fixed voxel x in the image, we notice that the velocity curve v_t is discontinuous at observation timepoints t_{obs} as both the red and blue curves are not "glued" together. We enforce the continuity at the observation timepoints by associating a new value to v_{obs} at t_{obs} that is equal to the velocity value at t_{obs}^- then we update t_{obs}^+ to establish the equality between the three discrete points in time. This generates a new velocity curve (in green) that is continuous in time.

As the estimated velocity is piecewise geodesic in the discretized time intervals, this imposed time-continuity constraint forces relevant final deformation maps in a way that would coincides with real evolution of the lesions. Therefore, the longitudinal metamorphosis-derived

analysis tools would be a solid ground for enhancing our understanding of stroke spatiotemporal behavior.

Next, we will validate the longitudinal metamorphosis model using stroke perfusion (Chapter 7) and diffusion (Chapter 8) clinical data.

Chapter 7

Metamorphosis clinical application I to perfusion-weighted MR images of stroke lesion

Contents

7.1 Context

Stroke perfusion images are dynamic and part of the acute-subacute perfusion value variability may be due to differences in the acute

ischemic lesion or clinical characteristics (eg: site of arterial occlusion, the adequacy of the collateral flow, etc). In this chapter, we use the longitudinal metamorphosis model (developed in Chapter 6) to track the continuous changes in perfusion abnormality from acute presentation, inside and outside the boundaries of the tissue that ultimately perished and appeared in the final T2-w image at ≥ 1 month after stroke. This will enable us to look into perfusion values variability and their relation to final outcome.

7.2 Data

Patient recruitment (10 patients): We tested the metamorphosis model on 10 representative patients from a study of serial MR imaging in hyperacute stroke, representing a range of stroke severity (NIHSS $= 12.6 \pm 8.9$), age (74 ± 94.7 years) and acute mean transit time (MTT) volume ($1.78 \pm 1.23\ 10^5\ mm^3$). We included patients who had PWI images at around 5 hours, the second at around 5 ± 1 days and the third at $10.5 + /2.5$ days after stroke and T2-weighted images lesion at ≥ 1 month after stroke. Furthermore, we have checked that swelling in the recruited patients did not distort DWI lesion boundary as it can mislead the interpretations of our results. To further simplify the analysis of the results, we excluded patients who received thrombolytic or other reperfusion therapies. The model was blind to all prior clinical data.

MR imaging and pre-processing steps: We used the same MR acquisition and preprocessing steps as in Chapter 5 Section 5.4.1 for more details. We used unthresholded MTT at this stage in model application as it generally includes both dead and at-risk tissues – allowing us to look at a wider range of perfusion values in the hypoperfused area.

7.3 Experiments and results

7.3.1 Metamorphic longitudinal matching applied to perfusion MR images of stroke

For every patient, we estimated a longitudinal metamorphosis of MTT lesion from acquisition timepoint t_1 to t_3. Both velocity and intensity paths were estimated (Fig 7.1). We empirically set the trade-off parameter σ such as $\frac{1}{\sigma^2} = 0.001$ for all patients. For the differential operator $L = -\alpha\nabla^2 + \gamma id$, we set $\alpha = 0.01$ and $\gamma = 0.001$.

Since the analysis of the set of estimated paths in our cohort to infer potential similarity patterns is not straightforward and may require computationally expensive statistics, we focused our analysis on examining residual maps. Indeed, the deformation residual map condenses in one image both the magnitude of the deformation and intensity variation in the lesion during its metamorphosis (see Fig.7.2).

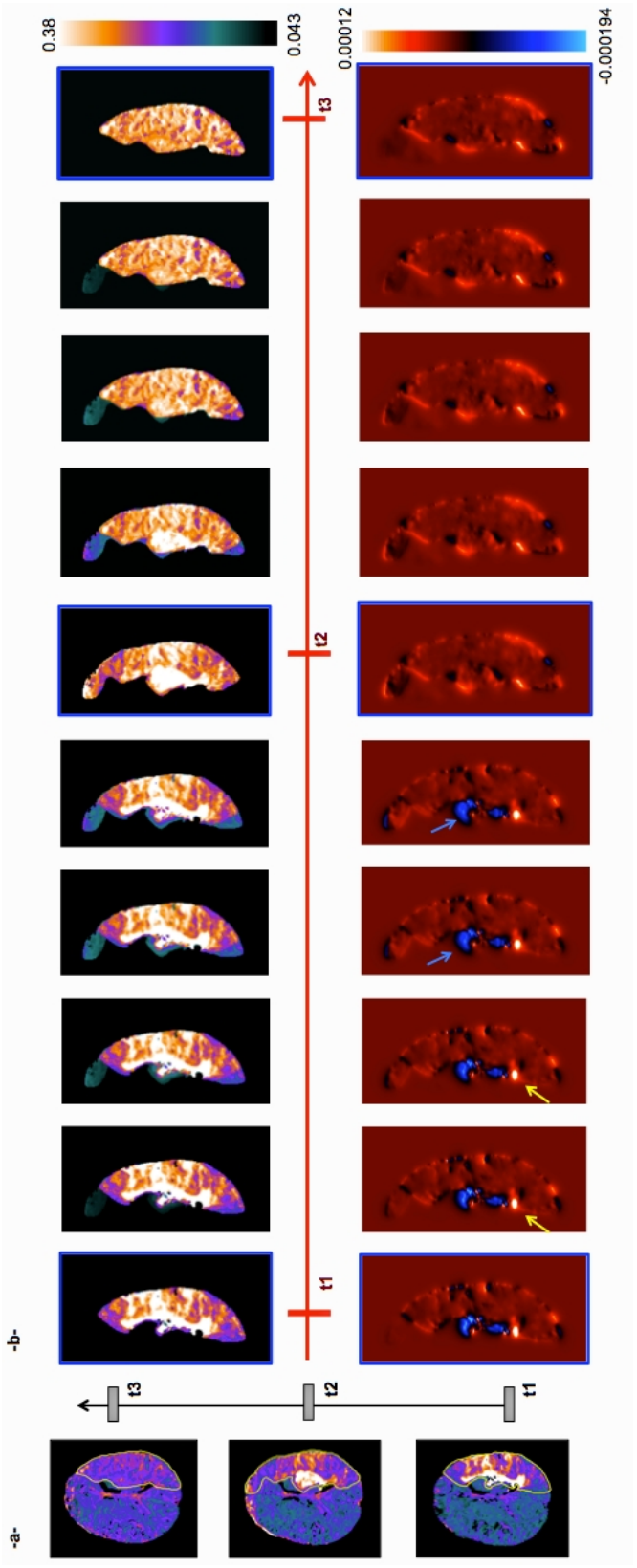

Figure 7.1: *Longitudinal metamorphosis.* (a) MTT maps at three acquisition timepoints superimposed with the manual segmentation of the lesion (in yellow). (b) Top row: screenshots of the estimated intensity path ($t \mapsto I_t$) from t_1 to t_3 of MTT lesion metamorphosis; bottom row: screenshots of the estimated velocity path ($t \mapsto v_t$) from t_1 to t_3. Yellow arrows point to contracting areas and blue arrows point to expanding areas.

7.3.2 Reconstruction of residual maps and automated thresholding

For each patient, we reconstruct the normalized residual map (rMap) by summing over time the estimated metamorphosis residuals located at the lesion voxel x as follows:

$$For\ x \in \Omega,\ rMap(x) = \sum_{t=0}^{T-1} |\Gamma(I_{t+1})(x + v_t(x)) - I_t(x)|^2_{L^2}. \quad (7.1)$$

Then we normalize it between 0 and 1 with respect to its mean value.

Residual maps quantify the variation in perfusion values inside the lesion under the action of the estimated deformation field. Therefore, residual areas with highest values mark where the most relevant dynamic change in both intensity and shape takes place. To detect these areas with highest MTT variation from t_1 to t_3, we define an automated threshold $R_{threshold}$ as the mean value of the residual map rMap.

Then, we generate a new normalized thresholded rMap ($rMap_{thresholded}$) by including all the voxels with values above this threshold. Figure 7.2 visualizes the steps of the algorithm pipeline run for every patient in our cohort. Finally, we compute the volumetric overlap (in %) between the thresholded residual map and T2-w lesion *w.r.t final T2-w volume*. This volumetric overlap indicates how

much of the final T2-w lesion is occupied by the thresholded residual map.

Using Eq. (7.1), the residual map does not inform us about the direction in which the perfusion change is going (positive direction ie. increasing values or negative direction ie. decreasing values). To interpret the thresholded rMap with regard to the direction of perfusion values variation –while only focusing on the acute and late perfusion changes, we generated a signed MTT map defined as the difference image between MTT image at t_3 and MTT at t_1:

For $x \in \Omega,\ map_{\Delta_{MTT}}(x) = MTT_{t_3}(x) - MTT_{t_1}(x)$.

Then, we marked areas in the thresholded residual map with negative $map_{\Delta_{MTT}}$ values (blue in Figure 7.3) and positive $map_{\Delta_{MTT}}$ values (red in Figure 7.3). This generates a signed thresholded residual map (Figure 7.3) that allows us to simultaneously look at perfusion areas that underwent the highest intensity and deformation changes with distinction of areas where MTT values decreased from t_1 to t_3 (negative $map_{\Delta_{MTT}}$ values) or increased from t_1 to t_3 (positive $map_{\Delta_{MTT}}$ values). Positive regions in the signed $rMap_{thresholded}$ represent 'extreme' areas where the perfusion abnormality has worsened. In the other hand, negative regions highlight areas where the blood flow increased.

Remark: the signed thresholded residual maps do not exceed the boundaries of the manual outlines of MTT lesions at the three acqui-

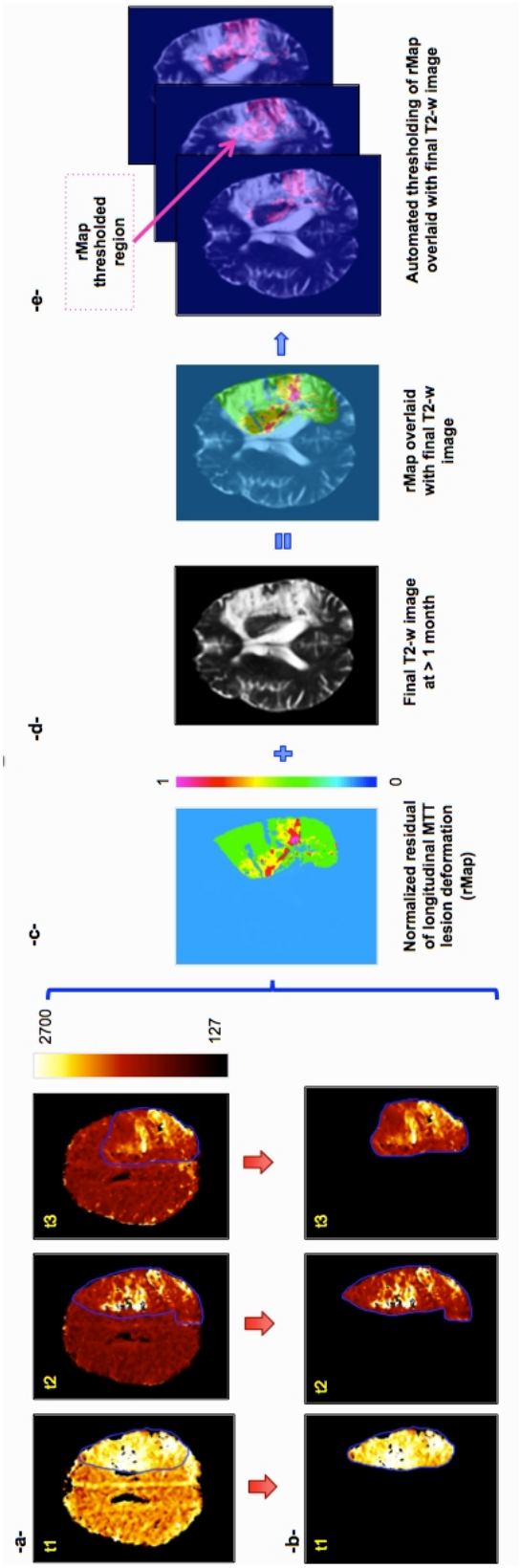

Figure 7.2: *Algorithm pipeline.* (a) Three MTT images at three successive acquisition timepoints. (b) Extraction of the manually segmented MTT lesions (observations) that will be used in the longitudinal metamorphosis estimation. (c) Reconstruction of the metamorphosis-derived normalized residual map (rMap). (d) Overlaying the residual map with the final T2-w image. (e) Automatically thresholding the residual map and detecting the areas of highest change (in pink) –superimposed with final T2-w image.

sition timepoints. We also would like to point out that we did not use equation 7.1 without the L^2 norm to generate the thresholded residual map so that we restrict our analysis on immediate change from acute (at t_1) to final dead tissue (at t_3) without looking into the intermediate change that is governed by many unnknown variables and pathophysiological 'laws'. Comparing only the first to final tissue states is a common clinical assessment routine. We used it to shed light on the thresholded residual map.

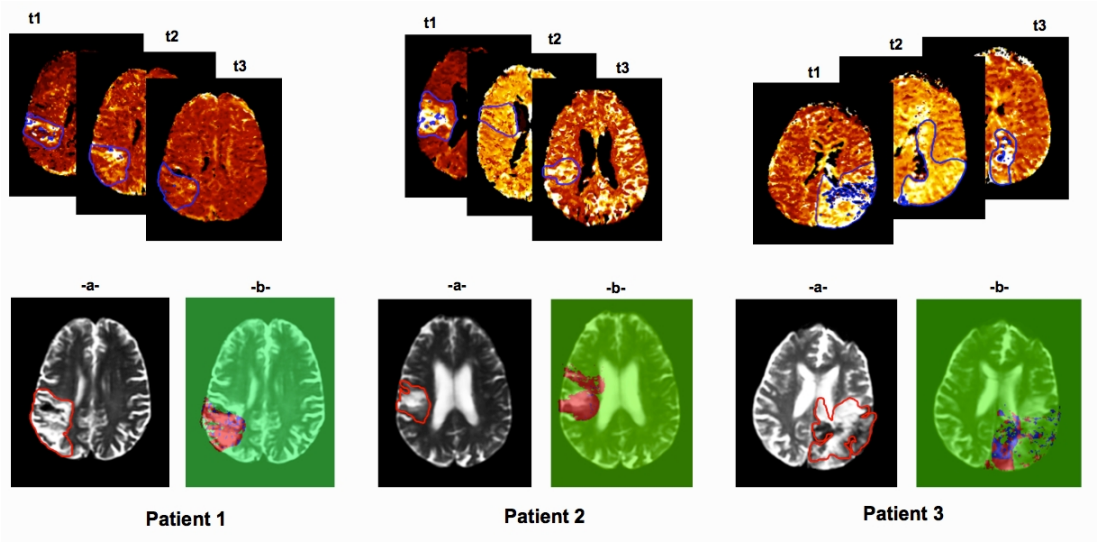

Figure 7.3: *Signed thresholded residual maps in three representative patients.* Top row: same axial slices of MTT lesion (outlined in blue) at three successive acquisition timepoints for three patients. Bottom row: (a) the final T2-w image where the final dead tissue is manually outlined in red. (b) Signed thresholded residual map (red color for positive values and blue color for negative values) overlaid with final T2-w image. Both images (a) and (b) represent the same axial slice.

7.3.3 Exploring the predictive potential of MTT maps using metamorphic residual maps

There exists a wide variation between patients in the total volumetric overlap between the thresholded metamorphic residual map and final T2-w lesion between patients (mean = 45.4%, standard deviation = 28% median = 32.8%). Positive skewness (Figure 7.4, box 1) suggests that most patients deviate from the median with a wider range of volumetric overlap. This shows that the thresholded residual map marking abnormal perfusion areas with highest change in shape and intensity identifies relatively large dead areas within the T2-w lesion.

The most dynamic part of PWI lesion where perfusion was improving (*ie* negatively signed thresholded residual map) overlapped with the final T2 volume with (range from 0 to 67%, mean = 26.1%, standard deviation = 19.3%, median = 17.1%) in our cohort. This shows that the acute-subacute improvement of the hemodynamics of the abnormal perfusion area does not imply that it will certainly end up outside the final T2-lesion. The negative overlap was evenly split at the median of the data (ie. zero skewness, Figure 7.4-box 2). Only Figures 7.4-box 2 and 7.3 show that the majority of areas in the $rMap_{thresholded}$ are positively signed (red areas Figure 7.3), *ie.* with worsened blood flow. This indicates that the thresholded residual map contains areas whose MTT values increased from t_1 to t_3, thus, identifying areas that are more likely to shift into an irreversible state

of tissue death.

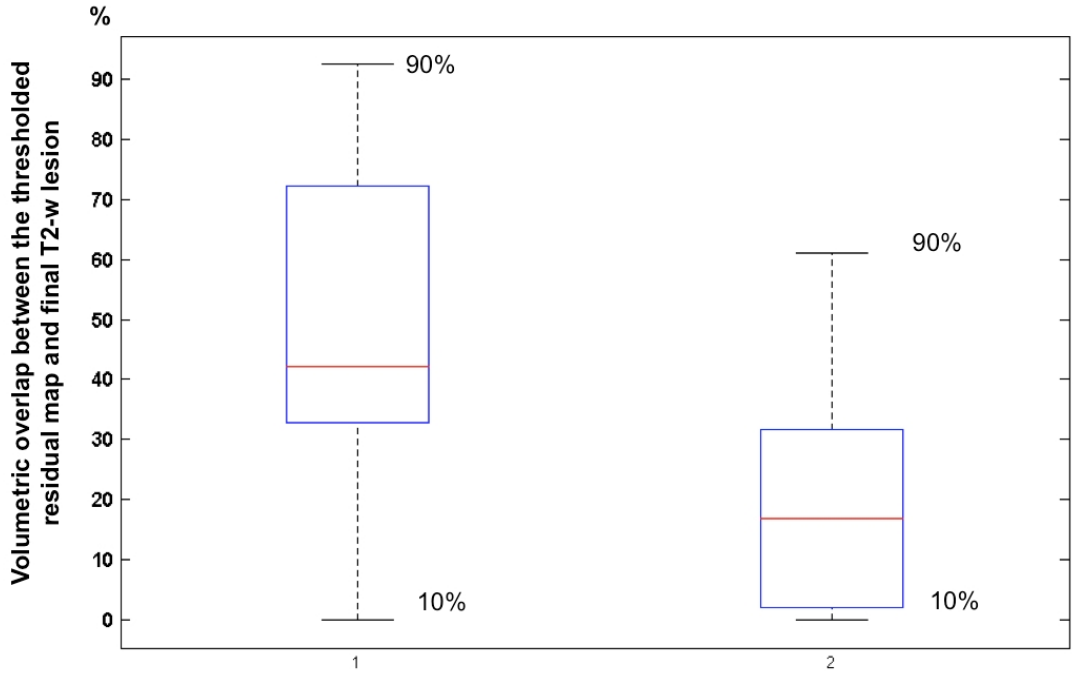

Figure 7.4: Boxplot illustrating the skewness in our cohort for the volumetric overlap between thresholded metamorphic residual map ($rMap_{thresholded}$) and final T2-w lesion (box 1). Box 2 shows the distribution of the volumetric overlap between negatively signed $rMap_{thresholded}$ and final T2-w lesion. The red line represents the median value of the volumetric overlap. The lower boundary of the blue box represents the 25 percentile and the upper bound represents the 75 percentile. The upper (vs. lower) horizontal line denotes the 90 (vs. 10) percentile.

7.4 Discussion

In the present work, we developed a longitudinal metamorphosis that goes exactly through the true observations and applied it to ischemic stroke using longitudinal perfusion data from acute to subacute stages. This provided us with a robust and sophisticated mathematical tool to extract both dynamic and intensity features of the

perfusion abnormality summed up in the estimated residual map of its intensity variation and shape deformation. We then used a static T2-w image at ≥ 1 month to read the reversibility of the metamorphic residual of perfusion abnormality evolution. The aim of this prospective application was to evaluate the hemodynamics of acute ischemic stroke differences in cerebral perfusion seen on time-series MTT images and identify the degree of dead/survived tissue in hypoperfused areas that underwent most shape and intensity variation in the expectation that a) these tissues would have been exposed to the largest differences in perfusion values and b) the values would be consistent between tissues that were behaving in the same way.

Using the automatically thresholded residual map, we showed that the amount of variation in MTT lesion shape and intensity identified a large portion of tissue that is irreversibility damaged. Thus, the MTT map showed promise for identifying dead tissue margins and tissue that survived, although there was substantial variation in the individual perfusion values. This means that it is difficult to identify any one MTT value that can be used to differentiate tissue destined to die from tissue that will survive across a range of patients as it is the dynamic properties of the MTT lesion that seem to determine tissue fate. The present model could be used to tailor more sophisticated models to predict areas that proceeded towards infarction and others that reversed using the estimated evolution of MTT lesion in both

shape and intensity or to examine other external factors that may influence ischemic lesion outcome such as blood pressure change or pharmacological treatment.

The signed residual maps showed that most of the perfusion abnormal tissue that underwent an increase in MTT values (with positive $map_{\Delta_{MTT}}$ values ie. worsening of blood flow) belonged to the final T2-w boundary. However, some portions (negative overlap: mean = 26.1%, standard deviation = 19.3%) of the acutely ischemic tissue whose MTT values decreased (ie. better blood flow) ended up as dead tissue. This highlights the potential for most active positive residuals to be used in further predictive models to identify the boundaries of the final dead tissue.

There was no single threshold for rMap that fitted all patients. Patient-specific thresholds were automatically defined using the metamorphic residual maps. These thresholds involved both variation in MTT perfusion values and lesion shape change as the lesion evolved $[t_1, t_3]$ – showing that the evolution of ischemic but still viable tissue is patient-specific. This is consistent with observations in a recent review paper [Dani 2012] which was not able to identify a specific threshold or even a specific range of perfusion values that would clearly discriminate the fate of tissue. Our method may have allowed us to capture some of the highly dynamic nature of perfusion values in individual parts of ischemic lesions for the first time in humans,

as for example have been shown in experimental models following spreading depolarizations [Strong 2007]. This points towards a new way of looking at perfusion values in stroke to map lesion changes while circumventing the need for 'universal' perfusion thresholds to identify at risk of infarction, dead and oligaemic tissue (see Chapter 4) [Rekik 2012a].

In our study, we demonstrated that the estimation of longitudinal metamorphic residual maps is a promising tool in tracking the spatiotemporal changes in both lesion shape and intensity. This overcomes the major limitations of the commonly used 2D or 3D voxel-based or volume-subtraction methods that do not allow the estimating of dynamic characteristics of lesion progression or regression [Beaulieu 1999, Wittsack 2002, Kluytmans 2000, Karonen 2000, Rekik 2012a]. Our model is fully automated and does not require any manual landmark matching. It is also generic so could be applied to other medical applications based on serial imaging.

Our study has some limitations. Perfusion lesions are heterogeneous: the values vary between gray and white matter [Koga 2005]. Grey and white matter segmentation were not performed in our longitudinal metamorphosis model –instead we considered the lesion in a volume of tissue and mapped point to point changes, as there are as yet no good methods for segmenting ischaemic grey and white matter visible on DWI- or FLAIR- or T2-w as the ischaemic signal change

distorts the segmentation algorithms. We also visually checked that the recruited patients did not have large amounts of lesion swelling (ie. mass effect) that could be misleading in computing the volume of the final dead tissue. However, accounting for the swelling and late stage ex vacuo effect using more sophisticated registration algorithms would increase the accuracy of our results and therefore the soundness of their interpretations. Our sample size was small – we chose these 10 patients to illustrate a range of lesion morphologies and changes over time to illustrate that the method was feasible and determine its potential for displaying dynamic stroke lesion pathophysiology. It was not our intention to provide definitive perfusion values or to examine how, for example perfusion values might influence diffusion values, or the impact of clinical variables. This would be for future work in larger datasets.

Several longitudinal studies have previously evaluated lesion evolution using standard thresholding and volumetric analysis techniques [Beaulieu 1999, Karonen 2000] to assess the combined role of perfusion or diffusion lesion in determining the degree of tissue survival or death. However, they did not explore the dynamic characteristics of lesion boundary evolution and their relation to its hemodynamics. A recent study [Carrera 2011] noted that MTT perfusion values –outside and also within the DWI lesion– could be used to improve the identification of final infarct boundary. Two different perfusion thresholds

were distinctively identified for two different datasets. In our study, we showed that perfusion values and spatiotemporal changes from acute to later stages are patient-specific and not dataset-specific. We also showed that, without reference to diffusion images, changes in acute and subacute perfusion abnormality might contribute to identifying final dead tissue. However, we also pointed out that acute-subacute areas with early improvements in perfusion could end up in the final T2-w lesion. This shows that using perfusion values and tracking their final to late changes is unlikely to be sufficient to determine with utmost precision ischemic tissue fate.

Identifying the shift in tissue abnormality, from being 'reversible' to being 'irreversible' in both space and time, is still one of the main challenges in stroke. The emergence of methods for dynamic modelling in stroke research shows potential for advancing our understanding of ischemic tissue dynamics. The key to a nuanced understanding of how perfusion values influence the spatial extent of tissue that will ultimately die or survive lies in refining the perfusion hypothesis [Butcher 2005]. This hypothesis states that abnormal perfusion areas where blood flow improved between acute and subacute stages will recover and those where blood flow worsened have the greatest likelihood to be irreversible. However, while this may be generally true, we have noticed in our study that there is substantial variation in perfusion values in space and time that limit use of specific perfusion values

in prediction of tissue fate. Exposing the 'laws' that govern the hemodynamics of stroke would revolutionize stroke research. This may be achievable by using a more sophisticated version of longitudinal metamorphosis (eg: by including tissue heterogeneity or other perfusion parameters) that we have demonstrated is now feasible.

7.5 Conclusion

In this chapter, we applied the longitudinal metamorphosis to track the evolution of the perfusion abnormality in stroke using time-series imaging. This model provided novel ways to identify the most active changes in ischemic lesion hemodynamics using signed residual maps. We believe this will be valuable in future stroke research to clarify what determines ischemic lesion evaluation and identify new potential targets for development of new treatments to improve clinical recovery.

Perfusion values are not sufficient to determine final tissue fate, as they do not inform us about other factors driving infarct evolution such as the swelling. Examining the spatiotemporal changes of the diffusion lesion and its relation to directional change of the perfusion values will give us a new angle on the 'nature' of stroke dynamics. That is the main goal of the next chapter.

Chapter 8

Metamorphosis clinical application II to diffusion-weighted and T2-weighted MR images of stroke lesion

---

Contents

8.1 Context

As the work in this thesis unfolds, we obtain a better understanding of the relationship between spatiotemporal changes in the perfusion and the diffusion lesion as we introduce more sophisticated modeling tools and measurement techniques. Our preliminary results in Chapters 5 and 7 highlighted the wide variability in perfusion and diffusion lesion behavior as we first displayed in Figures 3.5, 5.11 and 5.12. However, the main factors that determine tissue outcome after ischemic stroke in the individual patient remain elusive. In this chapter, we use the metamorphosis model to examine in depth the questions we raised in the introduction (Chapter 1): What factors influence stroke lesion evolution? Can a unique perfusion threshold fit a whole population of stroke patients and distinguish between dead and at-risk tissues or is one threshold too simplistic?

As the growth of the lesion core is generally thought to be dependent on perfusion values around the core, we attempt to answer these questions by exploring the relationship between dynamic features of DWI lesion evolution and static perfusion values at different timepoints.

The aims of this chapter are to:

1. Model the change in the acute diffusion lesion from the earliest imaging timepoint into the final T2-w lesion, for both solitary and multi-component lesions.

2. Extract dynamic features to explore stroke evolution hypotheses as proof of principle:

   (a) are areas of rapid lesion expansion or contraction also areas where PWI values are changing rapidly?, and

   (b) are highly contracting or expanding areas of the DWI lesion influenced by clinical features (eg: age, National Institutes of Health Stroke Scale (NIHSS), acute stroke lesion size (PWI or DWI volumes)?.

3. Further determine limitations of this approach and potential for exploring tissue-level factors that influence stroke lesion dynamics.

8.2 Data acquisition

Patients recruitment: We tested the metamorphosis model on 20 representative patients from a prospective study ([Rivers 2007]) of MR imaging in hyperacute stroke patients, chosen to represent a range of stroke severity (NIHSS, from 4 to 27, mean = 11.35), age (from

51.7 to 94 years, mean = 74.9), acute DWI volume (mean = 34.6 cm^3) and acute mean transit time (MTT) volume (mean = 126.6 cm^3). We used the MTT perfusion map to represent the PWI lesion as MTT is easily obtained and generally shows the PWI lesion as large.

We included patients who had DWI images at acute ($\sim$ 5hrs) and subacute ($\sim$ 5 $\pm$ 1 days) acquisition timepoints, an MTT map at least at the acute timepoint and T2-weighted image lesion at $\geq$ 1 month after stroke. Twelve patients had scattered DWI/MTT lesions and eight had solitary lesions. All patients had an MTT lesion at the first timepoint but only 12 had an MTT lesion visible at the second acquisition timepoint. In the included patients, we have checked that tissue swelling did not severely distort the DWI lesion boundary. The included patients did not receive any thrombolytic treatment, thus we present here the 'native' stroke lesion changes. The model was blind to all clinical data.

MR preprocessing steps: We used the same MR acquisition and preprocessing steps as in Chapter 5 Section 5.4.1 for more details. Furthermore, we generated for each patient relative MTT (rMTT) lesion maps by dividing the value of each lesion voxel by the mean perfusion value of the region contralateral to the MTT lesion. The resulting intensity rMTT has no unit.

8.3 Methods

8.3.1 Two-image based metamorphosis

The idea of metamorphosis is to morph one source 3D image into a target image by estimating the shortest path connecting each point on these two images. The metamorphosis model estimates both an intensity evolution path of the time-evolving lesion and a deformation path of the changing shape in finely discretized time and space intervals. In the present chapter, we applied the longitudinal metamorphosis model to two different phases of DWI lesion evolution:

1. we morphed DWI lesion at t1 (acute) to the DWI lesion at t2 (subacute) (phase 1) in 20 patients;

2. we morphed the subacute DWI lesion into the final T2-w at ≥ 1 month (phase 2) in 12/20 patients.

Retaining these two phases facilitated testing of acute separately from subacute clinical information against the lesion parameters. For each of these phases, in each patient we generated a total 3D deformation map (computed as the squared sum of the estimated speed along the metamorphosis path) and were able to identify contracting (negative deformation values) and expanding (positive deformation values) DWI regions during each phase Figure 8.1.

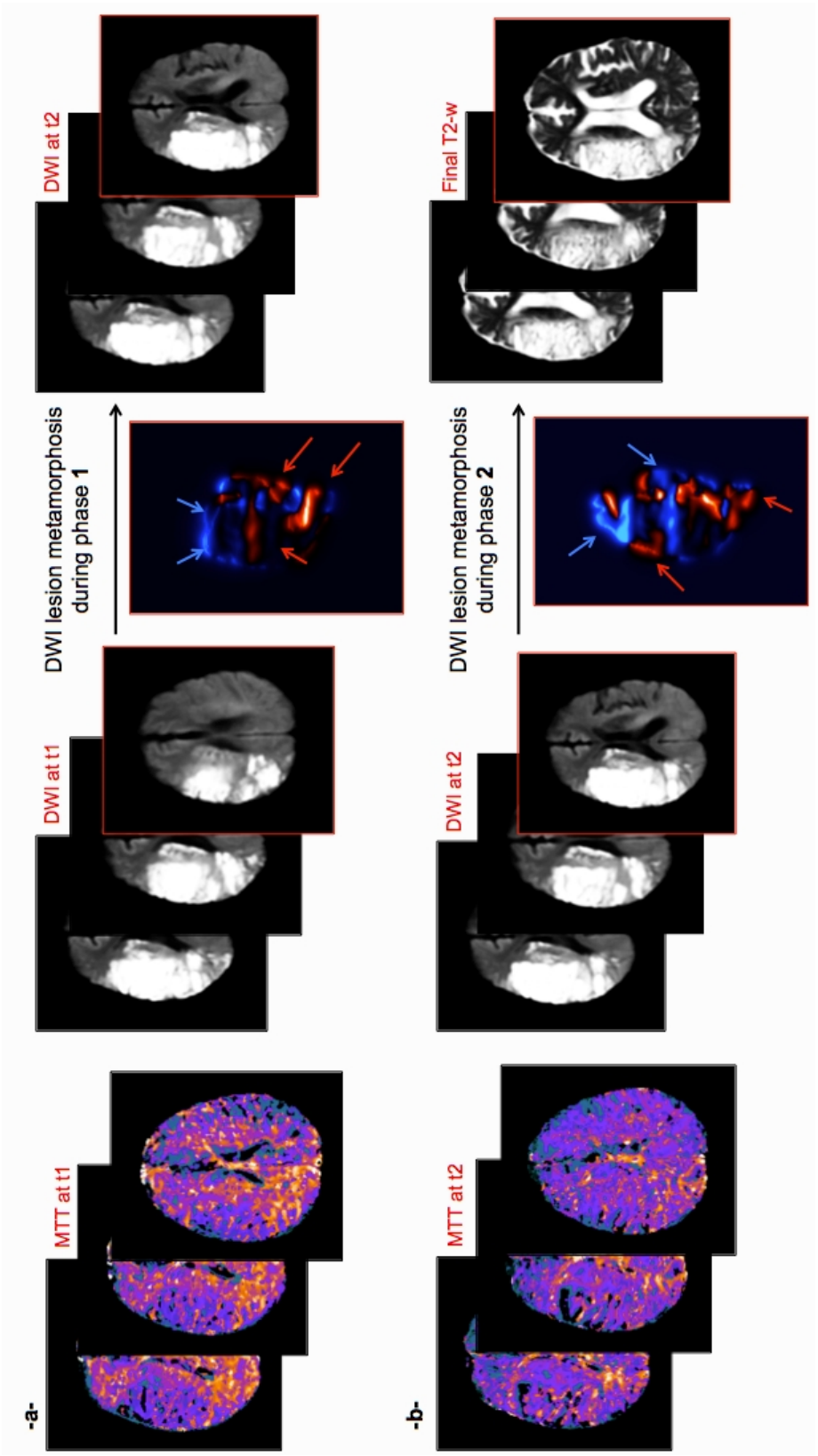

Figure 8.1: (a) Axial slices of acute MTT image (left), acute DWI image (middle) and subacute DWI image (right). (b) Axial slices of subacute MTT image (left), subacute DWI image (middle) and final T2-w image (right). During phase 1, we metamorphose DWI lesion at t_1 to DWI lesion at t_2. During phase 2 we deform the latter into final T2-w lesion. We estimate the deformation maps for phase 1 and phase 2 of DWI lesion evolution (images under the black arrows). The red arrows point to highly expanding areas and blue arrows point to highly contracting areas.

8.3.2 rMTT values relation to DWI lesion dynamics

We used the estimated deformation map associated with phase 1 to compute the mean of the DWI contraction magnitude and the mean of the DWI expansion magnitude for every acute rMTT value within the acute perfusion image. Then, for each of the twenty patients, we plotted the acute rMTT values against both their corresponding mean DWI contraction and expansion magnitudes (Figure 8.2). For phase 2, we used the deformation map of subacute DWI lesion deforming into final T2 and the subacute rMTT values for the twelve patients with a visible MTT lesion at t_2. In most cases, the acute rMTT values associated with the mean of phase-1 DWI deformation magnitude best fitted into a Gaussian distribution (Root-mean-square deviation (RMSE) = 0.0035 ± 0.0042 for contraction and 0.006 ± 0.014 for expansion –noting that when the fitting is exact RMSE = 0 (no residuals = perfect test)).

For phase 2, the data also best fitted into a Gaussian distribution (RMSE = 0.0029 ± 0.0032 for contraction and 0.0039 ± 0.0058 for expansion). Therefore, we used two Gaussian curves to approximate the relation between acute rMTT values and mean DWI deformation magnitude: one for contraction (purple curve in Figure 8.2) and one for expansion (pink curve in Figure 8.2). These Gaussian curves allowed us to estimate a confidence interval (I = [p1, p2]) for rMTT

values associated with rapidly changing (ie. contracting or expanding) DWI tissue. The upper bound p1 is the mean of the Gaussian curve minus its standard deviation and the lower bound p2 is the mean of the Gaussian curve plus its standard deviation.

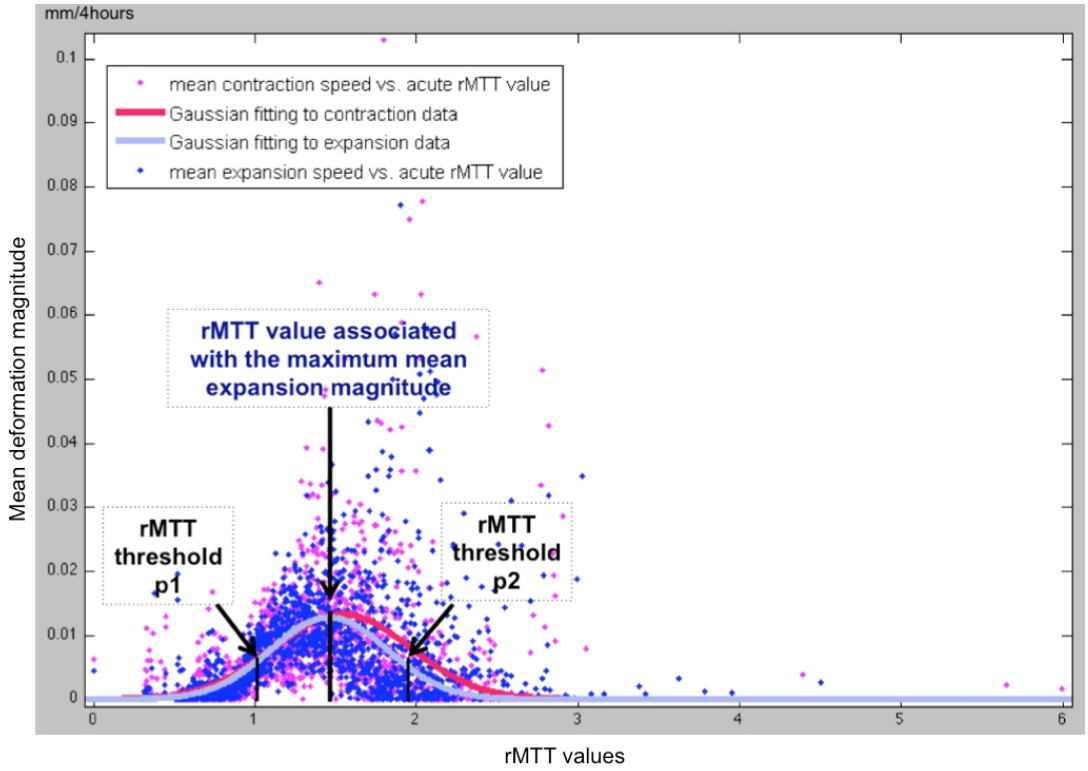

Figure 8.2: Distribution of perfusion values and the magnitude of the metamorphic deformation during phase 1 of DWI lesion evolution for one patient. rMTT values plotted against the mean magnitude of DWI metamorphic deformation magnitude associated with every perfusion value in the MTT map: blue dots for contracting (vs. pink for expanding) DWI areas. Each dot stands for an rMTT value in the PWI images. The mean of the fitted Gaussian curve (purple line) depicts the rMTT value associated with the maximum mean contraction magnitude and the pink line fits into the pink dot distribution. The black arrows point to the perfusion thresholds p1 and p2 representing the mean $\pm$ standard deviation of the fitted Gaussian curve.

8.3.3 Extracting highly dynamic regions of DWI lesion

We first define two key regions for our analysis:

Region R1: includes voxels in the DWI lesion at t_1 and t_2 and PWI lesion at t_1.

Region R2: includes voxels in the DWI lesion at t_2, final T2-lesion and PWI lesion at t_2.

We automatically thresholded the two total deformation maps generated for phase 1 and phase 2 of DWI lesion evolution to extract regions with high contractions and expansions. We defined high contractions as areas whose deformation magnitude exceeded the mean of the contraction speed over region R1 minus its standard deviation and high expansions as areas whose deformation magnitude exceeded the mean of the expansion speed over region R2 plus its standard deviation. These thresholds only depend on the estimated deformation map and on the R1 and R2 boundaries. We automatically set these thresholds to high values to focus on portions of the diffusion abnormality that underwent the most significant dynamic change. We also computed the volumetric proportion of the highly contracting or expanding areas in the regions R1 and R2 with respect to total DWI lesion volume.

8.3.4 Statistical analysis

We tested the difference between perfusion values in highly contracting/expanding DWI areas. We also performed an exploratory 'proof of principle' analysis to test the correlation between the clinical factors (NIHSS at admission, age, acute MTT and DWI volumes) and the center of the estimated rMTT confidence interval for highly contracting/expanding DWI areas using non-parametric statistic Spearman method. We also tested the correlation between NIHSS at admission and the proportion of the lesion by volume that was highly contracting or expanding separately for phase 1 and phase 2 with the Spearman method.

8.4 Experiments and results

8.4.1 Lesion metamorphosis and perfusion values: acute to subacute (phase 1)

The estimated confidence intervals for the acute rMTT values associated with DWI lesion deformation are shown in Figure 8.3, with the lower and the upper bounds for acute rMTT values associated with rapidly contracting (blue) and expanding (red) areas of the DWI lesion from acute to subacute times.

For the largest areas of DWI contraction, the rMTT maxima ranged from 0.68 to 3.05 (mean = 1.49 $\pm$ std 0.55); while the range

of rMTT values in contracting regions varied from 0.1 to 2.17 (mean = 0.74 ± 0.63). A similar range of rMTT maxima was noted for the highest DWI expansion: from 0.24 to 3.07 (mean = 1.37 ± std 0.62); and an even wider range of rMTT values was sen in DWI expanding areas from 0.1 to 3.18 (mean = 0.8 ± 0.82). Thus, for the whole population, the perfusion values for highly expanding and contracting DWI areas were nearly identical (correlation coefficient r = 0.86, p = 0.8) (Figure 8.2), ie there was no disparity (r = 0.86) between rMTT intervals corresponding with highly expanding or contracting regions in most patients, as both red and blue verticals bars overlapped (Figure 8.3). Only in five of the 20 patients (25%) were blue and red vertical bars distinct indicating that acute perfusion values differed between areas of DWI contraction and expansion (Figure 8.3). In some cases (7/20 in Figure 8.3), the red bars extend over the blue ones indicating that perfusion intervals associated with most rapidly expanding DWI areas encompass a wider range of acute MTT perfusion values than they do in areas of DWI contraction.

8.4.2 Lesion metamorphosis and perfusion values: subacute to late (phase 2)

We plotted the estimated subacute rMTT confidence intervals for the 12 patients with MTT lesion visible at t2 in phase 2 of the DWI metamorphosis (Figure 8.4). We saw the same overall patterns (r

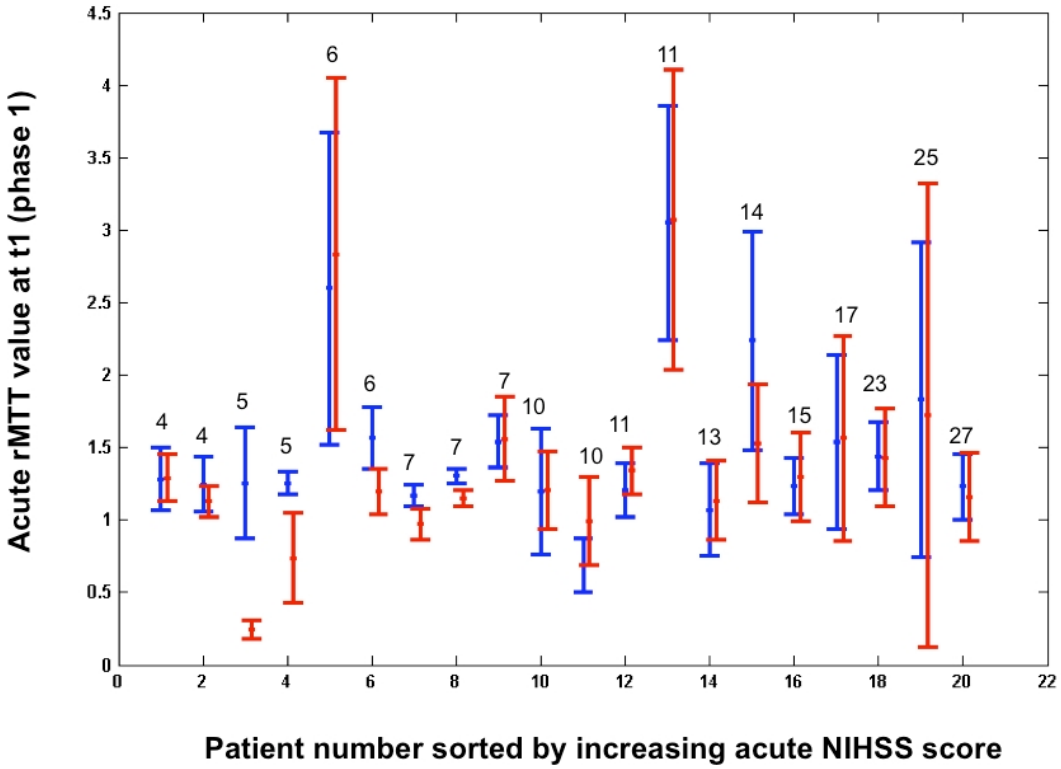

Figure 8.3: Acute rMTT values associated with rapidly deforming DWI lesion areas graphed for all patients –ordered left to right by increasing admission NIHSS score (values on top of the vertical bars). The centre dot = rMTT value associated with the maximum of DWI lesion mean deformation magnitude. The limits of the vertical blue and red bars represent the lower and the upper 95% CI for the acute rMTT values associated with rapidly contracting (blue) vs. expanding (red) DWI lesion areas between the acute and subacute timepoints.

= 0.91, p = 0.8) as for the acute to subacute phase (Phase 1). A wide range of rMTT maxima was found in areas of high DWI lesion deformation towards final T2-w: ranging from 0.85 to 2.12 with (mean = 1.36 ± 0.47) for high contractions with rMTT bar lengths ranging from 0.08 to 1.82 (mean = 0.75 ± 0.6) and from 0.73 to 2.02 (mean = 1.33 ± 0.41) for high expansions with rMTT bar lengths ranging from 0.07 to 1.97 (mean = 0.73 ± 0.6). This indicates that a) DWI lesions are still progressing into some areas and regressing in others and b) perfusion remains very variable at the subacute stage.

In 3/12 cases (25%), subacute rMTT intervals did not overlap indicating that perfusion values associated with contracting DWI areas are disparate from perfusion values associated with expanding DWI areas. In two other cases, red bars exceeded both limits of blue bars indicating a wider range of PWI values in expanding areas compared with contracting areas.

8.4.3 DWI dynamic evolution features

The proportion of highly expanding and contracting areas within volume R1 in phase 1 and volume $R2$ in phase 2 are shown in Figure 8.5 as box and whisker plots. These boxplots show that less of the DWI volume is in a highly dynamic state at the subacute stage than at the acute stage. They also show a wider variability in DWI volume undergoing a high dynamic change during phase 2 than phase 1.

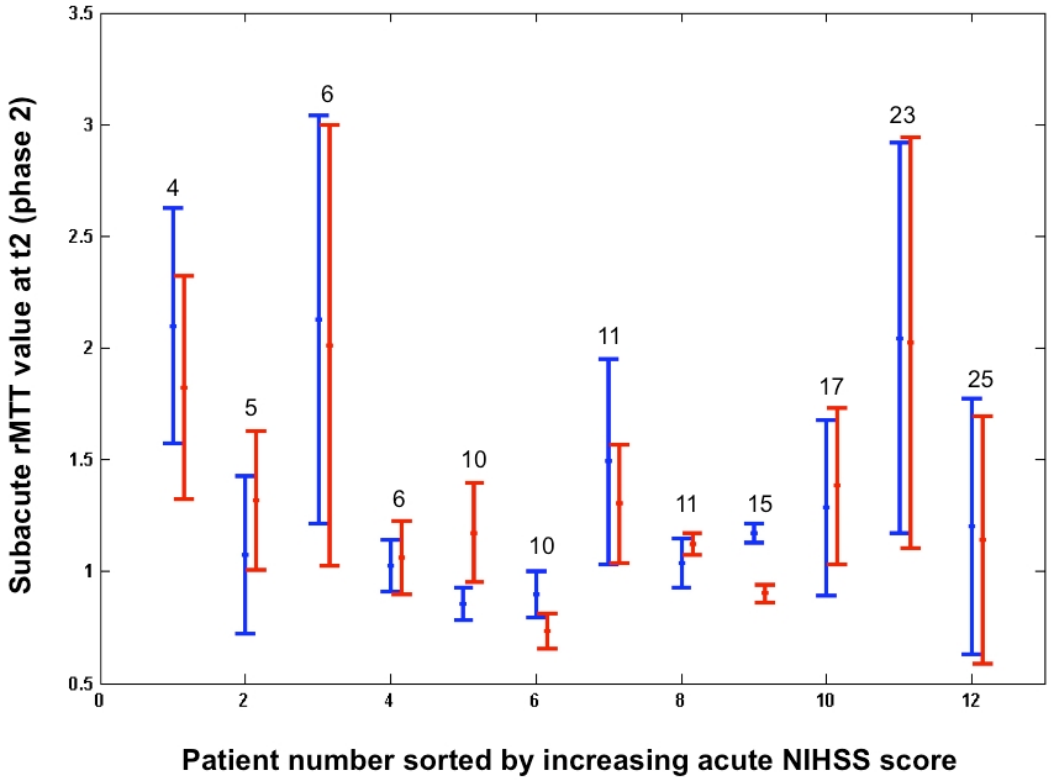

Figure 8.4: Subacute rMTT values associated with rapidly deforming DWI lesion areas graphed for all patients –ordered left to right by increasing admission NIHSS score (values on top of the vertical bars). The centre dot = rMTT value associated with with the maximum of DWI lesion mean deformation magnitude. The limits of the vertical blue and red bars represent the lower and the upper 95% CI for the subacute rMTT values associated with rapidly contracting (blue) vs. expanding (red) DWI lesion areas between the sucabute and late timepoints.

During phase 1, 55% of the patients had more volumetric portions of highly expanding DWI areas than were contracting. The percentage of contracting volume ranged from 0.28% to 9.09% with median = 3.39% *vs.* expanding from 0.36% to 12.61% with median = 4.38%. During phase 2, 55% of the patients still had more volumetric portions of highly expanding DWI areas than were contracting. The percentage of contracting volume ranged from 0.33% to 7.98% with median = 3.25% and of expanding volume varied from 0.42% to 14.95% with median = 3.69%. This indicates that subacute DWI lesions include some abnormal brain tissue that rapidly reversed to a normal state (ie. DWI lesion contracted). It also shows that the subacute diffusion lesion continues to expand rapidly in some areas and to contract in others in quite similar proportions, even late after stroke.

8.4.4 DWI metamorphosis and clinical features

During phase 1, there was no association between rMTT values in the most expanding areas of the DWI lesion and NIHSS ($r = 0.11$, $p = 0.63$) or in the most contracting areas ($r = 0.06$, $p = 0.77$). Similarly, during phase 2, there was no association between NIHSS and subacute rMTT values in rapidly contracting ($r = 0.007$, $p = 0.99$) or expanding ($r = -0.021$, $p = 0.95$) DWI lesion areas. The lack of association may reflect small sample sizes.

We investigated the association between the volumetric proportion

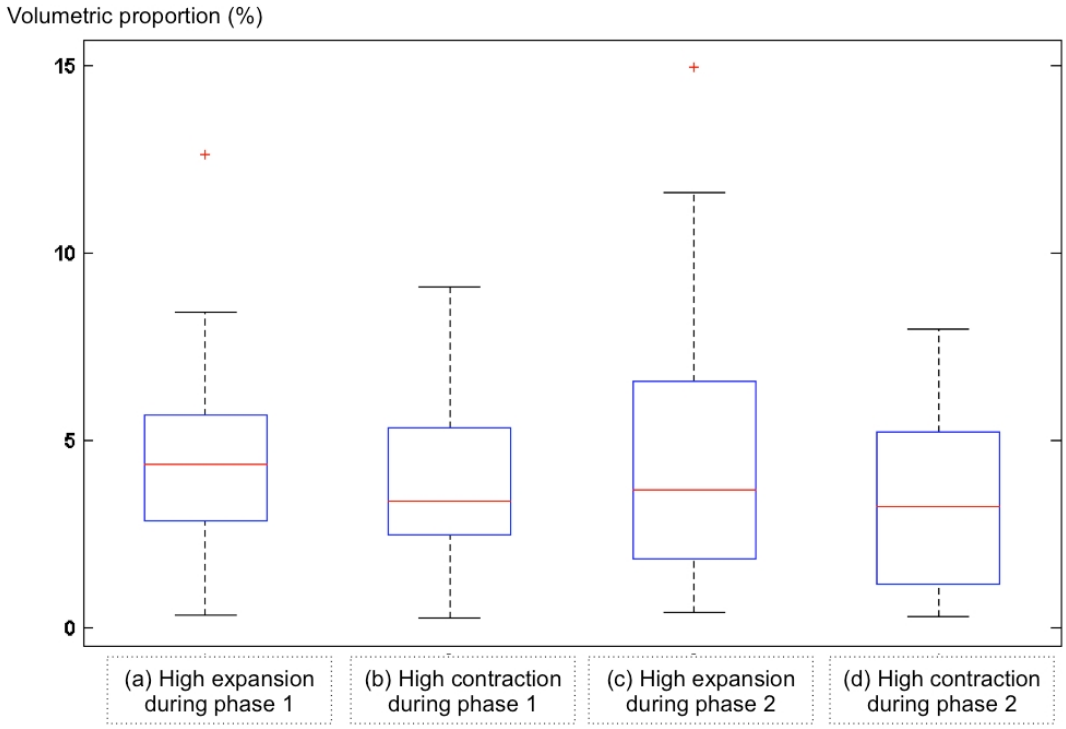

Figure 8.5: Boxplots illustrating the different skewness patterns in our cohort for the volumetric proportion (in%) of highly expanding/contracting areas within the region $R1$ (*vs.* $R2$) during phase 1 (*vs.* phase 2) of metamorphosis. $R1$ includes all bits of DWI lesion at t_1 and t_2 and PWI lesion at t_1 and $R2$ includes all bits of DWI lesion at t_2, final T2-lesion and PWI lesion at t_2. The red line represents the median value of the volumetric overlap. The lower boundary of the blue box represents the 25 percentile and the upper bound represents the 75 percentile. The upper (*vs.* lower) horizontal line denotes the 90 (*vs.* 10) percentile. The red crosses denote the 'outlier' values, outside the 90 percentile.

that was highly contracting/expanding during phase 1 and phase 2 and various clinical factors (NIHSS at admission, age, acute MTT volume, acute DWI volumes), but found no significant correlations. There was no obvious significant correlation between these clinical features and the dynamic signature of the abnormal diffusion tissue behavior in our small cohort.

8.5 Discussion

We applied the promising dynamic metamorphosis model –developed in Chapter 6– to model ischemic stroke using acute and subacute DWI, final T2-w and rMTT images. This provided us with a robust and sophisticated mathematical tool to visualize and extract dynamic features of the ischaemic lesion, such as the magnitude of the contracting and expanding DWI lesion and the most dynamically changing volumetric proportions of the DWI lesion. In our heterogeneous small but representative sample, we showed that (i) dynamic changes in diffusion lesion are not confined to the first few hours after stroke onset but continue for days or weeks with highly variable perfusion values, (ii) similar perfusion values are associated with large lesion shape deformations from acute to subacute timepoints but do not discriminate whether the deformation is contraction or expansion and (iii) there is a large variation between patients in DWI lesion dynamics and in the range of perfusion values in DWI lesion areas that

undergo the largest deformations.

This suggests that PWI values are far more dynamic and heterogeneous than has been suggested by analysis of DWI and PWI using regions of interest analysis so far and that it is unlikely that any threshold value will differentiate dead from survived or at-risk from not at-risk tissue with any precision at any one point in time. There is growing recognition of the heterogeneity of PWI values between different tissues and between patients influenced by age, underlying brain changes such as leukoaraiosis, spreading depolarization that affect perfusion levels, etc. A recent study [Nagakane 2011] introduced the idea of perfusion 'strata' to produce infarct risk maps. This shows that perfusion influence on DWI lesion dynamics cannot be fully investigated using a unique perfusion threshold: our results suggest that perfusion strata (or confidence intervals) might be more biologically relevant than single values.

Our study has some limitations. We used a small cohort but our purpose at this stage was to demonstrate the feasibility and strengths of the metamorphosis modeling approach. We found wide variability in perfusion values of highest DWI lesion dynamics, but our sample lacked statistical power to exclude associations between lesion behavior and clinical factors. Thus, we suggest that this method should be applied in larger datasets and different perfusion parameter maps could be explored.

The absence of a clear correlation between perfusion values of DWI lesion areas with high dynamics shows that DWI lesion progression or reversal may be governed by other unknown factors. The effects of occlusion site, collaterals, the heterogeneity of ischemia evolution in altering DWI lesion dynamics and the effect of rMTT levels and confidence intervals could be examined in future studies.

Our study also had strengths. We were careful to avoid the effects of swelling on lesion shape in our cohort, therefore any contracting DWI areas during phase 2 (DWI at t_2 evolving into final T2-w) would indicate diffusion abnormality reversal and any expanding DWI areas would indicate the new recruitment into the tissue. Therefore, deformation maps that identify these areas (Figure 8.1) would be useful in determining DWI lesion reversal and subsequent tissue recovery. Recruited patients did not receive thrombolysis so these changes represent the 'natural' lesion evolution and still demonstrate high variability.

The estimation of metamorphosis-derived deformation maps that indicate rapidly contracting/expanding areas using the longitudinal metamorphosis model gives us insights into the diffusion lesion dynamics and provides opportunities to tailor more sophisticated approaches to stroke lesion analysis. Furthermore, the longitudinal metamorphosis model is fully automated and does not require any manual landmark matching to estimate lesion shape metamorphosis.

As we show here, ischemic stroke evolution modeling is also able to handle a set of representative cases. These novel dynamic tools presented in Chapters 5 and 6 may help in interrogating factors governing diffusion core reversal and provide more sophisticated surrogate outcome measures for use in clinical trials of new treatments.

Dynamic models may fill gaps in the understanding of stroke evolution dynamics, and explain the lack of consistency between past studies [Dani 2011] and overcome problems with commonly used basic thresholding techniques in stroke [Rekik 2012a] (See Chapter 4).

8.6 Conclusion

Although stroke lesion evolution is very challenging and complex, we were able to define new features that were more encompassing and accurate (eg: speed of lesion contraction and expansion, residual and deformation maps) characterizing its spatiotemporal behavior as seen on DWI, PWI and T2-w images. Our aim was not to find clear-cut answers to the questions we raised in the Introduction of this thesis (Chapter 1), but rather to identify consistent observations in stroke lesion evolution using different 4D modeling approaches and propose tools that can be used in future studies on stroke. This presented work can be viewed as a promising 'take off' towards the development of more patient-specific and stroke-specific 4D models that would combine other clinical features not considered in this thesis.

Indeed, our preliminary results presented in this chapter direct investigations in stroke dynamics down new lines, such as (i) developing further models based on patient-specific and phase-specific perfusion intervals to predict the evolution of infarct core towards its final fate, (ii) identifying particular modes of contraction and expansion in the DWI lesion dynamics and (iii) exploring the role of perfusion values inside and outside diffusion lesions in modulating these modes. This may provide a more nuanced understanding of how perfusion intervals are likely to influence diffusion lesions towards different fates. This will be discussed with more detail in the final chapter of this thesis (Chapter 9) as we discuss the major results of the different modeling approaches, their key limitations and present new perspectives to address issues of stroke lesion pathophysiology.

We hope that this work stimulates interest in addressing issues of stroke lesion pathophysiology by exploring 4D models. These could have wide applications eg to assess early treatment response in early phase clinical trials. A similar approach could be used to model hematoma growth or development of white matter hyperintensities and effects of interventions. This model can be applied to any imaging modality where lesions are visible, eg CT or PET, as well as MR imaging.

Part V
Conclusions and Perspectives

"*I argue that science is being held back by centuries-old assumptions that have hardened into dogmas. The sciences would be better off without them: freer, more interesting and more fun.*"

Rupert Sheldrake; Science Delusion

Chapter 9

Conclusions and perspectives: A look back a look ahead

Contents

In this thesis we linked dynamic modeling approaches to stroke lesions on medical imaging. We have built our research on two different mathematical models which were shown to be suitable for capturing the dynamics of stroke lesion evolution using longitudinal data. Both the applied current-based diffeomorphic regression model and the developed longitudinal metamorphosis model were novel to the state of the art of stroke data. We then demonstrated the ability of these patient-specific models to simulate the evolution of stroke lesions in space and time using representative clinical data. This allowed us to

extract different patient-specific kinetic and hemodynamic features and to investigate these questions: "How does a stroke lesion evolve in perfusion and diffusion longitudinal data? What does perfusion and diffusion data tell us about the ultimate fate of the ischemic tissue?"

This thesis does not provide a clear-cut answer to these questions. At this stage in development of the modeling, our primary aim was to determine if the modeling would work: identifying patients or stroke-specific influences require much larger data samples. However, the work opens up new vistas on how to address these questions, presents a new set of observations on stroke dynamics and questions some long-standing assumptions in stroke research.

In this chapter, we summarize the contributions of each chapter and extend on some general methodological and clinical research perspectives.

9.1 Contributions

Dynamic modeling is a recent concept that was brought into medical image analysis leading to the emergence of outstanding research fields such as computational anatomy (studying shape variations in anatomical structures) [Gol 1999, Lev 2000, Pizer 2003, Fletcher 2004, Jos 2007, Michor 2003, Mangin 2004] and diagnosis and prognosis of brain diseases (eg: brain gliomas) [Clatz 2005, Konukoglu 2007, Konukoglu 2009, Menze 2011, Rekik 2012b]. More-

over, the ever-growing number of time-series imaging studies and use of imaging to monitor treatment responses raised the need for more sophisticated robust methods to extract and structure relevant information from longitudinal data. This led to the gradual evolution of generic patient-specific models analyzing brain lesions/abnormalities to identify features/patterns relevant to the pathology and investigate the key factors driving their evolution [Younes 2009]. Interestingly, this research line was unexplored in stroke as shown in Chapter 2. Instead of using the 'traditional' approach of basic thresholding and standard volumetric subtraction techniques to examine the evolution of stroke lesion on perfusion and diffusion data, we have tested mathematical modeling of clinical imaging observations at multiple timepoints –which led to the following contributions:

- **Indentifying untapped potentials and unexplored problems in stroke literature from a medical image analysis perspective.** We searched the literature for sophisticated medical image analysis methods and mathematical models to segment at-risk and dead tissue, predict final tissue fate and model the evolution of stroke lesions (Chapter 2). We narrowed down our search margins to identify methods that were innovative, computized and less likely to overlook important issues in stroke progression from its starting point to the final occurred damage. We proposed a research strategy that targeted stud-

ies that approached stroke from a novel modeling and technical perspectives. We then compactly summarized the unaddressed issues and untapped potentials in Table 4.4. We suggested some strategic points to be included in future models to provide more honed answers to challenging questions in stroke research. We believe that our main literature search findings constitute a set of starting points where stroke researchers can head from to develop new tools for stroke assessment. In this thesis, we chose "dynamic modeling using time-series MR imaging" as our starting point.

- **Personalized stroke lesion evolution (constraint: no topology change in the lesion).** We applied the current-based diffeomorphic regression model (Part III) to simulate the evolution of stroke lesion visible on DWI and PWI images from one acquisition time to the next one. The current-based deformation model aims to match the meshes of the acute surface, as they expand or contract, to the meshes at successive timepoints. One of the most remarkable aspects of this model is that it perfectly handles deformation between surfaces with different numbers of meshes at different timepoints. Thus the model can track lesions that expand and contract between timepoints. Moreover, we chose this 4D model because it imputes the evolution of the ischemic lesion down to much shorter time intervals between scans

based on the information available at the few imaging times. To the best of our knowledge, this work is the first that applied a 4D model as proof of principle that would more closely follow the dynamic true changes in stroke lesions between timepoints and thus allow closer scrutiny of what and how patient-related, stroke-related and treatment-related factors influence stroke lesion evolution in future large studies powered to determine modest differences. Therefore we chose eight patients representative of a range of stroke severities, ages and lesion sizes, within the caveats imposed by the modeling at this stage in its development. The model proved to be robust and accurate as it fitted into the multiple observations (lesion surfaces). Any flaw in the underlying equations or differential calculus would have lead to the model failing to fit the data. From a scientific perspective, what makes an applied mathematical model 'perfect' is its ability to fit into the different true observations (in our case the lesion surfaces). The simulation of acute surface evolution starts from the first timepoint and must evolve into the second and then the third surfaces. A dramatic change in the parameters can alter this process, and therefore, the estimated scenario will deviate from the observations. Contrary to most studies that use static snapshots to identify changes in stroke lesion, the 4D current-based regression method enabled us to model how the

lesion shape evolves from acute to final stages and to investigate specific kinetic features of its deformation.

- **Building a 4D model for solitary and scattered perfusion/diffusion lesion evolution with topology change.** In a clinical setting, visual assessment is commonly relied upon to detect changes of stroke over time for appropriate intervention. But there are three critical challenges limiting the scope of this method in stroke management. First, on axial images, it is quite difficult to judge accurately by eye if the stroke lesion has grown or decreased by 20% from one acquisition timepoint to another [Wardlaw 2010]. Second, visual assessment depends on the observer, therefore, leading to subjective conclusions about stroke evolution characteristics. Using a single image that shows to radiologists the main dynamic changes in the stroke lesion and quantifies how fast it grew or regressed and in which areas might overcome these problems and provide detailed information on what factors influence stroke lesion evolution. To address this issue and overcome the main limitations of the 4D current-based regression model, we developed the longitudinal metamorphosis model derived from the metamorphosis theory. We demonstrated the ability of the longitudinal metamorphosis model to provide information on the spatiotemporal variations in stroke lesion shape and intensity in representative patients.

We used the estimated longitudinal lesion metamorphosis scenario to exhibit total deformation (Figure 7.1) and residual maps (Figure 7.2) that extract patient-specific kinetic and geometric features of the lesion displayed on a single MR image. These metamorphosis-derived maps could constitute quantitative metrics of stroke severity and prognosis. To the best of our knowledge, this study is the first that uses time-series MR images to track spatiotemporal geometric and intensity changes in stroke lesions –regardless of their inherent topology –and relate their patient-specific clinical features.

One of the purposes of applying these models to stroke was to obtain greater dynamic insights that these 4D models can provide, rather than just considering a series of cross-sectional brain scans. These modeling approaches were motivated by clinical questions related to stroke dynamics. As a result, the aforementioned methodological contributions was able to examine further the following clinical assumptions about stroke evolution:

- **Perfusion in relation to diffusion abnormality evolution and the concept of PWI/DWI mismatch.** Several clinical trials and treatment strategies used the DWI-PWI mismatch concept for stroke treatment decisions, although validation is incomplete [Barber 1998, Arenillas 2002]

- **What do perfusion values tell us about diffusion lesion dynamics? Can one perfusion threshold discriminate dead from salvageable tissue?** Thresholding methods applied to perfusion and diffusion maps have been extensively used as "prognostic" and therapy-guiding tools and assessed by final T2-imaged and clinical outcomes [Wardlaw 2010, Dani 2012]. Although they have been extensively used and examined in stroke literature, there is a worrying lack of consensus on which threshold can identify the spatial extents of salvageable and dead tissue in stroke patients [Dani 2012, Wardlaw 2010]. Our investigation of perfusion thresholds was two-fold: (1) we examined perfusion values associated with perfusion lesion high dynamics and (2) we examined perfusion values associated with diffusion lesion high dynamics. Both experiments demonstrated that: (a) there was no single perfusion threshold that fitted all patients' various behavior and (b) perfusion values are far more dynamic and heterogeneous than has been suggested so far [Dani 2012]. They also highlighted the sheer breadth of the spectrum of perfusion values that was associated with high dynamics of the diffusion abnormality, thus confirming the ambiguity in relying on one unique threshold to discriminate final tissue status. This shows that it is very unlikely that we will find a universal perfusion threshold that will differentiate dead from survived and

at-risk from oligaemic tissue with any precision. Our findings also point towards a new way of looking at perfusion values in stroke to map lesion changes as being patient-specific and not population-specific. This may also advance our understanding of how perfusion values influence the spatial extent of the infarct core.

- **DWI abnormality reversal.** Parts of the acute DWI lesion reversed to a normal state as it contracted during its evolution from one timepoint to the next one. This observation was present in both representations of stroke lesion: as a 3D surface (current-based regression model) (Chapter 5) or an image (the longitudinal metamorphosis model) (Chapters 6, 7 and 8). Indeed, we showed that any contracting DWI areas would indicate diffusion abnormality reversal and any expanding DWI areas would indicate the new appearance of irreversibly dead tissue. We hope that more tailored dynamic models would identify factors governing diffusion lesion native dynamics and improve how we interpret diffusion abnormality.

To summarize, 4D modeling in stroke has the ability to provide considerable insight into stroke evolution in space and time, not identified so far by more conventional non-dynamic image analysis methods. Additionally, the 4D models presented here provide preliminary

evidence that some commonly used stroke hypotheses –such as the mismatch concept and the prognostic potentials of DWI and MTT abnormalities– may not fully account for the true lesion dynamic behavior. Further refinement of these models to fit an individual patient's lesions and possibly offer prediction of outcome requires substantially more data and will be a future target.

9.2 Perspectives

9.2.1 Methodological perspectives

Choosing an appropriate model in terms of robustness and complexity for stroke evolution modeling lays a solid ground for improving stroke prognosis. We chose two different models: one based on a diffeomorphic metric (the current-based model) and another based on a new Riemannian metamorphic metric (the metamorphosis model). We were able to evaluate these models using longitudinal stroke data and to demonstrate in Chapters 7 and 8 that we can estimate a mean evolution scenario for the lesion with the constraint of "no topology change" being on than turned off. Both models were able to accurately fit the clinical observations, thus, decreasing the prospect of erroneous interpretations.

However, both of these models did not handle all the issues stated in Table 4.4 and that were recommended for future studies on stroke.

Indeed, they had some limitations.

Swelling and the induced mass-effect not included. Swelling is very common in stroke particularly at the acute/subacute stage of its evolution. In this work, we tried to avoid the mass-effect by excluding patients with largely swollen lesions to avoid deriving erroneous conclusions about stroke dynamics. However, it is very difficult to detect between the few MR observations distant in time if the lesion has partly swollen up or shrunk in some areas. These changes may be subtle and occur in a narrow time-window so that they go undetected. Swollen lesions are endowed with more complex geometries that take more sophisticated mathematical approaches for modeling. To address the swelling issue in stroke, one could estimate for instance an additional deformation map based on some anatomical landmarks to quantify the brain edema. One also could model the swelling as an additional biomechanical transformation that modifies the true boundaries of stroke lesion as it was modeled in glioma growth [Clatz 2005]. Integrating this additional transformation into the 4D modeling approach would help us evaluate the swelling and identify the true margins of dead, at-risk and oligaemic tissue and their lesion boundary dynamics.

Spatial heterogeneity of stroke evolution. Stroke evolution is heterogeneous: perfusion values vary between normal white and gray matter and also vary in hypoperfused areas

[Wardlaw 2010, Phan 2009]. Our modeling approaches did not account for this important aspect of stroke evolution but neither have previous clinical studies of perfusion imaging. Perfusion values were interpreted regardless of their anatomical location. To tailor a more personalized heterogeneous dynamic model of stroke evolution, one could use white and gray matter masks. Examining stroke behavior with respect to its anatomical location could prove to be beneficial to derive more accurate and informative deformation and residual maps (Figures 7.1 and 7.2). Considering the heterogeneity of stroke evolution may improved the identification of brain areas with distinct hemodynamic properties [Baumgartner 2005].

Spontaneous reperfusion and collateral flow. Ideally, spontaneous reperfusion should be simulated and not overlooked. As a constructive critique to our methodology, we suggest for future studies to couple the collateral flow with perfusion maps to understand spatiotemporal changes in the perfusion abnormality. To investigate the likelihood of spontaneous reperfusion in stroke patients, one could use magnetic resonance angiography (MRA) images [Phan 2009]. For instance, different fluid-dynamic models could be coupled with the longitudinal metamorphosis model to simulate the reperfusion and the flow patterns [Steinman 2003, Mantha 2006, Alnæs 2007, Taylor 2010]. This would enable us to simulate the impact of the collateral blood flow on perfusion and diffusion lesion

dynamics.

Current-based diffeomorphic model improvement. The spatiotemporal metamorphosis model is very promising and led to encouraging results. However, it tracks the changes in stroke lesion as an image and not as a surface. It would be more interesting to merge the metamorphosis theory with the current-based approach to investigate the association between the estimated speed of the lesion surface evolution and corresponding PWI or DWI values and thus visualize in 4D the evolution of scattered lesions as in videos 1, 2 and 3[1]. Indeed, modeling the lesion as a 3D surface is richer and more informative than only considering its 3D spatial extents on images. Taking into account the grey level value of the image at the location of the surface voxels would be an interesting modification of the current-based diffeomorphic model. To incorporate information on tissue perfusion or diffusion values at the lesion edge, one may need to revise the mathematical framework of modeling surfaces using currents and potentially use a new mathematical concept to define colored metamorphic surfaces that can undergo the following topological transformations: merging, splitting, appearance and disappearance of new lesion components. We hope that the development of the theory of colored metamorphic currents will allow us to consider different biological parameters that may impact stroke lesion surface

[1]Check the web link for the supplementary material of [Rekik 2013c]: http://dx.doi.org/10.1155/2013/283593

metamorphosis.

Simplified assumptions about perfusion and diffusion lesions. Although the definition of perfusion and diffusion abnormality has evolved slightly over the years, it remains widely uncertain that the visible boundaries with the naked eye accurately coincide with the true boundaries of ischemic and dead tissue. Integrating probabilistic definitions for the spatial extents of perfusion and diffusion abnormality into the metamorphosis model would present one way of handling this uncertainty around tissue boundaries. This would yield to a pioneering probabilistic longitudinal metamorphosis model that would generate a probabilistic residual and deformation maps. This suggestion can be thoroughly explored in future studies on stroke modeling.

Good modeling is also about good data. The efficiency and robustness of a modeling approach for simulating evolution of brain diseases depend on two elements: the data and the model itself. Stroke data acquisition process is prone to many errors such as registration, interpolation, partial volume effects, intensity shading artifacts, MR signal inhomogeneity, etc (Section 3.6). Using more sophisticated registration methods such as iLogDemons [Mansi 2010] or deformable registration [Lester 1999, Mcinerney 1996, Maintz 1998] would improve the accuracy of our observations. In this thesis, we do not take into account these potential errors. However, this can be addressed

in future studies. Modeling stroke evolution using data with better spatial resolution and more acquisition timepoints would improve the accuracy of the estimated lesion evolution scenario and therefore define more advanced metrics for identifying abnormal tissue mechanical and hemodynamic changes.

Other imaging modalities for stroke modeling. Stroke behavior assumptions can also be investigated using other imaging modalities. In this thesis, we have only used MTT perfusion maps and DWI images. It is worth noting that the presented 4D models could also be applied to ADC maps or PET/DTI images. Using images from different modalities could help build more complete patient-specific 4D stroke model.

9.2.2 Clinical perspectives

The various studies performed during this work pave the way for the development of more personalized stroke modeling approaches that would ultimately provide valid answers to the questions raised in the introduction. We suggest in what follows some ideas that would contribute to reshaping the future of stroke research and improving stroke management.

New insights into stroke dynamics. It has become more evident through this thesis work that basic volumetric analysis tools and thresholding techniques cannot capture the dynamics of stroke lesion

evolution. However, dynamic models may be preferred for their accuracy in tracking small and large deformations of stroke lesion. We hope that this thesis work, along with its incremental value over state of the art analysis of stroke data, will be the starting point to turn the attention and enthusiasm of stroke researchers (clinicians and medical image analysists) towards exploring a wider spectrum of time-series imaging-based models [Klein 2009]. With more honed future studies challenging the limitations of previous models, stroke research field will have a quicker pace in finding the ideal model that would not only describe stroke lesion evolution but also predict it.

Towards a patient-specific stroke evolution predictive model. Predicting the evolution of stroke lesion using multimodal brain scans acquired at a unique timepoint constitutes one of the most thought-provoking goals to achieve at the crossroad of stroke and medical image analysis research lines. Noticing that this has already been achieved in brain glioma evolution modeling raises our hopes that it can also be achieved in stroke [Rekik 2012b]. Once developed and validated, this model could be used in a clinical setting to improve stroke diagnosis and prognosis. This could be achieved by looking at other patient-specific models applied to different pathologies (eg: using the reaction-diffusion equation to predict the growth of high grade and low grade glioma or in cardiac modeling) such as in [Konukoglu 2007, Konukoglu 2009, Mansi 2010, Relan 2011b, Relan 2011a]. Stroke may

seem more complex than brain cancer or cardiac pathologies as its research ground is shaken by yet unstable assumptions about its dynamics and unknown factors driving its evolution. However, we believe that this blurred vision can get clearer if the certainty about what the image is truly telling us increases. Sharper understanding of our observations founds the basics of such models to develop.

Probabilistic metamorphic perfusion/diffusion lesion atlas. As a long-term goal, we can use the metamorphic residual and deformation maps (Chapters 7 and 8) to build an atlas of brain lesions identifying anatomical areas where the highest dynamic change takes place. This could be achieved using different clinical datasets with similar acquisition protocols. Such an approach could help in studying hypotheses about stroke lesion behavior such as the PWI/DWI mismatch concept. It could also deal with issues such as variability in arterial vascular territories and boundaries which probably influence DWI/PWI lesion evolution. It could also determine the effect of background brain changes such as white matter hyperintensities on lesion evolution. One could also develop statistical models investigating the association between acute lesion characteristics and functional outcome and the effect of treatment. This atlas would present an efficient tool to gather patient-specific information using dynamic modeling techniques. Once built, it could be used to extract population-specific features and reliably predict final tissue fate using sophisticated sta-

tistical models as such in [Allassonnière 2007, Allassonnière 2010]. Another appealing research direction is to use statistical models to identify the changes in population-based lesion shape and intensity depending on their vascular territory and occlusion site using this probabilistic metamorphic atlas. It is preferable to build two atlases: one using perfusion data and another using diffusion data. Then, we can compare both of these atlases to examine the relation between population-specific hemodynamic alterations in perfusion abnormality and population-specific variations in diffusion abnormality. Besides, this atlas could help us identify the deformation modes that encode lesion shape variability –as mentioned in Section 8.6. Furthermore, rather than build two atlases, one could also consider a joint model of both datasets so that the two modalities may be better related to each other. This would provide cutting-edge research tools to tackle unsolved problems in stroke and choose the optimal therapeutical strategy.

9.2.3 Conclusions

The area of stroke research was distant from mathematical modeling. To the best of our knowledge, this thesis work is the first attempt to bridge that gap and bring new insights into stroke dynamics. Stroke dynamic behavior is an area in which it is easy to observe patterns and think that they are generally valid, but amazingly difficult to

pin them down with a proper proof or validation method. We need to be very careful that we are not overstretching the evidence that is available for our methods. It is always safe to keep some margins of uncertainty about our observations to not fall into dogmas. Our approach constitutes a novel way to study the 4D alterations of stroke lesion using time-series imaging and have some comprehension of the basic processes that are involved in stroke. We hope that this thesis will encourage stroke researchers to adopt the "dynamic modeling" path to gain better understanding of stroke lesion evolution. There are still wrinkles in perfusion and diffusion abnormality evolution "theories" but surely they will be ironed out as we gradually build a more unified view of stroke dynamics consistent and congruent with diverse clinical datasets. Finally, we would like to point out that the models presented in this thesis are not specific to stroke. They can be applied to other pathologies and other types of longitudinal data.

9.3 Publications

This thesis is largely based on the following first author publications, submitted articles and presentation talks:

Articles in peer-reviewed journals:

[Rekik 2012a] I. Rekik, S. Allassonnière, T. Carpenter, J. Wardlaw. Medical image analysis methods in MR/CT-imaged acute-subacute

ischemic stroke lesion: Segmentation, prediction and insights into dynamic evolution simulation; NeuroImage: Clinical 1(1) 164-178 (2012). PMCID: PMC3703431. *This paper is included in Chapter 4.*

[Rekik 2013c] I. Rekik, S. Allassonnière, S. Durrleman, T. Carpenter, J. Wardlaw. Spatiotemporal dynamic simulation of acute perfusion/diffusion ischemic stroke lesions: a pilot study derived from longitudinal MR patient data; Computational and Mathematical Methods in Medicine (2013). *This paper is included in Chapter 5*

[Rekik 2013a] I. Rekik, S. Allassonnière, T. Carpenter, J. Wardlaw. Development of longitudinal metamorphosis: application to ischemic stroke lesions on perfusion-weighted imaging and relation to final lesion outcome on T2-w imaging; Medical Image Analysis, **submitted** (2013).*This paper is included in Chapters 5 and 6*

[Rekik 2013b] I. Rekik, S. Allassonnière, T. Carpenter, J. Wardlaw. Evaluating acute ischemic stroke to final infarct evolution using 4D mathematical metamorphosis modeling; Nature Neuroscience, **to-submit** (2013). *This paper is included in Chapter 8.*

Conference Abstracts:

- "A 4D Patient-specific Metamorphosis-based Method to Model Ischemic Stroke Lesion Evolution from Acute Diffusion-weighted to Final T2-defined Outcome", **ISC** (International Stroke Conference), Hawaii, 2013; and **ASM** (Annual SINAPSE Meeting),

Aberdeen, 2013.

- "Dynamic simulation of acute ischemic stroke evolution using longitudinal MR patient data", **NRC** (Neuroradiology Research Conference, Stanford University), 2013.

- "A 4D spatio-temporal model to estimate stroke lesion evolution on MR perfusion-diffusion imaging following acute ischemic stroke", **ISMRM** (International Society for Magnetic Resonance in Medicine), Melbourne, 2012.

- "4D dynamic patient-specific modeling of ischemic stroke lesion evolution: From presentation to final damage using diffusion, perfusion and T2 MR imaging", **ESC**, Lisbon, 2012; and **ASM**, Dundee 2012.

- "Mathematical Image Processing Algorithms in determining Stroke Tissue Status and Predicting its Fate: Systematic Review reveals Untapped Potentials", **ESC**, Hamburg, 2011.

- "4D Growth Scenarios of MR Ischemic Stroke Lesions", **ASM**, Dundee, June, 2011.

Invited Talks and international lab visits:

R. Lucas Imaging Center (Stanford University), one-week visit, February 2013.

"Insights in the perfusion-diffusion mismatch from a dynamic perspective", **Melbourne Brain Centre at RMH (MBC, University of Melbourne)**, May 2012.

"Ischemic stroke evolution modeling", **Department of Informatics and Research (DIR, The University of Edinburgh)**, January 2012.

"A 4D spatio-temporal model simulating ischemic stroke lesion evolution using MR perfusion-diffusion imaging", **SRG (Stroke Research Group, Edinburgh)**, 2012.

Bibliography

[Agam 2007] G Agam, D Weiss, M Soman and K Arfanakis. *Probabilistic Brain Lesion Segmentation in DT-MRI.* pages 89–92, 2007. (Cited on page 55.)

[Albers 2006] G.W. Albers, V.N. Thijs, L. Wechsler, S. Kemp, G. Schlaug, E. Skalabrin, R. Bammer, W. Kakuda, M.G. Lansberg and A. Shuaib. *Magnetic resonance imaging profiles predict clinical response to early reperfusion: the diffusion and perfusion imaging evaluation for understanding stroke evolution (DEFUSE) study.* Annals of neurology, vol. 60, no. 5, pages 508–517, 2006. (Cited on page 28.)

[Allassonnière 2007] S. Allassonnière, Y. Amit and A. Trouvé. *Towards a coherent statistical framework for dense deformable template estimation.* Journal of the Royal Statistical Society: Series B (Statistical Methodology), vol. 69, no. 1, pages 3–29, 2007. (Cited on pages 122 and 234.)

[Allassonnière 2010] S. Allassonnière, E. Kuhn and A. Trouvé. *Construction of Bayesian deformable models via stochastic approximation algorithm: A convergence study.* Bernoulli Journal, vol. 16(3), pages 641–678, 2010. (Cited on pages 122 and 234.)

[Alnæs 2007] M.S. Alnæs, J. Isaksen, K.-A. Mardal, B. Romner, M.K. Morgan and T. Ingebrigtsen. *Computation of hemodynamics in the circle of Willis.* Stroke, vol. 38, no. 9, pages 2500–2505, 2007. (Cited on page 228.)

[Ames 1968] A Ames, R L Wright, M Kowada, J M Thurston and G Majno. *Cerebral ischemia. II. The no-reflow phenomenon.* Am J Pathol, vol. 52, no. 2, pages 437–53, Feb 1968. (Cited on page 57.)

[Arenillas 2002] J.F. Arenillas, Ä. Rovira, C.A. Molina, E. Grivé, J. Montaner and J. Älvarez-Sabín. *Prediction of early neurological deterioration using diffusion-and perfusion-weighted imaging in hyperacute middle cerebral artery ischemic stroke.* Stroke, vol. 33, no. 9, pages 2197–2205, 2002. (Cited on pages 26, 52, 59, 107 and 223.)

[Astrup 1977] J Astrup, L Symon, NM Branston and NA Lassen. *Thresholds of cerebral ischemia.* pages 16–21, 1977. (Cited on page 23.)

[Astrup 1981] J Astrup, B K Siesjö and L Symon. *Thresholds in cerebral ischemia - the ischemic penumbra.* Stroke, vol. 12, no. 6, pages 723–5, 1981. (Cited on pages 19, 23 and 63.)

[Axel 1980] L. Axel. *Cerebral blood flow determination by rapid-sequence computed tomography: theoretical analysis.* Radiology, vol. 137, no. 3, pages 679–686, 1980. (Cited on page 43.)

[Bagher-Ebadian 2011] H. Bagher-Ebadian, K. Jafari-Khouzani, P.D. Mitsias, M. Lu, H. Soltanian-Zadeh, M. Chopp and J.R. Ewing. *Predicting final extent of ischemic infarction using artificial neural network analysis of multi-parametric MRI in patients with stroke.* PLoS One, vol. 6, no. 8, page e22626, 2011. (Cited on pages 84 and 95.)

[Baird 1997] A.E. Baird, A. Benfield, G. Schlaug, B. Siewert, K.O. Lövblad, R.R. Edelman and S. Warach. *Enlargement of human cerebral ischemic lesion volumes measured by diffusion-weighted magnetic resonance imaging.* Annals of neurology, vol. 41, no. 5, pages 581–589, 1997. (Cited on pages 25, 40 and 107.)

[Bandera 2006] E. Bandera, M. Botteri, C. Minelli, A. Sutton, K.R. Abrams and N. Latronico. *Cerebral blood flow threshold of ischemic penumbra and infarct core in acute ischemic stroke a systematic review.* Stroke, vol. 37, no. 5, pages 1334–1339, 2006. (Cited on pages 19 and 47.)

[Bang 2008] O Y Bang, J L Saver, B H Buck, J R Alger, S Starkman, B Ovbiagele, D Kim, R Jahan, G R Duckwiler, S R Yoon,

F Viñuela, D S Liebeskind and UCLA Collateral Investigators. *Impact of collateral flow on tissue fate in acute ischaemic stroke.* J Neurol Neurosurg Psychiatry, vol. 79, no. 6, pages 625–9, Jun 2008. (Cited on page 56.)

[Barber 1998] P. Barber, D. Darby, P. Desmond, Q. Yang, R. Gerraty, D. Jolley, G. Donnan, B. Tress and S. Davis. *Prediction of stroke outcome with echoplanar perfusion-and diffusion-weighted MRI.* Neurology, vol. 51, no. 2, pages 418–426, 1998. (Cited on pages 25, 26, 52, 59, 107 and 223.)

[Barber 2004] P.A. Barber, M.W. Parsons, P.M. Desmond, D.A. Bennett, G.A. Donnan, B.M. Tress and S.M. Davis. *The Use of PWI and DWI Measures in the Design of "Proof-of-Concept" Stroke Trials.* Journal of Neuroimaging, vol. 14, no. 2, pages 123–132, 2004. (Cited on page 108.)

[Baron 1999] J. Baron. *Mapping the ischaemic penumbra with PET: implications for acute stroke treatment.* Cerebrovascular Diseases, vol. 9, no. 4, pages 193–201, 1999. (Cited on page 25.)

[Baron 2002] J. Baron. *Stroke: imaging and differential diagnosis.* Journal of Neural Transmission-Supplements only, no. 63, pages 19–36, 2002. (Cited on page 108.)

[Baumgartner 2005] C. Baumgartner, K. Gautsch, C. Böhm and S. Felber. *Functional cluster analysis of CT perfusion maps:*

a new tool for diagnosis of acute stroke? Journal of Digital Imaging, vol. 18, no. 3, pages 219–226, 2005. (Cited on page 228.)

[Beaulieu 1999] C. Beaulieu, A. De Crespigny, D.C. Tong, M.E. Moseley, G.W. Albers and M.P. Marks. *Longitudinal magnetic resonance imaging study of perfusion and diffusion in stroke: evolution of lesion volume and correlation with clinical outcome.* Annals of neurology, vol. 46, no. 4, pages 568–578, 1999. (Cited on pages 191 and 192.)

[Beg 2005] M.F. Beg, M.I. Miller, A. Trouvé and L. Younes. *Computing large deformation metric mappings via geodesic flows of diffeomorphisms.* International Journal of Computer Vision, vol. 61, no. 2, pages 139–157, 2005. (Cited on pages 122, 159, 162 and 172.)

[Bonita 1992] R. Bonita. *Epidemiology of stroke.* The Lancet, vol. 339, no. 8789, pages 342–344, 1992. (Cited on page 2.)

[Bookstein 1997] Fred L Bookstein. Morphometric tools for landmark data: geometry and biology. Cambridge University Press, 1997. (Cited on page 111.)

[Bosc 2003] M. Bosc, F. Heitz, J.-P. Armspach, I. Namer, D. Gounot and L. Rumbach. *Automatic change detection in multimodal serial MRI: application to multiple sclerosis lesion evolution.*

NeuroImage, vol. 20, no. 2, pages 643–656, 2003. (Cited on page 5.)

[Braun 2002] Juergen Braun, Johannes Bernarding, Hans-Christian Koennecke, Karl-Juergen Wolf and Thomas Tolxdorff. *Feature-based, automated segmentation of cerebral infarct patterns using T2- and diffusion-weighted imaging.* Comput Methods Biomech Biomed Engin, vol. 5, no. 6, pages 411–20, Dec 2002. (Cited on page 74.)

[Broderick 2013] J.P. Broderick, Y.Y. Palesch, A.M. Demchuk, S.D. Yeatts, P. Khatri, M.D. Hill, E.C. Jauch, T.G. Jovin, B. Yan and F.L. Silver. *Endovascular therapy after intravenous t-PA versus t-PA alone for stroke.* New England Journal of Medicine, vol. 368, no. 10, pages 893–903, 2013. (Cited on page 27.)

[Brott 1989] T Brott, J R Marler, C P Olinger, H P Adams Jr, T Tomsick, W G Barsan, J Biller, R Eberle, V Hertzberg and M Walker. *Measurements of acute cerebral infarction: lesion size by computed tomography.* Stroke, vol. 20, no. 7, pages 871–5, Jul 1989. (Cited on page 98.)

[Burdette 1999] J H Burdette, A D Elster and P E Ricci. *Acute cerebral infarction: quantification of spin-density and T2 shine-through phenomena on diffusion-weighted MR images.* Ra-

diology, vol. 212, no. 2, pages 333–9, Aug 1999. (Cited on page 55.)

[Butcher 2005] K. Butcher, M. Parsons, L. Macgregor, P. Barber, J. Chalk, C. Bladin, C. Levi, T. Kimber, D. Schultz and J. Fink. *Refining the perfusion-diffusion mismatch hypothesis.* Stroke, vol. 36, no. 6, pages 1153–1159, 2005. (Cited on page 193.)

[Calamante 2002] F. Calamante, D. Gadian and A. Connelly. *Quantification of Perfusion Using Bolus Tracking Magnetic Resonance Imaging in Stroke Assumptions, Limitations, and Potential Implications for Clinical Use.* Stroke, vol. 33, no. 4, pages 1146–1151, 2002. (Cited on page 47.)

[Cam 2001] Geodesic interpolating splines, volume Energy Minimization Methods in Computer Vision and Pattern Recognition. Springer, 2001. (Cited on page 111.)

[Campbell 2010] B.C.V. Campbell, S. Christensen, S. Foster, P. Desmond, M. Parsons, K. Butcher, P. Barber, C. Levi, C. Bladin and G. Donnan. *Visual assessment of perfusion-diffusion mismatch is inadequate to select patients for thrombolysis.* Cerebrovascular Diseases, vol. 29, no. 6, pages 592–596, 2010. (Cited on page 107.)

[Carano 1998] R A Carano, K Takano, K G Helmer, T Tatlisumak, K Irie, J D Petruccelli, M Fisher and C H Sotak. *Determination of focal ischemic lesion volume in the rat brain using multispectral analysis.* J Magn Reson Imaging, vol. 8, no. 6, pages 1266–78, 1998. (Cited on page 83.)

[Carpenter 2003] TK Carpenter, PA Armitage, ME Bastin and JM Wardlaw. *Artefacts in MR perfusion parametric images in ischaemic stroke-effects of variation in bolus arrival time.* Cerebrovasc Dis, vol. 16, page 92, 2003. (Cited on pages 48 and 54.)

[Carrera 2011] E. Carrera, P.S. Jones, J.A. Alawneh, I.K. Mikkelsen, T.H. Cho, S. Siemonsen, J.V. Guadagno, K. Mouridsen, L. Ribe and N. Hjort. *Predicting Infarction Within the Diffusion-Weighted Imaging Lesion Does the Mean Transit Time Have Added Value?* Stroke, vol. 42, no. 6, pages 1602–1607, 2011. (Cited on page 192.)

[Chalela 2007] J.A. Chalela, C.S. Kidwell, L.M. Nentwich, M. Luby, J.A. Butman, A.M. Demchuk, M.D. Hill, N. Patronas, L. Latour and S. Warach. *Magnetic resonance imaging and computed tomography in emergency assessment of patients with suspected acute stroke: a prospective comparison.* The Lancet, vol. 369, no. 9558, pages 293–298, 2007. (Cited on page 25.)

[Chapuisat 2008] G Chapuisat, M A Dronne, E Grenier, M Hommel, H Gilquin and J P Boissel. *A global phenomenological model of ischemic stroke with stress on spreading depressions.* Prog Biophys Mol Biol, vol. 97, no. 1, pages 4–27, May 2008. (Cited on pages 70, 85, 87, 88, 89 and 96.)

[Chapuisat 2010] G. Chapuisat, M. Dronne, E. Grenier, M. Hommel and J-P Boissel. *In silico study of the influence of intensity and duration of blood flow reduction on cell death through necrosis or apoptosis during acute ischemic stroke.* Acta Biotheor, vol. 58, no. 2-3, pages 171–90, Sep 2010. (Cited on pages 70, 85, 87, 95 and 96.)

[Chawla 2009] M. Chawla, S. Sharma, J. Sivaswamy and LT Kishore. *A method for automatic detection and classification of stroke from brain CT images.* vol. Engineering in Medicine and Biology Society, 2009. EMBC 2009. Annual International Conference of the IEEE, pages 3581–3584, 2009. (Cited on page 77.)

[Chemmanam 2010] T Chemmanam, B C V Campbell, S Christensen, Y Nagakane, P M Desmond, C F Bladin, M W Parsons, C R Levi, P A Barber, G A Donnan, S M Davis and EPITHET Investigators. *Ischemic diffusion lesion reversal is uncommon and rarely alters perfusion-diffusion mismatch.*

Neurology, vol. 75, no. 12, pages 1040–7, Sep 2010. (Cited on page 97.)

[Chen 2010] Ting Chen, Anand Rangarajan, Stephan J Eisenschenk and Baba C Vemuri. *Construction of neuroanatomical shape complex atlas from 3D brain MRI.* pages 65–72, 2010. (Cited on page 5.)

[Choi 2011] P. Choi, V. Srikanth and T. Phan. *"Fogging" resulting in normal MRI 3 weeks after ischaemic stroke.* BMJ Case Reports, vol. 2011, 2011. (Cited on page 55.)

[Chui 2003] H. Chui and A. Rangarajan. *A new point matching algorithm for non-rigid registration.* Computer Vision and Image Understanding, vol. 89, no. 2, pages 114–141, 2003. (Cited on page 111.)

[Ciccone 2013] A. Ciccone, L. Valvassori, M. Nichelatti, A. Sgoifo, M. Ponzio, R. Sterzi and E. Boccardi. *Endovascular treatment for acute ischemic stroke.* New England Journal of Medicine, vol. 368, no. 10, pages 904–913, 2013. (Cited on page 27.)

[Clatz 2005] O. Clatz, M. Sermesant, P.-Y. Bondiau, H. Delingette, S.K. Warfield, G. Malandain and N. Ayache. *Realistic simulation of the 3-D growth of brain tumors in MR images coupling diffusion with biomechanical deformation.* Medical Imaging,

IEEE Transactions on, vol. 24, no. 10, pages 1334–1346, 2005. (Cited on pages 218 and 227.)

[Commowick 2008] Olivier Commowick, Pierre Fillard, Olivier Clatz and Simon K Warfield. *Detection of DTI white matter abnormalities in multiple sclerosis patients.* pages 975–982, 2008. (Cited on page 5.)

[Contin 2010] L Contin, C Beer, M Bynevelt, H.J Wittsack and G.J Garrido. *Semi-automatic segmentation of core and penumbra regions in acute ischemic stroke: preliminary results.* IWSSIP International Conference, 2010. (Cited on pages 72, 73 and 74.)

[Coutts 2003] S.B Coutts, J.E Simon, A.I Tomanek, P.A Barber, J. Chan, M.E. Hudon, J.R. Mitchell, R. Frayne, M. Eliasziw, A.M Buchan and A.M Demchuk. *Reliability of assessing percentage of diffusion-perfusion mismatch.* Stroke, vol. 34, no. 7, pages 1681–3, Jul 2003. (Cited on pages 26, 52, 53 and 59.)

[Craene 2012] M. De Craene, G. Piella, O. Camara, N. Duchateau, E. Silva, A. Doltra, J. Dâhooge, J. Brugada, M. Sitges and A.F. Frangi. *Temporal diffeomorphic free-form deformation: application to motion and strain estimation from 3D echocardiography.* Medical Image Analysis, vol. 16, no. 2, pages 427–450, 2012. (Cited on page 157.)

[Cvoro 2010] V. Cvoro, I. Marshall, P.A. Armitage, M.E. Bastin, T. Carpenter, C.S. Rivers, M.S. Dennis and J.M. Wardlaw. *MR diffusion and perfusion parameters: relationship to metabolites in acute ischaemic stroke.* Journal of Neurology, Neurosurgery & Psychiatry, vol. 81, no. 2, pages 185–191, 2010. (Cited on page 43.)

[Dani 2011] K.A. Dani, R.G.R. Thomas, F.M. Chappell, K. Shuler, M.J. Macleod, K.W. Muir and J.M. Wardlaw. *Computed tomography and magnetic resonance perfusion imaging in ischemic stroke: definitions and thresholds.* Annals of neurology, vol. 70, no. 3, pages 384–401, 2011. (Cited on pages 47, 108 and 214.)

[Dani 2012] K.A. Dani, R.G.R. Thomas, F.M. Chappell, K. Shuler, K.W. Muir and J.M. Wardlaw. *Systematic Review of Perfusion Imaging With Computed Tomography and Magnetic Resonance in Acute Ischemic Stroke: Heterogeneity of Acquisition and Postprocessing Parameters.* Stroke, vol. 43, no. 2, pages 563–566, 2012. (Cited on pages 23, 26, 48, 54, 63, 91, 108, 190 and 224.)

[Dastidar 2000] P Dastidar, T Heinonen, J P Ahonen, M Jehkonen and G Molnár. *Volumetric measurements of right cerebral hemisphere infarction: use of a semiautomatic MRI segmenta-*

tion technique. Comput Biol Med, vol. 30, no. 1, pages 41–54, Jan 2000. (Cited on pages 69 and 72.)

[Davatzikos 1997] C. Davatzikos. *Spatial transformation and registration of brain images using elastically deformable models*. Computer Vision and Image Understanding, vol. 66, no. 2, pages 207–222, 1997. (Cited on page 111.)

[Davis 2007] B.C. Davis, P.T. Fletcher, E. Bullitt and S. Joshi. *Population shape regression from random design data*. vol. Computer Vision, 2007. ICCV 2007. IEEE 11th International Conference on, pages 1–7, 2007. (Cited on page 172.)

[Davis 2008] S.M. Davis, G.A. Donnan, M.W. Parsons, C. Levi, K.S. Butcher, A. Peeters, P.A. Barber, C. Bladin, D.A. De Silva and G. Byrnes. *Effects of alteplase beyond 3 h after stroke in the Echoplanar Imaging Thrombolytic Evaluation Trial (EPITHET): a placebo-controlled randomised trial*. The Lancet Neurology, vol. 7, no. 4, pages 299–309, 2008. (Cited on page 28.)

[Dawant 2000] B.M. Dawant and A.P. Zijdenbos. *Image segmentation*. Handbook of Medical Imaging, vol. 2, pages 71–127, 2000. (Cited on page 68.)

[Dronne 2004] M. Dronne, J-P Boissel, E. Grenier, H. Gilquin, M. Cucherat, M. Hommel, E. Barbier and G. Bricca. *Math-*

ematical modelling of an ischemic stroke: an integrative approach. Acta Biotheor, vol. 52, no. 4, pages 255–72, 2004. (Cited on pages 70, 85, 86, 88, 89 and 91.)

[Dronne 2006] M. Dronne, J-P Boissel and E. Grenier. *A mathematical model of ion movements in grey matter during a stroke.* J Theor Biol, vol. 240, no. 4, pages 599–615, Jun 2006. (Cited on pages 70, 85, 86, 87, 88, 89, 91, 95 and 96.)

[Dumont 2010] T. Dumont, M. Duarte, S. Descombes, M.A. Dronne, M. Massot and V. Louvet. *Simulation of human ischemic stroke in realistic 3D geometry: A numerical strategy.* Submitted to Bulletin of Math, Biology. Available on HAL (http://hal.archives-ouvertes.fr/hal-00546223), 2010. (Cited on pages 70, 87, 89 and 99.)

[Duncan 2000] J.S. Duncan and N. Ayache. *Medical image analysis: Progress over two decades and the challenges ahead.* Pattern Analysis and Machine Intelligence, IEEE Transactions on, vol. 22, no. 1, pages 85–106, 2000. (Cited on pages 63 and 99.)

[Dupuis 1998] P. Dupuis, U. Grenander and M.I. Miller. *Variational problems on flows of diffeomorphisms for image matching.* Quarterly of applied mathematics, vol. 56, no. 3, page 587, 1998. (Cited on page 157.)

[Durrleman 2009] S. Durrleman, X. Pennec, A. Trouvé, G. Gerig and N. Ayache. *Spatiotemporal atlas estimation for developmental delay detection in longitudinal datasets.* Medical Image Computing and Computer-Assisted Intervention (MICCAI) 2009, pages 297–304, 2009. (Cited on pages 112, 115 and 123.)

[Durrleman 2010] S. Durrleman. *Statistical models of currents for measuring the variability of anatomical curves, surfaces and their evolution.* These de sciences (PhD thesis), Université de Nice-Sophia Antipolis, 2010. (Cited on pages iii, 112, 115, 118, 123, 126, 127 and 128.)

[Durrleman 2011] S. Durrleman, X. Pennec, A. Trouvé, N. Ayache and J. Braga. *Comparison of the endocranial ontogenies between chimpanzees and bonobos via temporal regression and spatiotemporal registration.* Journal of human evolution, 2011. (Cited on pages 112, 115 and 123.)

[Durrleman 2013] S. Durrleman, X. Pennec, A. Trouvé, J. Braga, G. Gerig and N. Ayache. *Toward a comprehensive framework for the spatiotemporal statistical analysis of longitudinal shape data.* International Journal of Computer Vision, pages 1–38, 2013. (Cited on page 157.)

[Duval 2002] V. Duval, S. Chabaud, P. Girard, M. Cucherat, M. Hommel and J-P Boissel. *Physiologically based model of acute is-*

chemic stroke. J Cereb Blood Flow Metab, vol. 22, no. 8, pages 1010–8, Aug 2002. (Cited on pages 70, 85, 86, 89 and 96.)

[Dwyer 2008] M.G Dwyer, N. Bergsland, E. Saluste, J. Sharma, Z. Jaisani, J. Durfee, N. Abdelrahman, A. Minagar, R. Hoque, F.E Munschauer and R. Zivadinov. *Application of hidden Markov random field approach for quantification of perfusion/diffusion mismatch in acute ischemic stroke.* Neurol Res, vol. 30, no. 8, pages 827–34, Oct 2008. (Cited on page 76.)

[Erus 2010] G. Erus, E.I. Zacharaki and C. Bryan N.Davatzikos. *Learning high-dimensional image statistics for abnormality detection on medical images.* vol. Computer Vision and Pattern Recognition Workshops (CVPRW), 2010 IEEE Computer Society Conference on, pages 139–145, 2010. (Cited on page 103.)

[Fiehler 2004] J. Fiehler, T. Kucinski, K. Knudsen, M. Rosenkranz, G. Thomalla, C. Weiller, J. Röther and H. Zeumer. *Are there time-dependent differences in diffusion and perfusion within the first 6 hours after stroke onset?* Stroke, vol. 35, no. 9, pages 2099–2104, 2004. (Cited on page 42.)

[Fletcher 2004] P.T. Fletcher, C. Lu, S.M. Pizer and S. Joshi. *Principal geodesic analysis for the study of nonlinear statistics of shape.* Medical Imaging, IEEE Transactions on, vol. 23, no. 8, pages 995–1005, 2004. (Cited on page 218.)

[Ford 2012] A.L. Ford, H. An, K.D. Vo, W. Lin and J.M. Lee. *Defining the ischemic penumbra using hyperacute neuroimaging: deriving quantitative ischemic thresholds.* Translational Stroke Research, pages 1–7, 2012. (Cited on page 53.)

[Furlan 2006] A.J. Furlan, D. Eyding, G.W. Albers, Y. Al-Rawi, K.R. Lees, H.A. Rowley, C. Sachara, M. Soehngen, S. Warach and W. Hacke. *Dose escalation of desmoteplase for acute ischemic stroke (DEDAS) evidence of safety and efficacy 3 to 9 hours after stroke onset.* Stroke, vol. 37, no. 5, pages 1227–1231, 2006. (Cited on page 28.)

[Garcin 2005] L. Garcin and L. Younes. *Geodesic image matching: a wavelet based energy minimization scheme.* pages 349–364, 2005. (Cited on pages 159, 167 and 170.)

[Ghosh 2011] N. Ghosh, R. Recker, A. Shah, B. Bhanu, S. Ashwal and A. Obenaus. *Automated ischemic lesion detection in a neonatal model of hypoxic ischemic injury.* Journal of Magnetic Resonance Imaging, vol. 33, no. 4, pages 772–781, 2011. (Cited on page 73.)

[Ghosh 2012] N. Ghosh, Y. Sun, C. Turenius, B. Bhanu, A. Obenaus and S. Ashwal. *Computational Analysis: A Bridge to Translational Stroke Treatment.* Translational Stroke Research, pages 881–909, 2012. (Cited on page 97.)

[Ginsberg 1997] M. Ginsberg. *Injury Mechanisms in the Ischaemic Penumbra? Approaches to Neuroprotection in Acute Ischaemic Stroke.* Cerebrovascular Diseases, 1997. (Cited on page 23.)

[Glaunès 2004] J. Glaunès, M. Vaillant and M.I. Miller. *Landmark matching via large deformation diffeomorphisms on the sphere.* Journal of Mathematical Imaging and Vision, vol. 20, no. 1-2, pages 179–200, 2004. (Cited on page 111.)

[Gol 1999] Statistical shape analysis using fixed topology skeletons: Corpus callosum study, volume Information Processing in Medical Imaging. Springer, 1999. (Cited on page 218.)

[Grandin 2002] C.B Grandin, T.P Duprez, A.M Smith, C. Oppenheim, A. Peeters, A.R Robert and G. Cosnard. *Which MR-derived perfusion parameters are the best predictors of infarct growth in hyperacute stroke? Comparative study between relative and quantitative measurements.* Radiology, vol. 223, no. 2, pages 361–70, May 2002. (Cited on pages 55 and 107.)

[Grenander 1993] U. Grenander. General pattern theory: A mathematical study of regular structures. Clarendon Press, 1993. (Cited on page 115.)

[Grenier 2010] E Grenier, D Bresch, M.A Dronne, M Hommel and JP Boissel. *A phenomenological model of the growth of the*

necrotic area in ischemic stroke. Mathematical and Computer Modelling, vol. 51, no. 9-10, pages 1011–1025, 2010. (Cited on pages 70, 85 and 87.)

[Grunwald 2002] I. Grunwald and W. Reith. *Non-traumatic neurological emergencies: imaging of cerebral ischemia*. European Radiology, vol. 12, no. 7, pages 1632–1647, 2002. (Cited on page 49.)

[Grunwald 2007] I.Q. Grunwald, P. Papanagiotou, T. Struffert, M. Politi, C. Krick, B.F.M. Romaike, F. Ahlhelm and W. Reith. *Reversal of flow during carotid artery stenting: use of the Parodi antiembolism system*. Neuroradiology, vol. 49, no. 3, pages 237–241, 2007. (Cited on page 55.)

[Gupta 2008] V. Gupta, B. Prakash and W.L Nowinski. *Automatic and rapid identification of infarct slices and hemisphere in DWI scans*. Acad Radiol, vol. 15, no. 1, pages 24–39, Jan 2008. (Cited on page 54.)

[Hacke 2005] W. Hacke, G. Albers, Y. Al-Rawi, J. Bogousslavsky, A. Davalos, M. Eliasziw, M. Fischer, A. Furlan, M. Kaste and K.R. Lees. *The desmoteplase in acute ischemic stroke trial (DIAS) a phase II MRI-based 9-hour window acute stroke thrombolysis trial with intravenous desmoteplase*. Stroke, vol. 36, no. 1, pages 66–73, 2005. (Cited on page 28.)

[Hand 2002] P.J. Hand, C.S Rivers, A.M. Rowat, M.E Bastin, M.S Dennis and J.M. Wardlaw. *Does DWI lesion volume predict outcome after stroke?* Cerebrovasc Dis, vol. 13, no. 3, page 57, 2002. (Cited on page 26.)

[Heinonen 1998] T Heinonen, P Dastidar, P Kauppinen, J Malmivuo and H Eskola. *Semi-automatic tool for segmentation and volumetric analysis of medical images.* Med Biol Eng Comput, vol. 36, no. 3, pages 291–6, May 1998. (Cited on page 72.)

[Heiss 2000] W.-D. Heiss. *Ischemic Penumbra: Evidence From Functional Imaging in Man.* Journal of Cerebral Blood Flow & Metabolism, vol. 20, no. 9, pages 1276–1293, 2000. (Cited on page 25.)

[Hevia-Montiel 2007] Nidiyare Hevia-Montiel, Juan Ramón Jiménez-Alaniz, Verónica Medina-Bañuelos, Oscar Yáñez-Suárez, Charlotte Rosso, Yves Samson and Sylvain Baillet. *Robust nonparametric segmentation of infarct lesion from diffusion-weighted MR images.* Conf Proc IEEE Eng Med Biol Soc, vol. 2007, pages 2102–5, 2007. (Cited on page 75.)

[Hjort 2005] N. Hjort, K. Butcher, S. Davis, C. Kidwell, W. Koroshetz, J. Röther, P. Schellinger, S. Warach and L. Østergaard. *Magnetic resonance imaging criteria for thrombolysis*

in acute cerebral infarct. Stroke, vol. 36, no. 2, pages 388–397, 2005. (Cited on page 47.)

[Holden 2008] M. Holden. *A review of geometric transformations for nonrigid body registration.* Medical Imaging, IEEE Transactions on, vol. 27, no. 1, pages 111–128, 2008. (Cited on page 172.)

[Holland 2011] D. Holland and A.M. Dale. *Nonlinear registration of longitudinal images and measurement of change in regions of interest.* Medical image analysis, vol. 15, no. 4, pages 489–497, 2011. (Cited on page 120.)

[Hong 2012a] Y. Hong, S. Joshi, M. Sanchez, M. Styner and M. Niethammer. *Metamorphic Geodesic Regression.* Medical Image Computing and Computer-Assisted Intervention–MICCAI 2012, pages 197–205, 2012. (Cited on pages 158 and 160.)

[Hong 2012b] Y. Hong, Y. Shi, M. Styner, M. Sanchez and M. Niethammer. *Simple geodesic regression for image time-series.* pages 11–20, 2012. (Cited on page 157.)

[Huang 2010] S. Huang, Q. Shen and T.Q Duong. *Artificial neural network prediction of ischemic tissue fate in acute stroke imaging.* J Cereb Blood Flow Metab, vol. 30, no. 9, pages 1661–70, Sep 2010. (Cited on pages 84, 92 and 96.)

[Jacobs 2000] M A Jacobs, R A Knight, H Soltanian-Zadeh, Z G Zheng, A V Goussev, D J Peck, J P Windham and M Chopp. *Unsupervised segmentation of multiparameter MRI in experimental cerebral ischemia with comparison to T2, diffusion, and ADC MRI parameters and histopathological validation.* J Magn Reson Imaging, vol. 11, no. 4, pages 425–37, Apr 2000. (Cited on pages 72, 74, 77 and 95.)

[Jacobs 2001a] M A Jacobs, P Mitsias, H Soltanian-Zadeh, S Santhakumar, A Ghanei, R Hammond, D J Peck, M Chopp and S Patel. *Multiparametric MRI tissue characterization in clinical stroke with correlation to clinical outcome: part 2.* Stroke, vol. 32, no. 4, pages 950–7, Apr 2001. (Cited on pages 33, 74, 75 and 77.)

[Jacobs 2001b] M A Jacobs, Z G Zhang, R A Knight, H Soltanian-Zadeh, A V Goussev, D J Peck and M Chopp. *A model for multiparametric MRI tissue characterization in experimental cerebral ischemia with histological validation in rat: part 1.* Stroke, vol. 32, no. 4, pages 943–9, Apr 2001. (Cited on pages 74, 75 and 77.)

[James 2006] J.R James, K.K Yoder, O. Osuntokun, A. Kalnin, A. Bruno and E.D Morris. *A supervised method for calculating perfusion/diffusion mismatch volume in acute ischemic*

stroke. Comput Biol Med, vol. 36, no. 11, pages 1268–87, Nov 2006. (Cited on pages 53, 72 and 73.)

[Jos 2007] A novel representation for riemannian analysis of elastic curves in rn, volume Computer Vision and Pattern Recognition, 2007. CVPR'07. IEEE Conference on. IEEE, 2007. (Cited on page 218.)

[Joshi 2000] S.C. Joshi and M.I. Miller. *Landmark matching via large deformation diffeomorphisms*. Image Processing, IEEE Transactions on, vol. 9, no. 8, pages 1357–1370, 2000. (Cited on page 111.)

[Jóźwiak 2011] R. Jóźwiak, A. Przelaskowski and G. Ostrek. *Conceptual improvements in computer-aided diagnosis of acute stroke*. Journal of Medical Informatics & Technologies Selected full texts, vol. 17, pages 191–199, 2011. (Cited on page 54.)

[Kabir 2007] Y Kabir, M Dojat, B Scherrer, F Forbes and C Garbay. *Multimodal MRI segmentation of ischemic stroke lesions*. Conf Proc IEEE Eng Med Biol Soc, vol. 2007, pages 1595–8, 2007. (Cited on pages 76 and 94.)

[Kalafut 2000] M A Kalafut, D L Schriger, J L Saver and S Starkman. *Detection of early CT signs of > 1/3 middle cerebral artery infarctions : interrater reliability and sensitivity of CT inter-*

pretation by physicians involved in acute stroke care. Stroke, vol. 31, no. 7, pages 1667–71, Jul 2000. (Cited on page 98.)

[Kane 2007a] I. Kane, T. Carpenter, F. Chappell, C. Rivers, P. Armitage, P. Sandercock and J.M. Wardlaw. *Comparison of 10 different magnetic resonance perfusion imaging processing methods in acute ischemic stroke effect on lesion size, proportion of patients with diffusion/perfusion mismatch, clinical scores, and radiologic outcomes.* Stroke, vol. 38, no. 12, pages 3158–3164, 2007. (Cited on pages 26 and 47.)

[Kane 2007b] I. Kane, P. Sandercock and J. Wardlaw. *Magnetic resonance perfusion diffusion mismatch and thrombolysis in acute ischaemic stroke: a systematic review of the evidence to date.* Journal of Neurology, Neurosurgery & Psychiatry, vol. 78, no. 5, pages 485–491, 2007. (Cited on pages 53, 54 and 109.)

[Kane 2009] I. Kane, P. Hand, C. Rivers, P. Armitage, M. Bastin, R. Lindley, M. Dennis and J.M. Wardlaw. *A practical assessment of magnetic resonance diffusion-perfusion mismatch in acute stroke: observer variation and outcome.* Journal of neurology, vol. 256, no. 11, pages 1832–1838, 2009. (Cited on page 26.)

[Karonen 2000] J.O. Karonen, Y. Liu, R.L. Vanninen, L. Ãstergaard, P.K. Partanen, P.A. Vainio, E.J. Vanninen, J. Nuutinen, R. Roivainen and S. Soimakallio. *Combined Perfusion-and Diffusion-weighted MR Imaging in Acute Ischemic Stroke during the 1st Week: A Longitudinal Study1.* Radiology, vol. 217, no. 3, pages 886–894, 2000. (Cited on pages 191 and 192.)

[Keir 2000] S. Keir and J.M. Wardlaw. *Systematic review of diffusion and perfusion imaging in acute ischemic stroke.* Stroke, vol. 31, no. 11, pages 2723–2731, 2000. (Cited on pages 26, 40 and 107.)

[Kendall 1989] D.G. Kendall. *A survey of the statistical theory of shape.* Statistical Science, vol. 4, no. 2, pages 87–99, 1989. (Cited on page 112.)

[Kidwell 2000] C.S. Kidwell, J.L. Saver, J. Mattiello, S. Starkman, F. Vinuela, G. Duckwiler, Y.P. Gobin, R. Jahan, P. Vespa and M. Kalafut. *Thrombolytic reversal of acute human cerebral ischemic injury shown by diffusion/perfusion magnetic resonance imaging.* Annals of neurology, vol. 47, no. 4, pages 462–469, 2000. (Cited on page 42.)

[Kidwell 2003] C.S. Kidwell, J.R. Alger and J.L. Saver. *Beyond mismatch.* Stroke, vol. 34, no. 11, pages 2729–2735, 2003. (Cited on pages 107 and 108.)

[Klein 2009] A. Klein, J. Andersson, B.A. Ardekani, J. Ashburner, B. Avants, M.C. Chiang, G.E. Christensen, D.L. Collins, J. Gee and P. Hellier. *Evaluation of 14 nonlinear deformation algorithms applied to human brain MRI registration.* Neuroimage, vol. 46, no. 3, pages 786–802, 2009. (Cited on pages 120, 157 and 232.)

[Kluytmans 2000] M. Kluytmans, K.J. Van Everdingen, L. Kappelle, L. Ramos, M. Viergever and J. Van Der Grond. *Prognostic value of perfusion-and diffusion-weighted MR imaging in first 3 days of stroke.* European Radiology, vol. 10, no. 9, pages 1434–1441, 2000. (Cited on page 191.)

[Koga 2005] M. Koga, D.C. Reutens, P. Wright, T. Phan, R. Markus, B. Pedreira, G. Fitt, I. Lim and G.A. Donnan. *The existence and evolution of diffusion-perfusion mismatched tissue in white and gray matter after acute stroke.* Stroke, vol. 36, no. 10, pages 2132–2137, 2005. (Cited on pages 151 and 191.)

[Konukoglu 2007] E. Konukoglu, O. Clatz, P. Bondiau, M. Sermesant, H. Delingette and N. Ayache. *Towards an identification of tumor growth parameters from time series of images.* Medical Image Computing and Computer-Assisted Intervention-MICCAI 2007, pages 549–556, 2007. (Cited on pages 218 and 232.)

[Konukoglu 2009] E. Konukoglu, O. Clatz, B. Menze, B. Stieltjes, M. Weber, E. Mandonnet, H. Delingette and N. Ayache. *Image guided personalization of reaction-diffusion type tumor growth models using modified anisotropic eikonal equations.* Medical Imaging, IEEE Transactions on, vol. 29, no. 1, pages 77–95, 2009. (Cited on pages 218 and 232.)

[Kranz 2009] P. Kranz and J. Eastwood. *Does diffusion-weighted imaging represent the ischemic core? An evidence-based systematic review.* American Journal of Neuroradiology, vol. 30, no. 6, pages 1206–1212, 2009. (Cited on pages 40, 42 and 150.)

[Kummer 1997] R. Von Kummer, K.L. Allen, R. Holle, L. Bozzao, S. Bastianello, C. Manelfe, E. Bluhmki, P. Ringleb, D.H. Meier and W. Hacke. *Acute stroke: usefulness of early CT findings before thrombolytic therapy.* Radiology, vol. 205, no. 2, pages 327–333, 1997. (Cited on page 50.)

[Le Bihan 1986] D Le Bihan, E Breton, D Lallemand, P Grenier, E Cabanis and M Laval-Jeantet. *MR imaging of intravoxel incoherent motions: application to diffusion and perfusion in neurologic disorders.* Radiology, vol. 161, no. 2, pages 401–7, Nov 1986. (Cited on pages 33 and 52.)

[Lelekov-Boissard 2009] Taïssia Lelekov-Boissard, Guillemette Chapuisat, Jean-Pierre Boissel, Emmanuel Grenier and Marie-

Aimée Dronne. *Exploration of beneficial and deleterious effects of inflammation in stroke: dynamics of inflammation cells*. Philos Transact A Math Phys Eng Sci, vol. 367, no. 1908, pages 4699–716, Dec 2009. (Cited on page 67.)

[Lester 1999] H. Lester and S.R. Arridge. *A survey of hierarchical non-linear medical image registration*. Pattern recognition, vol. 32, no. 1, pages 129–149, 1999. (Cited on page 230.)

[Lev 2000] Statistical shape influence in geodesic active contours, volume Computer Vision and Pattern Recognition, 2000. Proceedings. IEEE Conference on 1. IEEE, 2000. (Cited on page 218.)

[Li 2004] W. Li, J. Tian, E. Li and J. Dai. *Robust unsupervised segmentation of infarct lesion from diffusion tensor MR images using multiscale statistical classification and partial volume voxel reclassification*. Neuroimage, vol. 23, no. 4, pages 1507–18, Dec 2004. (Cited on pages 76 and 94.)

[Li 2009] M Li, L Ai, H He, Z Zheng, B Lv, W Li and J Yi. *Segmentation of infarct in acute ischemic stroke from MR apparent diffusion coefficient and trace-weighted images*. Proceedings of SPIE, 2009. (Cited on page 75.)

[Lorenzi 2010] M. Lorenzi, G. Frisoni, N. Ayache and X. Pennec. *Mapping longitudinal changes in the brain affected by Alzheimer's disease*. hal.archives-ouvertes.fr, 2010. (Cited on page 5.)

[Lorenzi 2012a] M. Lorenzi, N. Ayache and X. Pennec. *Regional flux analysis of longitudinal atrophy in alzheimer's disease*. In Medical Image Computing and Computer-Assisted Intervention–MICCAI 2012, pages 739–746. Springer, 2012. (Cited on page 5.)

[Lorenzi 2012b] M. Lorenzi, N. Ayache, X. Pennec and G. Frisoni. *Differentiating pathological brain atrophy from normal aging: a promising diagnostic tool for Alzheimer's disease*. hal.inria.fr, 2012. (Cited on page 5.)

[Louvet 2011] V. Louvet, M. Massot, M. Duarte, M. Massot, S. Descombes, C. Tenaud, T. Dumont, V. Louvet and F. Laurent. *New Resolution Strategy for Multi-scale Reaction Waves using Time Operator Splitting and Space Adaptive Multiresolution: Application to Human Ischemic Stroke*. vol. 34, pages 277–290, 2011. (Cited on pages 70, 88, 96 and 99.)

[Ma 2011] H.K Ma, J.A Zavala, L. Churilov, J. Ly, P.M Wright, T.G Phan, S. Arakawa, S.M Davis and G.A Donnan. *The hidden mismatch: an explanation for infarct growth without perfusion-weighted imaging/diffusion-weighted imaging mis-*

match in patients with acute ischemic stroke. Stroke, vol. 42, no. 3, pages 662–8, Mar 2011. (Cited on page 53.)

[Maintz 1998] J. Maintz and M.A. Viergever. *A survey of medical image registration.* Medical image analysis, vol. 2, no. 1, pages 1–36, 1998. (Cited on page 230.)

[Majno 1967] G. Majno, A. Ames, J. Chiang and R.L. Wright. *No reflow after cerebral ischemia.* The Lancet, vol. 290, no. 7515, pages 569–570, 1967. (Cited on page 57.)

[Maldjian 2001] J A Maldjian, J Chalela, S E Kasner, D Liebeskind and J A Detre. *Automated CT segmentation and analysis for acute middle cerebral artery stroke.* AJNR Am J Neuroradiol, vol. 22, no. 6, pages 1050–5, 2001. (Cited on pages 77 and 94.)

[Mangin 2004] J.-F. Mangin, D. Riviere, A. Cachia, E. Duchesnay, Y. Cointepas, D. Papadopoulos-Orfanos, P. Scifo, T. Ochiai and F. BrunelleJ. Regis. *A framework to study the cortical folding patterns.* Neuroimage, vol. 23, pages S129–S138, 2004. (Cited on page 218.)

[Maniega 2004] S.M. Maniega, M. Bastin, P. Armitage, A. Farrall, T. Carpenter, P. Hand, V. Cvoro, C. Rivers and J.M. Wardlaw. *Temporal evolution of water diffusion parameters is different in grey and white matter in human ischaemic stroke.* Journal

of Neurology, Neurosurgery & Psychiatry, vol. 75, no. 12, pages 1714–1718, 2004. (Cited on pages 43 and 48.)

[Mansi 2010] T. Mansi, X. Pennec, M. Sermesant, H. Delingette and N. Ayache. *Logdemons revisited: Consistent regularisation and incompressibility constraint for soft tissue tracking in medical images.* pages 652–659, 2010. (Cited on pages 230 and 232.)

[Mantha 2006] A. Mantha, C. Karmonik, G. Benndorf, C. Strother and R. Metcalfe. *Hemodynamics in a cerebral artery before and after the formation of an aneurysm.* American Journal of Neuroradiology, vol. 27, no. 5, pages 1113–1118, 2006. (Cited on page 228.)

[Marchal 1993] G. Marchal, P. Rioux, M.C. Petit-Tabou, J. Derlon, J. Baron, C. Serrati, F. Viader, V. De La Sayette, F. Le Doze and P. Lochon. *PET imaging of cerebral perfusion and oxygen consumption in acute ischaemic stroke: relation to outcome.* The Lancet, vol. 341, no. 8850, pages 925–927, 1993. (Cited on page 25.)

[Martel 1999] A Martel, S Allder, G Delay, P Morgan and A Moody. *Measurement of infarct volume in stroke patients using adaptive segmentation of diffusion weighted MR images.* vol. Medical Image Computing and Computer-Assisted Intervention-

MICCAIâ99, pages 22–31, 1999. (Cited on pages 69, 76 and 77.)

[Matesin 2001] M. Matesin, S. Loncaric and D. Petravic. *A rule-based approach to stroke lesion analysis from CT brain images.* vol. Image and Signal Processing and Analysis, 2001. ISPA 2001. Proceedings of the 2nd International Symposium on, pages 219–223, 2001. (Cited on pages 72 and 74.)

[Mcinerney 1996] T. Mcinerney and D. Terzopoulos. *Deformable models in medical image analysis: a survey.* Medical image analysis, vol. 1, no. 2, pages 91–108, 1996. (Cited on page 230.)

[Meier 2003] D.S. Meier and C.R.G. Guttmann. *Time-series analysis of MRI intensity patterns in multiple sclerosis.* NeuroImage, vol. 20, no. 2, pages 1193–1209, 2003. (Cited on page 5.)

[Meiluonas 2003] M. Meiluonas, A. Usinskas, R. Kirvaitis and R.A. Dobrovolskis. *Automatic contouring of segmented human brain ischemic stroke region on CT images.* Mathematical Modelling and Analysis, vol. 8, no. 1, pages 43–50, 2003. (Cited on pages 72 and 74.)

[Menze 2011] B.H. Menze, E. Stretton, E. Konukoglu and N. Ayache. *Image-based modeling of tumor growth in patients with glioma.* Optimal control in image processing, 2011. (Cited on page 218.)

[Michor 2003] P.W. Michor and D. Mumford. *Riemannian geometries on spaces of plane curves*. arXiv preprint math/0312384, 2003. (Cited on page 218.)

[Mohr 1995] J. Mohr, J. Biller, S. Hilal, W. Yuh, T. Tatemichi, S. Hedges, E. Tali, H. Nguyen, I. Mun and H. Adams. *Magnetic resonance versus computed tomographic imaging in acute stroke*. Stroke, vol. 26, no. 5, pages 807–812, 1995. (Cited on page 40.)

[Montiel 2008] N.H. Montiel, C. Rosso, N. Chupin, S. Deltour, E. Bardinet, D. Dormont, Y. Samson and S. Baillet. *Automatic prediction of infarct growth in acute ischemic stroke from MR apparent diffusion coefficient maps*. Acad Radiol, vol. 15, no. 1, pages 77–83, Jan 2008. (Cited on pages 79 and 80.)

[Moseley 1990] M. Moseley, J. Kucharczyk, J. Mintorovitch, Y. Cohen, J. Kurhanewicz, N. Derugin, H. Asgari and D. Norman. *Diffusion-weighted MR imaging of acute stroke: correlation with T2-weighted and magnetic susceptibility-enhanced MR imaging in cats.* American Journal of Neuroradiology, vol. 11, no. 3, pages 423–429, 1990. (Cited on pages 31, 33, 40, 52 and 55.)

[Muir 2007] K.W Muir, J. Baird-Gunning, L. Walker, T. Baird, M. McCormick and S.B Coutts. *Can the ischemic penum-*

bra be identified on noncontrast CT of acute stroke? Stroke, vol. 38, no. 9, pages 2485–90, Sep 2007. (Cited on page 98.)

[Mukherjee 2000] P. Mukherjee, M.M. Bahn, R.C. Mckinstry, J.S. Shimony, T.S. Cull, E. Akbudak, A.Z. Snyder and T.E. Conturo. *Differences between Gray Matter and White Matter Water Diffusion in Stroke: Diffusion-Tensor MR Imaging in 12 Patients1.* Radiology, vol. 215, no. 1, pages 211–220, 2000. (Cited on page 25.)

[Mullins 2002] M.E. Mullins, P.W. Schaefer, A.G. Sorensen, E.F. Halpern, H. Ay, J. He, W.J. Koroshetz and R.G. Gonzalez. *CT and Conventional and Diffusion-weighted MR Imaging in Acute Stroke: Study in 691 Patients at Presentation to the Emergency Department1.* Radiology, vol. 224, no. 2, pages 353–360, 2002. (Cited on page 40.)

[Murray 2002] J.D. Murray. *Mathematical biology.* vol. 2, 2002. (Cited on page 87.)

[Na 2004] D.G Na, V.N Thijs, G.W Albers, M.E Moseley and M.P Marks. *Diffusion-weighted MR imaging in acute ischemia: value of apparent diffusion coefficient and signal intensity thresholds in predicting tissue at risk and final infarct size.* AJNR Am J Neuroradiol, vol. 25, no. 8, pages 1331–6, Sep 2004. (Cited on pages 55 and 63.)

[Nagakane 2011] Y. Nagakane, S. Christensen, C. Brekenfeld, H. Ma, L. Churilov, M.W Parsons, C.R Levi, K.S Butcher, A. Peeters, P.A Barber, C.F Bladin, D.A De Silva, J. Fink, T.E Kimber, D.W Schultz, K.W Muir, B.M Tress, P.M Desmond, S.M Davis, G.A Donnan and EPITHET Investigators. *EPITHET: Positive Result After Reanalysis Using Baseline Diffusion-Weighted Imaging/Perfusion-Weighted Imaging Co-Registration.* Stroke, vol. 42, no. 1, pages 59–64, Jan 2011. (Cited on pages 63 and 212.)

[Nguyen 2008] V. Nguyen, H. Pien, N. Menenzes, C. Lopez, C. Melinosky, O. Wu, A. Sorensen, G. Cooperman, H. Ay and W. Koroshetz. *Stroke tissue outcome prediction using a spatially-correlated model.* Program and Proceedings of PPIC, vol. 8, pages 238–241, 2008. (Cited on pages 82 and 83.)

[Niethammer 2011] M. Niethammer, Y. Huang and F-X Vialard. *Geodesic regression for image time-series.* pages 655–662, 2011. (Cited on pages 157 and 158.)

[Nomura 1994] Y. Nomura, H. Sakuma, K. Takeda, T. Tagami, Y. Okuda and T. Nakagawa. *Diffusional anisotropy of the human brain assessed with diffusion-weighted MR: relation with normal brain development and aging.* American journal of

neuroradiology, vol. 15, no. 2, pages 231–238, 1994. (Cited on page 38.)

[O'Brien 2004] P O'Brien, R J Sellar and J M Wardlaw. *Fogging on T2-weighted MR after acute ischaemic stroke: how often might this occur and what are the implications?* Neuroradiology, vol. 46, no. 8, pages 635–41, Aug 2004. (Cited on page 55.)

[Ogata 2011] T. Ogata, Y. Nagakane, S. Christensen, H. Ma, B.C.V. Campbell, L. Churilov, J.M. Olivot, P.M. Desmond, G.W. Albers and S.M. Davis. *A Topographic Study of the Evolution of the MR DWI/PWI Mismatch Pattern and Its Clinical Impact.* Stroke, vol. 42, no. 6, pages 1596–1601, 2011. (Cited on page 151.)

[Olivot 2009] J.M. Olivot, M. Mlynash, V.N. Thijs, S. Kemp, M.G. Lansberg, L. Wechsler, R. Bammer, M.P. Marks and G.W. Albers. *Optimal Tmax threshold for predicting penumbral tissue in acute stroke.* Stroke, vol. 40, no. 2, pages 469–475, 2009. (Cited on page 63.)

[Oppenheim 2001] C. Oppenheim, Y. Grandin C. Samson, A. Smith, T. Duprez, C. Marsault and G. Cosnard. *Is there an apparent diffusion coefficient threshold in predicting tissue viability in hyperacute stroke?* Stroke, vol. 32, no. 11, pages 2486–2491, 2001. (Cited on pages 26, 52, 59 and 107.)

[Østergaard 1996a] L. Østergaard, A.G. Sorensen, K.K. Kwong, R.M. Weisskoff, C. Gyldensted and B.R. Rosen. *High resolution measurement of cerebral blood flow using intravascular tracer bolus passages. Part II: Experimental comparison and preliminary results.* Magnetic Resonance in Medicine, vol. 36, no. 5, pages 726–736, 1996. (Cited on page 31.)

[Østergaard 1996b] L. Østergaard, R.M. Weisskoff, D.A. Chesler, C. Gyldensted and B.R. Rosen. *High resolution measurement of cerebral blood flow using intravascular tracer bolus passages. Part I: Mathematical approach and statistical analysis.* Magnetic Resonance in Medicine, vol. 36, no. 5, pages 715–725, 1996. (Cited on pages 31 and 43.)

[Østergaard 1998a] L. Østergaard, P. Johannsen, P. Høst-Poulsen, P. Vestergaard-Poulsen, H. Asboe, A.D. Gee, S.B. Hansen, G.E. Cold, A. Gjedde and C. Gyldensted. *Cerebral blood flow measurements by magnetic resonance imaging bolus tracking: comparison with [(15) O] H2O positron emission tomography in humans.* Journal of cerebral blood flow and metabolism: official journal of the International Society of Cerebral Blood Flow and Metabolism, vol. 18, no. 9, pages 935–940, 1998. (Cited on page 31.)

[Østergaard 1998b] L. Østergaard, D.F. Smith, P. Vestergaard-

Poulsen, S.B. Hansen, A.D. Gee, A. Gjedde and C. Gyldensted. *Absolute cerebral blood flow and blood volume measured by magnetic resonance imaging bolus tracking: comparison with positron emission tomography values.* Journal of Cerebral Blood Flow & Metabolism, vol. 18, no. 4, pages 425–432, 1998. (Cited on pages 31 and 43.)

[Petrella 2000] J R Petrella and J M Provenzale. *MR perfusion imaging of the brain: techniques and applications.* AJR Am J Roentgenol, vol. 175, no. 1, pages 207–19, Jul 2000. (Cited on pages 53 and 59.)

[Pham 2000] D.L. Pham, C. Xu and J.L. Prince. *Current Methods in Medical Image Segmentation 1.* Annual review of biomedical engineering, vol. 2, no. 1, pages 315–337, 2000. (Cited on pages 68, 72, 74, 78, 90 and 94.)

[Phan 2009] T.G. Phan, G.A. Donnan, V. Srikanth, J. Chen and D.C. Reutens. *Heterogeneity in infarct patterns and clinical outcomes following internal carotid artery occlusion.* Archives of neurology, vol. 66, no. 12, page 1523, 2009. (Cited on pages 103, 150 and 228.)

[Pizer 2003] S.M. Pizer, P.T. Fletcher, S. Joshi, A. Thall, J.Z. Chen, Y. Fridman, D.S. Fritsch, A.G. Gash, J.M. Glotzer and M.R. Jiroutek. *Deformable m-reps for 3D medical image segmenta-*

tion. International Journal of Computer Vision, vol. 55, no. 2-3, pages 85–106, 2003. (Cited on page 218.)

[Prakash 2006] K.N.B. Prakash, V. Gupta, M. Bilello, N.J Beauchamp and W.L Nowinski. *Identification, segmentation, and image property study of acute infarcts in diffusion-weighted images by using a probabilistic neural network and adaptive Gaussian mixture model.* Acad Radiol, vol. 13, no. 12, pages 1474–84, Dec 2006. (Cited on page 76.)

[Provenzale 2008] J. Provenzale, K. Shah, U. Patel and D. Mccrory. *Systematic review of CT and MR perfusion imaging for assessment of acute cerebrovascular disease.* American Journal of Neuroradiology, vol. 29, no. 8, pages 1476–1482, 2008. (Cited on page 47.)

[Qiu 2009] A. Qiu, M. Albert, L. Younes and M.I. Miller. *Time sequence diffeomorphic metric mapping and parallel transport track time-dependent shape changes.* NeuroImage, vol. 45, no. 1, pages S51–S60, 2009. (Cited on page 157.)

[Reith 1997] W. Reith, S. Heiland, G. Erb, T. Benner, M. Forsting and K. Sartor. *Dynamic contrast-enhanced T2*-weighted MRI in patients with cerebrovascular disease.* Neuroradiology, vol. 39, no. 4, pages 250–257, 1997. (Cited on page 43.)

[Rekik 2012a] I. Rekik, S. Allassonnière, T.K. Carpenter and J.M. Wardlaw. *Medical Image Analysis Methods in MR/CT-imaged Acute-subacute Ischemic Stroke Lesion: Segmentation, Prediction and Insights into Dynamic Evolution Simulation;* *http://www.sciencedirect.com/science/article/pii/S2213158212000228.* NeuroImage: Clinical, vol. 1, no. 1, pages 164–178, 2012. (Cited on pages 147, 191, 214 and 235.)

[Rekik 2012b] I. Rekik, S. Allassonnière, O. Clatz, E. Geremia, E. Stretton, H. Delingette and N. Ayache. *Tumor growth parameters estimation and source localization from a unique time point: Application to low-grade gliomas;* *http://www.sciencedirect.com/science/article/pii/S1077314212001476* . Computer Vision and Image Understanding, vol. 117, no. 3, pages 238–249, 2012. (Cited on pages 218 and 232.)

[Rekik 2013a] I. Rekik, S. Allassonnière, T.K. Carpenter and J.M. Wardlaw. *Development of longitudinal metamorphosis: application to ischemic stroke lesions on perfusion-weighted imaging and relation to final lesion outcome on T2-w imaging.* Medical Image Analysis, 2013. (Cited on page 236.)

[Rekik 2013b] I. Rekik, S. Allassonnière, T.K. Carpenter and J.M. Wardlaw. *Evaluating acute ischemic stroke to final infarct evo-*

lution using 4D mathematical metamorphosis modeling. Nature Neuroscience, 2013. (Cited on page 236.)

[Rekik 2013c] I. Rekik, S. Allassonnière, S. Durrleman, T.K. Carpenter and J.M. Wardlaw. *Spatiotemporal Dynamic Simulation of Acute Perfusion/Diffusion Ischemic Stroke Lesions Evolution: A Pilot Study Derived from Longitudinal MR Patient Data; http://www.hindawi.com/journals/cmmm/2013/283593.* Computational and Mathematical Methods in Medicine, vol. 2013, no. 283593, page 13, 2013. (Cited on pages 229 and 236.)

[Relan 2011a] J. Relan, P. Chinchapatnam, M. Sermesant, K. Rhode, M. Ginks, H. Delingette, C.A. Rinaldi, R. Razavi and N. Ayache. *Coupled personalization of cardiac electrophysiology models for prediction of ischaemic ventricular tachycardia.* Interface Focus, vol. 1, no. 3, pages 396–407, 2011. (Cited on page 232.)

[Relan 2011b] J. Relan, M. Pop, H. Delingette, G.A. Wright, N. Ayache and M. Sermesant. *Personalization of a cardiac electrophysiology model using optical mapping and MRI for prediction of changes with pacing.* Biomedical Engineering, IEEE Transactions on, vol. 58, no. 12, pages 3339–3349, 2011. (Cited on page 232.)

[Rha 2007] J Rha and J.L Saver. *The impact of recanalization on ischemic stroke outcome: a meta-analysis.* Stroke, vol. 38, no. 3, pages 967–73, Mar 2007. (Cited on page 56.)

[Rivers 2005] C.S. Rivers and J.M. Wardlaw. *What has diffusion imaging in animals told us about diffusion imaging in patients with ischaemic stroke?* Cerebrovascular Diseases, vol. 19, no. 5, pages 328–336, 2005. (Cited on page 40.)

[Rivers 2006] C. Rivers, J. Wardlaw, P. Armitage, M. Bastin, T. Carpenter, V. Cvoro, P. Hand and M. Dennis. *Do acute diffusion- and perfusion-weighted MRI lesions identify final infarct volume in ischemic stroke?* Stroke, vol. 37, no. 1, pages 98–104, 2006. (Cited on pages 57, 97, 136, 137 and 138.)

[Rivers 2007] C.S Rivers, J.M Wardlaw, P.A Armitage, M.E Bastin, P.J Hand and M.S Dennis. *Acute ischemic stroke lesion measurement on diffusion-weighted imaging–important considerations in designing acute stroke trials with magnetic resonance imaging.* J Stroke Cerebrovasc Dis, vol. 16, no. 2, pages 64–70, 2007. (Cited on pages 26, 42, 52, 55, 59 and 197.)

[Rose 2001] S.E. Rose, J.B. Chalk, M.P. Griffin, A.L. Janke, F. Chen, G.J. Mclachan, D. Peel, F.O. Zelaya and H.S. MarkusD.K. Jones. *MRI based diffusion and perfusion predictive model to*

estimate stroke evolution. Magnetic resonance imaging, vol. 19, no. 8, pages 1043–1053, 2001. (Cited on page 83.)

[Rose 2004] S.E Rose, A.L Janke, M. Griffin, M.W Strudwick, S. Finnigan, J. Semple and J.B Chalk. *Improving the prediction of final infarct size in acute stroke with bolus delay-corrected perfusion MRI measures*. J Magn Reson Imaging, vol. 20, no. 6, pages 941–7, Dec 2004. (Cited on page 83.)

[Rosso 2009] C. Rosso, N. Hevia-Montiel, S. Deltour, E. Bardinet, D. Dormont, S. Crozier, S. Baillet and Y. Samson. *Prediction of infarct growth based on apparent diffusion coefficients: penumbral assessment without intravenous contrast material*. Radiology, vol. 250, no. 1, pages 184–92, Jan 2009. (Cited on pages 79 and 80.)

[Sacco 2013] R. Sacco, S. Kasner, J. Broderick, L. Caplan, J. Connors, A. Culebras, M. Elkind, M. George, A. Hamdan and R. Higashida. *on behalf of the American Heart Association Stroke Council, Council on Cardiovascular Surgery and Anesthesia, Council on Cardiovascular Radiology and Intervention, Council on Cardiovascular and Stroke Nursing, Council on Epidemiology and Prevention, Council on Peripheral Vascular Disease, and Council on Nutrition, Physical Activity and Metabolism. An updated definition of stroke for the 21st cen-*

tury: a statement for healthcare professionals from the American Heart Association/American Stroke Association. Stroke, 2013. (Cited on page 15.)

[Saver 2006] J.L. Saver. *Time is brain–quantified.* Stroke, vol. 37, no. 1, pages 263–266, 2006. (Cited on page 3.)

[Scalzo 2012] F. Scalzo, Q. Hao, J. Alger, X. Hu and DS. Liebeskind. *Regional prediction of tissue fate in acute ischemic stroke.* Annals of Biomedical Engineering, pages 1–11, 2012. (Cited on pages 80 and 94.)

[Schaefer 2002] PW. Schaefer, GJ. Hunter, J. He, LM. Hamberg, AG. Sorensen, LH. Schwamm, WJ. Koroshetz and RG. Gonzalez. *Predicting cerebral ischemic infarct volume with diffusion and perfusion MR imaging.* AJNR Am J Neuroradiol, vol. 23, pages 1785–94, 2002. (Cited on page 107.)

[Seo 2009] H.J. Seo and P. Milanfar. *A non-parametric approach to automatic change detection in MRI images of the brain.* vol. Biomedical Imaging: From Nano to Macro, 2009. ISBI'09. IEEE International Symposium on, pages 245–248, 2009. (Cited on page 103.)

[Shen 2004] Qiang Shen, Hongxia Ren, Marc Fisher, James Bouley and Timothy Q Duong. *Dynamic tracking of acute ischemic tissue fates using improved unsupervised ISODATA analysis*

of high-resolution quantitative perfusion and diffusion data. J Cereb Blood Flow Metab, vol. 24, no. 8, pages 887–97, Aug 2004. (Cited on pages 83, 84, 85 and 95.)

[Shen 2005] Q. Shen, H. Ren, M. Fisher and T. Duong. *Statistical prediction of tissue fate in acute ischemic brain injury.* Journal of Cerebral Blood Flow & Metabolism, vol. 25, no. 10, pages 1336–1345, 2005. (Cited on pages 83, 84, 85 and 107.)

[Shen 2008] Q. Shen and T.Q Duong. *Quantitative prediction of ischemic stroke tissue fate.* NMR Biomed, vol. 21, no. 8, pages 839–48, Oct 2008. (Cited on pages 83, 84, 85, 92, 96 and 98.)

[Shih 2003] L.C Shih, J.L Saver, J.R Alger, S. Starkman, M.C Leary, F. Vinuela, G. Duckwiler, Y.P Gobin, R. Jahan, J.P Villablanca, P.M Vespa and C.S Kidwell. *Perfusion-weighted magnetic resonance imaging thresholds identifying core, irreversibly infarcted tissue.* Stroke, vol. 34, no. 6, pages 1425–30, Jun 2003. (Cited on page 63.)

[Soares 2009] B.P Soares, J.D Chien and M. Wintermark. *MR and CT monitoring of recanalization, reperfusion, and penumbra salvage: everything that recanalizes does not necessarily reperfuse!* Stroke, vol. 40, no. 3 Suppl, pages S24–7, Mar 2009. (Cited on page 57.)

[Sobesky 2005] J. Sobesky, O.Z. Weber, F.G. Lehnhardt, V. Hesselmann, M. Neveling, A. Jacobs and W.D. Heiss. *Does the mismatch match the penumbra? Magnetic resonance imaging and positron emission tomography in early ischemic stroke.* Stroke, vol. 36, no. 5, pages 980–985, 2005. (Cited on page 107.)

[Soltanian-Zadeh 2003] H. Soltanian-Zadeh, M. Pasnoor, R. Hammoud, M.A Jacobs, S.C Patel, P.D Mitsias, R.A Knight, Z.G Zheng, M. Lu and M. Chopp. *MRI tissue characterization of experimental cerebral ischemia in rat.* J Magn Reson Imaging, vol. 17, no. 4, pages 398–409, Apr 2003. (Cited on pages 33, 75 and 95.)

[Soltanian-Zadeh 2007] H. Soltanian-Zadeh, H. Bagher-Ebadian, J.R Ewing, P.D Mitsias, A. Kapke, M. Lu, Q. Jiang, S.C Patel and M. Chopp. *Multiparametric iterative self-organizing data analysis of ischemic lesions using pre- or post-Gd T1 MRI.* Cerebrovasc Dis, vol. 23, no. 2-3, pages 91–102, 2007. (Cited on pages 75, 77 and 95.)

[Sorensen 1996] A G Sorensen, F S Buonanno, R G Gonzalez, L H Schwamm, M H Lev, F R Huang-Hellinger, T G Reese, R M Weisskoff, T L Davis, N Suwanwela, U Can, J A Moreira, W A Copen, R B Look, S P Finklestein, B R Rosen and W J Koroshetz. *Hyperacute stroke: evaluation with combined*

multisection diffusion-weighted and hemodynamically weighted echo-planar MR imaging. Radiology, vol. 199, no. 2, pages 391–401, May 1996. (Cited on page 52.)

[Sorensen 1999] A.G. Sorensen, O. Wu, W.A. Copen, T.L. Davis, R.G. Gonzalez, W.J. Koroshetz, T.G. Reese, B.R. Rosen, V.J. Wedeen and R.M. Weisskoff. *Human Acute Cerebral Ischemia: Detection of Changes in Water Diffusion Anisotropy by Using MR Imaging1.* Radiology, vol. 212, no. 3, pages 785–792, 1999. (Cited on page 25.)

[Stein 2001] B. Stein, D. Lisin, J. Horowitz, E. Riseman and G. Whitten. *Statistical and deformable model approaches to the segmentation of MR imagery and volume estimation of stroke lesions.* vol. Medical Image Computing and Computer-Assisted Intervention–MICCAI 2001, pages 829–836, 2001. (Cited on pages 78, 79 and 94.)

[Steinman 2003] D.A. Steinman, J.S. Milner, C.J. Norley, S.P. Lownie and D.W. Holdsworth. *Image-based computational simulation of flow dynamics in a giant intracranial aneurysm.* American Journal of Neuroradiology, vol. 24, no. 4, pages 559–566, 2003. (Cited on page 228.)

[Stejskal 1965] E. Stejskal and J. Tanner. *Spin diffusion measurements: spin echoes in the presence of a time-dependent field*

gradient. The journal of chemical physics, vol. 42, no. 1, page 288, 1965. (Cited on page 34.)

[Straka 2010] M. Straka, G.W. Albers and R. Bammer. *Real-time diffusion-perfusion mismatch analysis in acute stroke*. Journal of Magnetic Resonance Imaging, vol. 32, no. 5, pages 1024–1037, 2010. (Cited on page 90.)

[Strong 2007] A.J. Strong, P.J. Anderson, H.R. Watts, D.J. Virley, A. Lloyd, E.A. Irving, T. Nagafuji, M. Ninomiya, H. Nakamura and A.K. Dunn. *Peri-infarct depolarizations lead to loss of perfusion in ischaemic gyrencephalic cerebral cortex*. Brain, vol. 130, no. 4, pages 995–1008, 2007. (Cited on page 191.)

[Studholme 2006] C. Studholme, C. Drapaca, B. Iordanova and V. Cardenas. *Deformation-based mapping of volume change from serial brain MRI in the presence of local tissue contrast change*. IEEE Trans Med Imaging, vol. 25, no. 5, pages 626–39, May 2006. (Cited on page 103.)

[Sudlow 1997] C. Sudlow and C. Warlow. *Comparable studies of the incidence of stroke and its pathological types: results from an international collaboration*. Stroke, vol. 28, no. 3, pages 491–499, 1997. (Cited on page 2.)

[Symon 1980] L. Symon. *The relationship between CBF, evoked potentials and the clinical features in cerebral ischaemia*. Acta

neurologica Scandinavica. Supplementum, vol. 78, page 175, 1980. (Cited on pages 17 and 107.)

[Takahashi 2005] N. Takahashi, Y. Lee, D-Y Tsai, K. Ishii and S. Kamio. *Improvement in visibility and detectability of early sign of acute stroke in nonenhanced CT images by using an adaptive partial smoothing filter.* Nihon Hoshasen Gijutsu Gakkai Zasshi, vol. 61, no. 11, pages 1531–41, Nov 2005. (Cited on page 98.)

[Taylor 2010] C.A. Taylor and D.A. Steinman. *Image-based modeling of blood flow and vessel wall dynamics: applications, methods and future directions.* Annals of biomedical engineering, vol. 38, no. 3, pages 1188–1203, 2010. (Cited on page 228.)

[Thompson 1996] J.E. Thompson. *The Evolution of Surgery for the Treatment and Prevention of Stroke The Willis Lecture.* Stroke, vol. 27, no. 8, pages 1427–1434, 1996. (Cited on page 14.)

[Tong 1998] D C Tong, M A Yenari, G W Albers, M O'Brien, M P Marks and M E Moseley. *Correlation of perfusion- and diffusion-weighted MRI with NIHSS score in acute (< 6.5 hour) ischemic stroke.* Neurology, vol. 50, no. 4, pages 864–70, Apr 1998. (Cited on pages 26, 52 and 59.)

[Trouvé 1995] A. Trouvé. *An approach of pattern recognition through infinite dimensional group action.* 1995. (Cited on page 157.)

[Trouvé 1998] A. Trouvé. *Diffeomorphisms groups and pattern matching in image analysis.* International Journal of Computer Vision, vol. 28, no. 3, pages 213–221, 1998. (Cited on pages 124 and 157.)

[Trouvé 2005] A. Trouvé and L. Younes. *Metamorphoses through lie group action.* Foundations of Computational Mathematics, vol. 5, no. 2, pages 173–198, 2005. (Cited on pages iii, 163 and 166.)

[Tsai 2005] D-Y Tsai, Y. Lee and N. Takahashi. *An Adaptive Enhancement Algorithm for CT Brain Images.* Conf Proc IEEE Eng Med Biol Soc, vol. 4, pages 3398–401, 2005. (Cited on page 98.)

[Ušinskas 2002] E. Ušinskas A. Pranckeviciene, T. Wittenberg, P. Hastreiter and B.F. Tomandl. *Automatic ischemic stroke segmentation using various techniques.* Neural Network and Soft Computing. Springer, pages 498–503, 2002. (Cited on pages 72 and 74.)

[Ušinskas 2004] A. Ušinskas, R.A. Dobrovolskis and B.F. Tomandl. *Ischemic stroke segmentation on CT images using joint fea-*

tures. Informatica, vol. 15, no. 2, pages 283–290, 2004. (Cited on pages 73 and 74.)

[Unger 1988] E. Unger, J. Littlefield and M. Gado. *Water content and water structure in CT and MR signal changes: possible influence in detection of early stroke.* American journal of neuroradiology, vol. 9, no. 4, pages 687–691, 1988. (Cited on page 50.)

[Vaillant 2005] M. Vaillant and J. Glaunes. *Surface matching via currents.* Information Processing in Medical Imaging; Springer, pages 1–5, 2005. (Cited on pages 112 and 115.)

[Wang 2003] Y. Wang, B.S. Peterson and L.H. Staib. *3D brain surface matching based on geodesics and local geometry.* Computer Vision and Image Understanding, vol. 89, no. 2, pages 252–271, 2003. (Cited on page 111.)

[Warach 1992] S Warach, W Li, M Ronthal and R.R Edelman. *Acute cerebral ischemia: evaluation with dynamic contrast-enhanced MR imaging and MR angiography.* Radiology, vol. 182, no. 1, pages 41–7, Jan 1992. (Cited on pages 40 and 52.)

[Wardlaw 1993] J.M. Wardlaw, M. Dennis, R. Lindley, C. Warlow, P. Sandercock and R. Sellar. *Does early reperfusion of a cerebral infarct influence cerebral infarct swelling in the acute*

stage or the final clinical outcome? Cerebrovascular Diseases, vol. 3, no. 2, pages 86–93, 1993. (Cited on page 56.)

[Wardlaw 1998] J.M Wardlaw, S. Lewis, M. Dennis, C. Counsell and M. Mcdowall. *Is visible infarction on computed tomography associated with an adverse prognosis in acute ischemic stroke?* Stroke, vol. 29, no. 7, pages 1315–1319, 1998. (Cited on pages 53 and 98.)

[Wardlaw 2002] J.M. Wardlaw, S. Keir, M. Bastin, P. Armitage and A. Rana. *Is diffusion imaging appearance an independent predictor of outcome after ischemic stroke?* Neurology, vol. 59, no. 9, pages 1381–1387, 2002. (Cited on page 26.)

[Wardlaw 2003] J.M. Wardlaw, T. West, P. Sandercock, S. Lewis and O. Mielke. *Visible infarction on computed tomography is an independent predictor of poor functional outcome after stroke, and not of haemorrhagic transformation.* Journal of Neurology, Neurosurgery & Psychiatry, vol. 74, no. 4, pages 452–458, 2003. (Cited on page 53.)

[Wardlaw 2005] J.M. Wardlaw and O. Mielke. *Early Signs of Brain Infarction at CT: Observer Reliability and Outcome after Thrombolytic Treatment –Systematic Review1.* Radiology, vol. 235, no. 2, pages 444–453, 2005. (Cited on pages 53 and 54.)

[Wardlaw 2007] J.M. Wardlaw, A.J. Farrall, D. Perry, R. Von Kummer, O. Mielke, T. Moulin, A. Ciccone and M. Hill. *Factors Influencing the Detection of Early CT Signs of Cerebral Ischemia An Internet-Based, International Multiobserver Study.* Stroke, vol. 38, no. 4, pages 1250–1256, 2007. (Cited on pages 53 and 54.)

[Wardlaw 2009] J.M. Wardlaw, V. Murray, E. Berge and G.J. Del Zoppo. *Thrombolysis for acute ischaemic stroke.* Cochrane Database Syst Rev, vol. 4, no. CD000213, 2009. (Cited on pages 27 and 54.)

[Wardlaw 2010] J.M Wardlaw. *Neuroimaging in acute ischaemic stroke: insights into unanswered questions of pathophysiology.* Journal of internal medicine, vol. 267, no. 2, pages 172–190, 2010. (Cited on pages 23, 29, 31, 40, 42, 47, 48, 49, 53, 56, 57, 107, 222, 224 and 228.)

[Wardlaw 2012] J.M. Wardlaw, V. Murray, E. Berge, G. Del Zoppo, P. Sandercock, R.L. Lindley and G. Cohen. *Recombinant tissue plasminogen activator for acute ischaemic stroke: an updated systematic review and meta-analysis.* The Lancet, vol. 379, no. 9834, pages 2364–2372, 2012. (Cited on pages 23, 27, 28, 29 and 42.)

[Weinman 2003] J Weinman, G Bissias, J Horowitz, E Riseman and A Hanson. *Nonlinear diffusion scale-space and fast marching level sets for segmentation of MR imagery and volume estimation of stroke lesions.* Medical Image Computing and Computer-Assisted Intervention-MICCAI 2003, pages 496–504, 2003. (Cited on pages 70, 78, 79 and 94.)

[Wimberger 1995] D.M. Wimberger, T.P. Roberts, A.J. Barkovich, L.M. Prayer, M.E. Moseley and J. Kucharczyk. *Identification of "premyelination" by diffusion-weighted MRI.* Journal of computer assisted tomography, vol. 19, no. 1, pages 28–33, 1995. (Cited on page 38.)

[Wittsack 2002] H. Wittsack. *MR imaging in acute stroke: Diffusion-weighted and perfusion imaging parameters for predicting infarct size1.* 2002. (Cited on page 191.)

[Wu 2001] O. Wu, W. Koroshetz, L. Ostergaard, F. Buonanno, W. Copen, R. Gonzalez, G. Rordorf, B. Rosen, L. Schwamm and R. Weisskoff. *Predicting tissue outcome in acute human cerebral ischemia using combined diffusion-and perfusion-weighted MR imaging.* Stroke, vol. 32, no. 4, page 933, 2001. (Cited on pages 82 and 107.)

[Wu 2007] O. Wu, T. Sumii, M. Asahi, M. Sasamata, L. Ostergaard, B.R Rosen, E.H Lo and R.M Dijkhuizen. *Infarct prediction*

and treatment assessment with MRI-based algorithms in experimental stroke models. J Cereb Blood Flow Metab, vol. 27, no. 1, pages 196–204, Jan 2007. (Cited on page 82.)

[Yang 2011] X. Yang, A. Goh and A. Qiu. *Approximations of the diffeomorphic metric and their applications in shape learning.* vol. Information Processing in Medical Imaging, pages 257–270, 2011. (Cited on page 158.)

[Yotter 2010] R.A Yotter, P.M Thompson, I. Nenadic and C. Gaser. *Estimating local surface complexity maps using spherical harmonic reconstructions.* pages 169–176, 2010. (Cited on page 5.)

[Younes 2009] L. Younes, F. Arrate and M.I. Miller. *Evolutions equations in computational anatomy.* NeuroImage, vol. 45, no. 1, pages S40–S50, 2009. (Cited on page 219.)

[Yuh 1991] W T Yuh, M R Crain, D J Loes, G M Greene, T J Ryals and Y Sato. *MR imaging of cerebral ischemia: findings in the first 24 hours.* AJNR Am J Neuroradiol, vol. 12, no. 4, pages 621–9, 1991. (Cited on page 33.)

[Zanette 1989] E M Zanette, C Fieschi, L Bozzao, C Roberti, D Toni, C Argentino and G L Lenzi. *Comparison of cerebral angiography and transcranial Doppler sonography in acute stroke.* Stroke, vol. 20, no. 7, pages 899–903, Jul 1989. (Cited on page 56.)

[Zhao 2011] L. Zhao, K. Barlinn, A.K. Bag, M. Kesani, L.F. Cava, C. Balucani, A.W. Alexandrov, J.A. Horton, D.E. Patterson and M.R. Harrigan. *Computed tomography perfusion prognostic maps do not predict reversible and irreversible neurological dysfunction following reperfusion therapies.* International Journal of Stroke, vol. 6, no. 6, pages 544–546, 2011. (Cited on page 109.)